Four, Three and Two Coordinated Cu(I) Complexes and their applications as Electrochromic materials

Ph.D. Thesis

By

Kharabe Laxman Sarjerao

DEPARTMENT OF CHEMISTRY

INDIAN INSTITUTE OF TECHNOLOGY INDORE

December 2025

Four, Three and Two Coordinated Cu(I) Complexes and their applications as Electrochromic materials

A THESIS

Submitted in partial fulfillment of the
requirements for the award of the degree
of
DOCTOR OF PHILOSOPHY

by

Kharabe Laxman Sarjerao

DEPARTMENT OF CHEMISTRY
INDIAN INSTITUTE OF TECHNOLOGY INDORE

December 2025

INDIAN INSTITUTE OF TECHNOLOGY INDORE

I hereby certify that the work which is being presented in the thesis entitled "**Four, Three and Two Coordinated Cu(I) Complexes and their applications as Electrochromic materials"** in the partial fulfillment of the requirements for the award of the degree of **DOCTOR OF PHILOSOPHY** and submitted in the **DEPARTMENT OF CHEMISTRY, Indian Institute of Technology Indore**, is an authentic record of my own work carried out during the time period from August 2020 to July 2025 under the supervision of **Dr. Abhinav Raghuvanshi**, Asst. Professor, Department of Chemistry, Indian Institute of Technology Indore.

The matter presented in this thesis has not been submitted by me for the award of any other degree of this or any other institute.

29/12/2025

Signature of the student with date

Kharabe Laxman Sarjerao

This is to certify that the above statement made by the candidate is correct to the best of my/our knowledge.

29/12/2025

Signature of Thesis Supervisor with date

Dr. ABHINAV RAGHUVANSHI

Kharabe Laxman Sarjerao has successfully given his Ph.D. Oral Examination held on 29/12/2025.

29/12/2025

Signature of Thesis Supervisor with date

Dr. ABHINAV RAGHUVANSHI

ACKNOWLEDGEMENTS

It has always been my dream to pursue a career in research and this would not have been possible without my supervisor **Dr. Abhinav Raghuvanshi**. I would like to express my deepest gratitude to him for his support and guidance throughout my Ph.D. journey. I am particularly grateful for his insightful feedback, which challenged me to think critically and refine my ideas. I am also thankful for the patience and understanding he has shown, allowing me the freedom to explore my ideas while providing the necessary guidance to keep me on track.

I would like to thank my PSPC members, **Prof. Apurba K. Das** and **Dr. Amrendra K. Singh**, for their valuable and constructive suggestions to improve my research over the past five years.

I am extremely grateful to **Prof. Rajesh Kumar**, Department of Physics, IIT Indore, for all the help and insightful suggestions during our collaborative work. I would also like to thank Dr. Tanushree Ghosh and Bhumika Sahu for their significant contributions to the electrochemical and electrochromic studies for our collaborative projects.

I extend my gratitude to the dedicated staff members Mr. Manish Kushwaha, Mrs. Vinita Kothari, Mr. Shouvik Debnath and Mr. Rameshwar Dauhare, of the Department of Chemistry, IIT Indore, without whose support in department-related activities and documentation none would have been possible. I am extremely grateful to Mr. Kinny Pandey, Mr. Ghanshyam Bhavsar, Dr. Ravinder and Mr. Nitin Upadhyay for their assistance in the various characterizations from SIC. A sincere appreciation goes to Mr. Tapesh Parihar, and Mr. Rahul Srivas for resolving all academic issues.

I express my sincere thanks to UGC India for their unwavering financial support that has been instrumental in carrying out my research. I would like to thank my lab members, Dr. Shivendu Mishra, Dr. Dilip Pandey, Mr. Anrudh Mishra, Mr. Sarvesh Kumar Maurya, Ms. Jyoti and Mr. Deepak

Kumar at IIT Indore. This journey would not have been possible without my friends Dr. Rajesh T. Bhawale, Mr. Ramakant Gavle, Mr. Kalu Ram Bajya, Dr. Lalita Wagh, Their valuable support and pep talks made the entire Ph.D. journey smooth.

I may have missed mentioning some friends and colleagues by name, I greatly appreciate all their support and help throughout my time at IIT Indore.

Now, I have reached this point where this journey would not have been started without the motivation, invaluable support of my father, Sarjerao Keshavrao Kharabe. It would never be enough to thank what he has done for me to reach this point. I am deeply indebted to my parents, Mr. Sarjerao Kharabe and Parvati Kharabe, my wife, Ashwini Kharabe, and my daughter, Avanisha Kharabe, who have sacrificed everything for my happiness. Their unending support, love, encouragement, and faith in my abilities have helped me accomplish more and better every day. I would like to express my gratitude to my brother, Mr. Nitin Kharabe, and my sister-in-Law, Anita Kharabe, who have encouraged and helped me to pursue my dream smoothly without any hurdles.

At last, I bow down to my Deity, my God for everything……

LAXMAN

Dedicated to God Ganesha and My Family

Synopsis

1. Introduction

Over the past few decades, due to rapid population growth, the demand for optoelectronic devices has increased steadily. A crucial way to address the existing issue of the energy crisis is to figure out ways to conserve and reuse the same. The significant advancements have been achieved in the development of optoelectronic devices, driven by progress in materials science. The Cu(I) complexes have shown promising potential to substitute the traditional heavy transition metal complexes. Copper is earth-abundant, inexpensive, and capable of forming diverse coordination environments, ranging from tetrahedral, trigonal planar to linear geometries *[1–4]*. Additionally, the synthesis of Cu(I) complexes has been extensively explored due to their intriguing photophysical properties, such as tunable emission, high photoluminescence quantum yields and lifetimes, long-lived excited states, and less shelf quenching effects due to d^{10} electronic configuration *[5–7]*. Predominantly, these properties of Cu(I) complexes are subjected to extensive investigation owing to their real-world application in organic light-emitting diodes (OLEDs), light-emitting electrochemical cells (LEECs), biological sensors, catalysis in organic transformations, etc. *[8,9]*.

Though Cu(I) complexes have been explored largely for the preparation of luminescent devices, there is no report for application in the development of electrochromic (EC) devices. The main principle that governs the electrochromic (EC) materials to change their optical property is the bias-induced redox mechanism. Cu(I) complexes exhibit fascinating redox and optical properties that can be easily altered by appropriately using different ligands. This makes them promising materials for electrochromic devices and opens up possibilities for designing electrochromic materials with a broad spectrum of colors and response times.

The thesis attempts to get high performance from ECDs in terms of stability, switching speeds, contrast value, and coloration efficiency using four, three and two-coordinated Cu(I) complexes. The presence of reversible redox-active complexes, different types of ligands, can play essential roles in tuning emissions and electrochromic properties. To develop Cu(I) substituted bidentate ligands, such as dicnq, cmdf and PhBz have been utilized. These ligands provide good conjugation and rigidity, which helps in better charge transfer transitions during the device's performance.

A comprehensive study has been conducted to explore the electrochromic applications of newly synthesized Cu(I) complexes, and the summary of the thesis chapters is discussed as follows:

Chapter 1. General Introduction

This chapter includes an overview of the definite advantages of Cu(I) complexes, including their photophysical properties, structural flexibility, and cost-effectiveness derived from the earth-abundant nature of copper. These attributes collectively validate the selection of the corresponding materials utilized in this thesis, highlighting their potential for practical implementation in electrochromic applications. Also, it contains the introduction of the electrochromism mechanism and electrochromic materials with their ECD performance. The discussion begins by emphasizing the crucial need for advanced strategies and the development of novel materials capable of addressing the inherent limitations of existing technologies. Furthermore, a brief overview of tetrahedral, trigonal planar and linear geometries of Cu(I) complexes is presented, with emphasis on their distinct structural features and photophysical properties, thereby positioning them as promising candidates for a wide range of real-world applications.

Chapter 2. Heteroleptic Cu(I) Complex with Vapochromism and its Application as Electrochromic Material

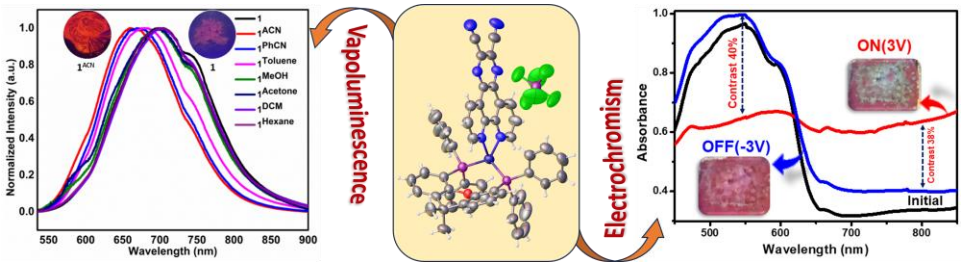

Figure Schematic representation of the vapochromic and electrochromic properties of four-coordinated Cu(I) complexes at room temperature.

This work aims to synthesize four-coordinated heteroleptic Cu(I) complexes using dicnq, a 1,10-phenanthroline-based cyano-substituted ligand, monodentate PPh_3 and a bulky as well as rigid chelating diphosphine ligands such as DPEphos and Xantphos. The synthesized complexes are characterized by multinuclear NMR and HRMS and described as $[Cu(PPh_3)_2(dicnq)]PF_6$ (**1**), $[Cu(DPEphos)(dicnq)]PF_6$ (**2**) and $[Cu(Xantphos)(dicnq)]PF_6$ (**3**). All complexes exhibit absorption within the range of 380-500 nm and emit around 700 nm, attributed to the metal-to-ligand charge transfer transition. Theoretical calculations suggest that the HOMO is predominantly located on the Cu(I) center, while LUMO is associated with the dicnq ligand. Furthermore, 3 was found to show vapoluminescence behavior and blue-shifted emission was observed in the presence of solvent vapors which show π-π interaction with dicnq. Notably, the complex **3** demonstrates electrochromic activity, prompting the fabrication of a device (ITO/P3HT/**3**/ITO) for an in-depth exploration of its electrochromic properties. The working potential range for the device was found to be ±3V. On and Off states show the device has an impressive contrast ratio of ~40% and 38% at 520 nm and 800 nm, respectively. In addition to this, the device shows rapid coloration and bleaching times of 0.8 and 0.5 seconds, respectively. In terms of contrast, switching speed,

stability, and efficiency values at two different wavelengths, the device shows good electrochromic results.

Chapter 3. Redox Dependent Color Modulating Copper(I) Complex for Flexible Electrochromic Device

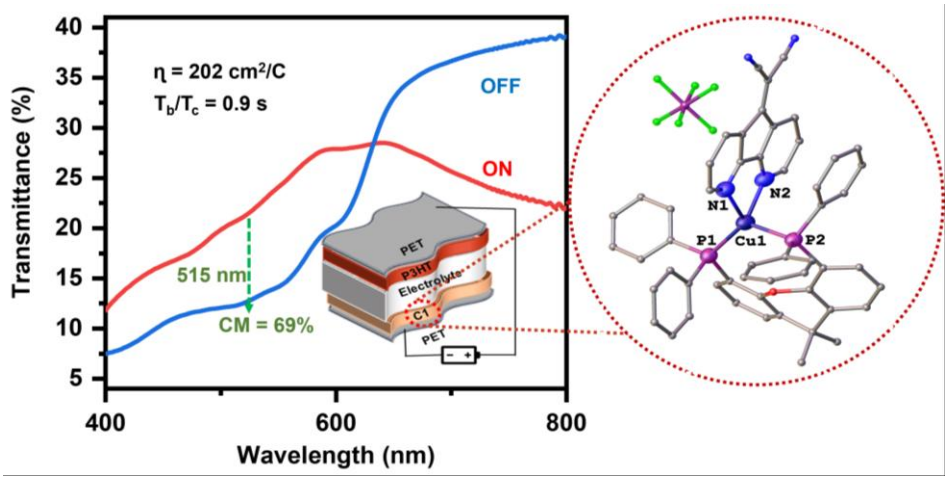

Figure Schematic representation of the response of the developed electrochromic device based on a four-coordinated Cu(I) complex.

This chapter presents the synthesis of heteroleptic copper(I) complexes $[(PPh_3)_2$-Cu-cmdf$]PF_6$ (**4**), [DPEphos-Cu-cmdf]PF_6 (**5**) and [Xantphos-Cu-cmdf]PF_6 (**6**), in high yield, using PPh_3, DPEphos, Xantphos and cmdf ligands. The complex has high thermal stability up to 160 °C and displays low-energy absorption between 360 and 470 nm due to the metal-to-ligand charge transfer (MLCT) transition. The electrochemical analysis confirmed the electrochromic properties of **6**. A bilayer electrochromic device (ECD) incorporating P3HT and **6** demonstrated excellent color modulation (45%) and rapid switching times 0.4 and 1.4 seconds. Furthermore, the flexible ECD utilizing 6 showed superior performance compared to its solid-state counterpart, with high efficiency (~200 cm²/C), color modulation (69%) and the same switching times for both coloration and bleaching which is about 0.9 seconds. The high coloration efficiency and fast switching time of the

ECDs developed from stable and cost-effective Cu(I) complex, 6, make it a promising candidate for real-world electrochromic applications.

Chapter 4. Custom-designed three-coordinated Cu(I) complex for energy-efficient flexible compatible electrochromic smart devices

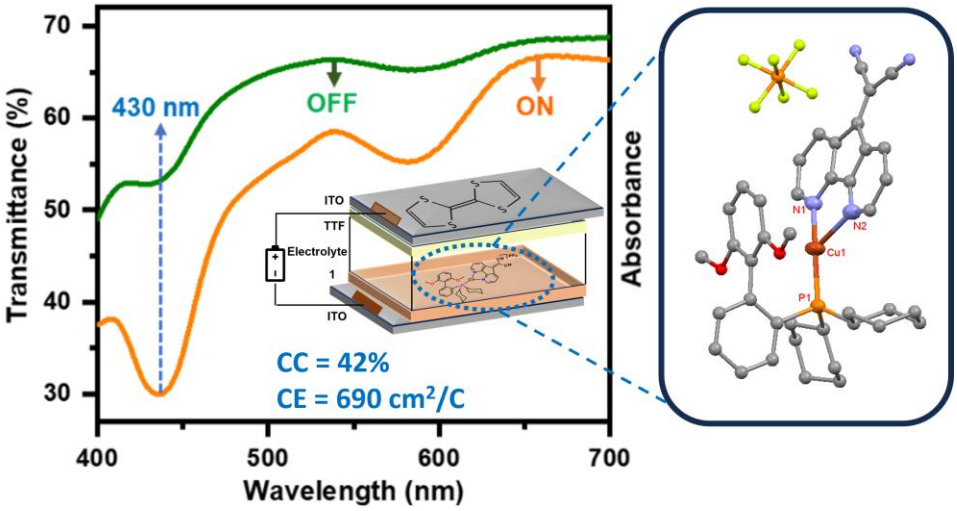

Figure Representation of the ECD performance fabricated from three coordinated Cu(I) complex.

This chapter highlights the first report of the synthesis and characterization of two three-coordinated heteroleptic Cu(I) complexes, [SphosCucmdf]PF_6 (**7**) and [XphosCucmdf]PF_6 (**8**) using bulky phosphine ligands such as Sphos and Xphos. Both complexes show similar absorption in the range of 350 to 470 nm due to MLCT. Furthermore, both complexes exhibit a vivid color change by application of external voltage, confirming the electrochromic nature. Complex 7 exhibits a more prominent redox couple compared to **8**; therefore, **7** was used as EC active layer for the fabrication of ECD to investigate the EC properties. It demonstrates exceptional electrochromic performance in both solid-state and flexible devices. The high color contrast of 42% and a coloration efficiency of 690 cm^2/C of the ECD make it highly promising for various applications. These findings

highlight the potential of Cu(I) complexes as viable alternatives to traditional electrochromic materials.

Chapter 5. Two Coordinated Mono and Bimetallic Cu(I) Complexes for Electrochromic Devices

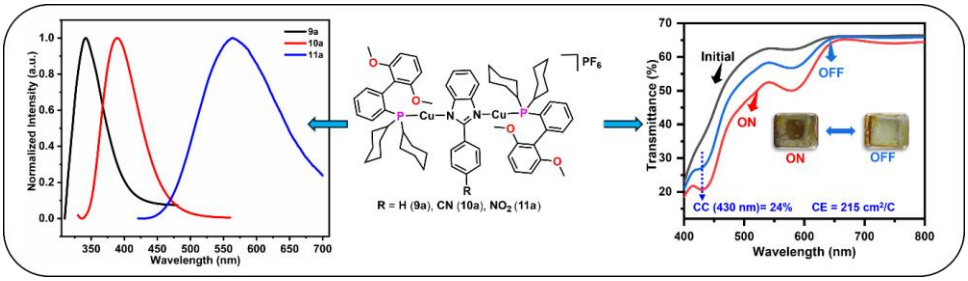

Figure Schematic representation of the tunable emissions and ECD performance fabricated from two coordinated Cu(I) complex 11a.

This study presents the synthesis and photophysical investigation of two-coordinated mono- and bimetallic Cu(I) complexes stabilized by sterically demanding monodentate phosphines such as Sphos and Xphos, while substituted 2-phenylbenzimidazole (PhBz) ligands act as N-donors. Monometallic complexes, [SphosCuPhBz]PF_6 (**9**), [SphosCuCNPhBz]PF_6 (**10**), [SphosCuNO_2PhBz]PF_6 (**11**), [XphosCuPhBz]PF_6 (**12**), [XphosCuCNPhBz]PF_6 (**13**), [XphosCuNO_2PhBz]PF_6 (**14**) and bimetallic [(SphosCu)$_2$PhBz]PF_6 (**9a**), [(SphosCu)$_2$CNPhBz]PF_6 (**10a**), [(SphosCu)$_2$$NO_2$PhBz]$PF_6$ (**11a**), [(XphosCu)$_2$PhBz]PF_6 (**12a**), [(XphosCu)$_2$CNPhBz]PF_6 (**13a**), [(XphosCu)$_2$$NO_2$PhBz]$PF_6$ (**14a**) were synthesized and thoroughly characterized by multinuclear NMR and molecular structures of one of the monometallic and bimetallic complexes were authenticated by SC-XRD analysis. To the best of our knowledge, this constitutes the first report of bimetallic linear two-coordinated Cu(I) complexes. These complexes display tunable emission across the UV-visible range, with nanosecond lifetimes (0.59–2.12 ns). Introduction of electron-withdrawing substituents such as cyano (CN) and nitro (NO_2) groups on the PhBz ligand framework modulates the electronic structure by

stabilizing the LUMO, resulting in progressively narrowed HOMO–LUMO energy gaps and red-shifted absorption/emission profiles. Furthermore, complexes 11 and 11a were utilized for the fabrication of monolayer ECDs. The ECD fabricated from complexes **11** exhibits a coloration efficiency of 58 cm^2/C with 6.6 and 8.5 seconds switching times, whereas the ECD fabricated from complexes **11a** shows a coloration efficiency of 215 cm^2/C with 11.4 and 2.7 seconds switching times. This analysis confirms the electrochromic behavior of two coordinated Cu(I) complexes and they show good performances in terms of color contrast and coloration efficiencies; therefore, they can be used for real-world ECD applications.

Conclusions

This thesis presents an exploration of the luminescence as well as electrochromic properties of newly synthesized four, three, and two coordinated Cu(I) coordination complexes. The findings focus on how their molecular structures and ligand environment influence their photophysical properties and potential for optoelectronic applications. The sightings demonstrate that most of the investigated Cu(I) complexes exhibit semiconducting behavior, which was successfully utilized in the development of electrochromic devices. These findings demonstrate the substantial potential of Cu(I) complexes in these advanced technological domains but also pave the way for future research aimed at improving their properties and extending their range of functionalities for real-world electrochromic applications.

References

1. Czerwieniec R., Leitl M.J., Homeier H.H.H., Yersin H., (2016), Cu(I) Complexes – Thermally Activated Delayed Fluorescence. Photophysical Approach and Material Design, Coord Chem Rev, 325, 2–28 (DOI: 10.1016/j.ccr.2016.06.016)
2. Benesperi I., Singh R., Freitag M., (2020), Copper Coordination Complexes for Energy-Relevant Applications, Energies, 13, 2198 (DOI: 10.3390/en13092198)
3. Zhang Y., Schulz M., Wächtler M., Karnahl M., Dietzek B., (2018), Heteroleptic Diimine–Diphosphine Cu(I) Complexes as an Alternative towards Noble-Metal Based Photosensitizers: Design Strategies, Photophysical Properties and Perspective Applications, Coord Chem Rev, 356, 127–146 (DOI: 10.1016/j.ccr.2017.10.016)
4. Chen J.-L., Cao X.-F., Wang J.-Y., He L.-H., Liu Z.-Y., Wen H.-R., Chen Z.-N., (2013), Synthesis, Characterization, and Photophysical Properties of Heteroleptic Copper(I) Complexes with Functionalized 3-(2′-Pyridyl)-1,2,4-Triazole Chelating Ligands, Inorg Chem, 52, 9727–9740 (DOI: 10.1021/ic4002829)
5. E. Housecroft C., C. Constable E., (2022) TADF: Enabling Luminescent Copper(i) Coordination Compounds for Light-Emitting Electrochemical Cells, J Mater Chem C, 10, 4456–4482 (DOI: 10.1039/D1TC04028F)
6. Linfoot C.L., Leitl M.J., Richardson P., Rausch A.F., Chepelin O., White F.J., Yersin H., Robertson N., (2014), Thermally Activated Delayed Fluorescence (TADF) and Enhancing Photoluminescence Quantum Yields of [CuI(Diimine)(Diphosphine)]+ Complexes—Photophysical, Structural, and Computational Studies, Inorg Chem, 53, 10854–10861 (DOI: 10.1021/ic500889s)
7. Beaudelot J., Oger S., Peruško S., Phan T.-A., Teunens T., Moucheron C., Evano G., (2022), Photoactive Copper Complexes: Properties and

Applications, Chem Rev, 122, 16365–16609 (DOI: 10.1021/acs.chemrev.2c00033)

8. Fresta E., Costa R.D., (2017), Beyond Traditional Light-Emitting Electrochemical Cells – a Review of New Device Designs and Emitters, J Mater Chem C, 5, 5643–5675 (DOI: 10.1039/C7TC00202E)
9. Mahoro G.U., Fernandez-Cestau J., Renaud J.-L., Coto P.B., Costa R.D., Gaillard S., (2020), Recent Advances in Solid-State Lighting Devices Using Transition Metal Complexes Exhibiting Thermally Activated Delayed Fluorescent Emission Mechanism, Adv Opt Mater, 8, 2000260 (DOI: 10.1002/adom.202000260)

List of publications

(A) Outcomes from Ph.D. thesis work:

Papers published:

1. **Laxman Sarjerao Kharabe**, Tanushree Ghosh, Dilip Pandey, Rajesh Kumar, Abhinav Raghuvanshi*
   Heteroleptic Cu(I) Complex with Vapochromism and Its Application as Electrochromic Material. Appl Organomet Chem., 2024, 38 (6), e7451, IF: 4.04, DOI: 10.1002/aoc.7451.
2. **Laxman Sarjerao Kharabe**, Bhumika Sahu, Shivendu Mishra, Rajesh Kumar, Abhinav Raghuvanshi*
   Redox Dependent Color Modulating Copper(I) Complex for Flexible Electrochromic Device, ChemPhotoChem, 2025, 9 (4), e202400354, IF: 2.81, DOI: 10.1002/cptc.202400354.

Papers unpublished:

1. **Laxman Sarjerao Kharabe**, Bhumika Sahu, Rajesh Kumar, Abhinav Raghuvanshi*
   Three-coordinated Cu(I) complexes for electrochromic devices with high coloration efficiency. (Under revision)

(B) Other outcomes outside from Ph.D. thesis work:

Papers published:

1. **Laxman Sarjerao Kharabe**, Khushboo Chaudhari, Anrudh Mishra, Abhinav Raghuvanshi*
   Two-Coordinate Mono- and Bimetallic Cu(I) Complexes: Ligand-Directed Emission and Solvatochromism, J. Organomet. Chem., 2025, 1041, 123841, IF: 2.33 DOI: 10.1016/j.jorganchem.2025.123841.
2. **Laxman Sarjerao Kharabe,** Jyoti Pannu, Lydie Viau, Soumen Ghosh, Abhinav Raghuvanshi*

Three-coordinated Heteroleptic Cu(I) complexes with bulky phosphine ligands: Influence of substituents on photophysical properties, Eur. J. Inorg. Chem. 2025, 28 (30), e202500319, IF: 1.78, DOI: 10.1002/ejic.202500319.

3. Dilip Pandey, Anrudh Mishra, **Laxman Sarjerao Kharabe**, Sarvesh Kumar Maurya, Abhinav Raghuvanshi* Semiconducting Copper(I) Iodide 2D-Coordination Polymers for Efficient Sunlight-Driven Photocatalysis in Dye Degradation, Cryst. Growth Des., 2024, 24 (14), 6051–6059, IF:3.4, DOI: 10.1021/acs.cgd.4c00699.
4. Dilip Pandey, Trivedi Samarth, **Laxman Sarjerao Kharabe**, Anrudh Mishra, Anupam Mishra, Abhinav Raghuvanshi* Manifesting the multi-stimuli-responsive behaviour of triazole-substituted triphenylamine, Luminescence, 2024, 39 (9), 4876-4882, IF: 3.30, DOI: 10.1002/bio.4876
5. Shivendu Mishra, Ajay Meena, **Laxman Sarjerao Kharabe**, Anrudh Mishra, Kuldeep Mahiya, Abhinav Raghuvanshi* Solvent- and stoichiometry-controlled assembly and mechanoresponsive behaviour of carbazole-pyrimidine derived Cu(I) coordination polymers, Cryst. Growth Des., 2025, IF:3.4, DOI: 10.1021/acs.cgd.5c00990

LIST OF CONFERENCES ATTENDED

1. Oral presentation in the Research and Industrial Conclave 2022, IIT Indore.
2. Poster presentation in 21st Modern Trends in Inorganic Chemistry (MTIC-XXI), December 14-17, 2024, IIT Kharagpur, India.
3. Oral presentation in the Chemistry In-house symposium (CHEM 2025).

TABLE OF CONTENTS

Chapter 5

Two Coordinated Mono and Bimetallic Cu(I) Complexes for Electrochromic Devices

LIST OF FIGURES

Chapter 1

Chapter 2

LIST OF TABLES

LIST OF SCHEMES

ABBREVIATIONS

Å	Angstrom
℃	Degree Celsius
θ	Diffraction angle
α	Alpha
mg	Milligram
mmol	Millimole
h	Hour
µL	Microliter
mL	Milliliter
m	Multiplet
V	Volume
Hz	Hertz
s	Second
δ	Chemical shift
cm	Centimeter
r.t.	Room temperature
K	Kelvin
eV	Electron Volt
nm	Nanometer
τ	Lifetime
π	Pi
MHz	Megahertz
T	Temperature
µm	Micrometer
λ	Wavelength
λ_{em}	Emission wavelength
λ_{ex}	Excitation wavelength

λmax	Emission maximum
min	Minute
ms	Millisecond
µs	Microsecond
Φ	Quantum yield
S	Siemen
V	Volt
°	Degree
ppm	Parts per million
k	Wavenumber of photo electron
e	Electron
E_{ads}	Energy of adsorption
C	Coulomb
g	Gram
F	Farade
kW	Kilowatt
Kg	Kilogram
MHz	Megahertz
kHz	Kilohertz
mV	Millivolt
I	Current
A	Ampere

ACRONYMS

Cu	Copper
$CDCl_3$	Chloroform-d
$CHCl_3$	Chloroform
DCM	Dichloromethane
DMSO	Dimethyl sulfoxide
DMF	Dimethyl formamide
ACN	Acetonitrile
FTIR	Fourier transform infrared Spectroscopy
MeOH	Methanol
NMR	Nuclear magnetic resonance
UV-Vis	UV-Visible spectroscopy
TGA	Thermogravimetric analysis
VOC	Volatile organic compounds
MOF	Metal-organic framework
1D	One-dimensional
2D	Two-dimensional
MLCT	Metal-ligand charge transfer
TADF	Thermally activated delayed fluorescence
HE	High energy
LE	Low energy
EC	Electrochromic
ECDs	Electrochromic Devices
CE	Coloration Efficiency
CC	Color Contrast
OD	Optical Density
PLQYs	Photoluminescence quantum yield

Chapter 1

General Introduction

1.1 General Introduction

The worldwide increase in global population, industrialization, and urbanization has concurrently heightened the demand for optoelectronic materials and devices. Scientists and researchers are dedicated to enhancing energy efficiency in the field of optoelectronics. A critical area of innovation addresses the increasing energy demands across various sectors, including buildings, transportation and industries, by developing more efficient optoelectronic materials, devices and systems. The principal aim is to reduce energy consumption while improving performance, contributing to a more sustainable and environmentally responsible future.

Copper is a reddish-brown metal, it has a low cost due to its relatively high abundance in the earth's crust (~60 ppm by mass), therefore, it is produced up to 19,400,000 tonnes per year. The most important feature of copper is that it can be directly used for various applications in electrical wiring, motors, transformers, electronic components, and power generation systems. Additionally, copper-derived materials have comparatively lower toxicity than other transition metal-based counterparts such as nickel, cobalt, cadmium and chromium *[1–4]*. From a biochemical point of view, copper is an essential trace element present in the human body at around 2 mg/kg in cytochrome c oxidase and superoxide dismutase that helps in various enzymatic processes, redox reactions, and electron transport mechanisms within living cells. Overall, these properties of copper make it a highly versatile and indispensable material in industrial, domestic and biological contexts.

According to Hard and Soft Acids and Bases (HSAB) theory, Copper(I) ion acts as a soft Lewis acid which can react with N-, S- and P-donor ligands to form various coordination compounds ranging from discrete molecules to extended multidimensional (0D to 3D) architecture *[5,6]*. Therefore, Copper(I) materials highlight their significance in coordination chemistry and materials science. The commonly observed coordination geometry for

the Cu(I) ion is tetrahedral, four-coordinate (18e$^-$ system), in which the metal center typically coordinates with four monodentate or two bidentate ligands. Additionally, other coordination geometries have been studied for Cu(I) complexes, such as trigonal planar, three-coordinate (16e$^-$ system) and linear, two-coordinate (14e$^-$ system). These low coordinated complexes can be stabilized by using bulky phosphine and carbene ligands. The presence of bulky substituents on the ligand provides sufficient steric hindrance in the complex, which prevents attack by solvent molecules and stabilizes the complex in air as well as in the solution phase.

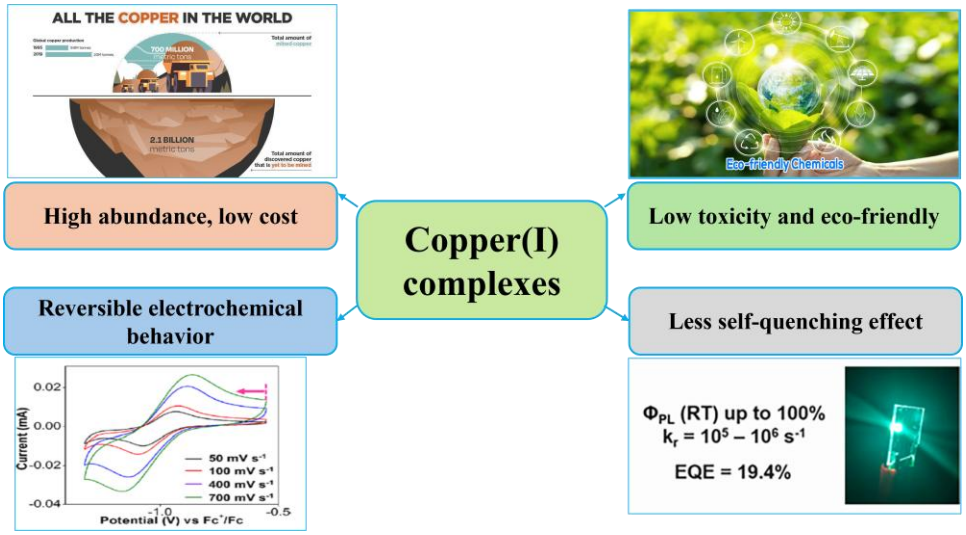

Fig. 1.1 Advantages of Cu(I) complexes.

1.1.1 Properties of Cu(I) complexes

1.1.1.1 Emissive properties

Luminescent materials based on Ir, Pt, Ru, etc. are traditionally used as emitters in optoelectronic devices, due to excellent emission properties with good photoluminescence quantum yields (PLQYs). Because of their high spin-orbit coupling these materials could achieve up to 100% PLQY. The main drawback of such materials is the low abundance in the earth's crust which leads to high cost. Cu(I) materials present a promising alternative to

traditional materials for optoelectronic devices. Particularly, Cu(I) has a d^{10} electronic configuration; therefore, it does not show d-d transitions and has less self-quenching effect, which reduces non-radiative transitions, thereby increasing the PLQYs *[7–9]*. These luminescent complexes generally feature in the emission mechanism of metal-to-ligand charge transfer (MLCT) via thermally activated delayed fluorescence (TADF) due to a small $\Delta E_{S\text{-}T}$ (less than 0.3 eV), resulting in high PLQYs up to 100% *[2,10–12]*. Additionally, the emission behaviour of Cu(I) complexes can be tuned by changing the ligands and modifying the substituents of the ligands *[13–18]*.

In the late 1970s, McMillin and coworkers reported the first homoleptic [Cu(N^N)$_2$] luminescent Cu(I) complexes including **Cu1** *[19]*. Upon photoexcitation, these complexes exhibit flattening distortions (Jahn-Teller distortions) to form a square-planar coordination geometry and nucleophiles (solvent molecules) attack on the Cu center leading to the formation of a five-coordinate exciplex resulting in quenching of emissions, therefore, this gives low photoluminescence quantum efficiencies. To avoid this problem, steric hindrance at the 2,9-positions of the 1,10 phenanthroline ligand has increased and also, synthesis of heteroleptic complexes using phosphine and N^N donor ligands.

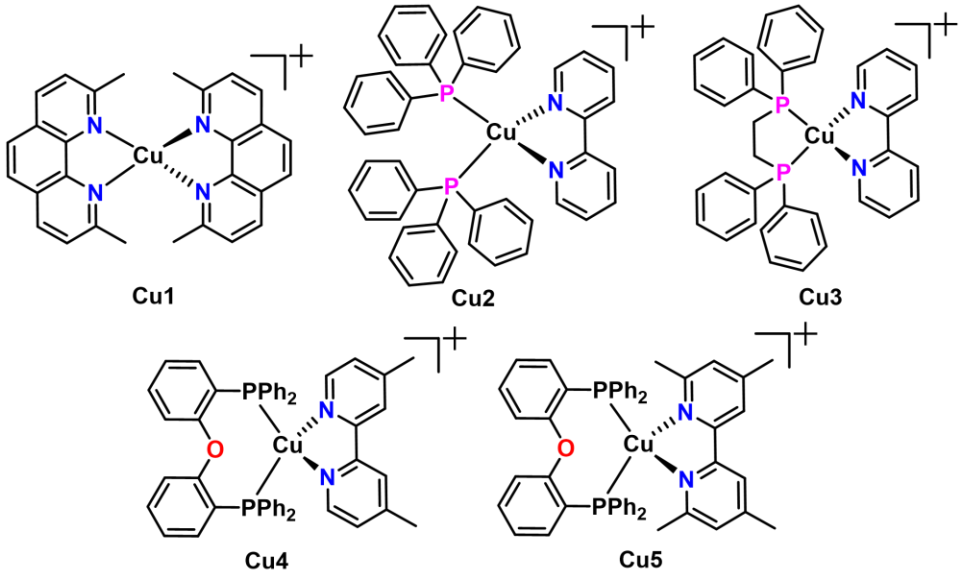

Fig. 1.2 Four-coordinated Cu(I) complexes.

In 1978, heteroleptic Cu(I) complexes, $[Cu(PPh_3)_2(bpy)]^+$ (**Cu2**) and $[Cu(dpe)(bpy)]^+$ (**Cu3**) (dpe = 1,2-bis(diphenyl phosphino)ethene and bpy = 2,2′-Bipyridine) were reported by Buckner and McMillin, These complexes show better emission properties compared to previously reported homoleptic complexes *[20]*. Moving from homoleptic $[Cu(N^N)2]^+$ to heteroleptic $[Cu(P^P)(N^N)]^+$ complexes, photoluminescence behaviour in terms of PLQYs is improved due to nonradiative transitions, much longer excited state lifetimes and less flattening distortions *[21]*. Recently, Yersin, Robertson and coworkers have reported and compared the photophysical properties of $[Cu(POP)(4,4'\text{-}Me_2bpy)][BF_4]$ (**Cu4**) and $[Cu(POP)(4,4',6,6'\text{-}Me_4bpy)][BF_4]$ (**Cu5**) complexes. They found that the rigid and steric hindrance at 6,6'-substituents helps in increasing radiative transitions, leading to increase in the PLQY from 9% to 55% *[9]*.

Though, several four-coordinated Cu(I) complexes have been investigated but due to pseudo-Jahn–Teller (PJT) distortion in the excited state, ligand exchange or dissociation, and relatively weak metal–ligand interactions cause fewer radiative transitions. Because of these limitations, changing the coordination geometry around the Cu(I) center may be an effective strategy

to improve the photophysical properties. The reducing coordination number (three and two) can be achieved by i) using bulky and sterically demanding ligands and ii) enriching the electron-donating capability of the ligand to stabilize the metal center. Furthermore, these three and two-coordinated Cu(I) complexes are less explored.

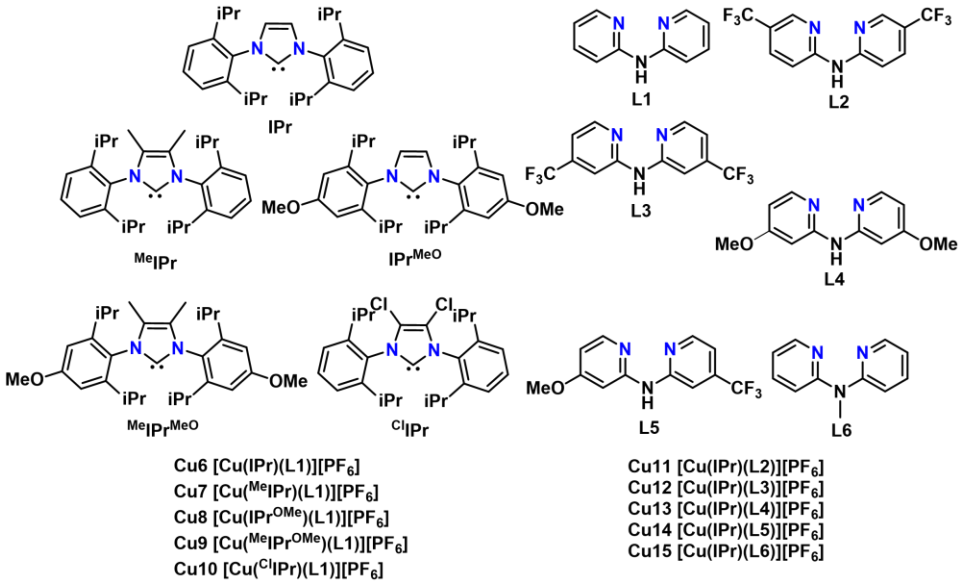

Fig. 1.3 Three-coordinated Cu(I) complexes.

Three coordinated complexes are reported using a sterically demanding N-heterocyclic carbene (NHC) and bidentate (N^N) ligands. In 2016, Gaillard, Costa and coworkers reported a series of three coordinated **Cu6-Cu15** NHC-Cu(I) complexes with 2,2'-dipyridylamine (dpa) derivatives. They have studied the influence of substituents on the photophysical properties of heteroleptic copper(I) complexes and observed a high quantum yield up to 86% *[20]*. There are some disadvantages regarding these types of materials in deciding whether TADF or phosphorescence phenomenon is observed for radiative decay.

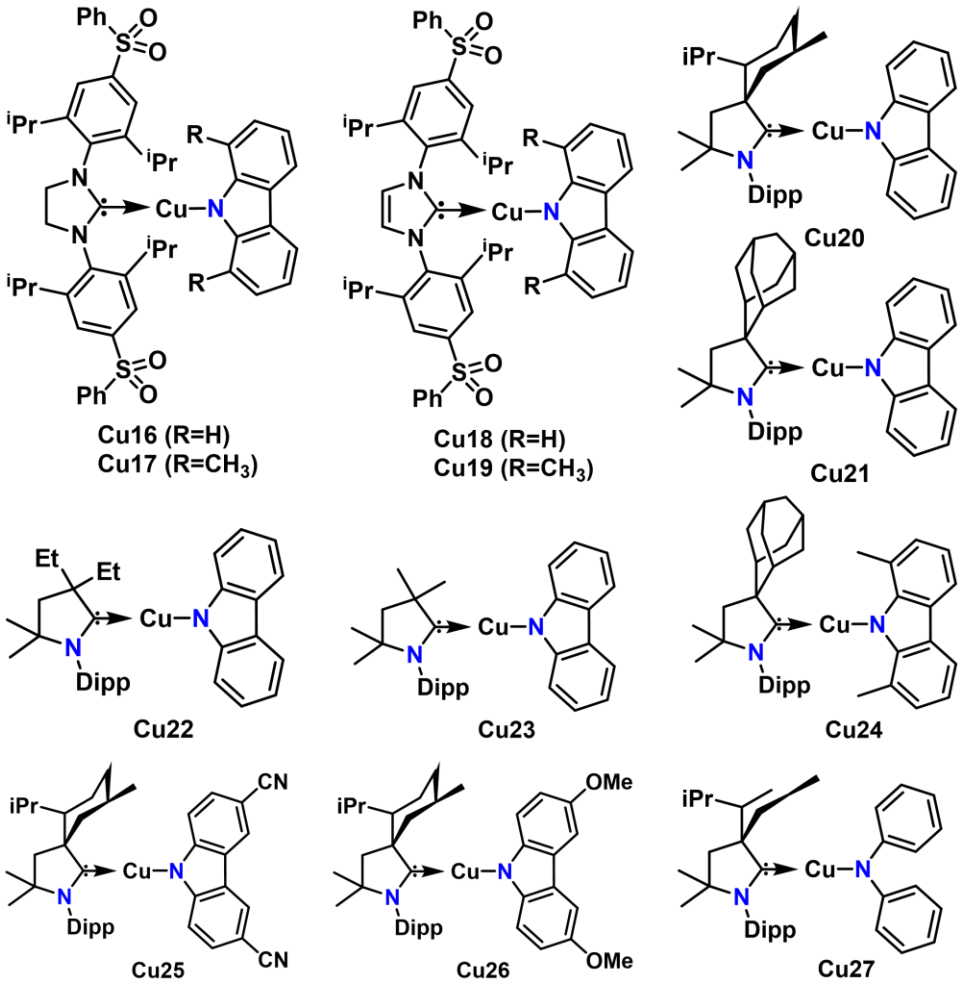

Fig. 1.4 Two-coordinated Cu(I) complexes.

Recently, scientists and researchers have moved towards the synthesis of two-coordinated Cu(I) complexes using electrophilic carbenes as acceptors and electron-rich amides as strong electron donors. Such complexes show emissions via TADF with good quantum efficiencies up to 100%. In 2021, Armands et al. have reported two coordinated NHC-Cu-Amide complexes (**Cu16-Cu19**) using carbazolide and carbene ligands with electron-accepting sulfonyl groups and achieved up to 90% of quantum yield *[21]*. Additionally, Thompson group reported a series of two-coordinate CAAC-Cu-amide complexes (**Cu20-Cu27**) having >99% PLQY *[12]*.

1.1.1.2 Electrochemical properties

Copper(I) complexes exhibit exciting reversible electrochemical properties, in which Cu(I) is converted to Cu(II). The oxidation potentials of these complexes are +0.50 V to +1.00 V *vs* SCE, whereas the reduction potentials are −1.40 V to −1.80 V *vs* SCE, suggesting that they can act as stronger electron donors than acceptors. During the oxidation process, loss of an electron from the HOMO which is localized on the Cu(I) center, while in the reduction, an electron gets added to π* orbitals of the LUMO, which is located on a more electron-withdrawing diimine ligand *[9]*. Furthermore, the redox property of these complexes depends on the electronic and steric effects of both ligands. Electron-withdrawing substituents on the ligands lowers the LUMO energy level, making redox process convenient. Presence of bulky and rigid ligands prevent structural distortions during this redox process. The structural tuning and redox properties of Cu(I) complexes make it a good candidate for real-world optoelectronic applications.

1.1.1.3 Applications of Cu(I) complexes

Cu(I) complexes have found diverse applications in optoelectronic devices including emitters in light-emitting diodes (LEDs), organic light-emitting diodes (OLEDs), light-emitting electrochemical cells (LECs), dye-sensitized solar cells (DSSCs), sensors for oxygen, and photoredox catalysts (**Fig. 1.5**) *[9,22–27]*.

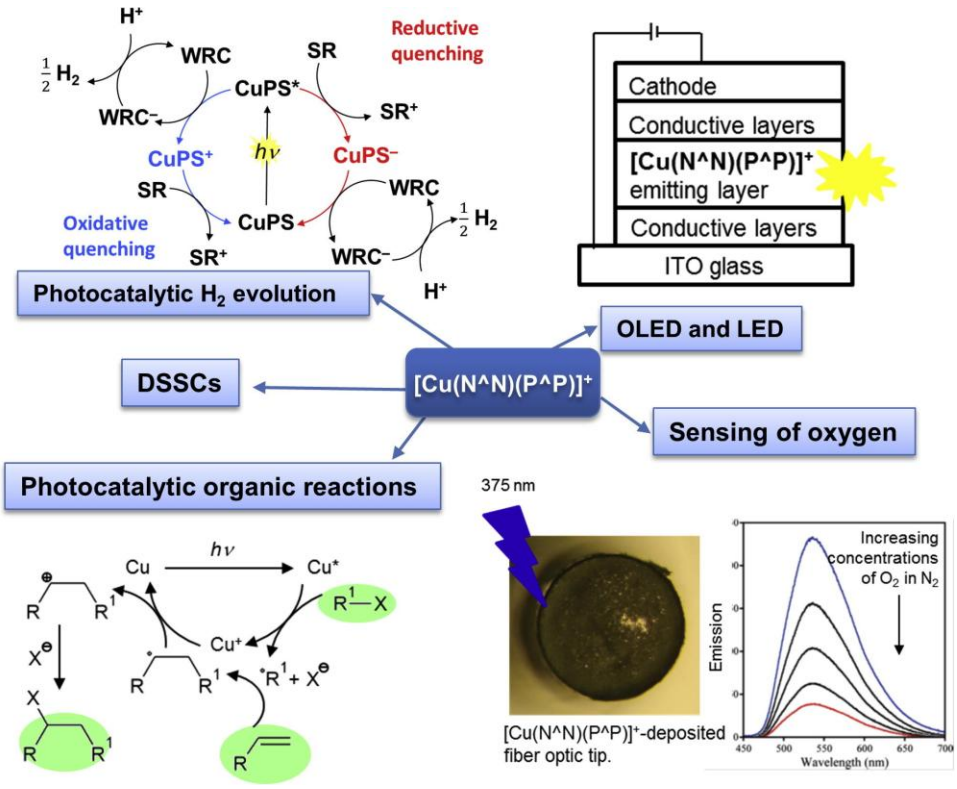

Fig. 1.5 Applications of Cu(I) complexes. Adapted with permission from ref. *[28]* Copyright {2018} Coordination Chemistry Reviews.

1.1.1.4 Optoelectronic Devices (OLEDs and LECs)

The efficient solid-state lighting devices such as LEDs and OLEDs have relatively complex multicomponent or multilayer devices and have replaced the earlier optoelectronic technologies. Further, in the mid-1990s, LECs an alternative viable technology were found. One important difference between OLEDs and LECs is the nature of the emissive material, i.e., OLED is made up of neutral materials while LECs contain charged species.

In 2021, Ying et al. have synthesized two coordinated Cu(I) complexes, [1,3-bis(2,6-diisopropylphenyl)-5,5-dimethyl-4-oxohexahydropyrimidin-2-yl][9,9-diphenylacridin-10(9*H*)-yl]copper(I) (MAC*-Cu-DPAC). They have fabricated an OLED device and achieved a high external quantum efficiency of 21.1% at a maximum and 20.1% at 1000 units *[29]*. In 2023, Wang, Hai-Jie et al. fabricated Vacuum-processed blue OLEDs using Cu(I)

complex which contains CF_3 substituted indolyl type donor and monoamido-amido carbene (MAC) acceptor and the device shows decent EQEs over 20% *[10]*.

R. D. Costa and S. Gaillard's group fabricated LECs using $[Cu(POP)(py_2PMePh)][PF_6]_2$ as the luminophore which shows yellow emission and an efficacy of 0.2 cd A^{-1} *[30]*. Furthermore, they have utilized three coordinated Carbene-Cu(I)-dpa complexes for LEC fabrications and found that this device shows good efficiency up to 0.29 cd/A because it has high PLQY in the solid state *[20]*.

1.1.1.5 Dye-sensitized solar cells (DSSCs)

The first example of a copper-based DSSC was reported by the Sauvage group in 1994. They have used homoleptic bis(2,9-diphenyl-1,10-phenanthroline) copper(I) complex, $[Cu(NN)_2]^+$ as a photosensitizer with TiO_2 film and a ZnO ceramic electrode *[31]*. They provided evidence that Cu(I) complexes are also effective sensitizers for this class of semiconductors. In 2008, Housecroft and Constable groups, with the Gratzel group, reported Cu(I) complexes using 6,6′-disubstituted 2,2′-bipyridines. These are effective sensitizers for TiO_2 and report surprisingly high incident-photon to current efficiencies (IPCE) for DSSCs *[32]*. In 2021, the Inomata and Masuda groups reported three homoleptic copper(I) complexes synthesized from potassium I-2-cyano-3-(6,6′-dimethyl-2,2′-bipyridine-4-yl)acrylate, 2-(3-(4-(dimethylamino)phenyl)-1H-pyrazol-1-yl)-6-methylisonicotinic acid and 6,6′-dimethyl-2,2′-bipyridine-4-carboxylic acid. They have fabricated a DSSC that reached up to 2.66% overall efficiency *[33]*.

The first example of heteroleptic Cu(I) complexes for DSSC was reported by the Robertson group in 2010. They used [CuPOP{*4*,*4′*(R)-bipyridyl}][BF_4] and [CuPOP{*4*,*4′*,*6*,*6′*(R)-bipyridyl}][BF_4] (R = Me, CO_2H, CO_2Et) complexes as emitters in DSSCs, which gives very low

efficiencies up to 0.053% *[34]*. Recently, the Gardner group reported heteroleptic Cu(I) complexes with 6,6′-dimethyl-2,2′-bipyridine-4,4′-dibenzoic acid (dbda) as anchoring ligand and (dmp, dap, bcp ,dsbtmp andbiq as ancillary ligands. They accepted the SALSAC method to synthesize DSSCs and achieved 2.05% overall conversion efficiency from a system based on bcp ligand *[35]*.

1.1.1.6 Sensors for oxygen

Oxygen-responsive luminescent devices fundamentally require two key features: extended excited-state lifetimes and the presence of oxygen-permeable voids. Smith, Conor S et al. have synthesized [Cu(xantphos)(dmp)]tfpb (where xantphos = 4,5-bis(diphenylphosphino)-9,9-dimethylxanthene; dmp = 2,9-dimethyl-1,10-phenanthroline; $tfpb^-$ = tetrakis(bis-3,5-trifluoromethylphenylborate) *[36]*. They have used this complex for oxygen gas sensing. This complex exhibits a good lifetime up to ∼30 μs with 0.66 PLQY, K_{SV} value of 5.65, and high response time about 51 ms for the 95% return constant. Furthermore, Medina-Rodríguez, Santiago, et al. have exchanged the counterion to form a [Cu(xantphos)(dmp)][PF_6] and used it in oxygen sensing. This complex shows better results in terms of K_{SV}, the values are found to be 9.74 kPa^{-1} between 0 to 1 kPa pO_2 and 5.59 kPa^{-1} between 0 and 10 kPa pO_2 *[8]*.

1.1.1.7 Photoredox catalyst

There are several homoleptic $[Cu(N\hat{}N)_2]^+$ and heteroleptic $[Cu(N\hat{}N)(P\hat{}P)]^+$ tri- and tetracoordinated Cu(I) complexes synthesized from diimine, mono or bisphosphine, hybrid P^N, and N-heterocyclic carbene (NHC) ligands were used as photoredox catalysts for organic transformations *[37]*. In 1987, Sauvage group reported the first example of a photoredox catalyst based on Cu(I) complex $[Cu(dap)_2]Cl$ for C–C coupling of benzylic bromides to form bibenzyl derivatives *[38]*.

Xiao, Pu, et al. have reported a heteroleptic Cu(I) complex, $[Cu(dmphen)(Xant)]^+$ for polymerization reaction *[39]*. Additionally, it is found that three coordinated Cu(I) photocatalysts function as highly potent oxidizing agent. Marion, Ronan, et al. have reported a series of NHC-based complexes, out of which $[Cu(mdmdpya)(IPr)]PF_6$ complex exhibits an extremely high ground-state oxidation potential of 1.99 V *[40]*.

1.2 Electrochromic applications

Though the Cu(I) complexes are used in optoelectronic devices, electrochromic applications remain less explored. In 2024, Hossain et al. reported a heterometallo-supramolecular polymer with Cu(I) and Fe(II) (PolyCuFe), which exhibits two reversible redox peaks at 0.29 and 0.78 V due to Cu(I) /Cu(II) and Fe(II) /Fe(III) couples, respectively. Furthermore, they utilized PolyCuFe as an electrochromic active layer in the ECD. This device exhibits multi-colour electrochromic behaviour at 465 and 575 nm by applying various potentials (-2.4, 1.6, -1.8 and 2.2 V), based on the distinct redox potentials of the two metal ions (**Fig. 1.6**) *[41]*. Recently, the same group used the Cu(I)-based metallo-supramolecular polymers (PolyCu) for ECD and found that the film shows a reversible green-to-black EC behaviour upon alternate application of -3 to +1 V, but with higher switching times of 1.35 and 1.04 s, respectively *[42]*.

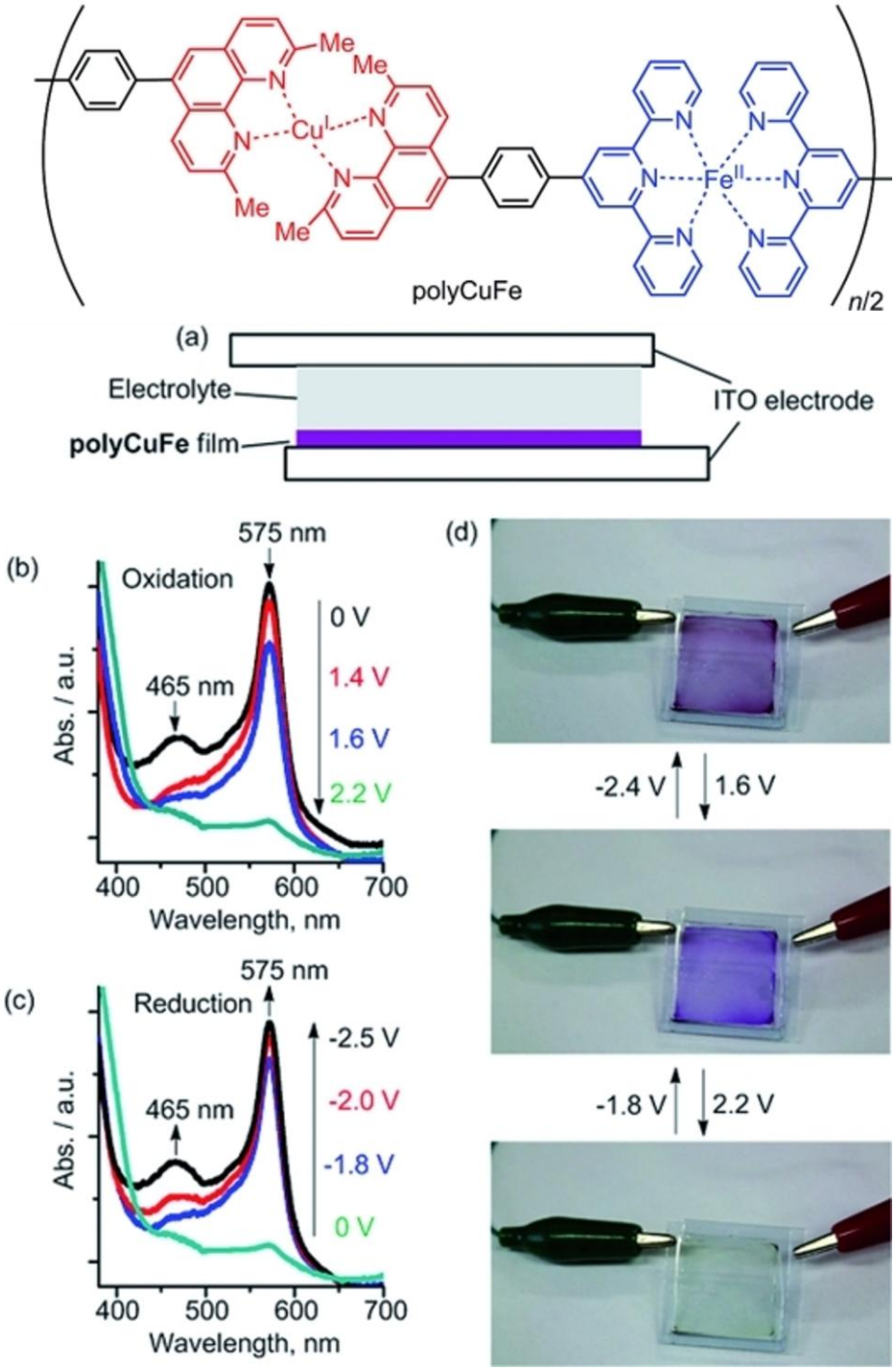

Fig. 1.6 Structure of PolyCuFe and electrochromic performance. Adapted with permission from ref. *[41]* Copyright {2014} European Journal of Inorganic Chemistry.

1.2.1 Electrochromic Properties

With the advancement of modern display technologies, the electrochromic display, a type of non-emissive display, has garnered significant attention. In 1930, a color change was observed by Kobosew and Nekrassow from the electrochemical reduction of a bulk tungsten oxide. Subsequently, in 1961, Platt documented a shift in the absorption and emission spectra of specific dyes when subjected to a strong electric field, coining the term "electrochromism". It can be described as a phenomenon of change in optical properties (color, transmittance, reflectance and absorbance) reversibly by applying external electrical bias. In 1969, Deb demonstrated electrochromism using tungsten oxide films, marking the true inception of electrochromic technology. In 1971, Blanc and Staebler produced an electrochromic (EC) effect which is superior to previously reported results in terms of efficiency and performance. In 1972, Beegle successfully developed a display incorporating identical counter and working electrodes. However, from 1973 to till date Deb's papers are widely cited as this work is responsible for the true beginning of electrochromic technology. In 1975, Faughan et al. made substantial improvements in the development of electrochromic displays and devices (ECDs), contributing to the enhancement of EC technologies. Interest in EC materials began to expand significantly in the mid-1980s, particularly with the introduction of power-efficient EC smart windows in building blocks involving two electrodes and electrolytes. The ability to precisely control the structure and properties of EC materials at the molecular level has opened new research opportunities. This molecular-level manipulation enables the fine-tuning of material characteristics, enhancing performance and expanding the potential uses across various fields. Additionally, industries, residential buildings, and transportation systems are increasingly adopting new technologies and practices designed to enhance energy efficiency which contribute to cost savings and environmental benefits.

1.2.1.1 Electrochromic Devices (ECDs)

The development of efficient electrochromic devices (ECDs) is one of the most important and speedily rising areas of optoelectronics technique. ECDs are a device that changes their color and optical state when an electric potential is applied *[24,43]*. The field of flexible electronics has been rapidly evolving, making the development of flexible electrochromic materials a key research focus *[44]*. This enables the integration of electrochromism with the mechanical adaptability of flexible substrates. Such EC materials can be bent, stretched, or rolled, which enables their applications in wearable electronics, electronic skins and other next-generation devices. Therefore, flexible ECDs have gained significant attention from both academia and industry *[45–49]*. A typical device structure of ECDs is shown in Fig. 1.7.

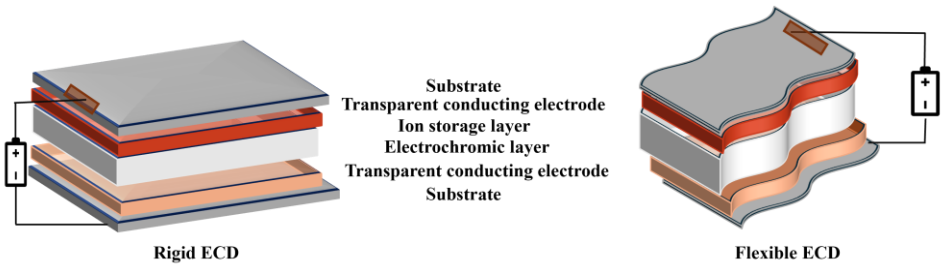

Fig. 1.7 Schematic representation of ECDs with important constituents.

As shown in Fig. 1.7, the electrochromic layer, an electrolyte and ion storage are stacked between two transparent conducting electrodes appropriately to form a solid state ECDs. Based on layers, ECDs can be classified into two types: a) Single layers ECD (only one electrochromic layer) b) Double layer ECDs (active and ion storage layers electrochromic in nature).

1.3 Components of ECD Geometry

1.3.1.1 Electrodes

The electrode substrates can provide the necessary bias to the devices and have maximum transmission or minimum absorption in the visible region. Generally, transparent glass substrates with a coating of indium tin oxide (ITO) and fluorine-doped tin oxide (FTO) substrates are used as electrodes for the fabrication of rigid ECDs. Additionally, these substates have sufficient resistance; ITO-coated and FTO-coated glass substrates have resistance up to 30-33 and 17-19 Ω/cm^2. Furthermore, for making flexible ECDs, ITO-coated glass substrates are replaced by ITO-coated or silver nanowires-coated polyethylene terephthalate (PET) substrates having a resistance of 60-65 Ω/cm^2.

1.3.1.2 Electrolytes

It is one of the most important components in ECD geometry which helps in charge movement or balancing (reversible color change) and the ion exchange process occurring during redox processes which occur when bias is applied to the device. Two types of electrolytes were used: liquid electrolytes (containing Li^+, Na^+, K^+, Zn^{2+}, Mg^{2+}, Ca^{2+}, Al^{3+}, H^+, etc., ions) and gel electrolytes (including hydrogels and organic gels). Liquid electrolytes contain a suitable solute dissolved in a solvent whereas gel electrolyte consists of a polymer gel matrix dissolved in an ionic solvent. A gel electrolyte is better than a liquid electrolyte because it provides appropriate ionic conduction, has less volatility, toxicity and does not have a leakage problem in ECDs. Further, gel electrolytes withstand higher voltages and enable the devices to operate at a higher temperature.

1.3.1.3 Ion storage layer

EC performance can be improved by the addition of an ion storage layer in ECDs and by controlling microstructure and materials. Several ion storage layers were used to fabricate ECDs, NPDS: a dense nickel oxide film (micro-sized NiO particles), a porous NiO film (nano-sized NiO particles) and a porous antimony tin oxide film (nano-sized ATO particles).

1.3.1.4 Electrochromic layer

This is the most important layer in the ECD, the EC materials which are sandwiched between the ion storage and electrode called the electrochromic layer. The EC materials discussed in 1.3.

1.3.2 Performance Parameters of ECD

The performance of ECDs is measured in terms of device parameters, including color contrast (CC), optical density (OD), and coloration efficiency(CE), etc.

1.3.2.1 Color Contrast (CC)

Color contrast is defined to quantify the optical changes that a device experiences when an external bias is applied. It is generally measured at specific wavelengths where the most significant color modulation occurs. By assessing the color contrast at these wavelengths, one can effectively evaluate the extent of optical response and the degree of color variation induced by the bias, offering valuable insights into the device's performance and its capacity for optical manipulation. Color contrast is calculated by the following equation;

$$CC = \frac{T_{on} - T_{off}}{T_{off}} \times 100\% \quad \text{.....1}$$

where, T_{on} represents the transmittance value in the ON condition and T_{off} represents the transmittance value in the OFF condition.

1.3.2.2 Optical Density (OD)

It is related to the optical properties of a material at a particular wavelength, which can be expressed in terms of absorbance or transmittance values. OD is expressed as follows:

$$OD = A \; or \; OD = log10\left(\frac{1}{T}\right) \quad \text{.....2}$$

1.3.2.3 Switching time

Switching (coloring or bleaching) time, also called response time, which is a critical factor for judging the ECDs' performance. The time taken by ECD to switch colors from one state to another is called switching time. In other words, full-switch contrast and time constant unequivocally define the switching process. In practical applications, a short switching time or high switching speed is very important. It depends on the composition of EC material, conductivity of electrolyte and substrate, applied field intensity as well as thickness of film and deposition technique used.

1.3.2.4 Coloration Efficiency (η)

This is one of the most important components of ECDs parameters; it is defined as the ratio of the change in optical density (ΔOD), at a specified wavelength (λ), to the injected or ejected charge (Q) per unit electrode area. The unit of coloration efficiency is cm^2/C and can be calculated by the following equation,

$$CE = \frac{\Delta\, OD\ (\lambda)}{C.D.} \quad \ldots\ldots\ldots\ldots\ldots\ldots\ldots\ldots\ldots\ldots\ldots\ldots\ldots\ldots\ldots\ldots\ldots\ldots 3$$

where CE represents coloration efficiency having unit cm^2/C, $\Delta\ OD\ (\lambda)$ and $C.D.$ represents a change in optical density at a specific wavelength and charge density per unit area, respectively.

The ideal electrochromic material or device would exhibit a large transmittance change with a small amount of charge, giving rise to a high CE.

1.3.2.5 Stability or cycle life

The most important parameter of ECDs is stability or cycle life, it reports how many times an ECD can be switched between the colored states without significant change in other parameters, including switching range, switching speed, transmission level of the bleached and colored (and

intermediate) states. It is usually defined in terms of several absorbance (or ON/OFF) cycles exhibited by ECDs. Additionally, better cycle life could be considered without cosmetic defects such as delamination, uneven coloring or bleaching, and non-switching areas. Applied electric field, environmental conditions and redox switching states of the device play an important role in calculating the stability of ECDs.

1.4 Electrochromic (EC) materials

EC materials have gained significant attention in recent years due to their ability to change optical properties in response to an applied electrical field. Materials that modulate their optical properties reversibly by applying external electrical bias are called EC materials. The phenomenon of electrochromism is attributed to a reversible redox reaction that takes place within the material, leading to changes in optical properties (Absorption, reflection, transmission, etc.) *[45,50–52]*.

1.4.1.1 Types of EC materials

There are different types of materials used for the fabrication of ECDs called electrochromic materials, which are discussed in Fig. 1.8. Electrochromic materials are classified based on their redox-active nature of materials. The p-type materials change their optical property on oxidation (for example, thiophene, pyrrole, nickel oxide, etc.). n-type materials switch their color on reduction (for example, viologens and oxides of vanadium, tungsten, etc.) *[43,53]*. Additionally, several numbers of EC materials have been explored, which can be categorized into organic molecules and conjugated organic polymers, inorganic metal oxides *[54]* (Ta_2O_5, Nb_2O_5, V_2O_3, V_2O_5 WO_3, NiO, MoO_3, MnO_2, CeO_2, $Na_2W_4O_{13}$), hybrid materials, metal plasmonic, metal (Ag, Au, Bi, Cu, Ni, and Mg) alloys, and transition metal complexes or polymers of Fe(II), Ru(II), Os(II), Mo(II), Pt(II), Pd(II), Cu(II), etc *[46,55,56]*. Types of Electrochromic (EC) materials are discussed in detail.

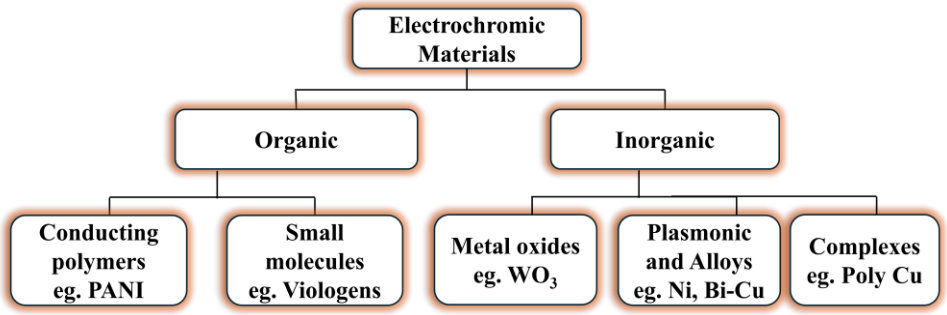

Fig. 1.8 Different types of electrochromic materials used in ECDs.

1.4.1.2 Organic Materials

Organic materials have gained significant attention owing to their inherent solution processability across a diverse array of solvents. This characteristic facilitates the development of flexible and scalable electronic devices, which can be fabricated using solution-based techniques such as inkjet printing, spin coating and roll-to-roll processing. In 2000 Alan J. Heeger, Alan MacDiarmid and Hideki Shirakawa received the Nobel Prize in Chemistry for the discovery and development of conducting organic polymers. Organic EC materials such as poly(3-hexylthiophene-2,5-diyl) (P3HT), viologen *[57]*, polyaniline (PANI) *[58]*, polythiophene, polypyrrole, PCBM, PEDOT, etc. Recently, P3HT and ethyl Viologen (EV) have been widely used to design and improve an electrochromic device for practical application purposes due to low operational driving voltage for color change, high contrast, switchable EC property, and easy cell construction. Additionally, these materials have another advantages including inexpensive, lightweight, flexible and good compatibility. The ECDs fabricated from organic molecules and conjugated polymers exhibit fast response times, high contrast ratios, and multiple colorations.Though some of these materials offer excellent electrochromic properties, there are several disadvantages associated with these materials. For example, organic polymers require multistep synthetic procedures and usually have poor stability, poor conductivity, over-oxidation and low optical contrast.

1.4.1.3 Metal oxides

WO_3 is the first discovered EC material and a widely studied metal oxide for EC applications. Furthermore, different types of metal oxide including SnO_2, Co_3O_4, IrO_2, Fe_3O_4,V_2O_5, MnO_2, RuO_2, Ta_2O_5, NiO, MoO_3, Nb_2O_5,TiO_2, ZnO, etc. were used to fabricate inorganic ECDs. Small cations including H^+, Li^+, etc, inserted into the lattice of inorganic metal oxides and show a change in color due to intervalence charge transfer on the application of bias. Physical and chemical vapour deposition, hydrothermal synthesis and electrochemical deposition methods are used for the preparation of Electrodes for conventional ECDs. EC behaviour can be varied by controlling the thickness and morphology of the deposited inorganic materials, typically in the form of a thin film. They show higher switching speeds in electrolytic medium as compared to solid state devices and have strong adhesion to the substrate. These metal oxides have been used for EC applications with various techniques developed for improved switching and color contrast. Metal oxides have a high bandgap, revealing a challenge to achieving many colors and high production costs and which is a main drawback. Recently, research has focused on multiple color generation, improving film thickness, electrical conductivity, strength, and transparency to improve the device's performance.

1.4.1.4 Metal Plasmonic and alloys

Metal plasmonic and alloys are broadly used as EC materials such as Ag, Bi, Cu, Ni, and Mg alloys from their salts in the EC device cell. They have nanostructures and show reversible electrodeposition as well as insertion and disinsertion of hydrogen in alloy films. When gold or silver nanoparticles are deposited on a transparent matrix show plasmonic absorption in the visible region, flagging the way for their use in EC devices. Metals plasmonic EC materials have been used to achieve multiple colors under low electrical voltage. Additionally, there are several metal alloys, including Ni-Mg, Ag-Cu, Cu-Pb, Bi-Cu, etc., that are generally used as

metal alloys for the fabrication of ECDs. The drawback associated with such EC materials pertains to their low optical contrast and stability regarding size and shape, tendencies toward aggregation and they are quite rare and expensive. The drawback associated with plasmonic materials pertains to their low optical contrast and stability regarding size and shape, primarily due to tendencies toward aggregation. Further, EC film polarizations (cathodic and anodic) are observed due to the interchange in optical states via redox reaction occurring in metal alloys.

1.4.1.5 Metal complexes

EC materials based on transition metal complexes including Fe(II), Ru(II), Os(II), Mo(II), Pt(II), Pd(II), etc. show distinct color changes due to d–d transition or ligand-to-metal charge transfer (LMCT), transitions which involve oxidation and reduction of the metal ions or ligands. Some complexes change their optical properties due to metal-to-ligand and ligand-to-ligand charge transfer (MLCT or LLCT) transitions. The color, stability, and electrochromic properties of metal complexes depend on the steric and electronic effects of the ligands (electron-withdrawing substituents decrease the π^* orbital energy of the ligand, whereas electron-donating substituents show the opposite effect). However, the oxidation states of transition metal ions are distinct and thus only the corresponding colors can be observed. The alteration in bulkiness and electronic properties of the ligands affects color, stability, and electrochemical properties of the corresponding metal–ligand complexes.

The first electrochromic inorganic complex used as EC material is iron(III) hexacyanoferrate(II) [$KFe^{III}[F^{eII}(CN)_6]$], also called Prussian blue. It has three colored electrochemically switchable oxidation states, changing between colorless, blue and brown as displayed. The electrochromism of Prussian blue simple but most impressive experiment for teaching purposes at schools and universities. The electrochemical reaction of Prussian blue can be described as;

$[M_2Fe^{II}Fe^{II}(CN)_6] \rightleftarrows [MFe^{III}Fe^{II}(CN)_6] + M^+ + e- \rightleftarrows [Fe^{III}Fe^{III}(CN)_6] + 2M+ + 2e-$.

Furthermore, there are several transition metal complexes or polymers of Fe(II), Ru(II), Os(II), Mo(II), Pt(II), Pd(II), Cu(II), etc have been used as EC materials *[46,55]*. Metal complexes form a stable, thin film of ECDs and are insoluble in the electrolyte medium. However, the individual colors observed in transition metal compounds are directly related to the significance of their altered oxidation states, this property restricts the realization of gradual color. Further, Cu(II) complexes are synthesized using salen ligands and used as electrochromic materials, but these show less color intensity compared to Ni and Pd-salen complexes in ECDs. The high cost and toxicity of other transition metal complexes make them unfavourable for industrial applications *[59]*. There is a need to overcome these issues associated with the development of EC materials with improved electrochemical performance.

1.5 Applications of ECDs

The potential applications of ECDs are in wearable and deformable optoelectronics, electronic papers, billboards, smart windows, smart labels, variable-reflectance mirrors, auto-dimming rearview mirrors, sensors, energy storage, etc *[60–65]*. They are usually used as auto-dimming rear-view mirrors, variable-reflectance mirrors in automobiles, information displays, and smart windows. Further, EC displays operate through fundamentally different mechanisms compared to conventional light-emitting displays (e.g., LCDs, LEDs, and OLEDs). For example, the light-absorption/reflection-based operation of EC displays permits many remarkable characteristics, such as eye friendliness and a wide viewing angle. The main advantage of EC displays is that we can see-through displays (known as transparent displays), therefore, many industries have tried to launch electronics products based on these displays (Google Glass, OPPO Air Glass, Mi TV LUX see-through television, etc.).

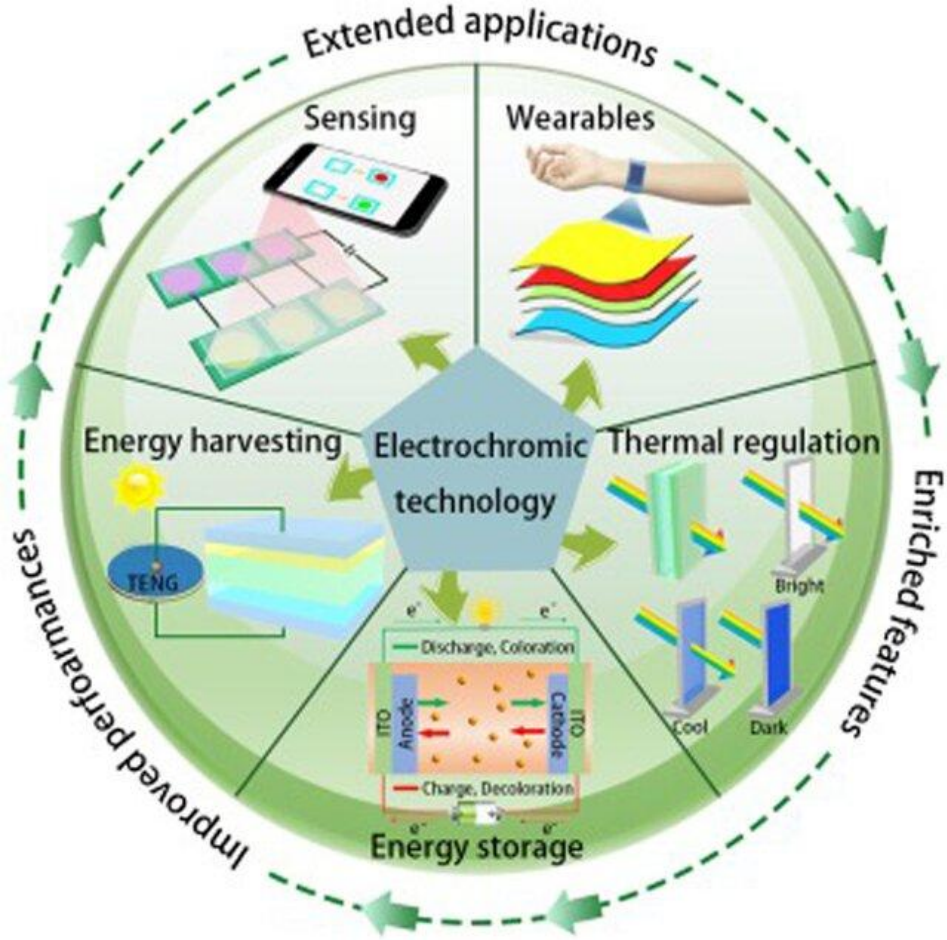

Fig. 1.9 Real-world applications of ECDs. Adapted with permission from ref. *[65]* Copyright {2020} Materials Science and Engineering: R: Reports.

Recently, wearable electronics and electronic skins have been attracting attention because of the increasing demand for real-time information communication and human-computer interaction. The low energy consumption, due to the optical memory effect and low driving voltage, makes them highly suitable for energy-efficient applications. At the last EC, displays are used in energy storage. The visualized EC energy storage will see considerable development as the global energy crisis continues to escalate and intensify.

Considering these applications of ECDs, there is a need to explore better performance and device fabrication technologies. Additionally, a deep understanding of the underlying scientific challenges is essential to

overcome current limitations and accelerate the commercialization of electrochromic (EC) displays, thereby enabling their integration into everyday applications.

1.6 Objectives

Herein, the main objectives are as follows:

- To explore the basic understanding of electrochromic properties of Cu(I) based materials using different electrochromic device geometries (rigid and flexible).
- To understand the various device parameters which involved in the fabrication of ECDs using Cu(I) materials and organic counterparts (P3HT).
- To explore the coordination geometry around Cu(I) to optimize the performance of ECDs using a definite device paradigm.
- To explore the possibility of flexible ECDs for real-world applications in different fields of wearable devices and smart windows.

1.7 References

1. Au V.K.-M., (2021), Organic Light-Emitting Diodes Based on Luminescent Self-Assembled Materials of Copper(I), Energy Fuels 35, 18982–18999, (DOI: 10.1021/acs.energyfuels.1c01956)
2. E Housecroft C., C Constable E., (2022), TADF: Enabling Luminescent Copper(i) Coordination Compounds for Light-Emitting Electrochemical Cells, J Mater Chem C, 10, 4456–4482 (DOI: 10.1039/D1TC04028F)
3. C. Su Z., C. Zheng C., Cheng G., Che C.-M., J. Xu S., (2017), Triplet Harvesting in Luminescent Cu(i) Complexes by the Thermally Activated Luminescence Transition Mechanism: Impact of the Molecular Structure, J Mater Chem C, 5, 4488–4494 (DOI: 10.1039/C7TC00773F)
4. Brown C.M., Carta V., Wolf M.O., (2018), Thermochromic Solid-State Emission of Dipyridyl Sulfoxide Cu(I) Complexes, Chem Mater, 30, 5786–5795 (DOI: 10.1021/acs.chemmater.8b02821)
5. Liu W., Fang Y., Li J., (2018), Copper Iodide Based Hybrid Phosphors for Energy-Efficient General Lighting Technologies, Adv Funct Mater, 28, 1705593 (DOI: 10.1002/adfm.201705593)
6. Cariati E., Lucenti E., Botta C., Giovanella U., Marinotto D., Righetto S., (2016), Cu(I) Hybrid Inorganic–Organic Materials with Intriguing Stimuli Responsive and Optoelectronic Properties, Coord Chem Rev, 306, 566–614 (DOI: 10.1016/j.ccr.2015.03.004)
7. Buckner M.T., McMillin D.R., (1978), Photoluminescence from Copper(I) Complexes with Low-Lying Metal-to-Ligand Charge Transfer Excited States, J Chem Soc Chem Commun, 759, (DOI: 10.1039/c39780000759)
8. Medina-Rodríguez S., J. Orriach-Fernández F., Poole C., Kumar P., Torre-Vega Á. de la, F. Fernández-Sánchez J., Baranoff E., Fernández-Gutiérrez A., (2015), Copper(i) Complexes as Alternatives

to Iridium (III) Complexes for Highly Efficient Oxygen Sensing, Chem Commun, 51, 11401–11404 (DOI: 10.1039/C5CC04326C)

9. Beaudelot J., Oger S., Peruško S., Phan T.-A., Teunens T., Moucheron C., Evano G., (2022), Photoactive Copper Complexes: Properties and Applications, Chem Rev 122, 16365–16609 (DOI: 10.1021/acs.chemrev.2c00033)
10. Wang H.-J., Liu Y., Yu B., Song S.-Q., Zheng Y.-X., Liu K., Chen P., Wang H., Jiang J., Li T.-Y., (2023), A Configurationally Confined Thermally Activated Delayed Fluorescent Two-Coordinate CuI Complex for Efficient Blue Electroluminescence, Angew Chem Int Ed, 62, e202217195 (DOI: 10.1002/anie.202217195)
11. Linfoot C.L., Leitl M.J., Richardson P., Rausch A.F., Chepelin O., White F.J., Yersin H., Robertson N., (2014), Thermally Activated Delayed Fluorescence (TADF) and Enhancing Photoluminescence Quantum Yields of $[Cu^{I}(Diimine)(Diphosphine)]^{+}$ Complexes—Photophysical, Structural, and Computational Studies, Inorg Chem, 53, 10854–10861 (DOI: 10.1021/ic500889s)
12. Hamze R., Peltier J.L., Sylvinson D., Jung M., Cardenas J., Haiges R., Soleilhavoup M., Jazzar R., Djurovich P.I., Bertrand G., (2019), Eliminating Nonradiative Decay in Cu(I) Emitters: >99% Quantum Efficiency and Microsecond Lifetime, Science 363, 601–606 (DOI: 10.1126/science.aav2865)
13. Babgi B.A., (2021), Synthetic Protocols and Applications of Copper(I) Phosphine and Copper(I) Phosphine/Diimine Complexes, J Organomet Chem, 956, 122124 (DOI: 10.1016/j.jorganchem.2021.122124)
14. Hamze R., Jazzar R., Soleilhavoup M., I. Djurovich P., Bertrand G., E. Thompson M., (2017), Phosphorescent 2-, 3- and 4-Coordinate Cyclic (Alkyl)(Amino)Carbene (CAAC) Cu(i) Complexes, Chem Commun, 53, 9008–9011 (DOI: 10.1039/C7CC02638B)

15. Leoni E., Mohanraj J., Holler M., Mohankumar M., Nierengarten I., Monti F., Sournia-Saquet A., Delavaux-Nicot B., Nierengarten J.-F., Armaroli N., (2018), Heteroleptic Copper(I) Complexes Prepared from Phenanthroline and Bis-Phosphine Ligands: Rationalization of the Photophysical and Electrochemical Properties, Inorg Chem 57, 15537–15549 (DOI: 10.1021/acs.inorgchem.8b02879)
16. Li C., Mackenzie C.F.R., Said S.A., Pal A.K., Haghighatbin M.A., Babaei A., Sessolo M., Cordes D.B., Slawin A.M.Z., Kamer P.C.J., (2021), Wide-Bite-Angle Diphosphine Ligands in Thermally Activated Delayed Fluorescent Copper(I) Complexes: Impact on the Performance of Electroluminescence Applications, Inorg Chem, 60, 10323–10339 (DOI: 10.1021/acs.inorgchem.1c00804)
17. Pan X., Kuang X.-N., Zhu N., Wang G., Yang Y.-P., Liu J.-M., Li Z.-F., Xin X.-L., Han H.-L., Jin Q.-H., (2020), Terahertz Time-Domain Absorption Spectra of Cu(i) Complexes Bearing Tetraphosphine Ligands: The Bridge between the C–H···π and Π···π Interactions and Photoluminescence Properties, Dalton Trans, 49, 14941–14950 (DOI: 10.1039/D0DT02542A)
18. Farias G., M. Salla C.A., Toigo J., Alves Duarte L.G.T., J. Bortoluzzi A., Girotto E., Gallardo H., Zambon Atvars T.D., Souza B. de, H. Bechtold I., (2022), Enhancing the Phosphorescence Decay Pathway of Cu(i) Emitters – the Role of Copper–Iodide Moiety, Dalton Trans, 51, 1008–1018 (DOI: 10.1039/D1DT03912A)
19. Blaskie M.W., McMillin D.R., (1980), Photostudies of Copper(I) Systems. 6. Room-Temperature Emission and Quenching Studies of Bis(2,9-Dimethyl-1,10-Phenanthroline)Copper(I), Inorg Chem, 19, 3519–3522 (DOI: 10.1021/ic50213a062)
20. Elie M., Sguerra F., Di Meo F., Weber M.D., Marion R., Grimault A., Lohier J.-F., Stallivieri A., Brosseau A., Pansu R.B., (2016), Designing NHC–Copper(I) Dipyridylamine Complexes for Blue

Light-Emitting Electrochemical Cells, ACS Appl Mater Interfaces, 8, 14678–14691 (DOI: 10.1021/acsami.6b04647)

21. Ruduss A., Turovska B., Belyakov S., Stucere K.A., Vembris A., Traskovskis K., (2022), Carbene–Metal Complexes As Molecular Scaffolds for Construction of through-Space Thermally Activated Delayed Fluorescence Emitters, Inorg Chem, 61, 2174–2185 (DOI: 10.1021/acs.inorgchem.1c03371)
22. Giereth R., Reim I., Frey W., Junge H., Tschierlei S., Karnahl M., (2019), Remarkably Long-Lived Excited States of Copper Photosensitizers Containing an Extended π-System Based on an Anthracene Moiety, Sustain. Energy Fuels, 3, 692–700 (DOI: 10.1039/C8SE00521D)
23. Jin X.-X., Li T., Shi D.-P., Luo L.-J., Su Q.-Q., Xiang J., Xu H.-B., Leung C.-F., Zeng M.-H., (2020), Luminescent Phosphine Copper(i) Complexes with Various Functionalized Bipyridine Ligands: Synthesis, Structures, Photophysics and Computational Study, New J Chem, 44, 13393–13400 (DOI: 10.1039/C9NJ05887G)
24. Ilmi R., Juma Al-busaidi I., Haque A., Khan M.S., (2018), Recent Progress in Coordination Chemistry, Photo-Physical Properties, and Applications of Pyridine-Based Cu(I) Complexes, J Coord Chem, 71, 3045–3076 (DOI: 10.1080/00958972.2018.1509070)
25. Lescop C., (2021), Coordination-Driven Supramolecular Synthesis Based on Bimetallic Cu(I) Precursors: Adaptive Behavior and Luminescence, Chem Rec, 21, 544–557 (DOI: 10.1002/tcr.202000144)
26. Lam C.-H., Tang W.K., Yam V.W.-W., (2023), Synthesis, Electrochemistry, Photophysics, and Photochemistry of a Discrete Tetranuclear Copper(I) Sulfido Cluster, Inorg Chem, 62, 1942–1949 (DOI:10.1021/acs.inorgchem.2c01707)
27. Tao X.-D., Chai W.-X., Song L., Wei Q.-H., Shi H.-S., Qin L.-S., (2018), Two Luminescent Pseudo-Polymorphic Cuprous Complexes

with Different Optical Properties: Synthesis, Characterization and TD-DFT Calculations, Polyhedron, 144, 36–43 (DOI: 10.1016/j.poly.2017.12.039)

28. Zhang Y., Schulz M., Wächtler M., Karnahl M., Dietzek B., (2018), Heteroleptic Diimine–Diphosphine Cu(I) Complexes as an Alternative towards Noble-Metal Based Photosensitizers: Design Strategies, Photophysical Properties and Perspective Applications, Coord Chem Rev, 356, 127–146 (DOI: 10.1016/j.ccr.2017.10.016)
29. Ying A., Huang Y.-H., Lu C.-H., Chen Z., Lee W.-K., Zeng X., Chen T., Cao X., Wu, C.-C., Gong S., (2021), High-Efficiency Red Electroluminescence Based on a Carbene–Cu(I)–Acridine Complex, ACS Appl Mater Interfaces, 13, 13478–13486 (DOI: 10.1021/acsami.0c22109.
30. Umuhire Mahoro G., Fresta E., Elie M., Nasso D. di, Zhang Q., Lohier J.-F., Renaud J.-L., Linares M., Wannemacher R., Cabanillas-Gonzalez J., (2021) Towards Rainbow Photo/Electro-Luminescence in Copper(i) Complexes with the Versatile Bridged Bis-Pyridyl Ancillary Ligand, Dalton Trans, 50, 11049–11060 (DOI: 10.1039/D1DT01689J)
31. Alonso-Vante N., Nierengarten J.-F., Sauvage J.-P., (1994), Spectral Sensitization of Large-Band-Gap Semiconductors (Thin Films and Ceramics) by a Carboxylated Bis(1,10-Phenanthroline)Copper(I) Complex, J Chem Soc Dalton Trans, 0, 1649–1654 (DOI: 10.1039/DT9940001649)
32. Bessho T., C. Constable E., Graetzel M., Redondo A.H., E. Housecroft C., Kylberg W., K. Nazeeruddin M., Neuburger M., Schaffner S., (2008), An Element of Surprise—Efficient Copper-Functionalized Dye-Sensitized Solar Cells, Chem Commun, 0, 3717–3719 (DOI: 10.1039/B808491B)
33. Inomata T., Hatano M., Kawai Y., Matsunaga A., Kitagawa T., Wasada-Tsutsui Y., Ozawa T., Masuda H., (2021), Synthesis and

Physico-Chemical Properties of Homoleptic Copper(I) Complexes with Asymmetric Ligands as a DSSC Dye, Molecules, 26, 6835 (DOI: 10.3390/molecules26226835)

34. L. Linfoot C., Richardson P., E. Hewat T., Moudam O., M. Forde M., Collins A., White F., Robertson N., (2010), Substituted [Cu(i)(POP)(Bipyridyl)] and Related Complexes: Synthesis, Structure, Properties and Applications to Dye -Sensitised Solar Cells, Dalton Trans, 39, 8945–8956 (DOI: 10.1039/C0DT00190B)
35. Franchi D., Leandri V., Pizzichetti A.R.P., Xu B., Hao Y., Zhang W., Sloboda T., Svanström S., Cappel U.B., Kloo L., (2022), Effect of the Ancillary Ligand on the Performance of Heteroleptic Cu(I) Diimine Complexes as Dyes in Dye-Sensitized Solar Cells, ACS Appl Energy Mater, 5, 1460–1470 (DOI: 10.1021/acsaem.1c02778)
36. Smith C.S., Branham C.W., Marquardt B.J., Mann K.R., (2010), Oxygen Gas Sensing by Luminescence Quenching in Crystals of Cu(Xantphos)(Phen)+ Complexes, J Am Chem Soc, 132, 14079–14085 (DOI: 10.1021/ja103112m)
37. M. Hockin B., Li C., Robertson N., Zysman-Colman, E., (2019), Photoredox Catalysts Based on Earth-Abundant Metal Complexes, Catal Sci Technol, 9, 889–915 (DOI: 10.1039/C8CY02336K)
38. Kern J.-M., Sauvage J.-P., (1987), Photoassisted C–C Coupling via Electron Transfer to Benzylic Halides by a Bis(Di-Imine) Copper(I) Complex, J Chem Soc Chem Commun, 0, 546–548 (DOI: 10.1039/C39870000546)
39. Xiao P., Dumur F., Zhang J., Fouassier J.P., Gigmes D., Lalevée J., (2014), Copper Complexes in Radical Photoinitiating Systems: Applications to Free Radical and Cationic Polymerization upon Visible LEDs, Macromolecules, 47, 3837–3844 (DOI: 10.1021/ma5006793)
40. Marion R., Sguerra F., Di Meo F., Sauvageot E., Lohier J.-F., Daniellou R., Renaud J.-L., Linares M., Hamel M., Gaillard S., (2014),

NHC Copper(I) Complexes Bearing Dipyridylamine Ligands: Synthesis, Structural, and Photoluminescent Studies, Inorg Chem, 53, 9181–9191 (DOI: 10.1021/ic501230m)

41. Hossain Md.D., Zhang J., Pandey R.K., Sato T., Higuchi M., (2014), A Heterometallo-Supramolecular Polymer with CuI and FeII Ions Introduced Alternately, Eur J Inorg Chem, 2014, 3763–3770 (DOI: 10.1002/ejic.201402468)
42. Hossain Md.D., Chakraborty C., Rana U., Mondal S., Holdt H.-J., Higuchi M., (2020), Green-to-Black Electrochromic Copper(I)-Based Metallo-Supramolecular Polymer with a Perpendicularly Twisted Structure, ACS Appl Polym Mater, 2, 4449–4454 (DOI: 10.1021/acsapm.0c00559)
43. Rai V., Singh R.S., Blackwood D.J., Zhili D., (2020), A Review on Recent Advances in Electrochromic Devices: A Material Approach, Adv Eng Mater, 22, 2000082 (DOI: 10.1002/adem.202000082)
44. Sahu B., Bansal L., Rath D.K., Kandpal S., Ghosh T., Ahlawat N., Rani C., Maximov M.Y., Kumar R., (2024), Bendable & Twistable Oxide-Polymer Based Hybrid Electrochromic Device: Flexible and Multi-Wavelength Color Modulation. Mater, Today Electron, 7, 100082 (DOI: 10.1016/j.mtelec.2023.100082)
45. Chaudhary A., Sivakumar G., K. Pathak D., Tanwar M., Misra R., Kumar R., (2021), Pentafluorophenyl Substituted Fulleropyrrolidine: A Molecule Enabling the Most Efficient Flexible Electrochromic Device with Fast Switching, J Mater Chem C, 9, 3462–3469 (DOI: 10.1039/D0TC04991C)
46. Wang B., Zhang W., Zhao F., Yu W.W., Elezzabi A.Y., Liu L., Li H., (2023), An Overview of Recent Progress in the Development of Flexible Electrochromic Devices, Nano Mater Sci, 5, 369–391 (DOI: 10.1016/j.nanoms.2022.08.002)
47. Li W., Bai T., Fu G., Zhang Q., Liu, J., Wang H., Sun Y., Yan H., (2022), Progress and Challenges in Flexible Electrochromic Devices,

Sol Energy Mater Sol Cells, 240, 111709 (DOI: 10.1016/j.solmat.2022.111709)

48. Li R., Ma,X., Li J., Cao J., Gao H., Li T., Zhang X., Wang L., Zhang Q., Wang G., (2021), Flexible and High-Performance Electrochromic Devices Enabled by Self-Assembled 2D TiO2/MXene Heterostructures, Nat Commun, 12, 1587 (DOI: 10.1038/s41467-021-21852-7)
49. Eh A.L.-S., Tan A.W.M., Cheng X., Magdassi S., Lee P.S., (2018), Recent Advances in Flexible Electrochromic Devices: Prerequisites, Challenges, and Prospects, Energy Technol, 6, 33–45 (DOI: 10.1002/ente.201700705)
50. Shin D., Kim J., Choi S., Song G., Rougier A., Lee C.S., (2023), Evaluation of Low-Voltage-Driven Multi-Colored Electrochromic Device Based on Dry-Deposited V2O5, Sol Energy Mater Sol Cells, 257, 112341 (DOI: 10.1016/j.solmat.2023.112341)
51. Alesanco Y., Viñuales A., Palenzuela J., Odriozola I., Cabañero G., Rodriguez J., Tena-Zaera R., (2016), Multicolor Electrochromics: Rainbow-Like Devices, ACS Appl Mater Interfaces, 8, 14795–14801 (DOI: 10.1021/acsami.6b01911)
52. Kandpal S., Ghosh T., Rani C., Rani S., Bansal L., Tanwar M., Bhatia R., Sameera I., Kumar R., (2022), MoS2 Doping and Concentration Optimization for Application-Specific Design of P3HT-Viologen-Based Solid State Electrochromic Device, J Phys Appl Phys, 55, 375101 (DOI: 10.1088/1361-6463/ac7426)
53. Kandpal S., Ghosh T., Rani C., Chaudhary A., Park J., Lee P.S., Kumar R., (2023), Multifunctional Electrochromic Devices for Energy Applications, ACS Energy Lett, 8, 1870–1886 (DOI: 10.1021/acsenergylett.3c00159)
54. Ghosh T., Rani C., Kandpal S., Tanwar M., Bansal L., Kumar R., (2022), Chronoamperometric Deposition of Transparent WO3 Film for Application as Power Efficient Electrochromic Auxiliary

Electrode, J Phys Appl Phys 55, 365103 (DOI: 10.1088/1361-6463/ac76f5)

55. Tao C., Li Y., Wang J., (2023), The Progress of Electrochromic Materials Based on Metal–Organic Frameworks, Coord Chem Rev, 475, 214891 (DOI: 10.1016/j.ccr.2022.214891)
56. Kumar R., Pathak D.K., Chaudhary A., (2021), Current Status of Some Electrochromic Materials and Devices: A Brief Review, J Phys Appl Phys, 54, 503002 (DOI: 10.1088/1361-6463/ac10d6)
57. Kumar R., Pillai R.G., Pekas N., Wu Y., McCreery R.L., (2012), Spatially Resolved Raman Spectroelectrochemistry of Solid-State Polythiophene/Viologen Memory Devices, J Am Chem Soc, 134, 14869–14876 (DOI: 10.1021/ja304458s)
58. Ghosh T., Kandpal S., Rani C., Bansal L., Tanwar M., Kumar R., (2023), Multiwavelength Color Switching from Polyaniline-Viologen Bilayer: Inching toward Versatile All-Organic Flexible Electrochromic Device, Adv Electron Mater, 9, 2201042 (DOI: 10.1002/aelm.202201042)
59. Rai V., Singh R.S., Blackwood D.J., Zhili D., (2020), A Review on Recent Advances in Electrochromic Devices: A Material Approach, Adv Eng Mater, 22, 2000082 (DOI: 10.1002/adem.202000082)
60. Argazzi R., Murakami Iha N.Y., Zabri H., Odobel F., Bignozzi C.A., (2004), Design of Molecular Dyes for Application in Photoelectrochemical and Electrochromic Devices Based on Nanocrystalline Metal Oxide Semiconductors, Coord Chem Rev, 248, 1299–1316 (DOI: 10.1016/j.ccr.2004.03.026)
61. Cannavale A., Ayr U., Fiorito F., Martellotta F., (2020), Smart Electrochromic Windows to Enhance Building Energy Efficiency and Visual Comfort, Energies, 13, 1449 (DOI: 10.3390/en13061449)
62. Bansal L., Sahu B., Rath D.K., Ahlawat N., Ghosh T., Kandpal S. Kumar R., (2024), Stoichiometrically Optimized Electrochromic Complex [V2O2+ξ(OH)3-ξ] Based Electrode: Prototype

Supercapacitor with Multicolor Indicator, Small, 20, 2312215 (DOI: 10.1002/smll.202312215)

63. Sahu B., Bansal L., Ghosh T., Kandpal S., Rath D.K., Rani C., Wesemann C., Bigall N.C., Kumar R., (2024), Metal Oxide-Mixed Polymer-Based Hybrid Electrochromic Supercapacitor: Improved Efficiency and Dual Band Switching, J Phys Appl Phys 57, 245110 (DOI: 10.1088/1361-6463/ad2dba)
64. Maraveas C., Loukatos D., Bartzanas T., Arvanitis K.G., Uijterwaal J.F., (2021), Smart and Solar Greenhouse Covers: Recent Developments and Future Perspectives, Front Energy Res, 9 (DOI: 10.3389/fenrg.2021.783587)
65. Wang Z., Wang X., Cong S., Geng F., Zhao Z., (2020), Fusing Electrochromic Technology with Other Advanced Technologies: A New Roadmap for Future Development, Mater Sci Eng R Rep, 140, 100524 (DOI: 10.1016/j.mser.2019.100524)

Chapter 2

Heteroleptic Cu(I) Complex with Vapochromism and its Application as Electrochromic Material

2.1 Introduction

A crucial way to address the existing energy crisis is to find ways to conserve and reuse energy. Scientists and researchers worldwide are contributing to the development of technologies such as batteries, supercapacitors, and solar panels, among others *[1–4]*. electrochromic devices (ECD) which change color on the application of the bias, stand on the same list and are being extensively studied as they behave as heat regulators by blocking or allowing certain components of the electromagnetic spectra. Among several materials, metal-organic frameworks with Cu metal have shown potential for the development of electrochromic materials *[5]*.

Herein, we have synthesized a heteroleptic Cu(I) complexes, $[Cu(PPh_3)_2(dicnq)]PF_6$ (**1**), $[Cu(DPEphos)(dicnq)]PF_6$ (**2**) and $[Cu(Xantphos)(dicnq)]PF_6$ (**3**) using different phosphine (PPh_3, DPEphos and Xantphos) and dicnq ligands. The phosphine ligands and rigid π-conjugated systems of dicnq could prevent the formation of exciplexes and dimeric aggregates as well as bending or rotation around the skeleton of the molecule therefore, such types of complexes show higher emission efficiency *[6–9]*. These complexes show emission at around 700 nm in both solid and solution. The complex **3** exhibited vapochromism in the solid state and was found to show blue-shifted emission in some solvent vapors. Moreover, complex **3** has been tested for electrochromic behavior and was found to be electrochromic active. The material has been coupled with another popular electrochromic active material, namely poly(3-hexylthiophene-2,5-diyl) (P3HT), in a well-established methodology so that a more efficient and practically viable device can be fabricated.

2.2 Experimental Section

2.2.1.1 Materials

Materials obtained from commercial suppliers were used without further purification unless otherwise stated. All glassware, magnetic stirring bars were thoroughly dried in a hot air oven. Reactions were monitored using thin-layer chromatography (TLC). Commercial TLC plates were used, and the spots were visualized under UV light at 365 nm. The complexation reactions have been performed using Schlenk techniques under a nitrogen atmosphere. The Xantphos ligand was purchased from Spectrochem, and dicnq was synthesized according to the literature procedure *[10]*. $[Cu(CH_3CN)_4]PF_6$ was synthesized using the reported procedure *[11]*.

2.2.1.2 Characterization methods

^{1}H, $^{13}C\{^{1}H\}$, and $^{31}P\{^{1}H\}$ NMR were recorded on a Fourier transform nuclear magnetic resonance spectrometer, model Bruker Avance 500 MHz spectrometer. ^{1}H and $^{13}C\{^{1}H\}$ NMR spectra were referenced relative to the residual solvent peak. The abbreviations such as s (singlet), d (doublet), t (triplet), dd (doublet of doublets), td (triplet of doublets), dt (doublet of triplet), m (multiplet), etc. are used for the multiplicity assignment. High-resolution mass spectral analyses (HRMS) were recorded on a Bruker-Daltonics micrOTOF-Q II mass spectrometer. Single crystal X-ray structural studies of crystals were performed on a XtaLAB Synergy – I Diffraction system (Dual Micro–focus source), made Rigaku Corporation, Japan. Using Olex 2 *[12]* the structure was solved with the SHELXT structure solution program using Intrinsic Phasing and refined with the SHELXL *[13]* refinement package using Least Squares minimization. Thermogravimetric analysis was performed on the powder sample using METTLER TOLEDO TGA/DSC 1 STARe System having a heating rate of 10 °C min^{-1}. UV-Vis spectroscopy was performed on a 3 mL solution using the Varian UV−vis spectrophotometer (Cary 100 Bio) in a quartz cuvette (1 cm × 1 cm). Photoluminescence (PL) spectra were recorded by using a Fluoromax-4 spectrofluorometer (HORIBA Jobin Yvon, model FM100) with an excitation and emission slit width at 5 nm. The crystal structure of

[Cu(Xantphos)(dicnq)]PF_6 was used for geometry optimization. Ground state DFT calculations were done by the ORCA 5.0.3 program package developed by Neese and coworkers *[14,15]* using B3LYP functional with a def2-TZVP basis set. Cyclic Voltammetry was performed using an AUTOLAB, PGSTAT 12 (Ecochemie, B.V. Netherlands) with GPES software (version 4.9) in a conventional blank ITO-coated glass slide as the working electrode, the CV curve was recorded in a potential range of ±3 V and at a scan rate of 100 mV/s.

2.3 Synthetic Details

2.3.1.1 Synthesis of 6,7-dicyanodipyrido[2,2-*d*:2',3'-*f*] quinoxaline (dicnq)

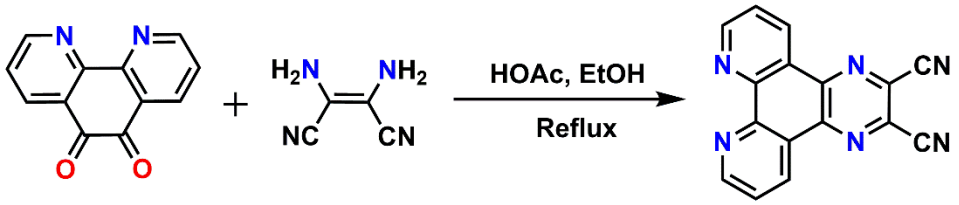

Scheme 2.1 Synthesis of 6,7-dicyanodipyrido[2,2-*d*:2',3'-*f*]quinoxaline (dicnq).

6,7-dicyanodipyrido[2,2-*d*:2',3'-*f*]quinoxaline (dicnq) was synthesized using some modification of the literature procedure *[10]*. In a clean and dry two-naked round bottom flask, under N_2 condition, 1 g of 1,10-phenanthroline-5,6-dione was dissolved in 15 mL of EtOH (ethanol), to this a solution of 0.756 g of diaminomaleonitrile in 10 mL of EtOH was added. The solution was stirred at 80 °C for 4 hours. After the reaction was finished, the solvent was concentrated to 5 mL and cooled to room temperature, and the brown-colored product was filtered and dried under a high vacuum to give a pure product with 93% yield. The formation of the product is confirmed by ^{1}H, $^{13}C\{^{1}H\}$ and ^{1}H-^{13}C HSQC NMR spectroscopies (**Fig. 2.1-2.3**). **^{1}H NMR** (500 MHz, DMSO-d_6): δ 9.41 (dd, J = 8.2, 1.7 Hz, 2H), 9.35 (d, J = 5.8 Hz, 2H), 8.04 (dd, J = 8.3, 4.3 Hz, 2H). **$^{13}C\{^{1}H\}$ NMR** (126 MHz, DMSO-d_6): δ 154.30, 148.10, 141.03, 133.82,

131.58, 125.27, 124.68, 114.53. **HRMS** (ESI, m/z): Calcd for $C_6H_6N_6Na$ $[M+nNa]^+$: 305.0546, Found: 305.0546.

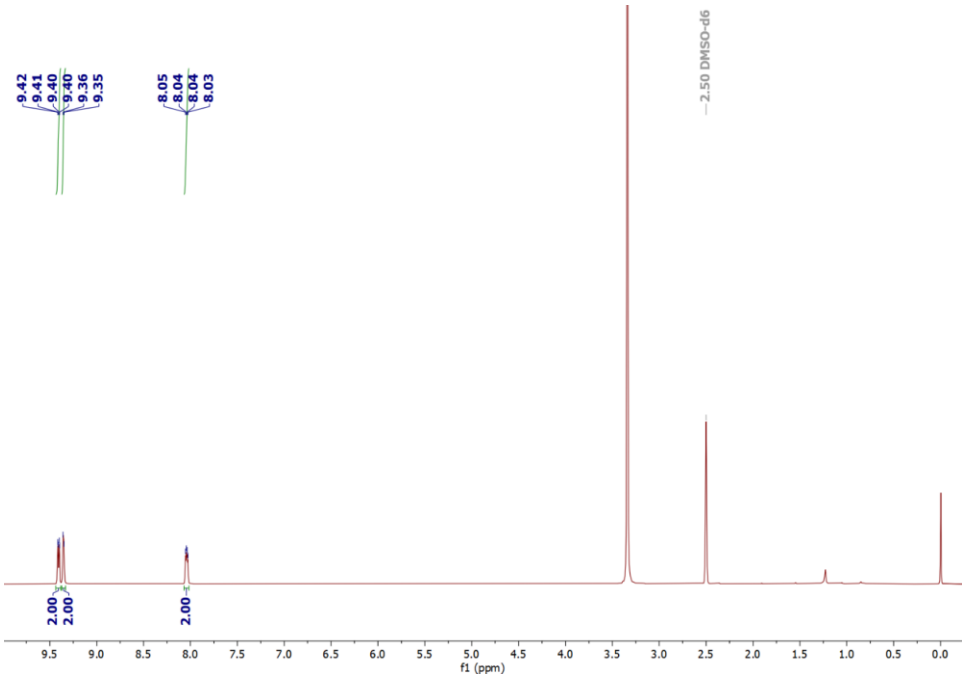

Fig. 2.1 ^1H NMR spectrum of **dicnq** in DMSO-d_6 (500 MHz).

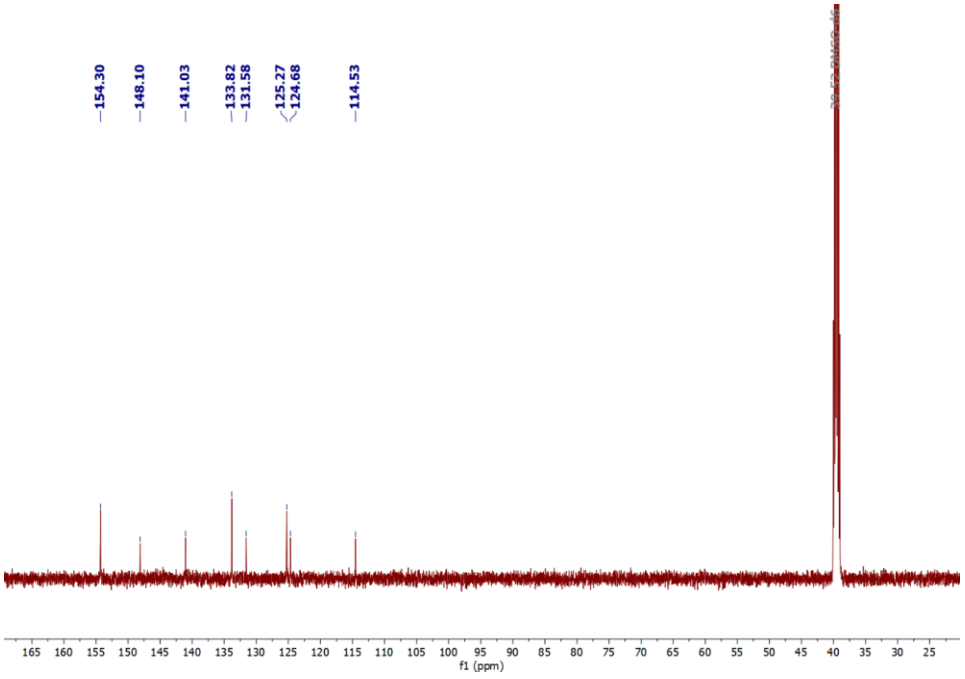

Fig. 2.2 $^{13}C\{^1H\}$ NMR spectrum of **dicnq** in DMSO-d_6 (126 MHz).

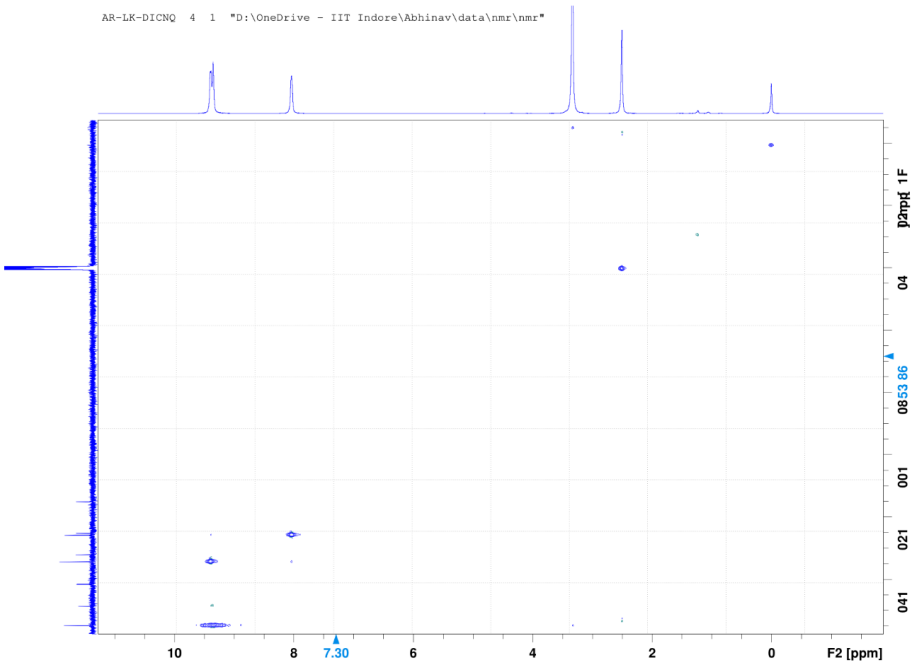

Fig. 2.3 $^{1}H–^{13}C$ HSQC spectra of **dicnq** DMSO-d_6 (500 MHz).

2.3.1.2 General procedure for Synthesis of complexes

In a clean and dry Schlenk tube, under N_2 condition, 1 eqv. phosphine ligand (in case of complex **1**, 2 eqv. of PPh_3) was dissolved in 4 mL of DCM. To this solution $[Cu(CH_3CN)_4]PF_6$ (1 eqv.) in DCM (4 mL) was added, and the resulting mixture was stirred for 2 hours at room temperature. After this, the solution of dicnq ligand (1 eqv.) in 4 mL of DCM was added, then the reaction mixture was further stirred for 2 hours. The solvent was evaporated by rotary evaporation and the product was dissolved in a small amount of DCM and addition of n-Hexane leads to the precipitation of pure compound as yellow powder.

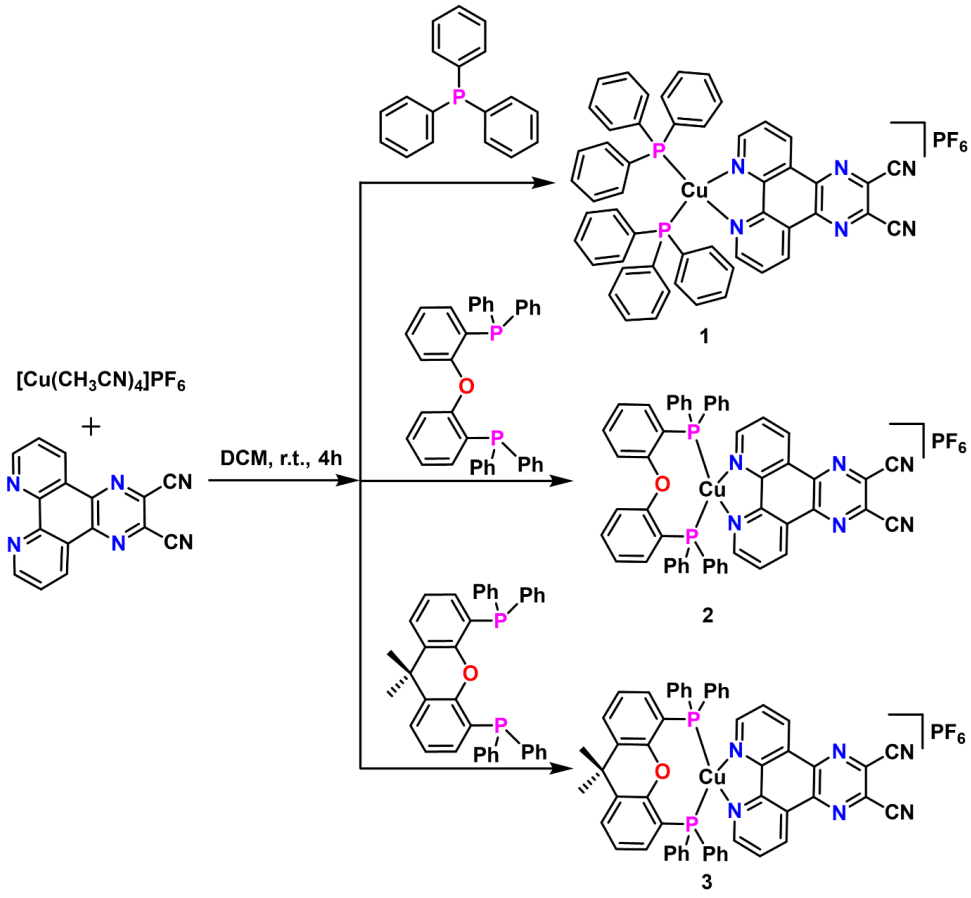

Scheme 2.2 Synthesis of complexes **1**-**3**.

2.3.1.2.1 Synthesis of $[Cu(PPh_3)_2(dicnq)]PF_6$ (1)

Using the general procedure, complex **1** was synthesized using PPh_3, $[Cu(CH_3CN)_4]PF_6$, and dicnq to get pure product as a yellow powder in 75% yield. The data obtained from different NMR spectroscopies (**Fig. 2.4-2.6**) and HRMS confirm the formation of complex **1**. **^{1}H NMR** (500 MHz, DMSO-d_6) δ 9.55 (d, J = 8.2 Hz, 2H), 9.15 (d, J = 4.9 Hz, 2H), 8.11 (dd, J = 8.2, 4.7 Hz, 2H), 7.40 (t, J = 7.4 Hz, 6H), 7.27 (t, J = 7.7 Hz, 12H), 7.17 (s, 12H). **^{13}C{^{1}H} NMR** (126 MHz, DMSO-d_6) δ 153.26, 145.12, 140.13, 135.27, 132.73, 132.64, 132.42, 130.17, 128.83, 127.02, 126.14, 114.27. **^{31}P{^{1}H}**(202 MHz, DMSO-d_6) δ 3.23, -144.15. **HRMS (ESI, m/z)**: Calcd for **$C_{34}H_{21}CuN_6P$ $[(M\text{-}PF_6)]^+$** with loss of one PPh_3 ligand: m/z 607.0856. Found: m/z 607.0897.

2.3.1.2.2 Synthesis of [Cu(DPEphos)(dicnq)]PF_6 (2)

The general procedure was used to synthesize complex **2**, DPEphos, [Cu $(CH_3CN)_4]PF_6$ and dicnq gave complex **2** as a yellow powder in 90% yield. The formation of complex **2** is confirmed by multinuclear NMR spectroscopies (**Fig. 2.7-2.9**) and HRMS. **^{1}H NMR** (500 MHz, DMSO-d_6) δ 9.54 (dd, *J* = 8.2, 1.5 Hz, 2H), 9.10 (d, *J* = 4.3 Hz, 2H), 8.07 (dd, *J* = 8.2, 4.9 Hz, 2H), 7.45 (td, *J* = 7.7, 1.8 Hz, 2H), 7.30 (t, *J* = 7.4 Hz, 4H), 7.23 (d, *J* = 8.1 Hz, 2H), 7.18 (t, *J* = 7.7 Hz, 8H), 7.11 (t, *J* = 7.8 Hz, 2H), 7.05 – 6.98 (m, 8H), 6.70 (ddp, *J* = 5.8, 4.1, 1.8 Hz, 2H). **^{13}C{^{1}H} NMR** (126 MHz, DMSO-d_6) δ 157.83, 152.82, 145.42, 140.41, 135.25, 133.76, 132.81, 132.59, 132.51, 130.21, 128.89, 127.04, 126.34, 125.33, 122.90, 120.71, 114.47. **^{31}P{^{1}H} NMR** (202 MHz, DMSO-d_6) δ -11.38, -144.17. **HRMS (ESI, m/z)**: Calcd for **$C_{52}H_{34}CuN_6OP_2$ [(M-PF_6)]$^+$**: 883.1560. Found: m/z 883.1591.

2.3.1.2.3 Synthesis of [Cu(Xantphos)(dicnq)]PF_6 (3)

A similar general synthetic procedure was used to synthesize complex **3**, Xantphos, $[Cu(CH_3CN)_4]PF_6$ and dicnq, a yellow powder was obtained in a 69% yield. The formation of complex **3** is confirmed by results of ^{1}H, ^{13}C{^{1}H} and ^{31}P{^{1}H}NMR spectroscopies (**Fig. 2.10-2.12**), HRMS elemental analysis and FT-IR. **^{1}H NMR** (500 MHz, DMSO-d_6): δ 9.51 (d, *J* = 8.3 Hz, 2H), 8.79 (d, *J* = 5.4 Hz, 2H), 8.09 (dd, *J* = 8.3, 4.7 Hz, 2H), 7.89 (d, *J* = 6.5 Hz, 2H), 7.29 (t, *J* = 7.6 Hz, 2H), 7.24 (t, *J* = 7.4 Hz, 4H), 7.10 (t, *J* = 7.6 Hz, 8H), 6.94 (q, *J* = 5.5 Hz, 8H), 6.75 – 6.65 (m, 2H), 1.75 (s, 6H). **^{13}C{^{1}H} NMR** (126 MHz, DMSO-d_6): δ 153.72, 152.16, 144.68, 139.71, 135.11, 133.33, 132.49, 132.03, 130.43, 129.74, 128.57, 128.16, 127.09, 125.91, 125.07, 118.27, 114.13, 35.50, 28.13. **^{31}P{^{1}H} NMR** (202 MHz, DMSO-d_6): δ -12.72, -144.20. **HRMS (ESI, m/z)**: Calcd for **$C_{55}H_{38}CuN_6OP_2$ [(M-PF_6)]$^+$:** 923.1873; Found: m/z 923.1894. **Anal. Calc. for $C_{55}H_{40}CuF_6N_6OP_3$:** C, 61.66; H, 3.76; N, 7.84. **Found:** C, 61.65; H, 3.72; N, 7.79%. **FT-IR** (cm^{-1}) 3061, 2968, 2956, 2348, 2329, 1573, 1508,

1479, 1460, 1434, 1403, 1372, 1220, 1095, 998, 875, 834, 737, 696, 556, 509, 421.

2.4 Characterisations of 1-3

2.4.1.1 NMR spectra of 1-3

The formation of complexes **1-3** was confirmed by the data obtained from ^{1}H, $^{13}C\{^{1}H\}$, $^{31}P\{^{1}H\}$ NMR in DMSO-d_6 and HRMS (**Fig. 2.4-2.12**). In the ^{1}H spectra of complex **1**, the protons corresponding to the phenyl rings of PPh_3 (12H, 12H, and 6H) were observed at 7.17 ppm, 7.27 ppm, and 7.40 ppm while in the ^{1}H NMR spectrum of complexes **2** and **3**, the signals of phenyl protons preset on DPEphos ligand were observed at 7.5 (m, 8H), 7.18 (t, 8H), 7.30 (t,8H), and phenyl protons of Xantphos ligand show signals at 6.94 ppm (q, 8H), 7.10 ppm (t, 8H), and 7.24 ppm (t, 4H), respectively. Additionally, a singlet at 1.75 ppm corresponds to six methyl protons present on the bridging carbon atom between two phenyl rings of Xantphos. The downfield doublet signals range from 8.07 to 9.55 ppm, corresponding to pyridinyl protons of the dicnq ligand present in all complexes.

$^{13}C\{^{1}H\}$ NMR spectrum of complexes **1-3** showed the peaks of phenyl carbons in the range of 120 to 150 ppm, whereas in complex **3** the bridging carbon atom between two phenyl rings of Xantphos was observed at 35.50 ppm, while methyl groups substituted on this bridging carbon were observed at 28.13 ppm. The singlet at 3.23, -11.38 and -12.72 ppm in the $^{31}P\{^{1}H\}$ NMR spectrum of all complexes confirms the coordinated phosphine ligands, whereas the characteristic septet around -144 ppm confirms the presence of PF_6 counterion. HRMS of **1** characteristic isotopic signature of copper with loss of one PPh_3 ligand: m/z = 607.0897 (607.0856 calcd for $[M\text{-}PF_6]^+$) while complexes **2** and **3** showed the m/z of 883.1591 and 923.1894 (883.1560, 923.1873 calcd for $[M\text{-}PF_6]^+$).

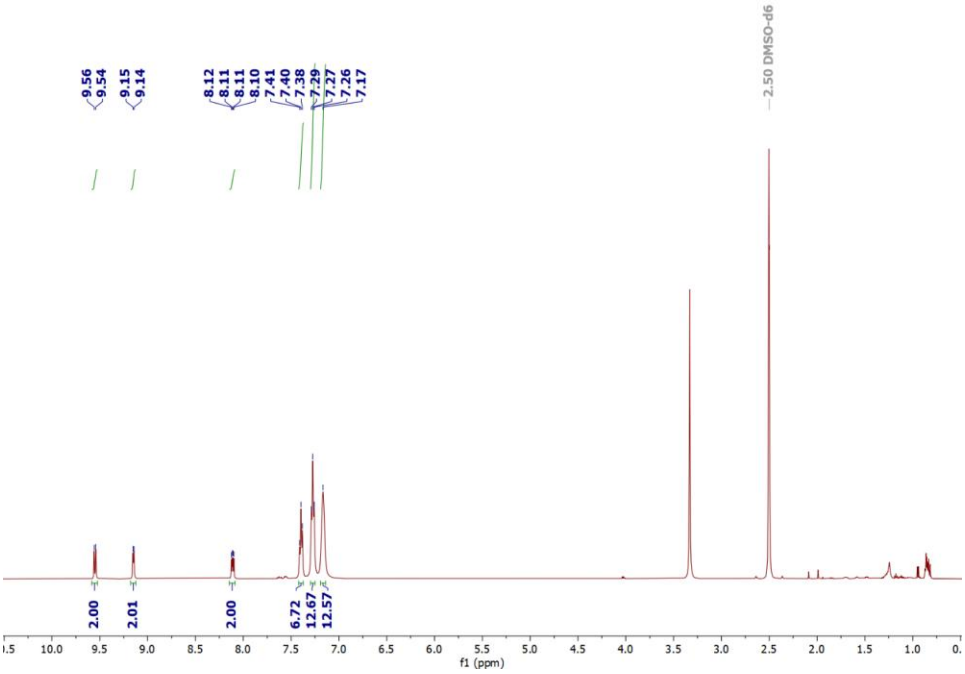

Fig. 2.4 ^{1}H NMR spectra of **1** in DMSO-d_6 (500 MHz).

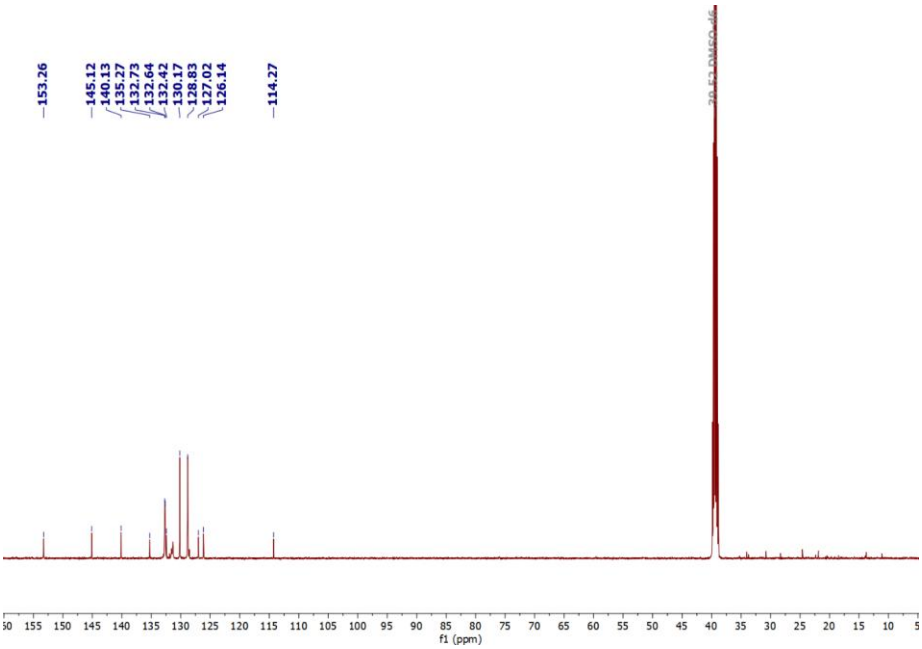

Fig. 2.5 ^{13}C{H} NMR spectra of **1** in DMSO-d_6 (126 MHz).

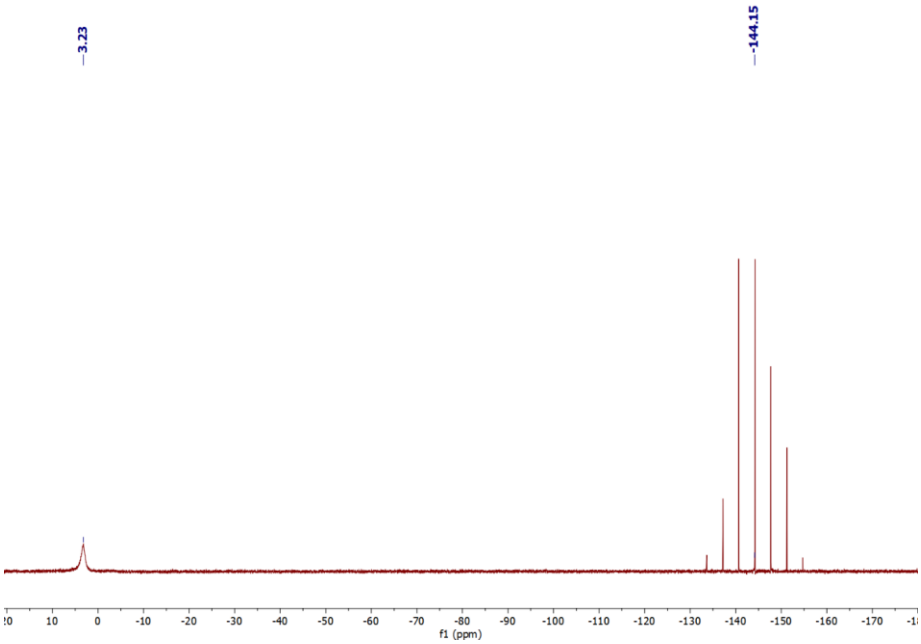

Fig. 2.6 $^{31}P\{H\}$ NMR spectra of **1** in DMSO-d_6 (202 MHz).

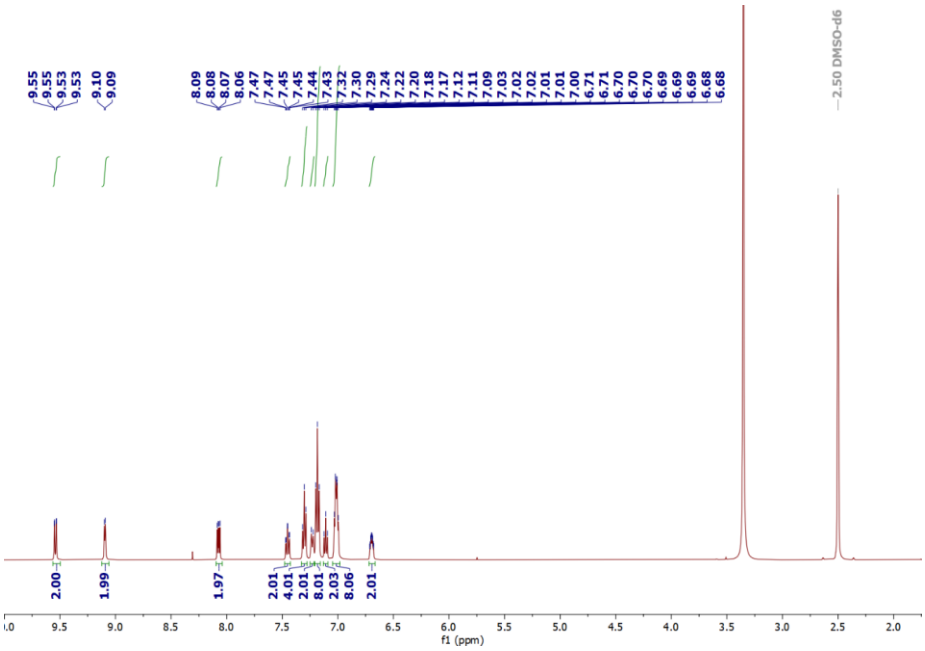

Fig. 2.7 ^{1}H NMR spectra of **2** in DMSO-d_6 (500 MHz).

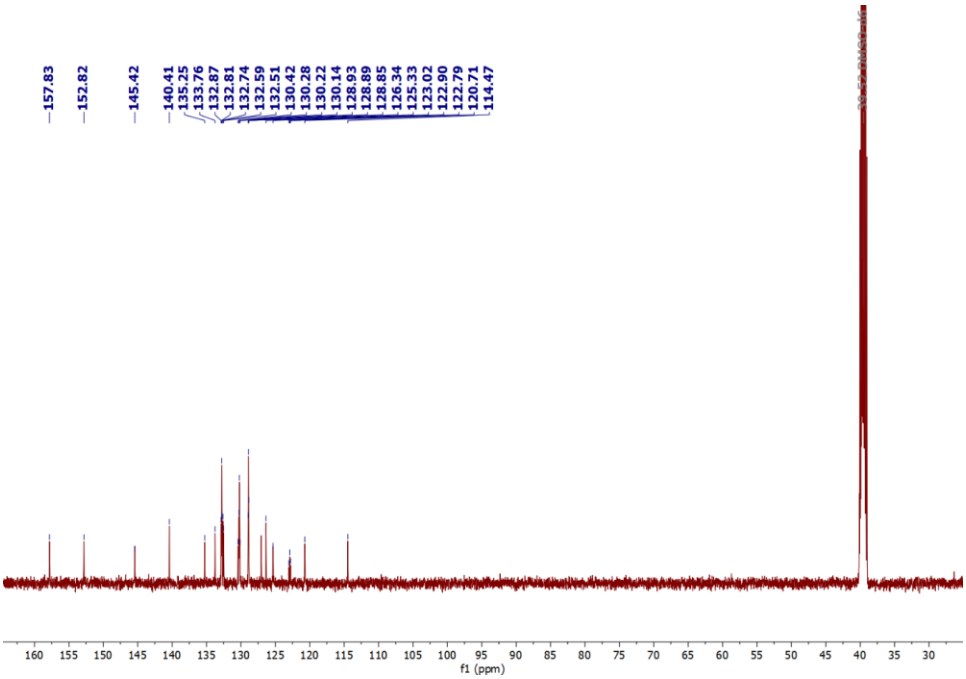

Fig. 2.8 $^{13}C\{H\}$ NMR spectra of **2** in DMSO-d_6 (126 MHz).

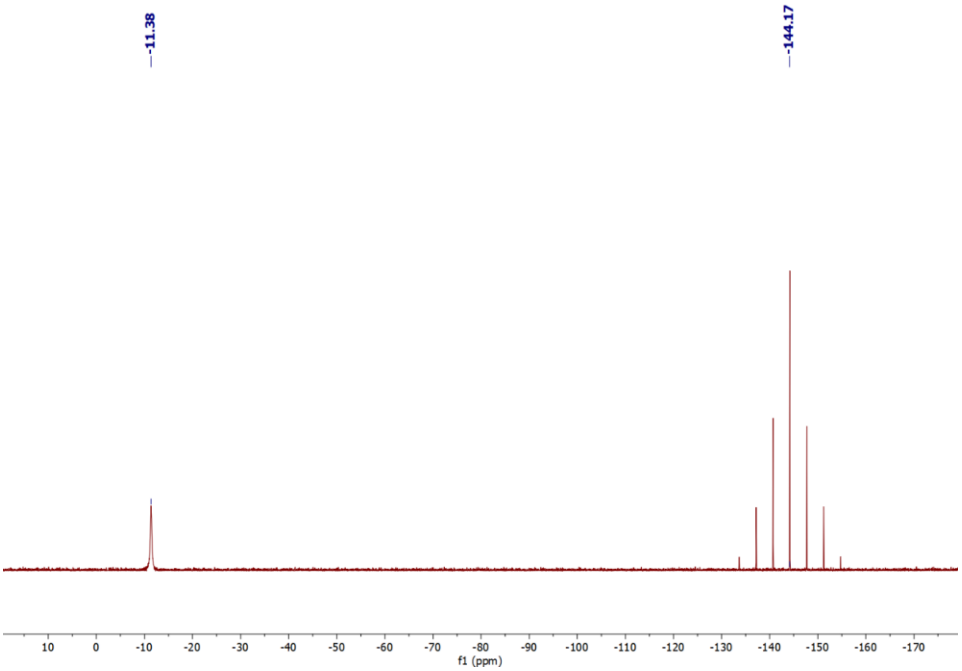

Fig. 2.9 $^{31}P\{H\}$ NMR spectra of **2** in DMSO-d_6 (202 MHz).

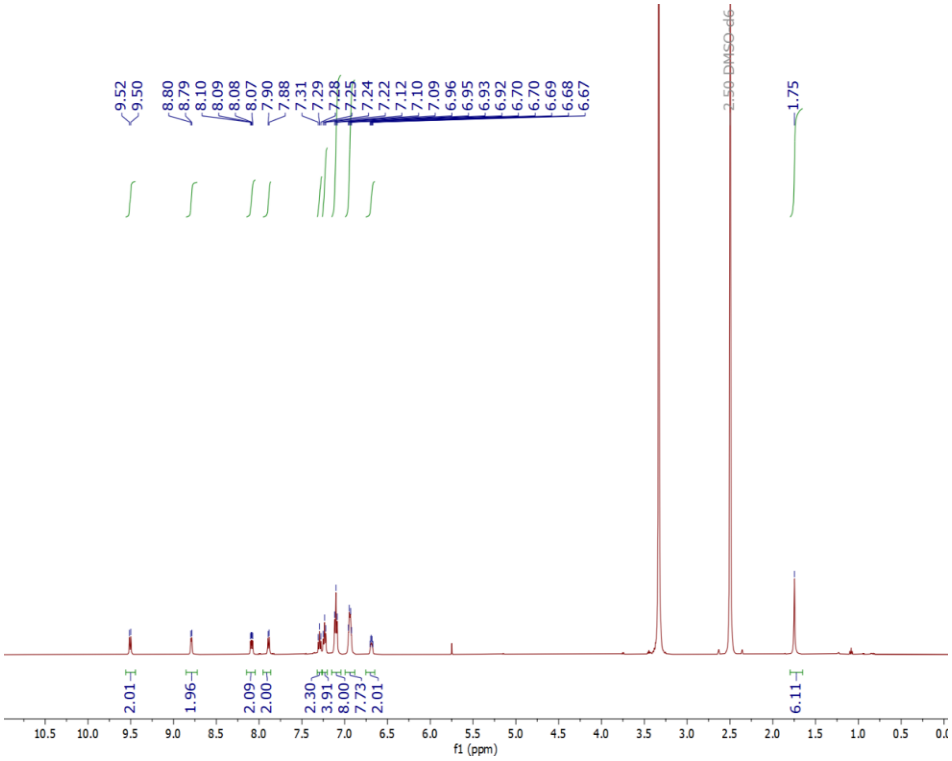

Fig. 2.10 ^{1}H NMR spectrum of **3** in DMSO-d_6 (500 MHz).

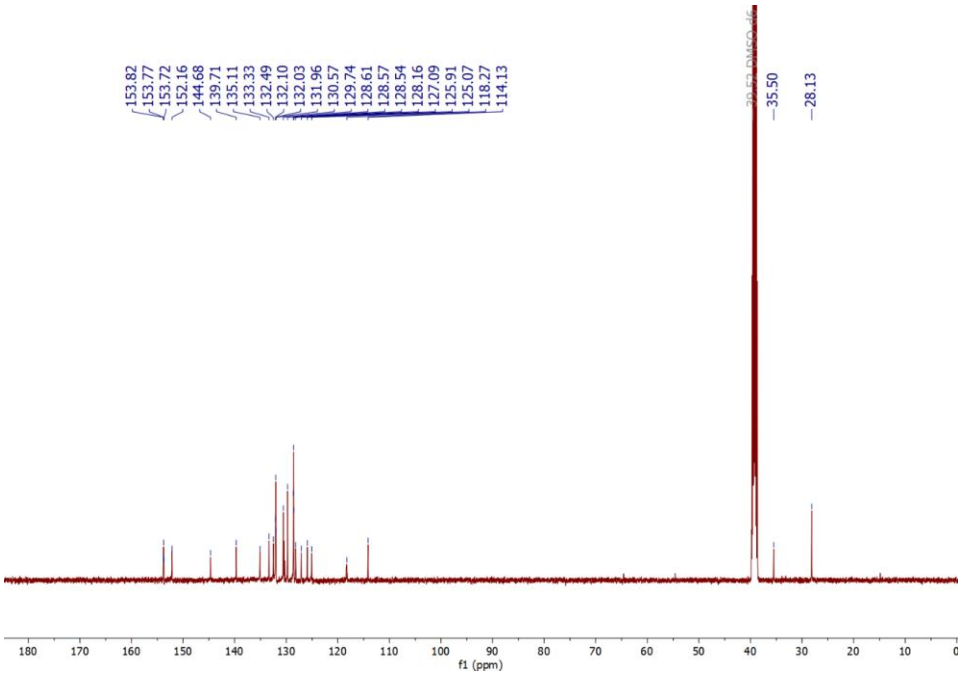

Fig. 2.11 ^{13}C{^{1}H} NMR spectrum of **3** in DMSO-d_6 (126 MHz).

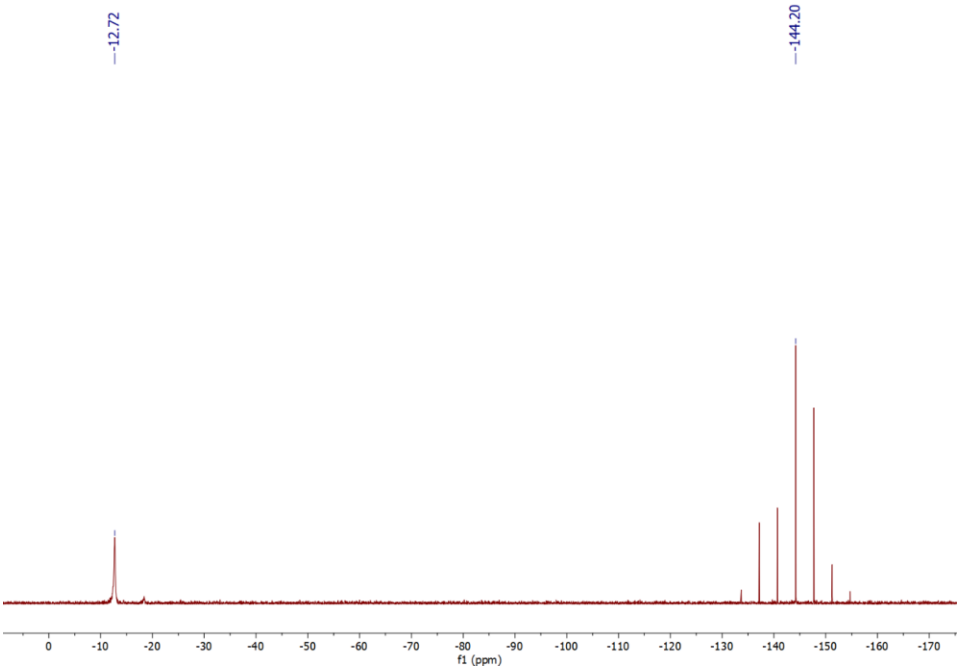

Fig. 2.12 $^{31}P\{^{1}H\}$ NMR spectrum of **3** in DMSO-d_6 (202 MHz).

2.4.1.2 Structural analysis

Single crystals of complexes **1** and **2**, suitable for single-crystal X-ray diffraction (SCXRD) studies, were grown from vapor diffusion of DCM and hexane as an anti-solvent while the crystals of **3** was grown from acetonitrile solvent. The obtained molecular structures are shown in **Fig. 2.13**. Complexes **1** and **2** were crystallized in a triclinic crystal system having *P-1* space group whereas complex **3** has monoclinic crystal system with a *P21/n* space group. The complete crystallographic data and structure refinement details are summarized in **Table 2.1**. The geometry around the copper center was found to be distorted tetrahedral, in which Cu(I) ion is coordinated with two phosphorous from phosphine ligands and two nitrogen of dicnq ligand.

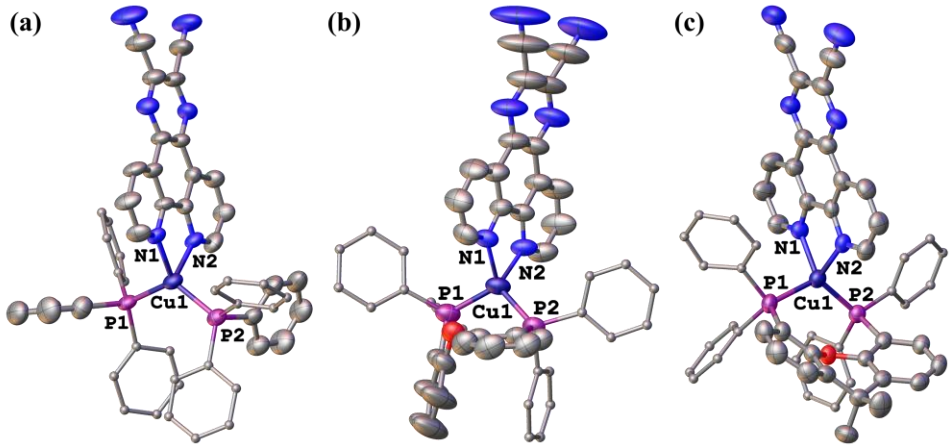

Fig. 2.13 Molecular structures of the heteroleptic Cu(I) complexes **1-3**. Hydrogen atoms, solvent and counterions are omitted for clarity.

A comparison of bond lengths and angles is tabulated in **Table 2.2** and **2.3**, the bond distances between Cu-P are between 2.28 to 2.23 Å, whereas the Cu-N bond distance ranges from 2.06 Å to 2.09 Å. The bond angles between P-Cu-P are in the range of 111° to 122° while N-Cu-N bond angles are around 80°, which is similar to those observed in the previously reported four coordinated Cu(I) complexes *[16,17]*.

Table 2.1 Crystal and refinement data table of complexes **1-3**.

Complex	**1**	**2**	**3**
Empirical formula	$C_{52}H_{36}CuF_6N_6P_3$	$C_{52}H_{34}CuF_6N_6OP_3$	$C_{55.5}H_{38.75}CuF_6N_{6.25}OP_3$
Formula weight	156.90	1029.30	1079.12
Crystal system	triclinic	triclinic	monoclinic
Space group	P-1	P-1	$P2_1/n$
a/Å	10.7422(8)	13.5873(10)	11.6633(2)
b/Å	16.0390(14)	13.8787(4)	25.6479(4)
c/Å	20.3861(16)	16.0252(6)	17.1381(4)
α/°	73.909(7)	111.448(3)	90
β/ °	74.945(7)	107.979(6)	100.809(2)

γ/°	81.912(7)	95.907(4)	90
V/ Å^3	3250.0(5)	2594.6(2)	5035.72(17)
Z	2	2	4
ρ_{calc}g/cm^{-3}	1.122	1.317	1.424
μ/mm^{-1}	0.578	0.577	0.599
R1 (R1 all data) [I > 2σ(I)]	0.1445	0.0945	0.0975
wR2 (wR2 all data)	0.1930	0.1884	0.1481
Data/restraints/parameters	11864/0/616	9118/0/595	10732/30/722
GOF	0.934	1.079	1.025

Table 2.2 Selected bond lengths of complexes **1**-**3**.

Bond length (Å)	**1**	**2**	**3**
P1-Cu1	2.2887	2.23	2.27
P2-Cu1	2.2675	2.23	2.23
N1-Cu1	2.097	2.06	2.06
N2-Cu1	2.115	2.05	2.09

Table 2.3 Selected bond angles of complexes **1**-**3**.

Bond Angle (°)	**1**	**2**	**3**
P1-Cu1- P2	122.66	111.71	120.61
P1-Cu1-N1	110.73	116.80	105.72
P2-Cu1-N2	111.56	117.30	111.98
N1-Cu1-N2	79.37	80.31	79.95

2.4.1.3 Thermogravimetric analysis

TGA analyses have been performed to measure the thermal stability of complexes under N_2 flow (20 mL/ min) with an increase in temperature of 10 °C/ min (**Fig. 2.14**). The TGA curve of complexes **1-3** suggests that all complexes were thermally stable up to 150 °C. It is found that the presence of bidentate DPEphos and Xantphos ligands provides greater thermal stability to the complexes as compared to the PPh_3. In complexes **1-3**, the first step of decomposition is about 10-12 % weight loss corresponding to counter ion. Furthermore, the second loss of 26-30% corresponds to the dicnq ligand and the last degradation of 52-54% represents the loss of the phosphine ligands. The thermal stability of all complexes, suggesting that they can endure temperatures up to 100 °C during further applications.

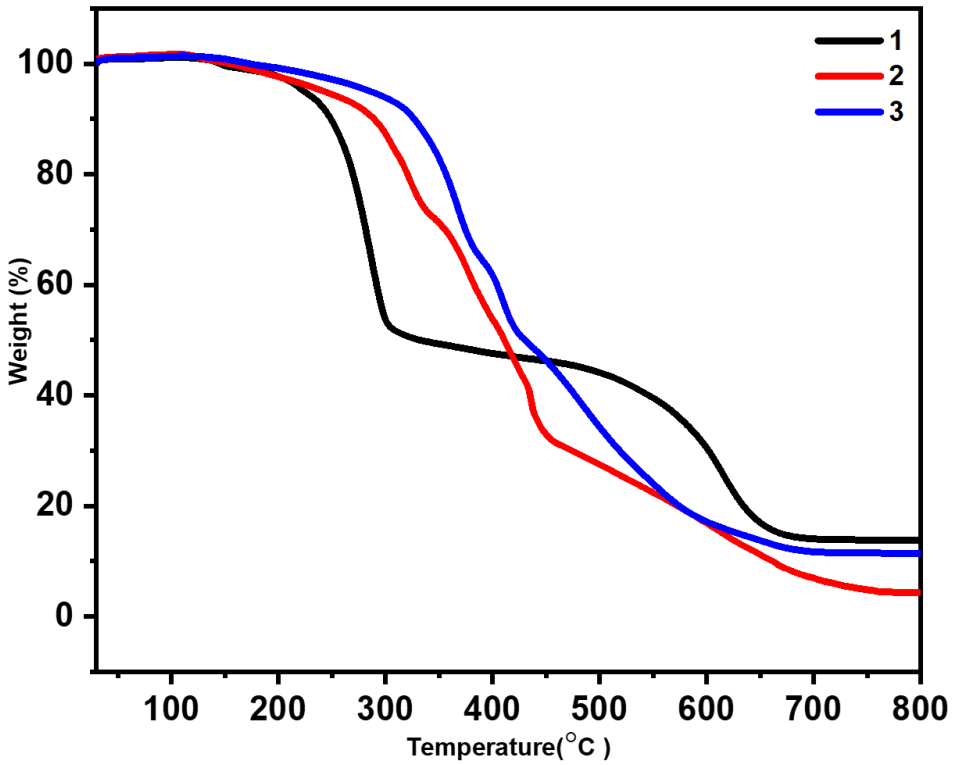

Fig. 2.14 TGA curves of **1-3** under nitrogen atmosphere with the temperature heating rate of 10 °C min^{-1}.

2.5 Photophysical properties

2.5.1.1 Absorption, emission and theoretical calculations

The UV-Vis spectra of complexes **1-3** were recorded in toluene with 10^{-4} M solution which is displayed in **Fig. 2.15a**. This shows that high energy absorption bands between 280 to 350 nm were observed due to the ligand-centered π-π* transition in both dicnq and phosphine ligands *[18–24]*. The weak absorption band ranges from 380 to 500 nm, which arises due to the metal-to-ligand charge transfer transition (MLCT) from the spin-allowed transition that involves the 3d orbital of the Cu(I) with some involvement of the phosphine ligand and π* orbital of the dicnq ligand *[25–27]*. The emission of complexes **1-3** in solution was recorded in the same solvent, on the excitation of 360 nm, showing an emission between 680-700 nm (**Fig. 2.15b**). It has been observed that the presence of a significant charge transfer character in the excited state results in broadband emission spectra without distinct vibrational peaks *[28]*.

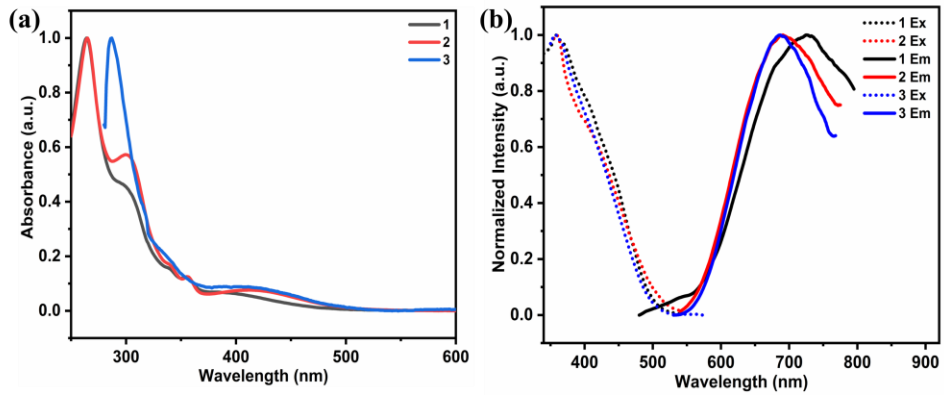

Fig. 2.15 (a) Absorption spectra and (b) Excitation and Emission spectra (λ_{ex} = 360 nm) of complexes **1-3** in toluene at room temperature.

As all complexes show similar absorption bands, complex 3 was chosen for theoretical studies, including density functional theory (DFT) and time-dependent density functional theory (TD-DFT) using the B3LYP/ Def2TZVP basis set. Based on the DFT studies it is found that the HOMO

is distributed on the 3d orbital of the Cu(I) with a significant contribution of the Xantphos ligand. In contrast, the LUMO is present on the dicnq ligand (**Fig. 2.19**). Therefore, it is concluded that the electronic transition occurs via metal-to-ligand charge transfer transition (MLCT), i.e., from the Cu(d) orbital to the π* orbital of the dicnq *[29]*. The energy of HOMO is -8.092 eV while the energy of LUMO is -5.517 eV and the HOMO-LUMO energy gap is 2.575 eV. Additionally, TD-DFT calculation suggests that the major orbital composition (HOMO → LUMO) is about 98% is contributed by the singlet excited state (S_1). As a result, it is found that the S_1 excited state as emerging from the transition between the HOMO and LUMO frontier orbitals. However, The S_1 excited state near the frontier orbitals exhibits CT behavior and this state is assigned as an (M+L)LCT excited state because HOMO is present on Cu(I) center and some contribution of Xantphos and the LUMO is located on the dicnq.

2.5.1.2 Solid-state Emission and Vapochromic Properties of Complex 3

In daylight, complex **3** was a pure yellow solid that showed a broad UV-Vis diffuse reflectance spectrum in the range of 250 to 500 nm in solid-state (**Fig. 2.16a**), and emission in the near IR region under UV light. The emission spectra of **3** were recorded on the photoluminescence (PL) mode of Raman spectroscopy. It was found that the emission peak was observed at 700 nm with a shoulder at 740 nm upon the excitation of 532 nm (**Fig. 2.16b**).

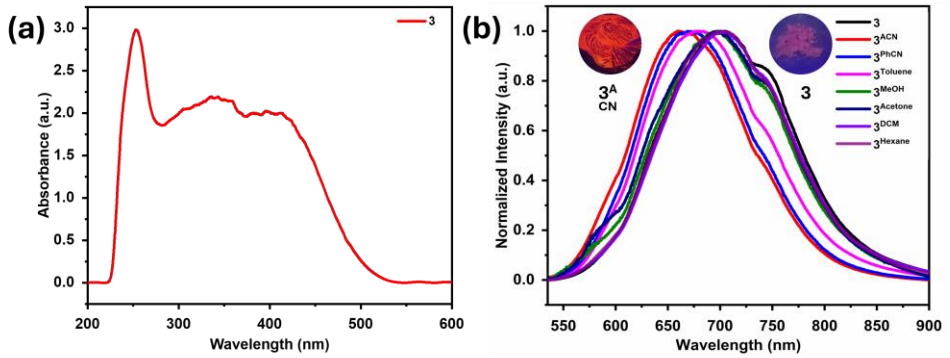

Fig. 2.16 a) Solid-state UV–visible diffuse reflectance spectra (DRS) at room temperature, b) Normalized solid-state emission spectra of **3** at an excitation wavelength of 532 nm, and Vapochromism of **3** with vapours of different organic solvents.

Several Cu(I) complexes are known to show changes in photophysical behaviour when subjected to external stimuli such as temperature, pressure, solvent vapours, etc *[30–35]*. The photophysical properties of stimuli-responsive material transform through structural modification, crystalline to amorphous phase conversion, cuprophilic (Cu-Cu) interaction, formation of cation-anion exciplex, and interactions with the solvent molecules *[36–41]*. When **3** was exposed to different solvent vapours, a substantial change in luminescence was observed as illustrated in **Fig. 2.16b**. It was observed that there is no change in emission in the presence of vapours of dichloromethane (**3^{DCM}**), methanol (**3^{MeOH}**), acetone (**3^{Acetone}**) and n-hexane (**3^{Hexane}**), however, a blue-shifted emission was observed with acetonitrile (**3^{ACN}**), benzonitrile (**3^{PhCN}**) and toluene (**3^{Toluene}**) vapours. A maximum of 40 nm blue-shifted emission at 660 nm was observed in **3^{ACN}**.

To understand the role of solvents, we have tried to grow crystals under different solvent systems. Fortunately, we were able to get crystals suitable for a single-crystal X-ray diffraction (SC-XRD) study under ACN (**3^{ACN}**) and DCM (**3^{DCM}**) solvents. Though the data obtained for **3^{ACN}** was of good quality, even after several attempts, we could not get good-quality single-

crystal data for $\mathbf{3^{DCM}}$. Even with the poor-quality data of $\mathbf{3^{DCM}}$, we could see the structure, observe atom-to-atom connectivity, and use it for comparison with $\mathbf{3^{ACN}}$. The obtained structures are shown in **Fig. 2.17**.

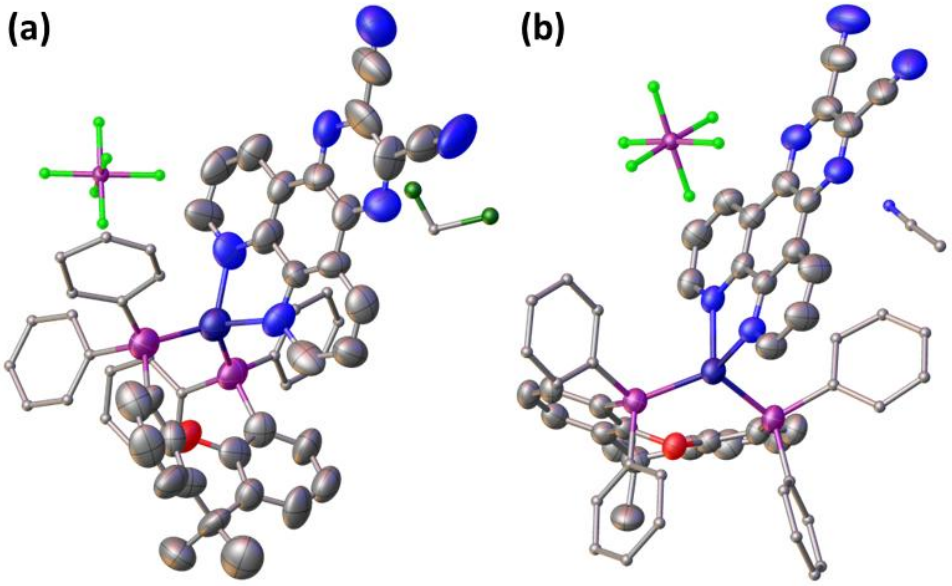

Fig. 2.17 Molecular structures of the heteroleptic Cu(I) complexes a) $\mathbf{3^{DCM}}$ and b) $\mathbf{3^{ACN}}$. Hydrogen atoms are omitted for clarity.

The geometry around the copper in both $\mathbf{3^{DCM}}$ and $\mathbf{3^{ACN}}$ was found to be distorted tetrahedral, as expected. In both structures, the bond distances between Cu-P are between 2.28 to 2.23 Å, whereas the Cu-N bond distance ranges from 2.07 Å to 2.09 Å. Notably, the P-Cu-P bond angle in $\mathbf{3^{DCM}}$ (113.94°) is found smaller than $\mathbf{3^{ACN}}$ (120.61°), whereas the N-Cu-N bond angle, having the more rigid backbone, increased from 78.43° in $\mathbf{3^{DCM}}$ to 79.95° in $\mathbf{3^{ACN}}$. The dihedral angle between the planes of both the ligands for $\mathbf{3^{DCM}}$ is about 82.71° while in $\mathbf{3^{ACN}}$ this angle increased upto 85.76°. A comparison of bond angles is tabulated in **Table 2.4** and bond distance of $\mathbf{3^{ACN}}$ is presented in **Table 2.5**. Overall, there are no significant changes in the bond distances but significant changes in bond angles are present around Cu(I) center.

For a similar observation of vapochromism with the Cu(I) complex, it is reported that the structural changes are responsible for blue-shifted emissions *[42]*. The crystal structures of $\mathbf{3}^{\mathbf{DCM}}$ and $\mathbf{3}^{\mathbf{ACN}}$ clearly suggest that the presence of solvent molecules alters the ligands arrangement around the metal as well as molecular packing (**Fig. 2.18 and 2.19**).

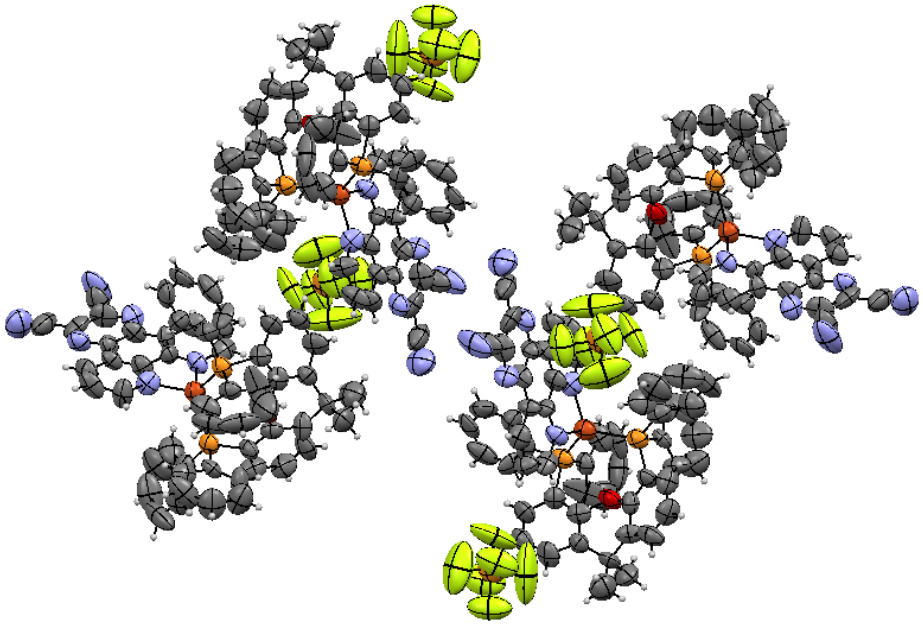

Fig. 2.18 Molecular Packing of $\mathbf{3}^{\mathbf{DCM}}$**.**

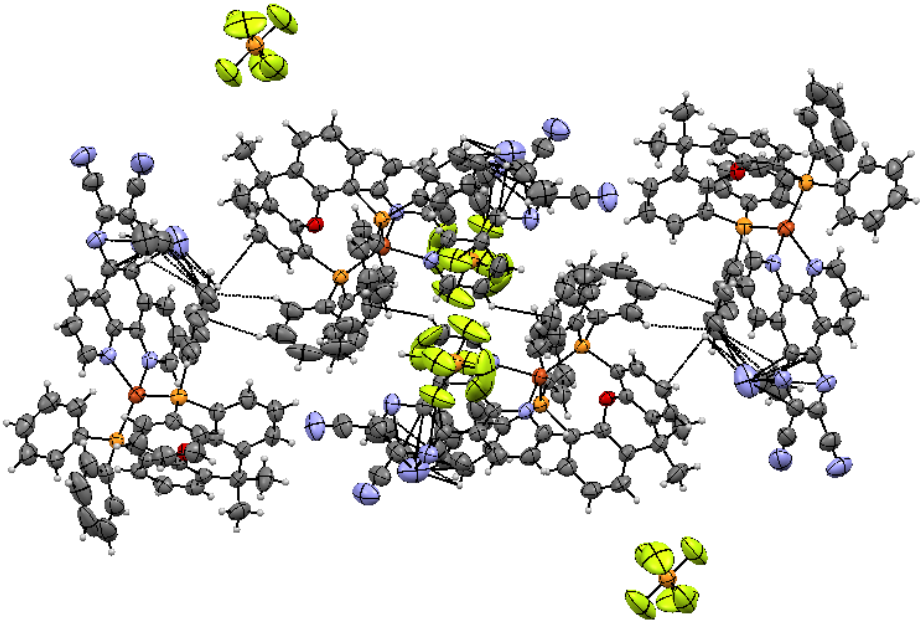

Fig. 2.19 Molecular Packing of $\mathbf{3^{ACN}}$.

Further, the FT-IR spectrum of **3**, $\mathbf{3^{DCM}}$ and $\mathbf{3^{ACN}}$ (**Fig. 3.20**) shows stretching frequencies of C-N triple bond of dicnq ligand at 3061 and 2968 cm^{-1}. In ACN solvate complex the additional peak was observed at 2253 cm^{-1} corresponding to the ACN solvent present in the lattice. The bands 1372-1600 cm^{-1} correspond to the stretching frequencies of C-C and C-N of the ligands. In addition, data obtained from elemental analysis suggests the presence of solvent molecules (**Table 3.6**).

Table 2.4 Selected bond angles of $\mathbf{3^{DCM}}$ and $\mathbf{3^{ACN}}$.

Bond Angle (°)	$\mathbf{3^{DCM}}$	$\mathbf{3^{ACN}}$
P1-Cu1- P2	113.94	120.61
P1-Cu1-N1	107.18	105.72
P2-Cu1-N2	114.30	111.98
N1-Cu1-N2	78.43	79.95

Table 2.5 Selected bond lengths of $\mathbf{3^{ACN}}$.

Bond length (Å)	$\mathbf{3^{ACN}}$
P1-Cu1	2.27
P2-Cu1	2.23
N1-Cu1	2.06
N2-Cu1	2.09

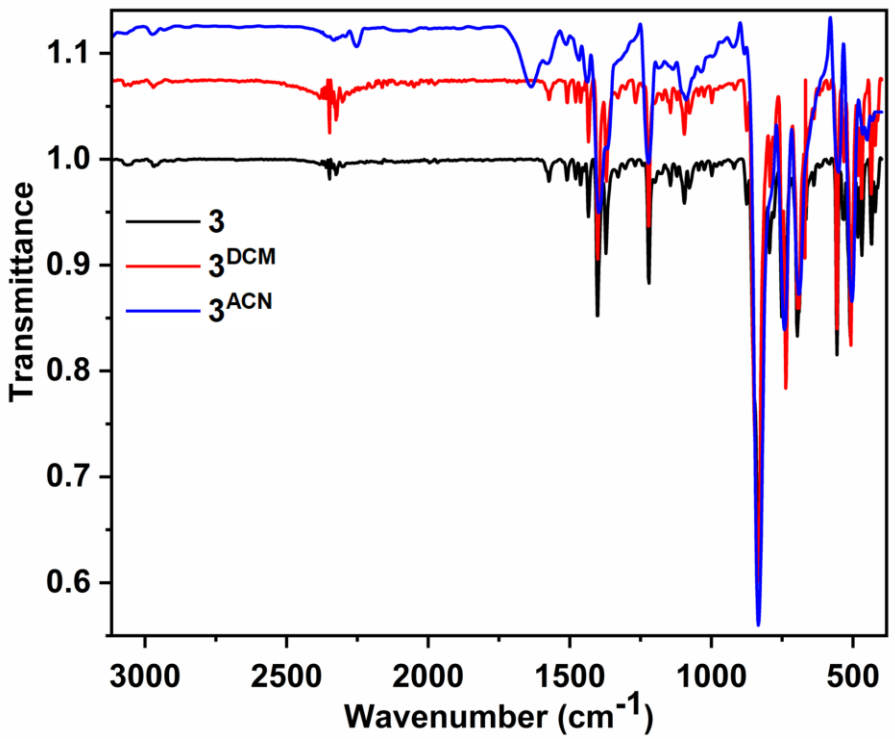

Fig. 2.20 FTIR spectrum complex **3** and it solvates (**3**^{DCM} and **3** ^{ACN}).

Table 2.6 Elemental analysis data for the characterization of the **3**, **3**^{DCM} and **3**^{ACN}.

	3		**3**^{DCM}		**3**^{ACN}	
	Calc. for $C_{55}H_{40}CuF_6N_6OP_3$	**Found**	**Calc. for $C_{56}H_{42}Cl_2CuF_6N_6OP_3$**	**Found**	**Calc. for $C_{57}H_{43}CuF_6N_7OP_3$**	**Found**
C	61.66	61.65	58.17	58.11	61.54	61.52
H	3.76	3.72	3.66	3.59	3.90	3.90
N	7.84	7.79	7.27	7.20	8.81	8.63

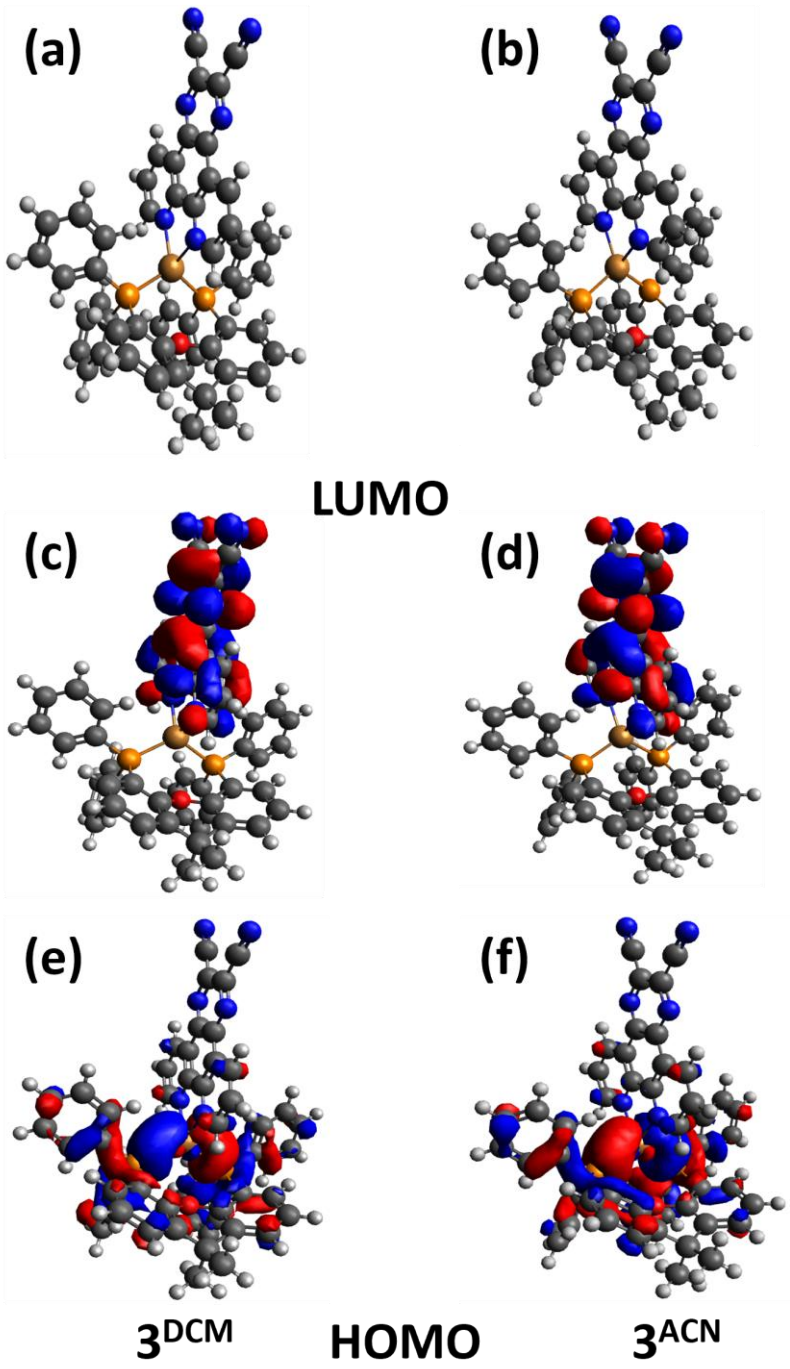

Fig. 2.21 a) and b) Optimized molecular structures and frontier molecular orbitals (c and d) LUMO (e and f) HOMO orbitals of $\mathbf{3}^{\mathbf{DCM}}$ and $\mathbf{3}^{\mathbf{ACN}}$ at B3LYP/def2-TZVP level of theory(Cu = Brown, P = Orange, N = blue, O = red, C = black and H = grey). Counter ion is omitted for clarity.

DFT calculations for $\mathbf{3^{ACN}}$ and $\mathbf{3^{DCM}}$ suggest no significant change in energies of frontier orbitals (**Fig. 2.21**). However, acetonitrile is not aromatic and cannot exhibit π-π interaction. In the case of $\mathbf{3^{ACN}}$, during the analysis of molecular structure, it is found that, C-N π-bond of acetonitrile show interaction with the dicnq ligand and the above-mentioned structural changes, also observed due to the dipole-π interactions of acetonitrile molecules and dicnq. These interactions with ACN are depicted in **Fig. 2.22**.

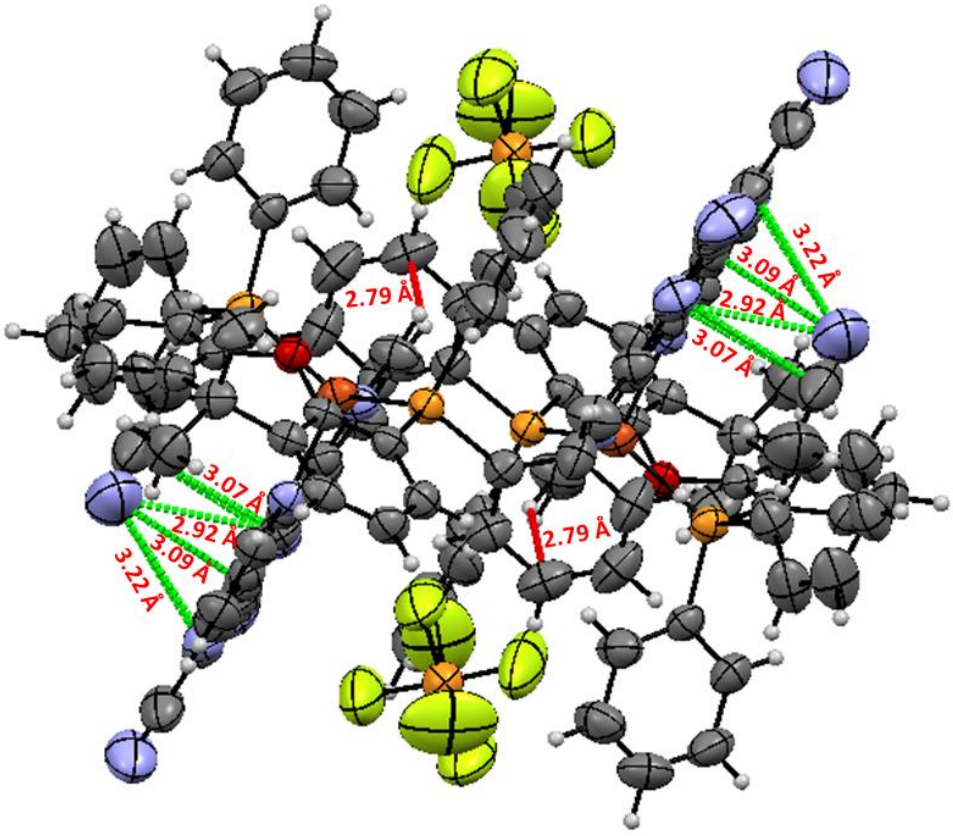

Fig. 2.22 Weak Interactions including, C-H---π intermolecular and π---π interactions observed between ACN (acetonitrile) and dicnq ligands in $\mathbf{3^{DCM}}$ and $\mathbf{3^{ACN}}$

Further, closer observations suggest that blue-shifted emissions were only observed with solvent vapors that can interact with the dicnq unit through π-π interactions. There is no shift for other polar/ nonpolar solvents as mentioned in **Table 2.4** and **Fig. 2.16b**. This observation suggests that π-π interaction plays a significant role in controlling the emission. Probably, the

interaction leads to stabilization of ligand π-orbitals and destabilization of LUMO of **3**, present on the dicnq unit (Since the LUMO and LUMO-1 are located on dicnq), resulting in higher energy emission.

2.6 Electrochemical and Electrochromic Studies

Further, to understand the electrochemical behaviour of complex **3**, cyclic voltametric curves were recorded in a three-electrode cell setup in ACN solution. For that having 0.5 mg of complex was taken with 0.1 M $LiClO_4$ as a supporting electrolyte. Using a blank ITO-coated glass slide as the working electrode, the CV curve was recorded in a potential range of ±3 V and at a scan rate of 100 mV/s, as shown in **Fig. 2.23a**. A distinct redox couple confirmed its active electrochemical property *[43]*. Interestingly, the color of complex **3** was found to change from light yellowish in its initial state to brownish when a bias of -3 V was applied and the process was found to be reversible (**Fig. 2.23a, inset**). This observation indicates that the complex is electrochromic active and further studies have been carried out later on to confirm the same.

As previously established, complex **3** was found to be electrochromic active in the solution state, however, practical application demands results in a compact solid-state device structure. To obtain the same, a five-layered ECD has been fabricated following a typical device schematic (**Fig. 2.23b**) with the incorporation of a suitable electrolytic layer. During CV scans, complex **3** was found to behave as an n-type EC material and therefore for a successful complementary pair formation, a p-type EC material was required. Polythiophene (P3HT), a very well-studied p-type EC active polymer therefore employed in the device structure to achieve overall better performance *[44]*.

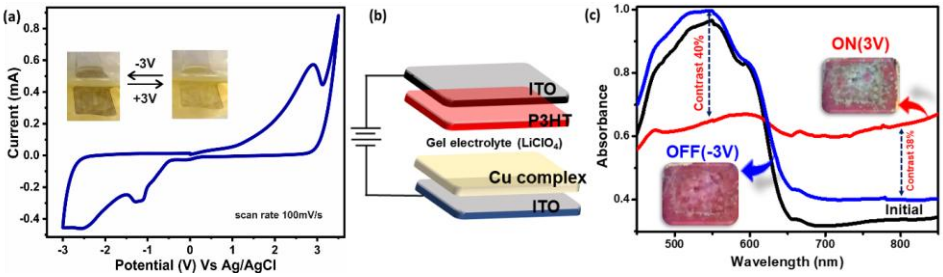

Fig. 2.23 Presentation of the (a) Cyclic voltammogram of **3** in 1 M solution of $LiClO_4$ in ACN at 100 mV/s scan rate vs Ag/AgCl at 25 °C. (b) EC device schematic and (c) in-situ absorption curves recorded for the device at ±3V.

2.6.1.1 Step-by-step device fabrication recipe:

1. ITO-coated glass slides of 1*2 size were first thoroughly cleaned in a 1:1:1 solution of Methanol, IPA, and Acetone under ultrasonication for 10 minutes.
2. A 0.5 wt% solution of complex **3** in DCB was first spin-coated onto the conducting surface of an ITO glass slide for 120 s duration at 150 rpm and later dried off at 80 °C.
3. The P3HT electrode has been spin-coated over another ITO glass slide from a 100 µl solution of 0.3 wt% P3HT in DCB solution for 120 s duration at 600 rpm.
4. The two glass slides were then sandwiched together after filling a 0.1 M $LiClO_4$ electrolyte in between them.

2.6.1.2 Electrochromic performance of ECD

The working potential range for the device was found to be ±3V. In-situ absorption spectra recorded from the device (**Fig. 2.23c**) in its initial, On, and Off states show that the device has an impressive contrast ratio of ~40% and 38% at 520 nm and 800 nm, respectively. In its original state, the color of the device is maroon (black curve) owing to the strong maroon color from the P3HT layer. However, during the ON state of the device i.e., on the application of 3 V bias with respect to the P3HT layer, it gets oxidized and due to the formation of a bipolaronic state, changes its color to blue.

Simultaneously, the complex **3** layer being fed with a -3 V gets reduced and changes color to brownish blue. The overall effects lead the device to appear bluish as can be seen from the inset images in **Fig. 3c** and the red curve represents the corresponding absorbance spectra. Upon bias reversal, i.e., the OFF condition, the original state of the device is restored, blue curve, pertaining to good reversibility between the two states.

After having established the EC ability of the device, it was further tested for performance with the help of device kinematics. For the same, the device has been fed with a 5 s pulse of ±3 V for 500 s and the stability has been checked (**Fig. 2.24a**) at 520 nm wavelength. The minute change in absorbance value towards the end of 100 cycles establishes that the device has good cycling capacity. Choosing one such cycle, the switching time has been calculated. The coloration and bleaching times i.e., the time taken by the device to change to 90% of its maximum absorbance value have been obtained to be 0.8 s and 0.5 s, respectively (**Fig. 2.24b**). Furthermore, a very important parameter, namely coloration efficiency (CE) has been calculated using the current and potential v/s time graph (**Fig. 2.24c and 2.24d**).

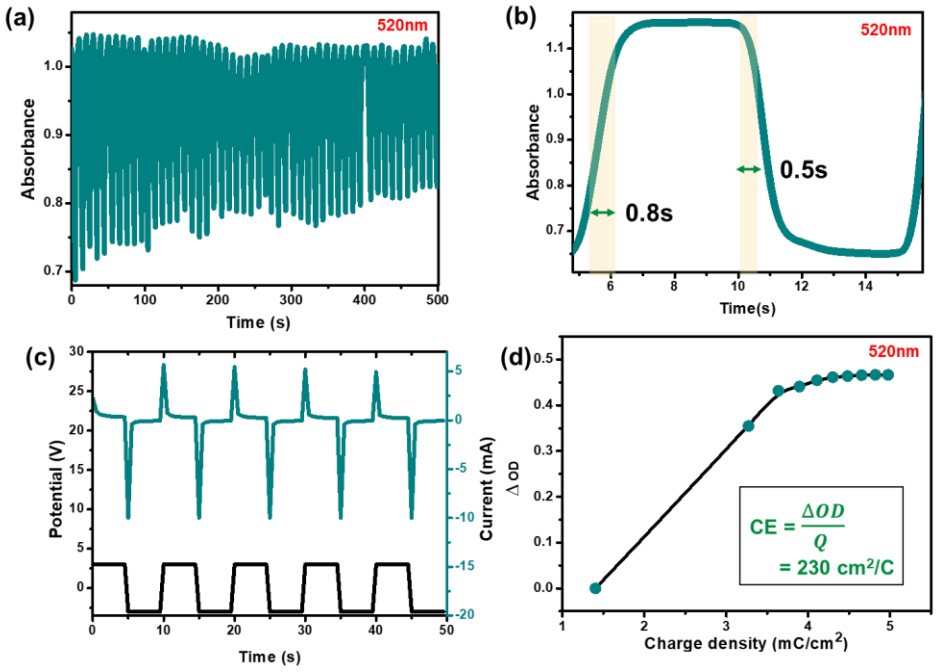

Fig. 2.24 Device kinematics recorded from the device at 520 nm wavelength showing (a) stability (b) switching times (c) potential and current v/s time graph and (d) coloration efficiency curve.

CE, which refers to the ratio of the change in optical density upon the amount of intercalated charge, is a parameter that dictates the overall device performance, and therefore, a value of 230 cm^2/C suggests that the ECD possesses a moderately high efficiency. This value can be further increased by optimizing a few parameters, like the thickness of EC layers, etc *[45]*. the details of which are beyond the scope of this work. Following a similar trail, all the device parameters were also obtained for 800 nm wavelength (**Fig. 2.25**) only to find consistent results.

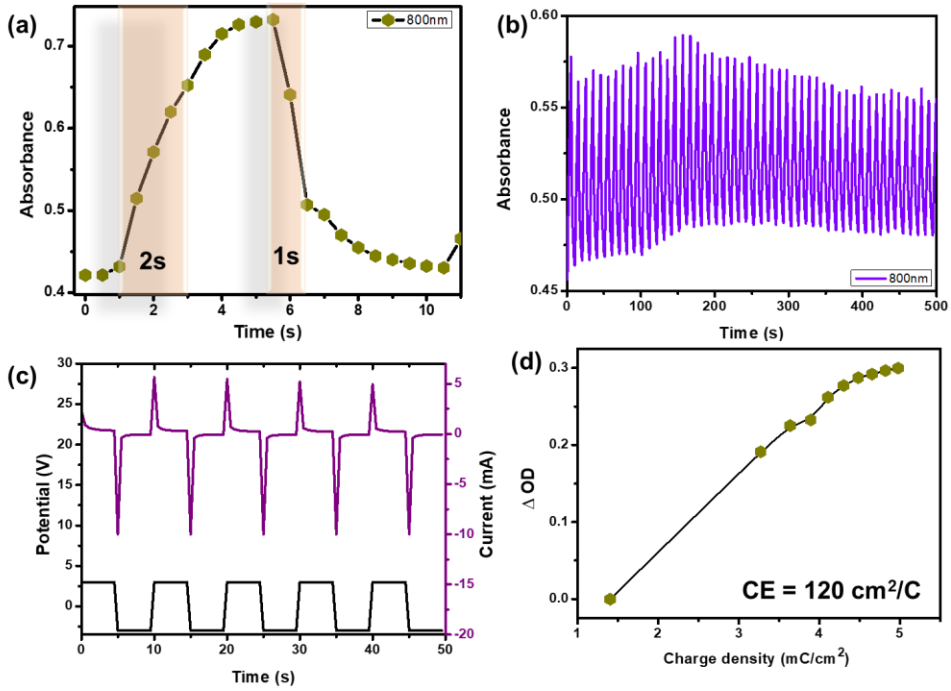

Fig. 2.25 Device kinematics was studied at 800 nm wavelength using a 5 s pulse train of ±3V showing (a) switching speed (b) device stability (c) potential and current v/s time and (d) calculation of coloration efficiency.

To consolidate the discussion, the ITO/P3HT/Cu complex/ITO device shows good EC results in terms of contrast, switching speed, stability, and

efficiency values, at two different wavelengths, thus establishing the complex ability to show EC active performance.

2.7 Conclusion

In summary, we have synthesized a series of heteroleptic complexes $[Cu(PPh_3)_2(dicnq)]PF_6$ (**1**), $[Cu(DPEphos)(dicnq)]PF_6$ (**2**) and $[Cu(Xantphos)(dicnq)]PF_6$ (**3**) using different phosphine (PPh_3, DPEphos and Xantphos) and dicnq ligands. The synthesized complexes are well characterized by different characterization techniques. These complexes show absorption in the UV-visible region (380-500 nm) and emission around 700 nm. DFT calculations provided insights into electronic transitions, the distribution of the HOMO is on Cu(I) with some contribution of phosphine ligands whereas LUMO is present on dicnq ligand and suggested charge transfer occurs via MLCT, from Cu(I) center to dicnq. In addition, **3** shows vapochromism in the solid state with different organic solvent vapours. It was observed that solvents that can interact with dicnq through π-π interactions lead to high-energy emissions due to the destabilization of LUMO orbitals. Furthermore, complex **3** shows EC properties which have been understood from its bias-induced color-changing behaviour during the CV scans as revealed using in-situ spectroelectrochemical measurements. The same has been later established by fabricating a bi-layered liquid electrolyte less ECD in association with another polymer, P3HT. Decent values of stability, switching speeds, contrast value, and coloration efficiency, finally establish that the complex can be used as an EC active layer, with much scope for performance enhancement. This work contributes to the broader landscape of materials science, offering a new platform for the development of electrochromic materials. Our further research endeavors will focus on refining the design and application of Cu(I) complexes to meet the demand of real-world applications, thereby advancing the practical impact of these materials in various technological contexts.

2.8 References

1. El-Kady M.F., Shao Y., Kaner R.B., (2016), Graphene for Batteries, Supercapacitors and Beyond, Nat Rev Mater, 1, 16033 (DOI: 10.1038/natrevmats.2016.33)
2. Kandpal S., Ghosh T., Rani C., Chaudhary A., Park J., Lee P.S., Kumar R., (2023), Multifunctional Electrochromic Devices for Energy Applications, ACS Energy Lett, 1870–1886 (DOI: 10.1021/acsenergylett.3c00159)
3. Lin D., Liu Y., Cui Y., (2017), Reviving the Lithium Metal Anode for High-Energy Batteries, Nat Nanotechnol, 12, 194–206 (DOI: 10.1038/nnano.2017.16)
4. Peng H.-J., Huang J.-Q., Cheng X.-B., Zhang Q., (2017), Review on High-Loading and High-Energy Lithium-Sulfur Batteries, Adv Energy Mater, 7, 1700260 (DOI: 10.1002/aenm.201700260)
5. Tao C., Li Y., Wang J., (2023), The Progress of Electrochromic Materials Based on Metal–Organic Frameworks, Coord Chem Rev, 475, 214891 (DOI: 10.1016/j.ccr.2022.214891)
6. Giereth R., Reim I., Frey W., Junge H., Tschierlei S., Karnahl M., (2019), Remarkably Long-Lived Excited States of Copper Photosensitizers Containing an Extended π-System Based on an Anthracene Moiety, Sustain Energy Fuels, 3, 692–700 (DOI: 10.1039/C8SE00521D)
7. Zhang Y., Schulz M., Wächtler M., Karnahl M., Dietzek B., (2018), Heteroleptic Diimine–Diphosphine Cu(I) Complexes as an Alternative towards Noble-Metal Based Photosensitizers: Design Strategies, Photophysical Properties and Perspective Applications, Coord Chem Rev, 356, 127–146 (DOI: 10.1016/j.ccr.2017.10.016)
8. Cuttell D.G., Kuang S.-M., Fanwick P.E., McMillin D.R., Walton R.A., (2002), Simple Cu(I) Complexes with Unprecedented Excited-State Lifetimes, J Am Chem Soc, 124, 6–7 (DOI: 10.1021/ja012247h)

9. Shahroosvand H., Rezaei S., Mohajerani E., Mahmoudi M., Ali Kamyabi M., Nasiri S., (2014), Key Role of Ancillary Ligands in Imparting Blue Shift in Electroluminescence Wavelength in Ruthenium Polypyridyl Light-Emitting Diodes, New J Chem, 38, 5312–5323 (DOI: 10.1039/C4NJ01078G)
10. Shahroosvand H., Rezaei S., Mohajerani E., Mahmoudi M., (2015), Toward White Electroluminescence by Ruthenium Quinoxaline Light Emitting Diodes, New J Chem, 39, 3035–3042 (DOI: 10.1039/C4NJ01938E)
11. Serpell C.J., Chall R., Thompson A.L., Beer P.D., (2011), Chloride Anion Triggered Motion in a Bis-Imidazolium Rotaxane, Dalton Trans, 40, 12052–12055 (DOI: 10.1039/C1DT10186B)
12. Dolomanov O.V., Bourhis L.J., Gildea R.J., Howard J. a. K., Puschmann H., OLEX2: A Complete Structure Solution, Refinement and Analysis Program, J Appl Crystallogr, 42, 339–341 (DOI: 10.1107/S0021889808042726)
13. Sheldrick G.M., Schneider T.R, (1997), [16] SHELXL: High-Resolution Refinement, In Methods in Enzymology; Macromolecular Crystallography Part B; Academic Press, 277, 319–343.
14. Neese F., Wennmohs F., Becker U., Riplinger C., (2020), The ORCA Quantum Chemistry Program Package, J Chem Phys, 152, 224108 (DOI: 10.1063/5.0004608)
15. Neese F., The ORCA Program System, (2012), WIREs Comput Mol Sci, 2, 73–78 (DOI: 10.1002/wcms.81)
16. Pathaw L., Maheshwaran D., Nagendraraj T., Khamrang T., Velusamy M., Mayilmurugan R., (2021), Tetrahedral Copper(I) Complexes of Novel N,N-Bidentate Ligands and Photophysical Properties, Inorganica Chim Acta, 514, 119999 (DOI: 10.1016/j.ica.2020.119999)
17. Li C., Mackenzie C.F.R., Said S.A., Pal A.K., Haghighatbin M.A., Babaei A., Sessolo M., Cordes D.B., Slawin A.M.Z., Kamer P.C.J.,

(2021), Wide-Bite-Angle Diphosphine Ligands in Thermally Activated Delayed Fluorescent Copper(I) Complexes: Impact on the Performance of Electroluminescence Applications, Inorg Chem, 60, 10323–10339 (DOI: 10.1021/acs.inorgchem.1c00804)

18. Zhang F., Guan Y., Chen X., Wang S., Liang D., Feng Y., Chen S., Li S., Li Z. Zhang F., (2017), Syntheses, Photoluminescence, and Electroluminescence of a Series of Sublimable Bipolar Cationic Cuprous Complexes with Thermally Activated Delayed Fluorescence, Inorg Chem, 56, 3742–3753 (DOI: 10.1021/acs.inorgchem.6b01847)
19. S. Murray N., Keller S., C. Constable E., E. Housecroft C., Neuburger M., Prescimone A., (2015), [Cu(N^N)(P^P)] + Complexes with 2,2′:6′,2″-Terpyridine Ligands as the N^N Domain. Dalton Trans, 44, 7626–7633 (DOI: 10.1039/C5DT00517E)
20. Paderina A., Ramazanov R., Valiev R., Müller C., Grachova E., (2022), So Close, Yet so Different: How One Donor Atom Changes Significantly the Photophysical Properties of Mononuclear Cu(I) Complexes, Inorg Chem, 61, 11629–11638 (DOI: 10.1021/acs.inorgchem.2c01145)
21. Sandoval-Pauker C., Santander-Nelli M., Dreyse P., (2022), Thermally Activated Delayed Fluorescence in Luminescent Cationic Copper(i) Complexes, RSC Adv 12, 10653–10674 (DOI: 10.1039/D1RA08082B)
22. Keller S., Brunner F., Junquera-Hernández J.M., Pertegás A., La-Placa M., Prescimone A., Constable E.C., Bolink H.J., Ortí E., Housecroft C.E., (2018), CF_3 Substitution of [Cu(P^P)(Bpy)][PF_6] Complexes: Effects on Photophysical Properties and Light-Emitting Electrochemical Cell Performance, ChemPlusChem, 83, 217–229 (DOI: 10.1002/cplu.201700501)
23. Santander-Nelli M., Sanhueza L., Navas D., Rossin E., Natali M., Dreyse P., (2022), Unusual Fluorescence Behaviour of a Heteroleptic Cu(i) Complex Featuring Strong Electron Donating Groups on a

Diimine Ligand, New J Chem, 46, 1693–1703 (DOI: 10.1039/D1NJ04811B)

24. Leoni E., Mohanraj J., Holler M., Mohankumar M., Nierengarten I., Monti F., Sournia-Saquet A., Delavaux-Nicot B., Nierengarten J.-F., Armaroli N., (2018), Heteroleptic Copper(I) Complexes Prepared from Phenanthroline and Bis-Phosphine Ligands: Rationalization of the Photophysical and Electrochemical Properties, Inorg Chem, 57, 15537–15549 (DOI: 10.1021/acs.inorgchem.8b02879)
25. Wang D.-D., Song L., Wang Y.-Y., Guo J.-Y., Shen H.-Y., Wang X.-R., Chai W.-X., (2020), Heteroleptic [Cu(NN)P2]+-Type Cuprous Complexes and Their Structural Modulation on Phosphorescent Color: Synthesis, Structural Characterization, Properties, and Theoretical Calculations, Appl Organomet Chem, 34, e5561 (DOI: 10.1002/aoc.5561)
26. Fresta E., Volpi G., Milanesio M., Garino C., Barolo C., Costa R.D., (2018), Novel Ligand and Device Designs for Stable Light-Emitting Electrochemical Cells Based on Heteroleptic Copper(I) Complexes, Inorg Chem, 57, 10469–10479 (DOI: 10.1021/acs.inorgchem.8b01914)
27. Farias G., Salla C.A.M., Heying R.S., Bortoluzzi A.J., Curcio S.F. Cazati T., Santos P.L. dos, Monkman A.P., Souza B. de, Bechtold I.H., (2020) Reducing Lifetime in Cu(I) Complexes with Thermally Activated Delayed Fluorescence and Phosphorescence Promoted by Chalcogenolate–Diimine Ligands, J Mater Chem C, 8, 14595–14604 (DOI: 10.1039/D0TC03660A)
28. Huang C.-H., Yang M., Chen X.-L., Lu C.-Z., (2021), Bright Bluish-Green Emitting Cu(i) Complexes Exhibiting Efficient Thermally Activated Delayed Fluorescence, Dalton Trans, 50, 5171–5176 (DOI: 10.1039/D0DT04424E)
29. Wada A., Zhang Q., Yasuda T., Takasu I., Enomoto S., Adachi C., (2012), Efficient Luminescence from a Copper(i) Complex Doped

in Organic Light-Emitting Diodes by Suppressing C–H Vibrational Quenching, Chem Commum, 48, 5340–5342 (DOI: 10.1039/C2CC31509B)

30. Hasegawa T., Kobayashi A., Ohara H., Yoshida M., Kato M., (2017), Emission Tuning of Luminescent Copper(I) Complexes by Vapor-Induced Ligand Exchange Reactions, Inorg Chem, 56, 4928–4936, (DOI: 10.1021/acs.inorgchem.6b03122)
31. Kondo S., Yoshimura N., Yoshida M., Kobayashi A., Kato M., (2020), Vapochromic Luminescence of a Spin-Coated Copper(I) Complex Thin Film by the Direct Coordination of Vapour Molecules, Dalton Trans, 49, 16946–16953 (DOI: 10.1039/D0DT03167D)
32. Chen X.-W., Yuan H.-L., He L.-H., Chen J.-L., Liu S.-J., Wen H.-R., Zhou G., Wang J.-Y., Wong W.-Y., (2019), A Sublimable Dinuclear Cuprous Complex Showing Selective Luminescence Vapochromism in the Crystalline State, Inorg Chem,58, 14478–14489 (DOI: 10.1021/acs.inorgchem.9b01972.
33. Moussa M.E.S., Evariste S., Wong H.-L., Bras L.L., Roiland C., Polles L.L., Guennic B.L., Costuas K., W.-W. Yam V., Lescop C., (2016), A Solid State Highly Emissive Cu(i) Metallacycle: Promotion of Cuprophilic Interactions at the Excited States, Chem. Commun, 52, 11370–11373 (DOI: 10.1039/C6CC06613E)
34. Tang S.-Y., Song L., Jia Y.-F., Xu W.-Z., Yang Y.-X., Sun L.-J., Shen H.-Y., Chai W.-X., (2023), Three Heteroleptic Copper(I) Complexes with [Cu(P∧P)N2]+ Structure and Their Fluorescence Sensing for VOCs, Appl Organomet Chem, 37, e7242 (DOI: 10.1002/aoc.7242)
35. Dai Z.-Q., Song L., Wang Y.-Y., Wang J.-T., Jia Y.-F., Zhang D.-Q., Yan S., Chai W.-X., (2023), Two Luminescent Materials of CuI Clusters Based on Mono-Phosphine Ligands and Their Fluorescence Sensing Properties, J Clust Sci, 34, 2497–2507 (DOI: 10.1007/s10876-022-02401-8)

36. Cariati E., Lucenti E., Botta C., Giovanella U., Marinotto D., Righetto S., (2016), Cu(I) Hybrid Inorganic–Organic Materials with Intriguing Stimuli Responsive and Optoelectronic Properties, Coord Chem Rev, 306, 566–614 (DOI: 10.1016/j.ccr.2015.03.004)
37. Yu X., Li X., Cai Z., Sun L., Wang C., Rao H., Wei C., Bian Z., Jin Q., Liu Z., (2021), Mechanochromic Properties in a Mononuclear Cu(i) Complex without Cuprophilic Interactions, Chem Commun, 57, 5082–5085 (DOI: 10.1039/D1CC01229K)
38. Kobayashi A., Kato M., (2017), Stimuli-Responsive Luminescent Copper(I) Complexes for Intelligent Emissive Devices, Chem Lett, 46, 154–162 (DOI: 10.1246/cl.160794)
39. Chen X.-W., He L.-H., Ju P., Chen J.-L., Liu S.-J., Wen H.-R., (2020), Mechanochromic Luminescent Materials of Bimetallic Cu(I) Complexes Showing Thermally Activated Delayed Fluorescence, J Mater Chem C, 8, 16160–16167 (DOI: 10.1039/D0TC04607H)
40. Jia Y.-F., Song L., Xu, W.-Z., Wu J.-T., Jin H.-X., Zhu Y.-F., Lai, J.-Q., Shen H.-Y., Chai W.-X., (2023), A Three-Coordinate Cuprous Complex Exhibiting Both Photochromic and Fluorescent Sensing Properties, and Some TD-DFT Calculations, J Mol Struct, 1292, 136134 (DOI: 10.1016/j.molstruc.2023.136134)
41. Chai W., Hong M., Song L., Jia G., Shi H., Guo J., Shu K., Guo B., Zhang Y., You W., (2015), Three Reversible Polymorphic Copper(I) Complexes Triggered by Ligand Conformation: Insights into Polymorphic Crystal Habit and Luminescent Properties, Inorg Chem, 54, 4200–4207 (DOI: 10.1021/ic502709b)
42. Ravaro L.P., Mafud A.C., Li Z., Reinheimer E., Simone C.A., Mascarenhas Y.P., Ford P.C., de Camargo A.S.S., (2018), New Emissive Mononuclear Copper (I) Complex: Structural and Photophysical Characterization Focusing on Solvatochromism, Rigidochromism and Oxygen Sensing in Mesoporous Solid Matrix, Dyes Pigments, 159, 464–470 (DOI: 10.1016/j.dyepig.2018.07.020)

43. Waelder J., Vasquez R., Liu Y., Maldonado S., (2022), A Description of the Faradaic Current in Cyclic Voltammetry of Adsorbed Redox Species on Semiconductor Electrodes, J Am Chem Soc, 144, 6410–6419 (DOI: 10.1021/jacs.2c00782)
44. Chaudhary A., Pathak D.K., Tanwar M., Koch J., Pfnür H., Kumar R., (2020), Polythiophene-nanoWO $_3$ Bilayer as an Electrochromic Infrared Filter: A Transparent Heat Shield, J Mater Chem C, 8, 1773–1780 (DOI: 10.1039/C9TC05523A)
45. Mortimer R.J., (2011), Electrochromic Materials, Annu Rev Mater, Res, 41, 241–268 (DOI: 10.1146/annurev-matsci-062910-100344)

Chapter 3

Redox Dependent Color Modulating Cu(I) Complex for Flexible Electrochromic Device

3.1 Introduction

The development of flexible electrochromic devices (FECDs) is one of the most important and rapidly growing areas of optoelectronics due to their potential applications in wearable and deformable optoelectronics, electronic papers, billboards, smart windows, smart labels, variable-reflectance mirrors, auto-dimming rearview mirrors, sensors, and energy storage *[1–7]*. The main difference between rigid and FECDs is device architecture, i.e., flexible substrate, but fabrication presents significant challenges such as poor flexibility, performance decay upon deformation, and electrolyte leakage through mechanical strain or stress. Furthermore, the field of flexible electronics has been rapidly evolving, making the development of flexible electrochromic materials a key research focus.[8] This enables the integration of electrochromism with the mechanical adaptability of flexible substrates. Such EC materials can be bent, stretched, or rolled, which enables their applications. Therefore, FECDs have gained significant attention from both academia and industry *[9–13]*.

In continuation of our work on exploring the EC performance of Cu(I) complexes, herein, we synthesize Cu(I) complexes, $[Cu(PPh_3)(cmdf)]PF_6$ (**4**), $[Cu(DPEphos)(cmdf)]PF_6$ (**5**) and $[Cu(Xantphos)(cmdf)]PF_6$ (**6**). The resulting complexes show absorption between 360 and 470 nm due to metal-to-ligand charge transfer (MLCT) transitions. As all complexes show similar absorption properties therefore complex **6** was chosen for studying the electrochromic properties. The promising results obtained from the EC performance of **6** prompted us to explore it in the bilayer solid-state and flexible EC devices. Both devices give excellent performance in terms of color modulation and switching time, which is comparable to some of the best-reported inorganic EC devices.

3.2 Experimental Section

3.2.1.1 Materials

Materials obtained from commercial suppliers and used without further purification unless otherwise stated. All glassware, magnetic stirring bars, and needles were thoroughly dried in a convection oven at 70 °C. All complexes were synthesized using Schlenk techniques under an inert N_2 atmosphere. The Cu(I) source $[Cu(CH_3CN)_4]PF_6$ was synthesized using the reported procedure *[14]*. The cmdf ligand was synthesized using modification in the previously reported method.[15] Commercial grade chemicals, Xantphos (Spectrochem) polyethylene oxide (PEO, Alfa Aesar, MW=100,000), poly (3-Hexyl thiophene-2,5 diyl) (P3HT, regioregular, Sigma Aldrich^{TM}), 1,2-Dichlorobenzene (DCB, anhydrous, 99%, Sigma Aldrich^{TM}), lithium perchlorate, and acetonitrile (ACN, anhydrous, 99%, Sigma Aldrich^{TM}) were used for device fabrication. Indium-doped tin oxide (ITO) coated glass substrate was purchased from Macwin India. ITO-coated polyethylene terephthalate (PET) was purchased from Sigma Aldrich^{TM}.

3.2.1.2. Characterization methods

^{1}H, $^{13}C\{^{1}H\}$, and $^{31}P\{^{1}H\}$ NMR were recorded on a Fourier transform nuclear magnetic resonance (NMR) spectrometer, model Bruker Avance 500 MHz spectrometer. ^{1}H and $^{13}C\{^{1}H\}$NMR spectra were referenced relative to the residual solvent peak. High-resolution mass spectral analyses (HRMS) were recorded on a Bruker-Daltonics micrOTOF-Q II mass spectrometer. Single crystal X-ray analysis was performed on Saxi-CrysalisPro-abstract goniometer imported SAXI images and the data were collected at 293(2) K. Using Olex2 *[16]*, the structure was solved with the SHELXT structure solution program using Intrinsic Phasing and refined with the SHELXL refinement package using Least Squares minimization *[17]*. Thermogravimetric analysis was performed on the powder sample using METTLER TOLEDO TGA/DSC 1 STARe System having a heating rate of 10 °C min^{-1} under a nitrogen atmosphere. UV-Vis spectroscopy was performed on Agilent Cary 60 UV−vis spectrophotometer in a quartz cuvette (1 cm ×1 cm). In-situ bias-dependent color modulation was studied

using a Lambda 365 spectrophotometer (PerkinElmer make) and a Keithley 2450 workstation. The electrochemical measurement was done using a Metrohm-Multi Autolab M204 potentiostat. The crystal structure of **4** and **6** was used for geometry optimization. Ground state DFT calculations were done by the ORCA 5.0.3 program package developed by Neese and coworkers *[18,19]* using B3LYP functional with a def2-TZVP basis set. Cyclic Voltammetry was performed using an AUTOLAB, PGSTAT 12 (Ecochemie, B.V. Netherlands) with GPES software (version 4.9) in a conventional blank ITO-coated glass slide as the working electrode, the CV curve was recorded in a potential range of ±3 V and at a scan rate of 100 mV/s.

3.3 Synthetic Details

3.3.1.1 Synthesis of 4,5-diazafluoren-9-one (DAFO)

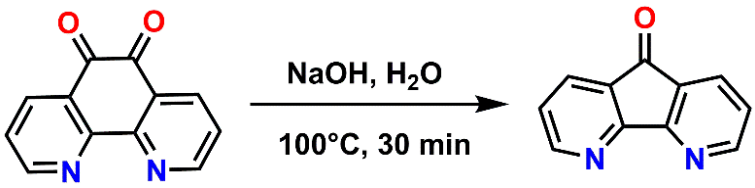

Scheme 3.1 Synthesis of DAFO.

DAFO was synthesized using a modified reported procedure *[20]*, in a 100 mL round-bottom flask, 1,10-phenanthroline-5,6-dione (250 mg, 1.189 mmol) was taken. To this NaOH (142 mg, 3.0 equiv., 3.567 mmol) in 12 mL of water was added. The resulting mixture was stirred at 100 °C for 30 min. The product was extracted with DCM (3x10 mL and the organic part was washed with brine and dried over anhydrous Na_2SO_4. The solvent was evaporated by a rotary evaporator to give the DAFO as a yellow powder with 85% yield. ^{1}H NMR (500 MHz, $CDCl_3$) δ 8.80 (dd, J = 5.0, 1.7 Hz, 2H), 8.00 (dd, J = 7.6, 1.7 Hz, 2H), 7.35 (dd, J = 7.6, 5.0 Hz, 2H). HRMS (ESI): calculated for $C_{11}H_6N_2ONa$ $[M+Na]^+$: 205.0372, Found: 205.0377.

3.3.1.2 Synthesis of 9-dicyanomethylene-4, 5-diazafluorene (cmdf)

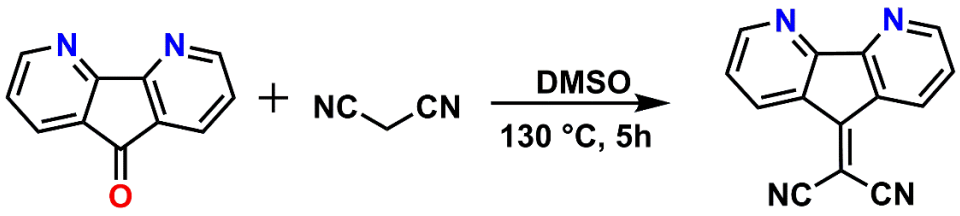

Scheme 3.2 Synthesis of the cmdf ligand.

In a clean round-bottom flask, 4,5-diazafluoren-9-one (0.54 mmol) and malononitrile (0.81 mmol) were taken and 3 mL of DMSO was added. The resulting mixture was stirred at 130 °C for 5 hours. After completion of the reaction, the mixture was cooled to room temperature, and the yellow-colored needle-shaped crystals were obtained in the solvent. Then the product was filtered and washed with acetonitrile, and a yellow crystalline compound was obtained. (Yield = 98%). **^{1}H NMR** (500 MHz, $CDCl_3$) δ 8.80 (dd, *J* = 5.0, 1.4 Hz, 2H), 8.69 (dd, *J* = 7.9, 1.5 Hz, 2H), 7.41 (dd, *J* = 8.0, 5.0 Hz, 2H). **^{13}C{^{1}H} NMR** (126 MHz, $CDCl_3$) δ 159.99, 156.82, 155.55, 133.93, 129.44, 124.91, 112.57, 80.36. **HRMS** (ESI): calculated for $C_{14}H_6N_4Na$ $[M+Na]^+$: 253.0485, Found: 253.0478.

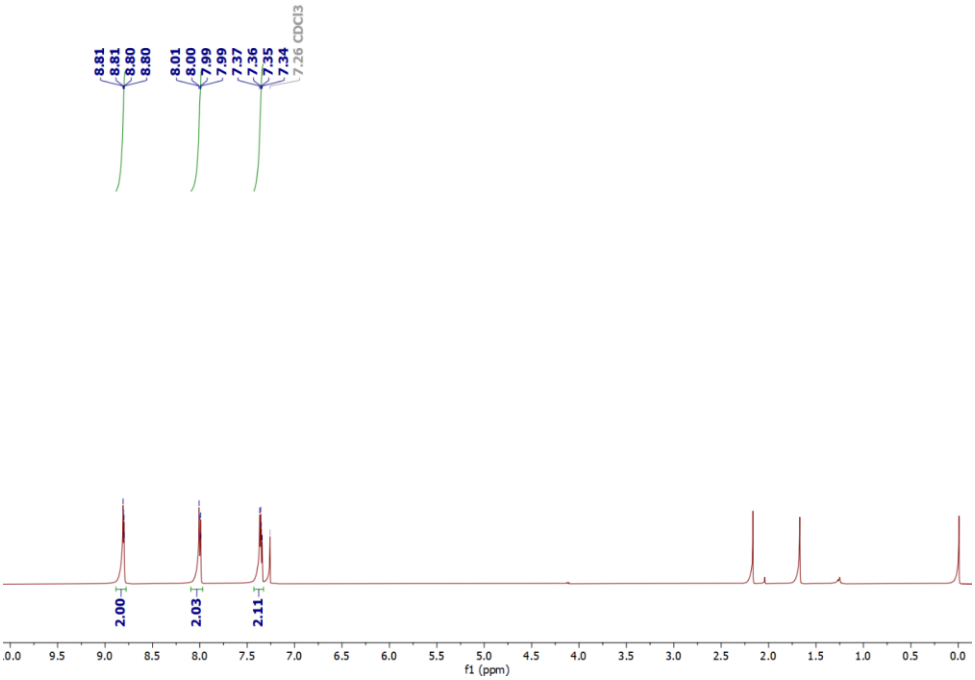

Fig. 3.1 ^{1}H NMR spectrum of **DAFO** in $CDCl_3$ (500 MHz).

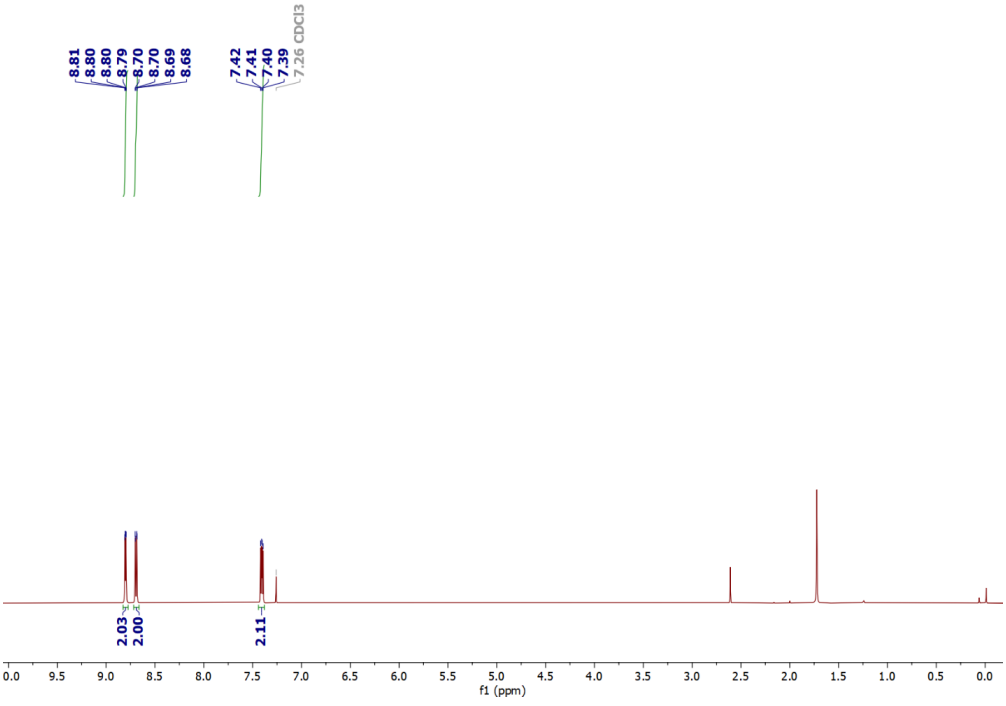

Fig. 3.2 ^{1}H NMR spectrum of **cmdf** in $CDCl_3$ (500 MHz).

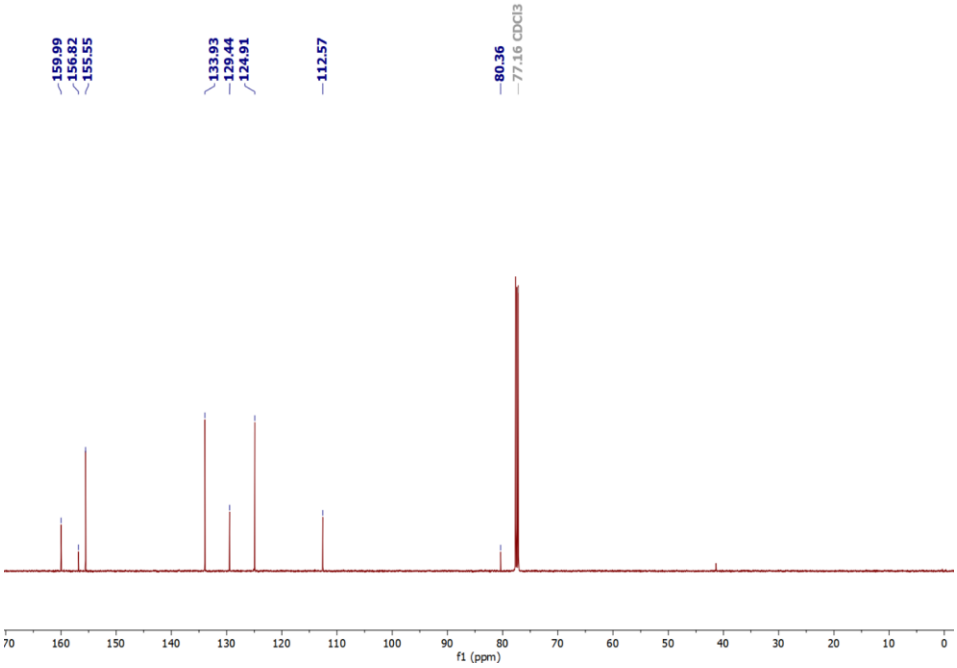

Fig. 3.3 $^{13}C\{^{1}H\}$ NMR spectrum of **cmdf** in $CDCl_3$ (126 MHz).

3.3.1.3 General procedure for Synthesis of complexes

In a clean and dry Schlenk tube, 1 eqv. phosphine ligand (in the case of complex **4**, 2 eqv. of PPh_3) was dissolved in 4 mL of DCM. To this solution of $[Cu(CH_3CN)_4]PF_6$ (1 eqv.) in DCM (4 mL) was added, and the resulting mixture was stirred for 2 hours at room temperature in the presence of an inert N_2 atmosphere. After this, the solution of cmdf ligand (1 eqv.) in 4 mL of DCM was added, then the reaction mixture was stirred further for 2 hours. The solvent was evaporated by rotary evaporation and the product was dissolved in a small amount of DCM and precipitated by the addition of n-Hexane.

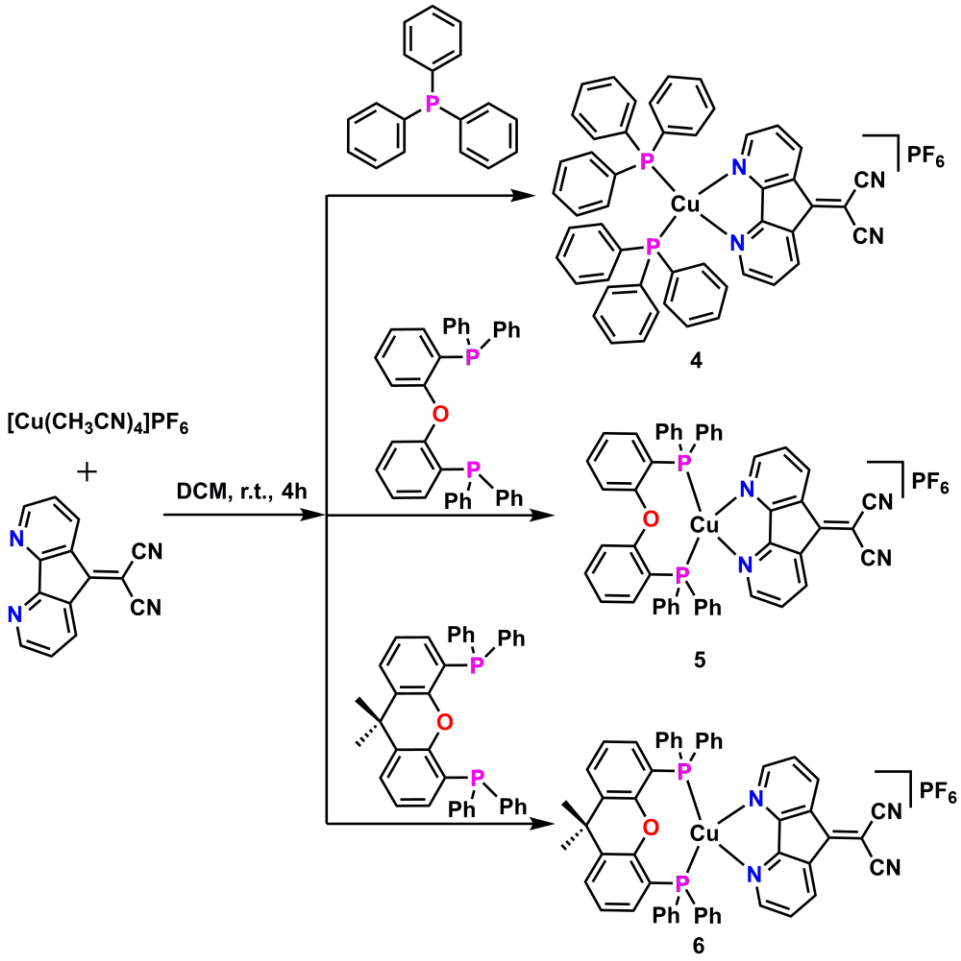

Scheme 3.3 General synthetic procedure of complexes **4**-**6**.

3.3.1.3.1 Synthesis of $[Cu(PPh_3)_2(cmdf)]PF_6$ (4)

Following the general procedure, using PPh_3 (1 eqv.), $[Cu(CH_3CN)_4]PF_6$ (1 eqv.), and cmdf (1 eqv.) gave complex **4** as a brown powder in 65% yield. **^{1}H NMR** (500 MHz, DMSO-d6) δ 8.77 (d, *J* = 5.3 Hz, 2H), 8.60 (d, *J* = 8.1 Hz, 2H), 7.65 (dd, *J* = 8.1, 5.0 Hz, 2H), 7.47 (t, *J* = 7.4 Hz, 6H), 7.37 (t, *J* = 7.6 Hz, 12H), 7.25 (d, *J* = 6.1 Hz, 12H). **^{13}C{^{1}H} NMR** (126 MHz, DMSO-d6) δ 157.61, 155.01, 153.54, 133.92, 133.22, 133.12, 132.07, 131.85, 130.39, 129.21, 128.97, 126.36, 112.43. **^{31}P{^{1}H} NMR** (202 MHz, DMSO-d6) δ -1.87, -144.18. **HRMS (ESI, m/z)**: Calcd for **$C_{50}H_{36}CuN_4P_2$ [(M-PF_6)]$^+$**: 817.1706. Found: m/z 817.1651.

3.3.1.3.2 Synthesis of [Cu(DPEphos)(cmdf)]PF_6 (5)

Complex **5** was synthesized using the general procedure. DPEphos (1 eqv.), [Cu(CH_3CN)$_4$]PF_6 (1 eqv.) and cmdf (1 eqv.) gave complex **5** as a brown powder in 95% yield. **^{1}H NMR** (500 MHz, DMSO-d6) δ 8.67 (d, *J* = 5.2 Hz, 2H), 8.61 (dd, *J* = 7.9, 1.4 Hz, 2H), 7.66 (dd, *J* = 7.9, 5.0 Hz, 2H), 7.42 (d, *J* = 7.3 Hz, 4H), 7.38 (d, *J* = 7.6 Hz, 8H), 7.36 (d, *J* = 1.7 Hz, 2H), 7.23 (q, *J* = 7.5, 6.7 Hz, 8H), 7.07 (d, *J* = 7.6 Hz, 4H), 6.75 – 6.68 (m, 2H). **^{13}C{^{1}H} NMR** (126 MHz, DMSO-d6) δ 157.53, 155.22, 153.42, 133.82, 133.71, 133.24, 133.14, 132.18, 130.69, 130.32, 129.18, 128.89, 126.29, 125.00, 123.15, 120.23, 112.46. **^{31}P{^{1}H} NMR** (202 MHz, DMSO-d6) δ -16.71, -144.19. **HRMS (ESI, m/z)**: Calcd for **$C_{50}H_{34}CuN_4OP_2$ [(M-PF_6)]$^+$**: 831.1498. Found: m/z 831.1471.

3.3.1.3.3 Synthesis of [Cu(Xantphos)(cmdf)]PF_6 (6)

A similar general synthetic procedure was used to synthesize complex **6**, Xantphos (1 eqv.), [Cu(CH_3CN)$_4$]PF_6 (1 eqv.) and cmdf (1 eqv.), a brown-colored powder was obtained in a 90% yield. The formation of complex **6** is confirmed by ^{1}H, ^{13}C{^{1}H} and ^{31}P{^{1}H}NMR spectroscopies (**Fig. 3.10-3.12**). **^{1}H NMR** (500 MHz, DMSO-d6) δ 8.77 (d, *J* = 5.2 Hz, 2H), 8.60 (d, *J* = 6.9 Hz, 2H), 7.76 (d, *J* = 6.7 Hz, 2H), 7.63 (dd, *J* = 8.0, 5.0 Hz, 2H), 7.42 (t, *J* = 7.4 Hz, 4H), 7.35 (t, *J* = 7.6 Hz, 8H), 7.26 (q, *J* = 7.2, 6.7 Hz, 10H), 6.65 (m, *J* = 8.1, 4.0 Hz, 2H), 1.62 (s, 6H). **^{13}C{^{1}H} NMR** (126 MHz, DMSO-d6) δ 153.70, 133.26, 132.90, 132.83, 132.77, 130.64, 129.94, 128.67, 128.64, 128.60, 127.50, 125.53, 124.81,113.37, 71.99, 40.05, 27.96. **^{31}P{^{1}H} NMR** (202 MHz, DMSO-d6) δ -17.56, -144.19. **HRMS** (ESI, m/z): Calcd for **$C_{53}H_{38}CuN_4OP_2$** [(M-PF_6)]$^+$: 871.1811; Found: m/z 871.1836.

3.3.1.4 Characterisations of 4-6.

The purity of complexes **4-6** was confirmed by the data obtained from multinuclear NMR techniques in DMSO-d_6 (**Fig. 3.4-3.12**) and HRMS. In the ^{1}H NMR spectra of all complexes, the protons corresponding to the phenyl rings of PPh_3, DPEphos and Xantphos were observed in the range

of 7.23 to 7.63 ppm. Additionally, in complex **6**, a singlet (s, 6H) at 1.62 ppm indicates the presence of six methyl protons attached to the bridging carbon atom between two phenyl rings of Xantphos. In the deshielded region of all complexes, doublets were observed from 8.77 to 7.65 ppm are attributed to protons of the cmdf ligand. $^{13}C\{^{1}H\}$ NMR spectrum showed the peaks for the dicyanide group of cmdf ligand observed around 112 and 113 ppm. The remaining aromatic carbon signals (150 to 124 ppm) correspond to both ligands. Additionally, in complex **6**, a signal at 40.05 ppm corresponds to the bridging carbon atom between two phenyl rings of Xantphos, whereas methyl groups present on these bridging carbon atoms show signals at 27.96 ppm. In the $^{31}P\{^{1}H\}$ NMR spectrum of all complexes the singlet at -1.87, -16.71 and -17.56 ppm corresponds to the coordinated phosphine ligands, whereas the characteristic septet around -144 ppm confirms the presence of PF_6 counterion. HRMS of **4** shows characteristic isotopic signature of copper with loss of one PPh_3 ligand: m/z = 607.0897 (607.0856 calcd for $[M\text{-}PF_6]^+$) while complexes **5** and **6** show the m/z of 883.1591 and 923.1894 (883.1560 and 923.1873 calcd for $[M\text{-}PF_6]^+$).

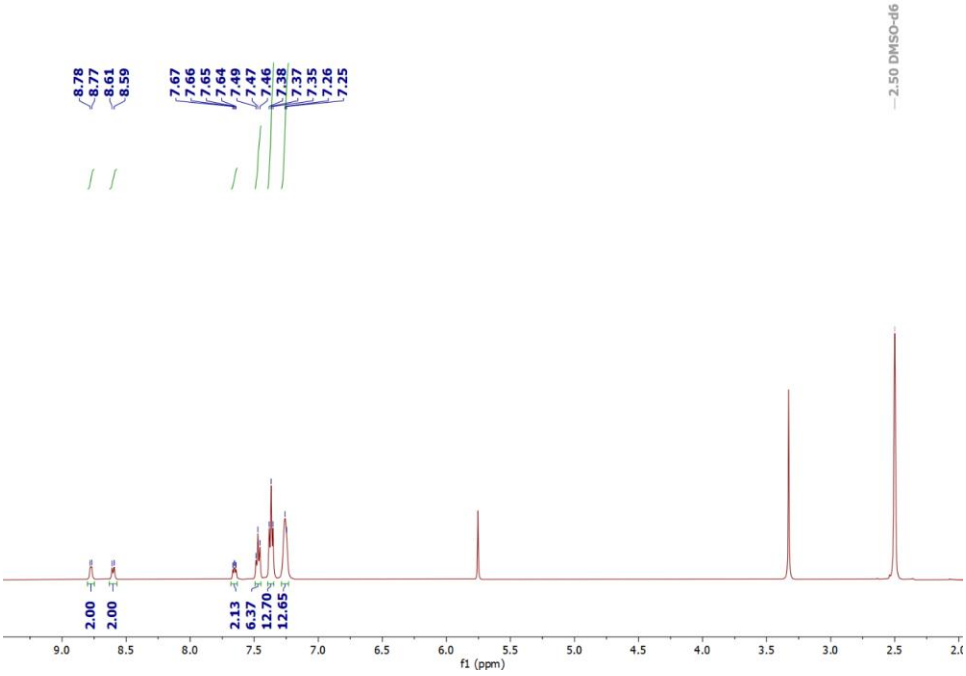

Fig. 3.4 ^{1}H NMR spectra of **4** in DMSO-d_6 (500 MHz).

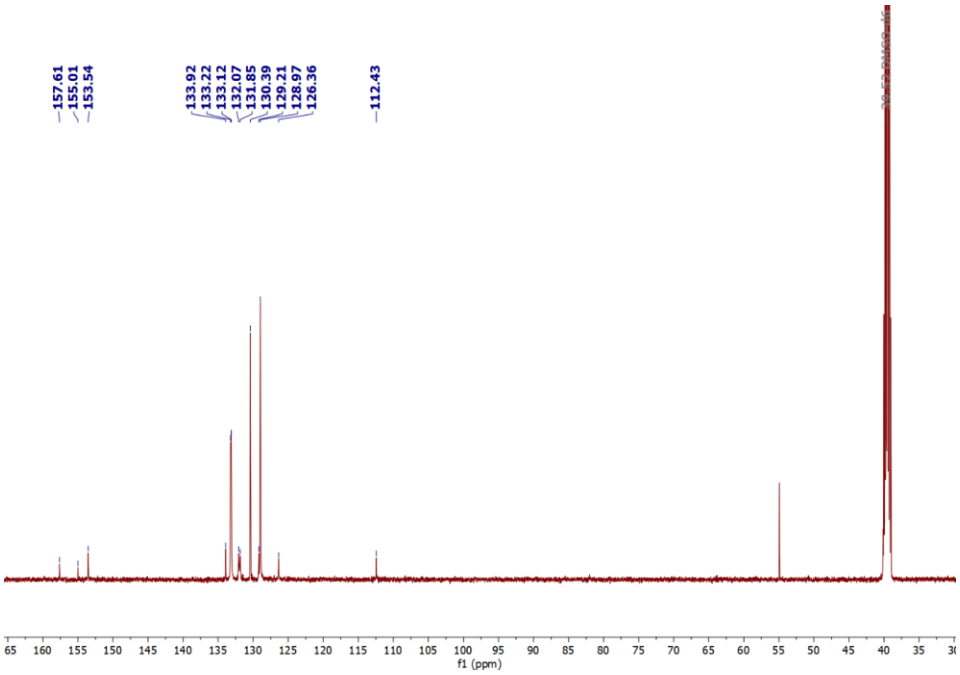

Fig. 3.5 $^{13}C\{H\}$ NMR spectra of **4** in DMSO-d_6 (126 MHz).

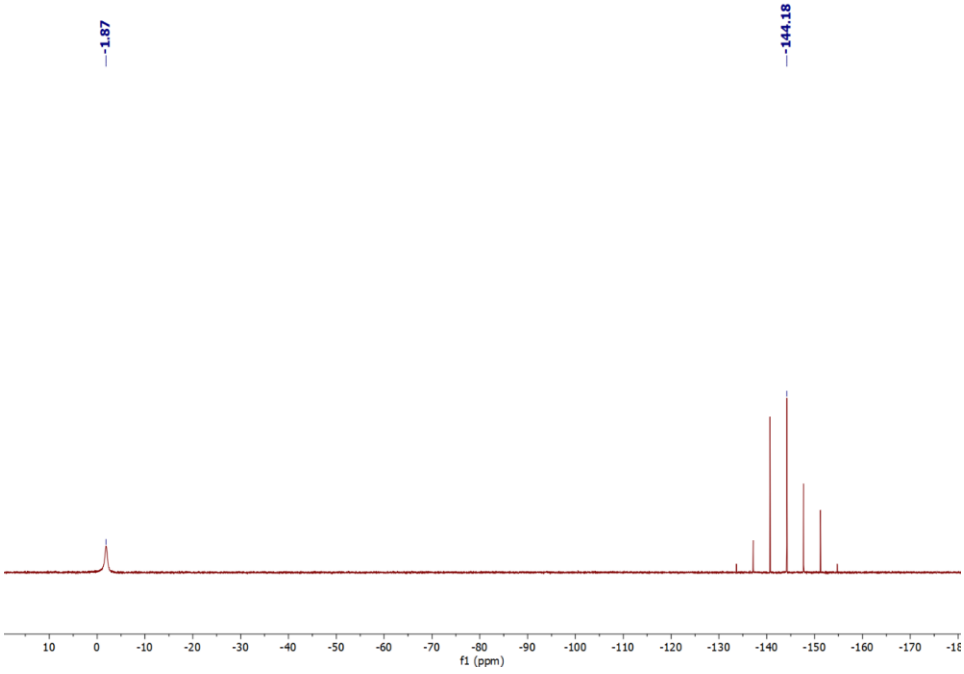

Fig. 3.6 $^{31}P\{H\}$ NMR spectra of **4** in DMSO-d_6 (202 MHz).

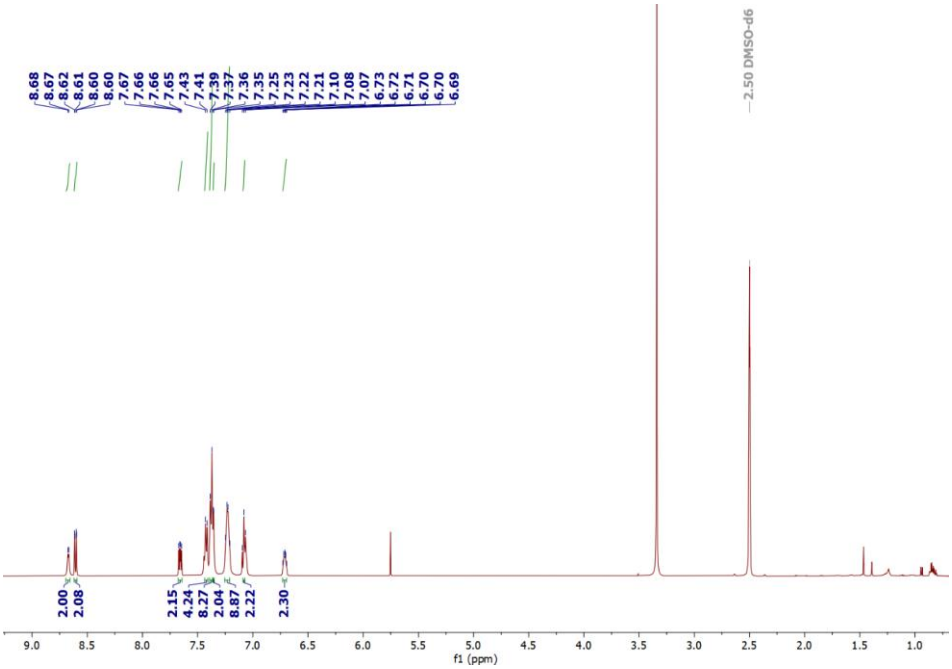

Fig. 3.7 ^{1}H NMR spectra of **5** in DMSO-d_6 (500 MHz).

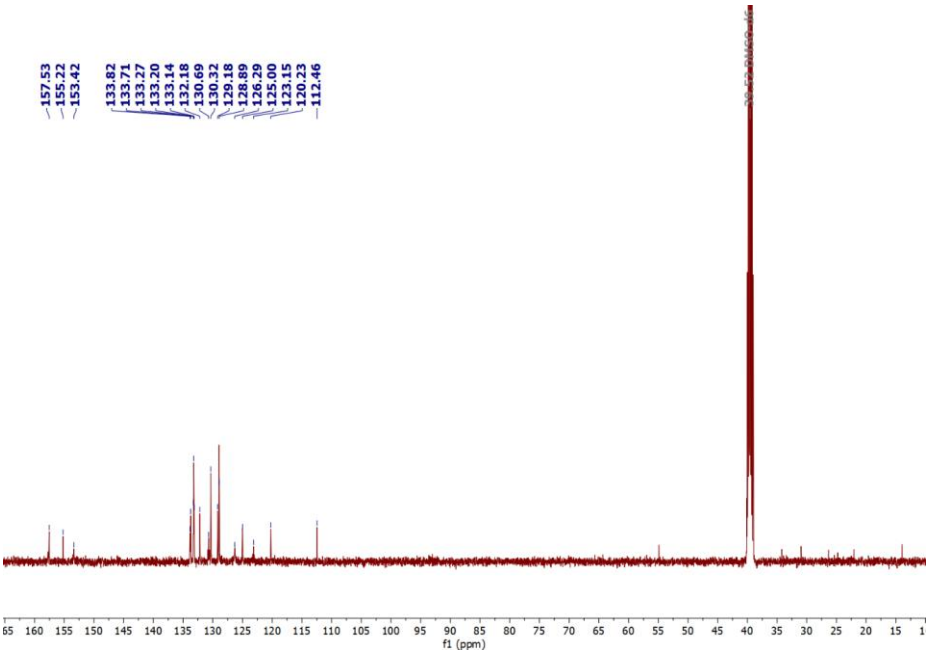

Fig. 3.8 ^{13}C{H} NMR spectra of **5** in DMSO-d_6 (126 MHz).

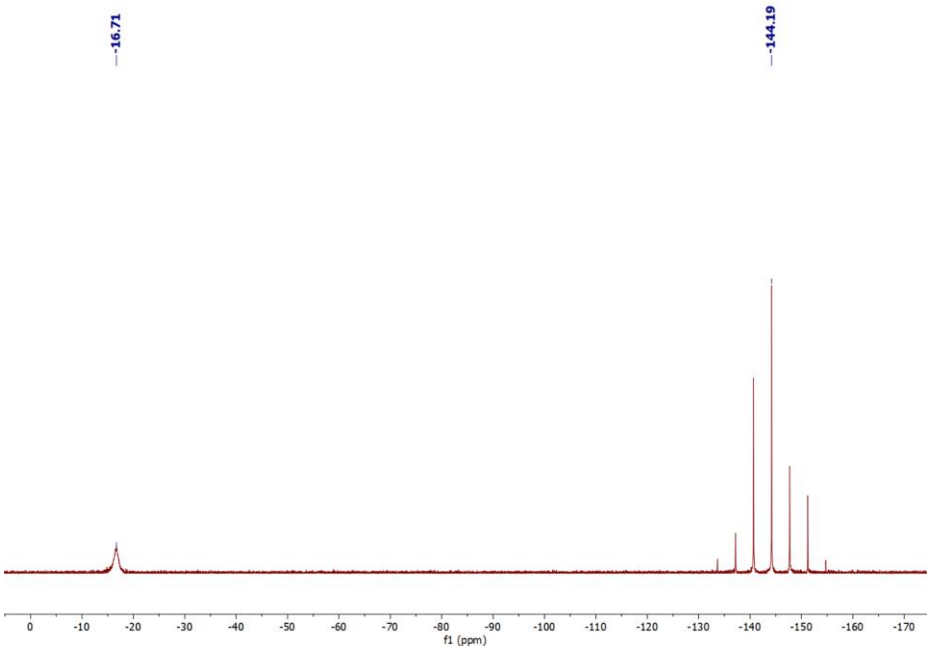

Fig. 3.9 $^{31}P\{H\}$ NMR spectra of **5** in DMSO-d_6 (202 MHz).

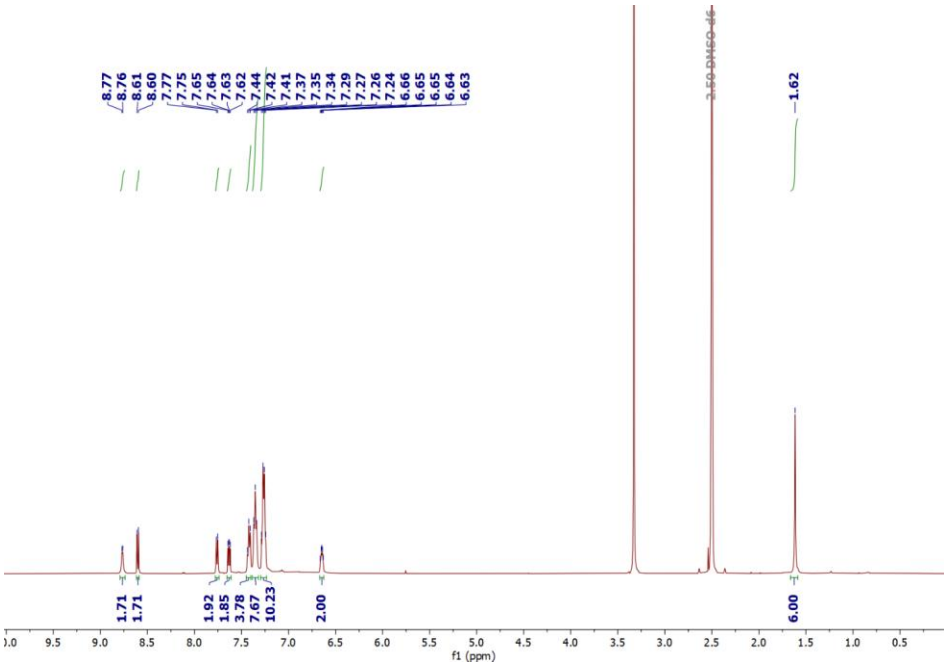

Fig. 3.10 ^{1}H NMR spectrum of **6** in DMSO-d_6 (500 MHz).

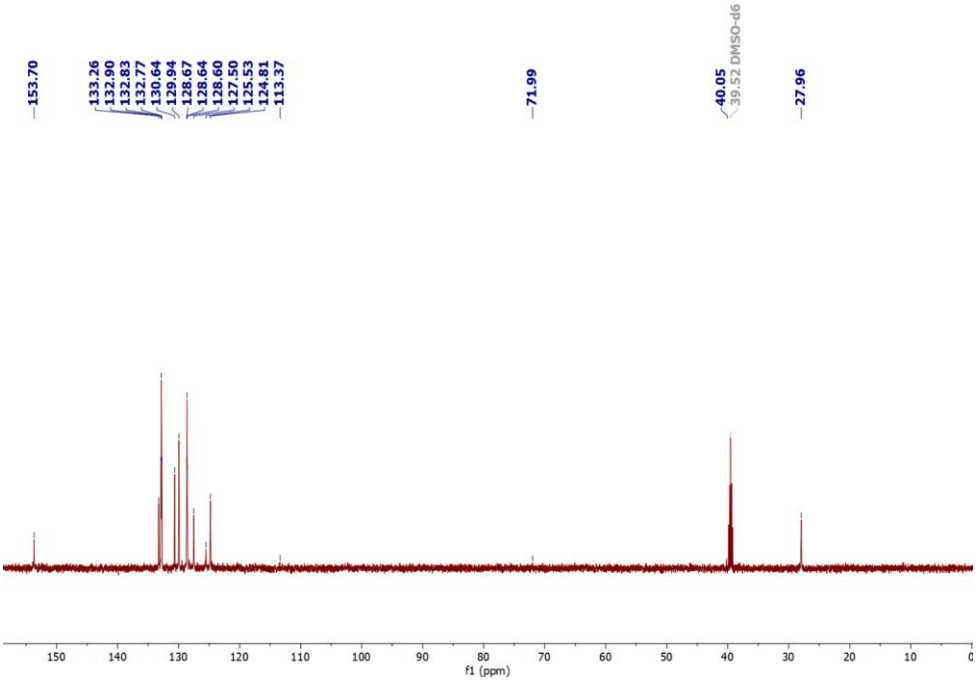

Fig. 3.11 $^{13}C\{^{1}H\}$ NMR spectrum of **6** in DMSO-d_6 (126 MHz).

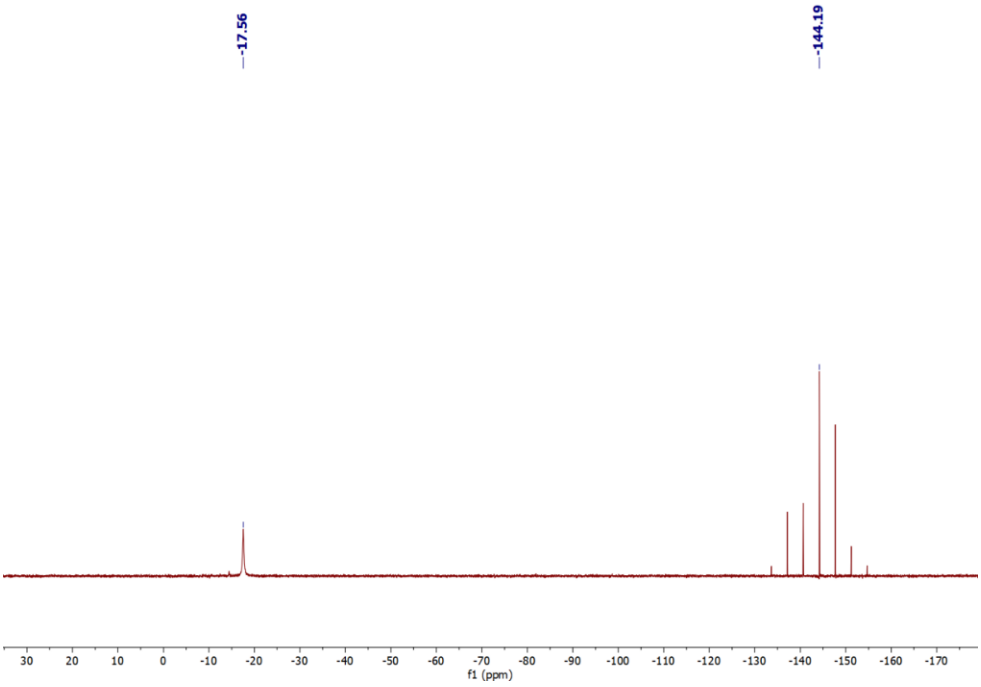

Fig. 3.12 $^{31}P\{^{1}H\}$ NMR spectrum of **6** in DMSO-d_6 (202 MHz).

3.4 Structural analysis

Single crystals of **4** and **6**, suitable for single-crystal X-ray diffraction analysis were grown from slow evaporation of a DCM solution with layering of n-hexane at room temperature. The obtained molecular structures are shown in **Fig. 3.13**. Complexes **4** and **6** were crystallized in monoclinic and triclinic crystal systems having Cc and P-1 space groups, respectively. The complete crystallographic data and structure refinement details are summarized in **Table 3.1**.

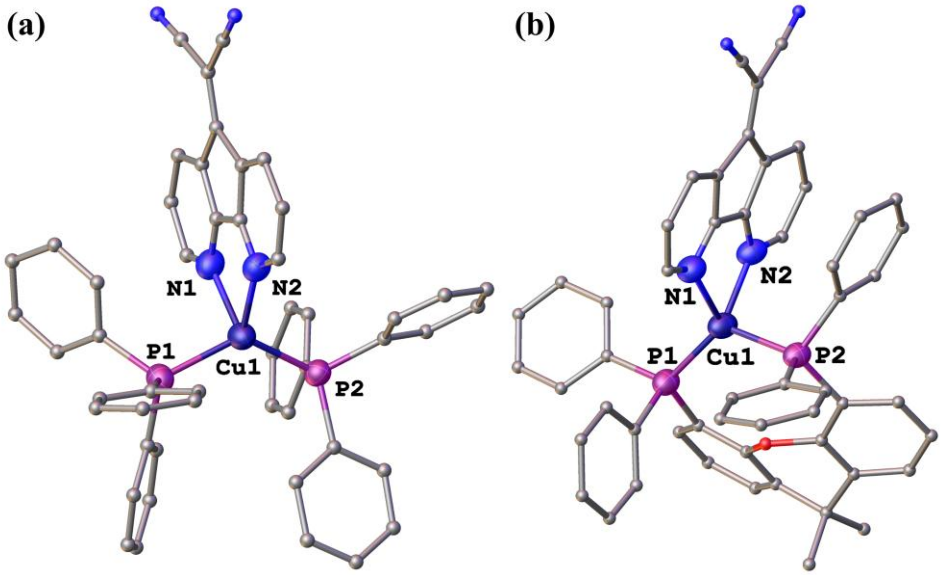

Fig. 3.13 Molecular structures of complexes **4** and **6**. Hydrogen atoms, solvent and counterions are omitted for clarity.

The coordination geometry around the Cu(I) center is found to be distorted tetrahedral, in which the Cu(I) atom binds with two nitrogen atoms of the cmdf ligand and two phosphine atoms from Xantphos ligands similar to previously reported Cu(I) complexes *[21–24]*. A comparison of bond lengths and angles is tabulated in **Tables 3.2** and **3.3**. It is found that Cu-P bond distances lie between 2.22 and 2.29 Å, whereas the Cu-N bond distances are 2.25 and 2.12 Å. In addition, the bond angles between P1-Cu1-P2, P1-Cu1-N1, P2-Cu1-N2, and N1-Cu1-N2 are found to be 122.71,

120.07, 101.78 and 83.04° respectively. Further, the dihedral angle between the N–Cu–N and P–Cu–P planes is found to be 88.56°, which is close to the ideal tetrahedral coordination geometry found in previously reported four-coordinated Cu(I) complexes *[25]*. Additionally, the inter- and intra-molecular interactions provide additional stability to the molecular structure of corresponding molecules.

Table 3.1 Crystal and refinement data table of complexes **4** and **6**.

Complex	**4**	**6**
Empirical formula	$C_{51}H_{38}Cl_2CuF_6N_4P_3$	$C_{53}H_{38}CuF_6N_4OP_3$
Formula weight	1048.20	1016.82
Crystal system	monoclinic	triclinic
Space group	Cc	P-1
a/Å	10.7632(4)	14.3404(2)
b/Å	23.8722(9)	16.9795(3)
c/Å	21.5043(7)	24.3539(4)
α/°	90	91.0810(10)
β/ °	96.262(3)	95.4240(10)
γ/°	90	114.7180(10)
V/ $Å^3$	5492.4(3)	5351.36(15)
Z	4	4
$\rho_{calc}g/cm^{-3}$	1.268	1.262
μ/mm^{-1}	0.638	0.558
R1 (R1 all data) [I > 2σ(I)]	0.0708	0.0770
wR2 (wR2 all data)	0.1559	0.2467
Data/restraints/parameters	9587/171/616	24521/0/1229
GOF	1.046	1.094

Table 3.2 Selected bond lengths of complexes **4-6**.

Bond length (Å)	**4**	**6**
P1-Cu1	2.2798	2.2212
P2-Cu1	2.2754	2.2955
N1-Cu1	2.169	2.258
N2-Cu1	2.329	2.126

Table 3.3 Selected bond angles of complexes **4** and **6**.

Bond Angle (°)	**4**	**6**
P1-Cu1- P2	129.05	122.71
P1-Cu1-N1	109.22	120.07
P2-Cu1-N2	106.29	101.78
N1-Cu1-N2	81.78	83.04

3.4.1.1 Weak interactions observed in complexes 4 and 6.

The weak interactions provide good stability to complexes. In complex **4** C-H····N interactions were observed (2.515 Å) between N atom of nitrile and C-H of phenyl ring present on PPh_3 ligand, also C-H····F interactions (2.504 and 2.399 Å) between PF_6 counter ion and C-H of cmdf ligand and DCM molecule present in the complex (**Fig. 3.14**). In contrast, complex **6** shows intermolecular C-H···π interactions between the C-H atom of one phosphine ligand and the π cloud of another phosphine ligand with a distance of 2.729 Å. Additionally, it shows inter- and intramolecular C-H···F interactions between PF_6 counter ion and C-H of phosphine ligands, having distances ranging from 2.362 to 2.578 Å (**Fig. 3.15**).

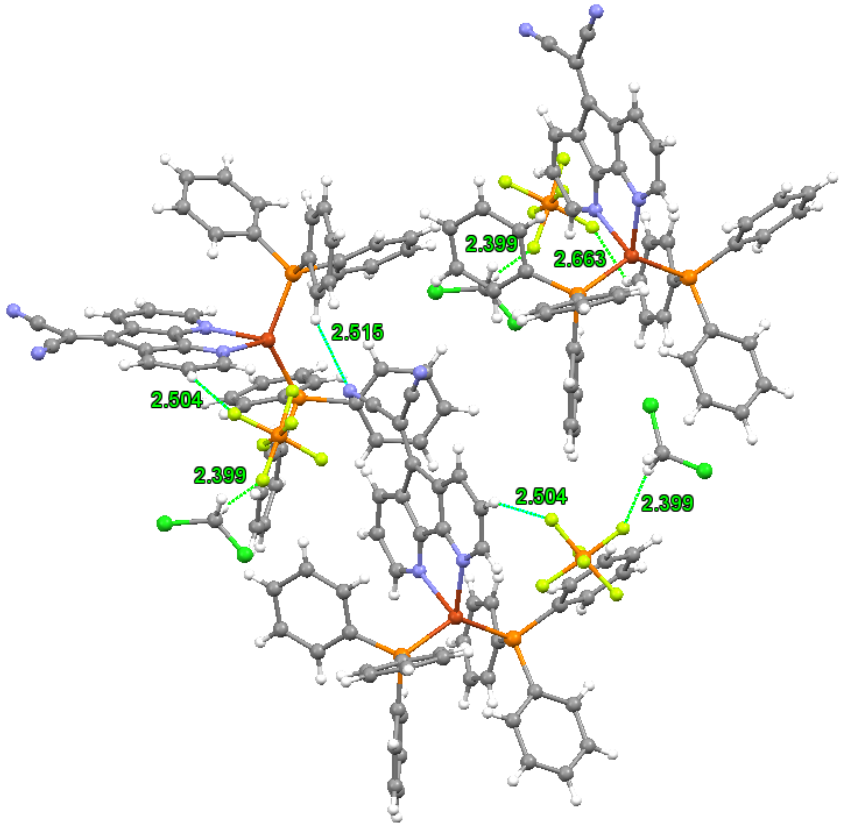

Fig. 3.14 C-H···N and C-H···F weak interactions observed in complex **4**.

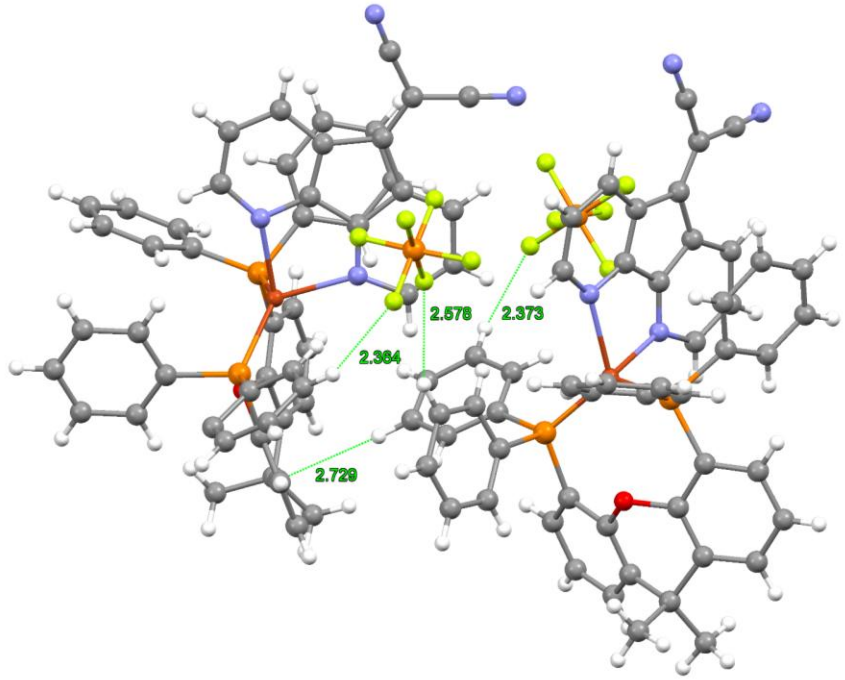

Fig. 3.15 C-H···π, inter and intramolecular C-H···F interactions in **6**.

3.4.1.2 Thermogravimetric analysis

The TGA curve of complexes **4** and **5** suggests that these complexes were thermally stable up to 150 °C, whereas complex **6** is thermally stable up to 240 °C (**Fig. 3.16**). It is found that the presence of bidentate DPEphos and Xantphos ligands provides greater stability to the complexes as compared to PPh_3-containing counterparts. The first step of decomposition is about 10-15% weight loss corresponding to the counterion, while the 65-70% weight loss is for the phosphine ligands. Furthermore, decomposition occurs around 300 °C when the cmdf ligands begin to dissociate.

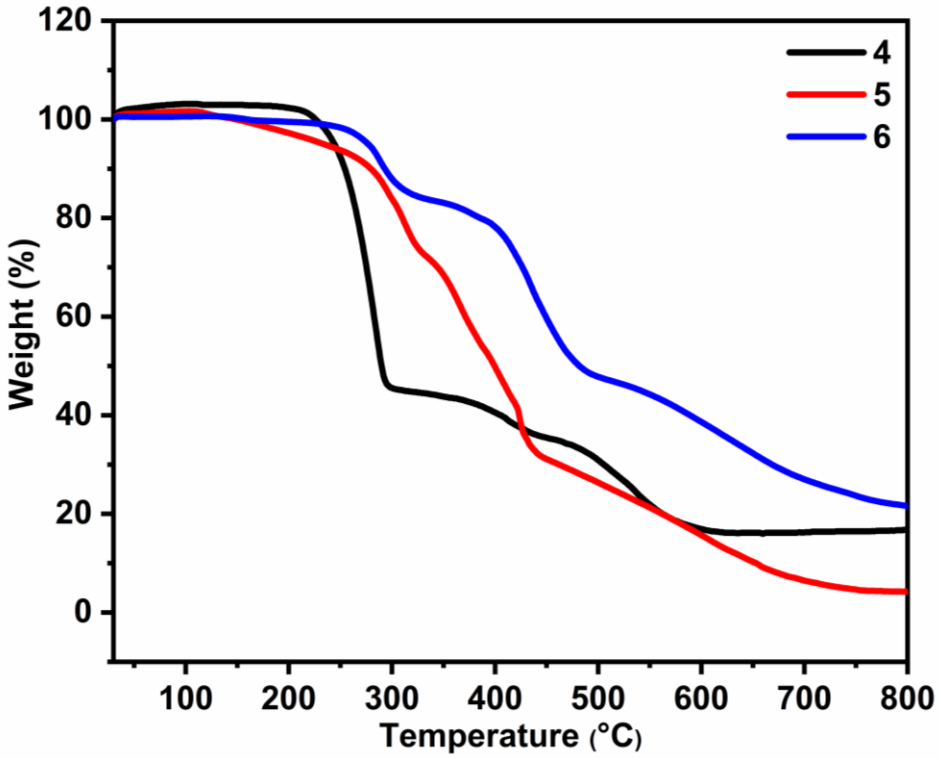

Fig. 3.16 TGA curve of **4-6** under nitrogen atmosphere with the temperature heating rate of 10 °C min^{-1}.

3.5 Photophysical properties and theoretical calculations

The UV-Vis absorption of complexes **4-6** was investigated in DCM (0.01 mM), which is depicted in **Fig. 3.17a**. It consists of two absorption bands, the high-energy band ranging from 250 nm to 350 nm, and the low-energy

band in the 360 to 480 nm range. The high-energy band can be assigned to the π→π* transition in ligands, whereas the low-energy band arises due to the spin-allowed metal-to-ligand charge transfer transition (MLCT) from the 3d orbital of the copper(I) to π* orbital of the cmdf ligand *[22,26–29]*.

As in the solution form all complexes show similar absorption; therefore, only complex **6** was used for further study. The solid-state UV-visible DRS of **6** was performed on the powder sample exhibiting similar absorption behaviour with a broad absorption from 220 to 480 nm with a shoulder around 400 nm (**Fig. 3.17b**). Based on results obtained from the Kubelka−Munk method applied to solid-state DRS absorption, the band gap energy of **6** is found to be 2.89 eV, suggesting the semiconducting nature of this complex (**Fig. 3.17c**) *[30–36]*.

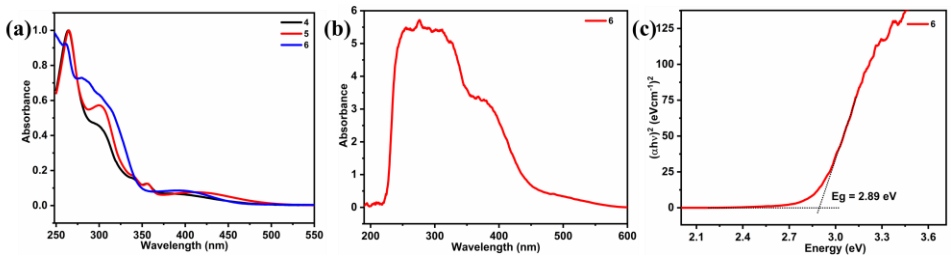

Fig. 3.17 (a) Room temperature absorption spectra of **4-6** in DCM, (b) Solid state UV–Visible diffuse reflectance spectra (DRS) at room temperature and (c) Kubelka−Munk function band gap of **3** obtained from solid-state DRS.

Density functional theory (DFT) calculations were performed using the B3LYP functional and Def2TZVP basis set *[37,38]* to understand the electronic nature of complexes **4-6**. It was found that the HOMO is situated on the Cu(I) center with some involvement of the phosphine ligands, whereas the LUMO is positioned on the cmdf ligand (**Fig. 3.18**).

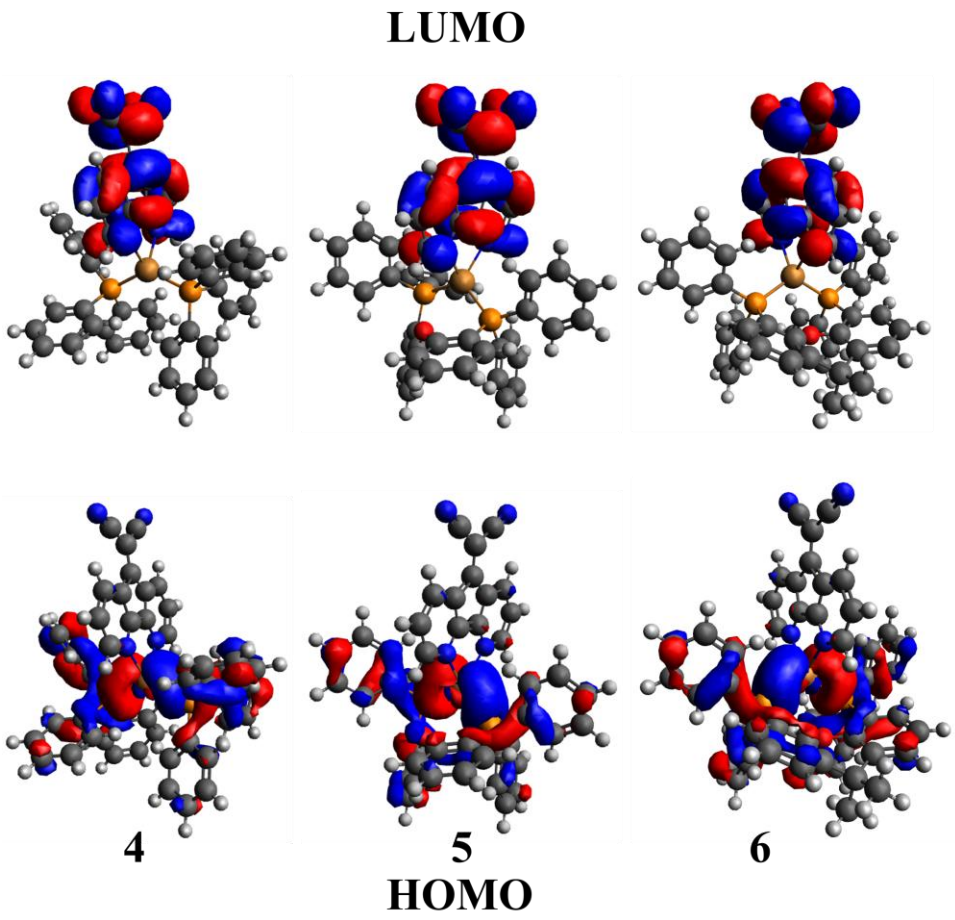

Fig. 3.18 Frontier molecular orbitals obtained from B3LYP/def2-TZVP level of theory (Cu = Brown, P = Orange, N = blue, O = red, C = black and H = grey). The counterions are omitted for clarity.

Hence, it is concluded that the electronic transitions arise from the 3d orbital of the copper(I) center to the π* orbital of the cmdf ligand, which is responsible for the low-energy charge transfer transitions.

3.6.1.1 Electrochemical studies and Electrochromic behaviour of 6.

The electrochemical activity of complex **6** in solution is evaluated from a three-electrode system consisting of blank ITO as the working, Pt wire as counter and Ag/AgCl as reference electrodes. The solution was prepared by adding 5 mg of complex **6** into the 0.1 M $LiClO_4$ in ACN. The cyclic voltammetry (CV) was carried out in the potential window of +3 V to -3 V

at a scan rate of 100 mV/s (**Fig. 3.19a**). Prominent redox couple peaks at -0.46 V (oxidation) and -1.9 V (reduction) confirmed the redox nature of **3**. During CV, it was observed that the complex was reversibly changing color from transparent to dark state (**Fig. 3.19a** inset), which is an important condition for the material to be called electrochromic active.

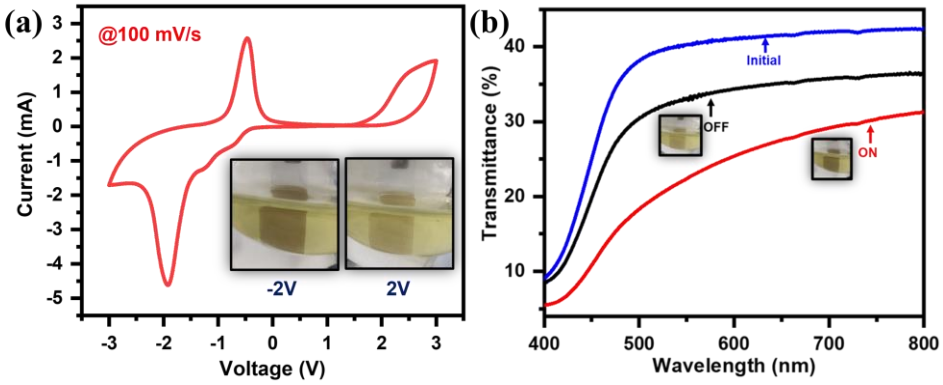

Fig. 3.19 (a) Cyclic voltammetry curve of **6**, (b) Spectro-electrochemical study of **3**/ITO electrode in initial, ON (-2 V) and OFF (2 V) states.

To check the electrochromic behaviour of the **6,** the spectro-electrochemical study has been performed using the same solution and three-electrode setup as mentioned above by applying the potential of ±2 V **(Fig. 3.19b)**. Initially, due to the transparent state of ITO, a blue curve was obtained (initial). When the bias of -2 V is applied to the system (ON state), the color of the ITO changes from a transparent state to a dark state (**Fig. 3.19b, inset**), as a result, the overall absorbance value increases **(red curve, Fig. 3.19b)**. Again, when the reverse bias of 2 V is applied to the system (OFF state), the ITO comes back to its transparent state (**Fig. 3.19b, inset**) as can be seen from the decreased absorbance values **(black curve, Fig. 3.19b)**. The above-mentioned spectro-electrochemical analysis of the **6** demonstrates its potential as a suitable counter ion for the fabrication of electrochromic devices.

3.6.1.2 Recipe for Rigid and Flexible ECDs Fabrication

Complex **6** was proved to be an EC active counter ion when tested in a solution-based electrochemical cell, but practical implementation demands replication of color modulation performance in a solid-state device. Hence, a simple solid-state mono-layer ECD in the configuration "ITO/ TTF //complex **6**/ ITO" has been fabricated using TTF(Tetrathiafulvalene) as an ion storage layer by a flip-chip method *[39–43]*.

1. Fabrication of solid-state **6**-electrochromic device (***3****-ECD*).

a. Firstly, ITO-coated glass of dimension 2×1 cm^2 was used as an electrode, which was thoroughly cleaned by ultrasonication in a solution containing acetone, isopropanol and deionized water in an equal ratio for 10 minutes.

b. Approximately 0.5 wt.% complex **6** solution in acetonitrile (ACN) was spin-coated over the cleaned ITO substrate at 200 rpm for 60 minutes and was dried at 80 °C for a few minutes.

c. The Tetrathiafulvalene (TTF), an ion storage layer was prepared by dissolving 0.5 wt.% TTF in ACN and was drop casted (~50 µL) over ITO and dried at 80 °C for 5 minutes.

d. The gel electrolyte was prepared by mixing 0.1 M $LiClO_4$ in ACN and 5 wt.% polyethylene oxide (PEO) in equal proportion. The prepared gel electrolyte was sandwiched between the two above-prepared electrodes and was stuck together using the flip-chip method.

2. Fabrication of bilayer solid-state P3HT and **6**-based electrochromic device (***P3HT-complex 6 ECD***).

   a. The complex **6-based** electrode was prepared using the recipe discussed in 1b.

   b. The P3HT electrode was prepared by dissolving 0.3 wt.% poly (3-hexylthiophene-2,5-diyl) in dichlorobenzene (DCB) and

was spin-coated at 600 rpm for 60 minutes and later dried at 80 °C for 5 minutes.

- The above two prepared electrodes were sandwiched together by filling gel electrolyte (recipe 1d) in between them using the flip-chip method.

3. Fabrication of flexible P3HT and **6** complex-based electrochromic device (***f-P6HT-complex 6 ECD***).
    a. For the fabrication of a flexible device, the ITO was replaced by a PET substrate and the same recipe was adopted for fabricating *f-P3HT-complex 3 ECD*.

3.6.1.3 Electrochromic Performances of ECDs

The schematic visualization of the fabricated complex **6**-electrochromic device (***6-****ECD*) is shown in **Fig. 3.20a** with the actual photographs of the device in the colored and bleached state obtained under different bias conditions. The in-situ bias-dependent transmittance spectra of the ***6-****ECD* have been recorded in the visible range (400 nm to 800 nm) by giving a bias of 2 V. As seen in the CV curve (**Fig. 3.20b**), **6** was given a reduction peak at around -2 V and maximum color change was also observed at -2 V potential, so 2 V was chosen to study the performance of the device.

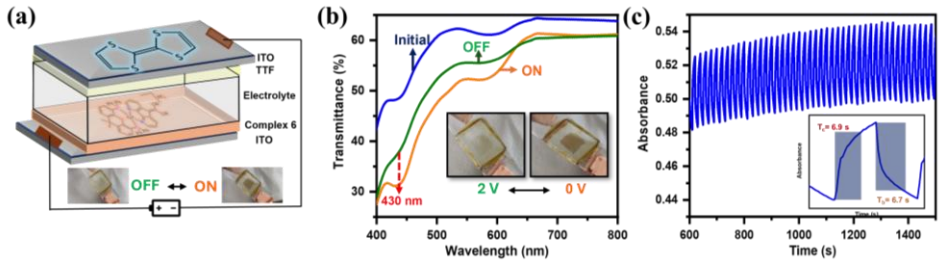

Fig. 3.20 (a) schematic of the control device with its actual photographs in ON and OFF states (inset), (b) in-situ transmittance spectra of the device with actual photographs (inset), and (c) switching cyclic stability of the device with single switching cycle (inset).

Initially, during the unbiased state, the ***6****-ECD* was transparent (blue curve, **Fig. 3.20b**). When a bias of 2 V is applied (ON state), such that the TTF electrode is getting +2 V and the **6** electrode is getting -2 V, the color of the device changes to brown color (colored state) (orange curve, **Fig. 3.20b**). During this process, the electron given by the TTF molecule is received by the **6**, causing a color change. When the device is again subjected to the unbiased state, the reverse redox reaction between the electrodes causes the device to return to its original transparent state (bleached state) (green curve, **Fig. 3.20b**). The bias-dependent optical spectra show the maximum change in color at 430 nm (**Fig. 3.20b**).

The evaluated color modulation at 430 nm was obtained to be 15%, which is only due to the color change of the **6**. Afterward, the other crucial parameters of the device were checked. Firstly, the **6**-*ECD's* stability (**Fig. 3.20c**) was investigated for 45 cycles by giving a pulse train of ±2 V and 0 V of 10 seconds each (**Fig. 3.21a**).

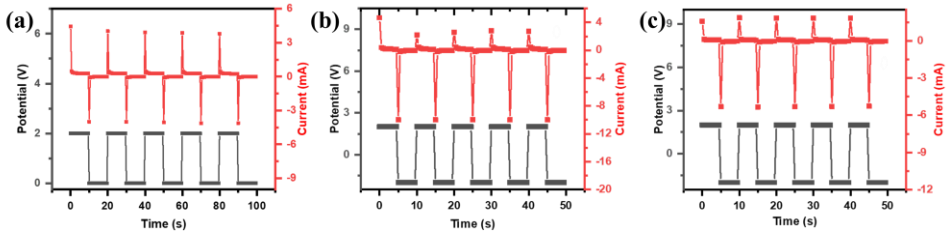

Fig. 3.21 Pulse train of ±2V for each and unbiased state of (a) complex ***6****-ECD* for 10 seconds (b) *P3HT-****6*** *ECD* for 5 seconds and (c) *f-P3HT-****6*** *ECD* for 5 seconds.

Pulse train of 2V and unbiased state of 10 seconds each for ***6****-ECD.* The device shows reasonable stability and reversibility throughout the cycle, with minimum change in absorbance value for 900 s (45 full cycles). Another important parameter is switching kinematics, that is the time taken to switch between the two states (transparent ↔ brown). The switching time for ***3****-ECD* was found to be 6.9 and 6.7 s for the coloration and bleaching, respectively, which is calculated at 90% of total coloration and bleaching.

Even though the electrochromic performance of the device is moderate, as measured by parameters like switching time, cycle life and color modulation, the above experiments establish the electrochromic nature of **6**.

As the device's performance was not very satisfactory, appropriate modifications in device architecture must be made to enhance the performance of **6**-based solid-state ECD. Since complex **6** is an n-type EC active material, hence a complementary p-type material is required and poly(3-hexylthiophene-2,5-diyl) (P3HT) is one such extensively studied conducting polymer, which changes color on the application of positive bias *[44,45]*. Therefore, a bilayer electrochromic device has been fabricated by replacing the TTF layer with a P3HT layer which is compatible with EC active complex **6** for fabricating a solid-state device. The complementary redox reaction is expected to enhance the overall performance of the device. Hence, a bilayer ECD in the configuration "ITO/P3HT//complex **6**/ITO" has been fabricated (Recipe 2) and the same schematic is shown in **Fig. 3.22a** (inset). The in-situ bias-dependent spectra were recorded in the visible range 400 to 800 nm to study the reversible change in fabricated solid-state P3HT-**6** electrochromic device (*P3HT-**6** ECD*) at ±2 V of bias. The original state of fabricated *P3HT-**6** ECD* is magenta in color due to the natural color of P3HT and the transparent nature of **6** (red curve, **Fig. 3.22a**). When a bias of 2 V (concerning the P3HT electrode) is applied, the device changes its color from magenta to light brown (colored state) due to the redox activity taking place between the two active materials (colored state) (orange curve, **Fig. 3.22a**). As soon as the bias is applied the P3HT goes to its bipolaronic state by getting oxidized and simultaneously complex **6** gets reduced, resulting in a change of color of the device from magenta to brown. When a reverse bias is applied (-2 V concerning P3HT electrode) the device regains its original color magenta (bleached state) (blue curve, **Fig. 3.22a**), showing excellent reversibility of the device as the curves for unbiased state and reversed bias state are almost coinciding with each other. The maximum

variation in transmittance spectra was observed at 515 nm with a high color modulation of 45%.

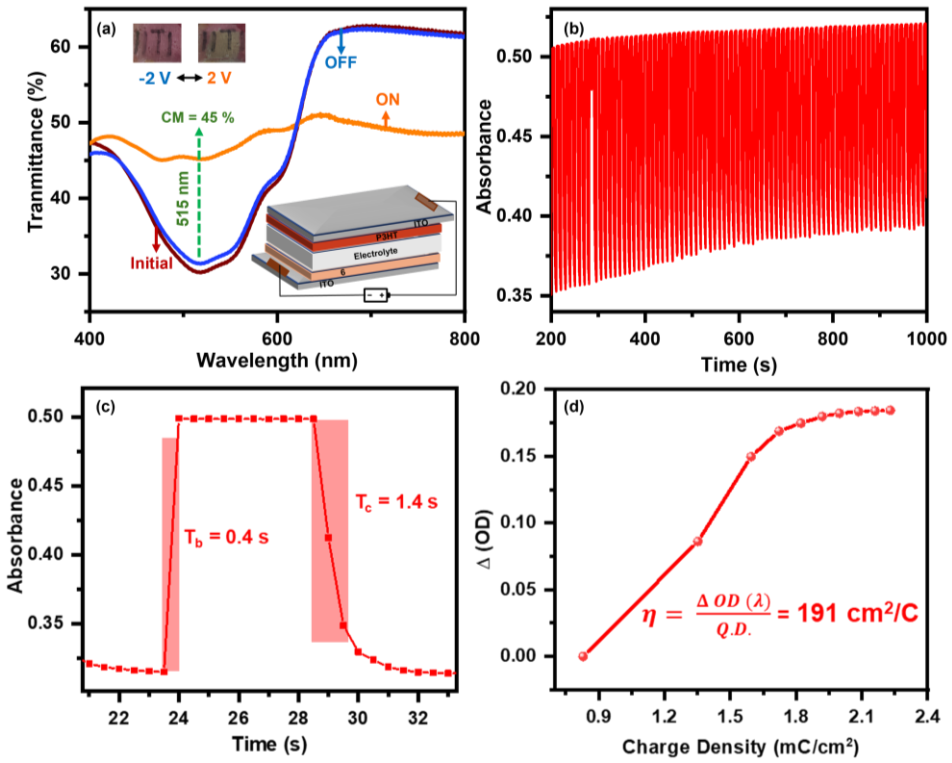

Fig. 3.22 (a) In-situ transmittance spectra with actual photographs and schematic of the device (inset), (b) cyclic stability, (c) single switching cycle, and (d) Coloration efficiency of *P3HT-**6** ECD*

Afterward, the stability of the *P3HT-**6** ECD* was checked at 515 nm by applying a continuous square pulse of ±2 V for 5 seconds each (**Fig. 3.21b**). This shows high stability for 800 s (80 full cycles of switching) with a slight change in the absorbance value, which might be due to some charge storage property of the device(**Fig. 3.22b**). The switching time was found to be 0.4 and 1.4 s for the bleaching and coloration cycle, respectively (**Fig. 3.22c**). This shows that the switching time has been significantly improved by using P3HT in the ion storage layer due to the faster redox reaction between the two electrode materials. Another important factor, coloration efficiency (CE) found to be 191 cm^2/C. The appreciable value of CE shows that the device is efficient in terms of power consumption. The replacement of the

ion storage layer has significantly enhanced the color modulation of the device due to the complementary redox nature of the two electrochromic active materials, and the switching time of the device has also been minimized.

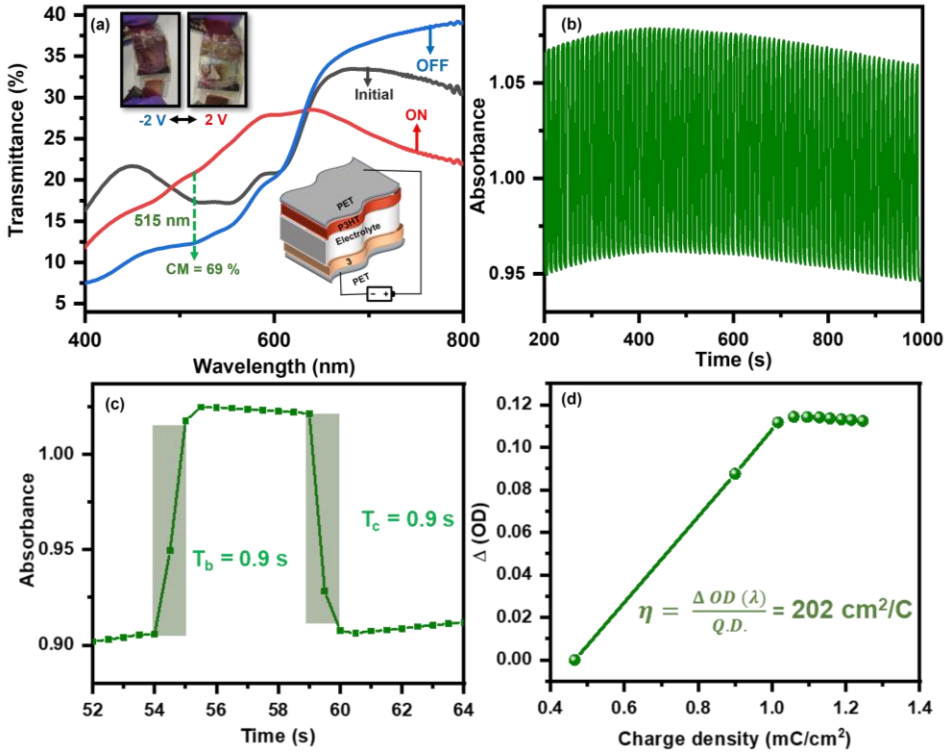

Fig. 3.23 (a) In-situ transmittance spectra with actual photographs and schematic of the flexible device (actual device and schematic in inset), (b) cyclic stability, (c) single switching cycle, and (d) coloration efficiency of the *f-P3HT-**6** ECD*.

Intrigued with the appreciable performance of *P3HT-**6** ECD,* a flexible ECD using P3HT and complex **6** has been fabricated (Recipe 3) using ITO-coated PET as substrate in the structure "PET/P3HT//complex **6**/PET". The schematic of the device along with actual photographs in ON and OFF state is shown in **Fig. 3.23** (inset). The performance of the *f-P3HT-**6** ECD* was studied using in-situ bias-dependent transmittance spectra by applying ±2 V. Initially, the *f-P3HT-**6** ECD* has a magenta color (black curve, **Fig. 3.23a**) during the unbiased condition, when 2 V bias is applied (with respect

to P3HT electrode) the color of device changes from magenta to light brown (red curve, **Fig. 3.23a**). Afterward, when -2 V is applied, the device comes back to its magenta color (blue curve, **Fig. 3.23a**). The high color modulation of 69% was evaluated at 515 nm. The stability and the switching time of the *f-P3HT-**6** ECD* was investigated by applying a square pulse train of ±2 V of 5 seconds each (**Fig. 3.21c**). The *f-P3HT-**6** ECD* shows high stability for 80 full cycles of switching (800 seconds) (**Fig. 3.23b**). The time taken to switch between the colored and bleached state is only 0.9 s, demonstrating great switching speed due to the rapid redox reaction between the two electrodes (**Fig. 3.23c**). The CE of the *f-P3HT-**6** ECD* was found to be 202 cm^2/C (**Fig. 3.23d**). The value is in a similar range to the solid-state device, establishing that the efficiency is not compromised even in the flexible state. The *f-P3HT-**6** ECD* also shows appreciable results, making it suitable for practical application in flexible ECD.

Table 3.4 Comparison of ECD performances with previously reported ECDs.

Sr. No.	EC systems/materials	Color Modulation (%)	Response time (s) Coloration/ Bleaching	Ref.
1	ITO/P3HT/**3**/ITO	45	0.4/1.4	Present work
2	PET/P3HT//**3**/PET	69	0.9	Present work
3	ITO/P3HT/Cu complex/ITO	38	0.8/0.5	*[22]*
4	ITO/$LiClO_4$/PolyCu/ITO	-	1.35/1.04	*[4]*
5	ITO/ gel electrolyte /PolyCuFe/ITO	-	4.8/1.1	*[46]*
6	/ITO/ WO_3–Nb_2O_5/Nb_2O_5/NiVOx/ ITO	-	7.0/0.7	*[47]*

7	glass/ITO/ $WO_3/Ta_2O_5/NiO/ITO/glass$	50	13/5	*[48]*
8	WO_3 film on ITO/PET gel electrolyte	49	1.6/ 5.88	*[49]*
9	V_2O_5 EC film, 1M$LiClO_4$–PC, V_2O_5/rGO EC film	35	6.3/11.8	*[50]*
10	V_2O_5:Fe (1%) EC film 1 M $LiClO_4$	46.29	2/3.7	*[51]*
11	Viologen in ionic liquid	65	5/15	*[52]*
12	ITO/ferrocene-Fc^+ /P3HT/viologen/ITO	-	0.5/0.9	*[53]*
13	ITO/P3HT/viologen/ITO	-	1.7/1.2	*[54]*
14	PANI–PSS//PEDOT–PSS PEO–PC–$LiClO_4$	40	8.8/ 9.7	*[55]*
15	PProDOTEt_2, 0.1MTBAP/ACN	75	2/2	*[56]*
16	Os-polypyridyl complex	39	0.5/0.5	*[57]*
17	Fe-polypyridyl complex	65	1/1	*[57]*
18	Bithiophene-pyridine Ru(III)-porphycene, 0.1MnBu_4NPF_6—CH_2Cl_2	-	3.7/2.3	*[58]*
19	ITO/PolyOsRu/ITO	58	0.78/0.34	*[59]*
20	ITO/PolyRu-LIIM/ITO	70	1.1	*[60]*
21	PolyRuFe/PB ECD	48	0.9/3.6	*[61]*
22	CuTCA 0.1 M $LiClO_4$/PC	65	5	*[62]*

Overall, the *P3HT-**3** ECD* and *f-P3HT-**6** ECD* show high color modulation and high switching speed with great stability and appreciable CE, which can be utilized to make solid-state and flexible ECDs for real-world

applications. Furthermore, the device performance of *f-P3HT-**6** ECD* in terms of color modulation and response time with previously reported EC materials (**Table 3.4**) and it is found that our device performance is comparable to that of some of the best-performing EC materials. Additionally, the use of convenient synthesis and cost-effective precursors gives synthesized Cu(I) material a significant advantage over others for fabricating ECD for practical applications.

3.7. Conclusion

In this study, we have synthesized a series of heteroleptic complexes $[Cu(PPh_3)_2(cmdf)]PF_6$ (**4**), $[Cu(DPEphos)(cmdf)]PF_6$ (**5**) and $[Cu(Xantphos)(cmdf)]PF_6$ (**6**) using different phosphine (PPh_3, DPEphos and Xantphos) and cmdf ligands. The complexes showed absorption in the UV-Vis region in the 360 to 480 nm range, assigned to MLCT transition. All complexes show the same absorption properties hence complex **6** was used to study the EC performance. Based on electrochemical analysis, **6** possesses reversible electrochromic behaviour. Furthermore, a monolayer electrochromic device based on **6** demonstrated reversible color change but limited color modulation. On the other hand, a bilayer electrochromic device using P3HT and **6** achieves high color modulation of 45% and a fast-switching time of less than a second, highlighting its potential for electrochromic applications. Moreover, **6** exhibited excellent compatibility with flexible substrates, as demonstrated by the fabrication of a flexible electrochromic device. This flexible device showed better performance than the solid-state counterpart, with a high efficiency of approximately 200 cm^2/C and sub-second switching times. The combination of high stability, efficiency and flexibility positions this material as a promising candidate for practical applications, including camouflage systems, flexible electrochromic displays, and sensors. This study highlights the importance of Cu(I) complexes as a promising material for the development of next-generation ECDs.

3.8 References

1. Argazzi R., Murakami Iha N.Y., Zabri H., Odobel F., Bignozzi C.A., (2004), Design of Molecular Dyes for Application in Photoelectrochemical and Electrochromic Devices Based on Nanocrystalline Metal Oxide Semiconductors, Coord Chem Rev, 248, 1299–1316 (DOI: 10.1016/j.ccr.2004.03.026)
2. Cannavale A., Ayr U., Fiorito F., Martellotta F., (2020), Smart Electrochromic Windows to Enhance Building Energy Efficiency and Visual Comfort, Energies, 13, 1449 (DOI: 10.3390/en13061449)
3. Park S., Thi Thuy D., Sarwar S., Van Tran H., In Lee S., Sung Park H., Han Song S., Han C.-H., Hong S., (2020), Synergistic Effects of Ti-Doping Induced Porous Networks on Electrochromic Performance of WO3 Films, J Mater Chem C, 8, 17245–17253, (DOI: 10.1039/D0TC04420B)
4. Hossain Md.D., Chakraborty C., Rana U., Mondal S., Holdt H.-J., Higuchi M., (2020), Green-to-Black Electrochromic Copper(I)-Based Metallo-Supramolecular Polymer with a Perpendicularly Twisted Structure, ACS Appl Polym Mater, 2, 4449–4454 (DOI: 10.1021/acsapm.0c00559)
5. Bansal L., Sahu B., Rath D.K., Ahlawat N., Ghosh T., Kandpal S., Kumar R., (2024), Stoichiometrically Optimized Electrochromic Complex [V2O2+ξ(OH)3-ξ] Based Electrode: Prototype Supercapacitor with Multicolor Indicator, Small, 20, 2312215 (DOI: 10.1002/smll.202312215)
6. Sahu B., Bansal L., Ghosh T., Kandpal S., Rath D.K., Rani C., Wesemann C., Bigall N.C., Kumar R., (2024), Metal Oxide-Mixed Polymer-Based Hybrid Electrochromic Supercapacitor: Improved Efficiency and Dual Band Switching, J Phys Appl Phys, 57, 245110 (DOI: 10.1088/1361-6463/ad2dba)
7. Bansal L., Ahlawat N., Sahu B., Rath D.K., Chondath S.K., Ghosh T., Kumar R., (2024), Nano-Nest Type Porous NiCo2S4@polyindole

Core–Shell Array: Efficient Energy Storage Supercapacitor Device, ACS Mater Let, 6, 3736–3744 (DOI: 10.1021/acsmaterialslett.4c00866.

8. Sahu B., Bansal L., Rath D.K., Kandpal S., Ghosh T., Ahlawat N., Rani C., Maximov M.Y., Kumar R., (2024), Bendable & Twistable Oxide-Polymer Based Hybrid Electrochromic Device: Flexible and Multi-Wavelength Color Modulation, Mater Today Electron, 7, 100082 (DOI: 10.1016/j.mtelec.2023.100082)
9. Chaudhary A., Sivakumar G., K. Pathak D., Tanwar M., Misra R., Kumar R., (2021), Pentafluorophenyl Substituted Fulleropyrrolidine: A Molecule Enabling the Most Efficient Flexible Electrochromic Device with Fast Switching, J Mater Chem C, 9, 3462–3469 (DOI: 10.1039/D0TC04991C)
10. Wang B., Zhang W., Zhao F., Yu W.W., Elezzabi A.Y., Liu L., Li H., (2023), An Overview of Recent Progress in the Development of Flexible Electrochromic Devices, Nano Mater Sci, 5, 369–391 (DOI: 10.1016/j.nanoms.2022.08.002)
11. Li W., Bai T., Fu G., Zhang Q., Liu J., Wang H., Sun Y., Yan H., (2022), Progress and Challenges in Flexible Electrochromic Devices, Sol Energy Mater Sol Cells, 240, 111709 (DOI: 10.1016/j.solmat.2022.111709)
12. Li R., Ma X., Li J., Cao J., Gao H., Li T., Zhang X., Wang L., Zhang Q., Wang G., (2021), Flexible and High-Performance Electrochromic Devices Enabled by Self-Assembled 2D TiO2/MXene Heterostructures, Nat Commun, 12, 1587 (DOI: 10.1038/s41467-021-21852-7)
13. Eh A.L.-S., Tan A.W.M., Cheng X., Magdassi S., Lee P.S., (2018), Recent Advances in Flexible Electrochromic Devices: Prerequisites, Challenges, and Prospects, Energy Technol, 6, 33–45 (DOI: 10.1002/ente.201700705)

14. J. Serpell C., Chall R., L. Thompson A., D. Beer P., (2011), Chloride Anion Triggered Motion in a Bis-Imidazolium Rotaxane, Dalton Trans, 40, 12052–12055 (DOI: 10.1039/C1DT10186B)
15. Zhao J.-F., Chen L., Sun P.-J., Hou X.-Y., Zhao X.-H., Li W.-J. Xie L.-H., Qian Y., Shi N.-E., Lai W.-Y., (2011), One-Pot Synthesis of 2-Bromo-4,5-Diazafluoren-9-One via a Tandem Oxidation–Bromination-Rearrangement of Phenanthroline and Its Hammer-Shaped Donor–Acceptor Organic Semiconductors, Tetrahedron, 67, 1977–1982 (DOI: 10.1016/j.tet.2010.12.065)
16. Dolomanov O.V., Bourhis L.J., Gildea R.J., Howard J. a. K., Puschmann H., (2009), OLEX2: A Complete Structure Solution, Refinement and Analysis Program, J Appl Crystallogr, 42, 339–341 (DOI: 10.1107/S0021889808042726)
17. Sheldrick G.M., Schneider T.R., (1997), [16] SHELXL: High-Resolution Refinement. In Methods in Enzymology; Macromolecular Crystallography Part B; Academic Press, 277,319–343
18. Neese F., Wennmohs F., Becker U., Riplinger C., (2020), The ORCA Quantum Chemistry Program Package, J Chem Phys, 152, 224108 (DOI: 10.1063/5.0004608)
19. Neese F., (2012), The ORCA Program System, WIREs Comput Mol, Sci, 2, 73–78 (DOI: 10.1002/wcms.81)
20. Haldar C., Bisht R., Chaturvedi J., Guria S., Hassan M.M.M., Ram B., Chattopadhyay B., (2022), Ligand- and Substrate-Controlled Para C–H Borylation of Anilines at Room Temperature, Org Lett 24, 8147–8152 (DOI: 10.1021/acs.orglett.2c03188)
21. Li C., Mackenzie C.F.R., Said S.A., Pal A.K., Haghighatbin M.A., Babaei A., Sessolo M., Cordes D.B., Slawin A.M.Z., Kamer P.C.J., (2021), Wide-Bite-Angle Diphosphine Ligands in Thermally Activated Delayed Fluorescent Copper(I) Complexes: Impact on the Performance of Electroluminescence Applications, Inorg Chem, 60, 10323–10339 (DOI: 10.1021/acs.inorgchem.1c00804)

22. Kharabe L.S., Ghosh T., Pandey D., Kumar R., Raghuvanshi A., (2025), Heteroleptic Cu(I) Complex with Vapochromism and Its Application as Electrochromic Material, Appl Organomet Chem, 38, e7451 (DOI: 10.1002/aoc.7451)
23. Crestani M.G., Manbeck G.F., Brennessel W.W., McCormick T.M., Eisenberg R., (2011), Synthesis and Characterization of Neutral Luminescent Diphosphine Pyrrole- and Indole-Aldimine Copper(I) Complexes, Inorg Chem, 50, 7172–7188 (DOI: 10.1021/ic2007588)
24. Farias G., M. Salla C.A., Heying, R.S., J. Bortoluzzi A., F. Curcio S., Cazati T. Santos P.L. dos, P. Monkman A., de Souza B., H. Bechtold I., (2020), Reducing Lifetime in Cu(i) Complexes with Thermally Activated Delayed Fluorescence and Phosphorescence Promoted by Chalcogenolate–Diimine Ligands, J Mater Chem C, 8, 14595–14604 (DOI: 10.1039/D0TC03660A)
25. Paderina A., Ramazanov R., Valiev R., Müller C., Grachova E., (2022), So Close, Yet so Different: How One Donor Atom Changes Significantly the Photophysical Properties of Mononuclear Cu(I) Complexes, Inorg Chem, 61, 11629–11638 (DOI: 10.1021/acs.inorgchem.2c01145)
26. Zhang Y., Schulz M., Wächtler, M., Karnahl M., Dietzek B., (2018), Heteroleptic Diimine–Diphosphine Cu(I) Complexes as an Alternative towards Noble-Metal Based Photosensitizers: Design Strategies, Photophysical Properties and Perspective Applications, Coord Chem Rev, 356, 127–146 (DOI: 10.1016/j.ccr.2017.10.016)
27. Wada A., Zhang Q., Yasuda T., Takasu I., Enomoto S., Adachi C., (2012), Efficient Luminescence from a Copper(i) Complex Doped in Organic Light-Emitting Diodes by Suppressing C–H Vibrational Quenching, Chem Commun, 48, 5340–5342 (DOI: 10.1039/C2CC31509B)

28. Vogler A., Kunkely H., (2002), Excited State Properties of Transition Metal Phosphine Complexes, Coord Chem Rev, 230, 243–251 (DOI: 10.1016/S0010-8545(01)00438-6)
29. Li Z.-X., Kuang X.-N., Wang G. Zhu N., Sun Z.-Z., Han H.-L., Yang Y.-P., Li Z.-F., Xin X.-L., Jin Q.-H., (2021), A Series of Luminescent Cu(i) Complexes Based on the Diphosphine Ligand and Diimine Ligand: Weak Intermolecular Interactions, Terahertz Spectroscopy and Photoproperties, CrystEngComm, 23, 8323–8333 (DOI: 10.1039/D1CE01132D)
30. Guo X., Yin D., Khaing K.K. Wang J., Luo Z., Zhang Y., (2021), Construction of MOF/COF Hybrids for Boosting Sunlight-Induced Fenton-like Photocatalytic Removal of Organic Pollutants, Inorg Chem, 60, 15557–15568 (DOI: 10.1021/acs.inorgchem.1c02198)
31. Wang J., Rao C., Lu L., Zhang S., Muddassir M., Liu J., (2021), Efficient Photocatalytic Degradation of Methyl Violet Using Two New 3D MOFs Directed by Different Carboxylate Spacers, CrystEngComm, 23, 741–747 (DOI: 10.1039/D0CE01632B)
32. Pandey D., Mishra A., Kharabe L.S., Maurya S.K., Raghuvanshi A., (2024), Semiconducting Copper(I) Iodide 2D-Coordination Polymers for Efficient Sunlight-Driven Photocatalysis in Dye Degradation, Cryst Growth Des, 24, 6051–6059 (DOI: 10.1021/acs.cgd.4c00699)
33. Lee H.-A., Yatsu K., Kim T.I., Kwon H.-I., Park I.-J., (2022), Synthesis of Vacancy-Controlled Copper Iodide Semiconductor for High-Performance p-Type Thin-Film Transistors, ACS Appl Mater Interfaces, 14, 56416–56426 (DOI: 10.1021/acsami.2c18865)
34. Sharma B., Rabinal M.K., (2013), Ambient Synthesis and Optoelectronic Properties of Copper Iodide Semiconductor Nanoparticles, J Alloys Compd, 556, 198–202 (DOI: 10.1016/j.jallcom.2012.12.120)
35. Dutta P., Mandal R., Bhattacharyya S., Dey R., Dhar R.S., (2021), Fabrication and Characterization of Copper Based Semiconducting

Materials for Optoelectronic Applications, Microsyst Technol, 27, 3475–3482 (DOI: 10.1007/s00542-020-05145-5)

36. Kumar M., Meena B., Subramanyam P., Suryakala D., Subrahmanyam C., (2022), Emerging Copper-Based Semiconducting Materials for Photocathodic Applications in Solar Driven Water Splitting, Catalysts, 12, 1198 (DOI: 10.3390/catal12101198)
37. Neese F., Wennmohs F., Becker U., Riplinger C., (2020), The ORCA Quantum Chemistry Program Package, J Chem Phys, 152, 224108 (DOI: 10.1063/5.0004608)
38. Neese F., (2012), The ORCA Program System, WIREs Comput Mol Sci, 2, 73–78 (DOI: 10.1002/wcms.81)
39. Kandpal S., Ghosh T., Rani C., Rani S., Pathak D.K., Tanwar M., Bhatia R., Sameera I., Kumar R., (2022), MoS2 Nano-Flower Incorporation for Improving Organic-Organic Solid State Electrochromic Device Performance, Sol Energy Mater Sol Cells, 236, 111502 (DOI: 10.1016/j.solmat.2021.111502)
40. Kandpal S., Ghosh T., Rani C., Tanwar M., Sharma M., Rani S., Pathak D.K., Bhatia R., Sameera I., Jayabalan J., (2022), Bifunctional Application of Viologen-MoS2-CNT/Polythiophene Device as Electrochromic Diode and Half-Wave Rectifier, ACS Mater Au, 2, 293–300 (DOI: 10.1021/acsmaterialsau.1c00064)
41. Chaudhary A., Pathak D.K., Mishra S., Yogi P., Sagdeo P.R., Kumar R., (2019), Enhancing Viologen's Electrochromism by Incorporating Thiophene: A Step Toward All-Organic Flexible Device, Phys Status Solidi A, 216, 1800680 (DOI: 10.1002/pssa.201800680)
42. Mishra S., Yogi P., K. Saxena S., Roy S., R. Sagdeo P., Kumar R., (2017), Fast Electrochromic Display: Tetrathiafulvalene–Graphene Nanoflake as Facilitating Materials, J Mater Chem C, 5, 9504–9512 (DOI: 10.1039/C7TC02913F)
43. Min Kim Y., Li X., Kim K.-W., Hyun Kim S., Chul Moon H., (2019), Tetrathiafulvalene: Effective Organic Anodic Materials for WO3 -

Based Electrochromic Devices, RSC Adv, 9, 19450–19456 (DOI: 10.1039/C9RA02840D)

44. Chaudhary A., Pathak D.K., Tanwar M., Yogi P., Sagdeo P.R., Kumar R., (2019), Polythiophene–PCBM-Based All-Organic Electrochromic Device: Fast and Flexible, ACS Appl Electron Mater, 1, 58–63 (DOI: 10.1021/acsaelm.8b00012)
45. Chaudhary A., Pathak D.K., Mishra S., Yogi P., Sagdeo P.R., Kumar R., (2018), Polythiophene -Viologen Bilayer for Electro-Trichromic Device, Sol Energy Mater Sol Cells, 188, 249–254 (DOI: 10.1016/j.solmat.2018.08.029)
46. Hossain Md.D., Zhang J., Pandey R.K., Sato T., Higuchi M., (2014), A Heterometallo-Supramolecular Polymer with CuI and FeII Ions Introduced Alternately, Eur J Inorg Chem, 2014, 3763–3770 (DOI: 10.1002/ejic.201402468)
47. Tang C.-J., He J.-L., Jaing C.-C., Liang C.-J., Chou C.-H., Han C.-Y., Tien C-L., (2019), An All-Solid-State Electrochromic Device Based on WO3–Nb2O5 Composite Films Prepared by Fast-Alternating Bipolar-Pulsed Reactive Magnetron Sputtering, Coatings, 9, 9, (DOI: 10.3390/coatings9010009)
48. Chen P.-W., Chang C.-T., Ali Md.M., Wu J.-Y., Li Y.-C., Chen M.-H., Jan D.-J., Yuan C.-T., (2018), Tantalum Oxide Film Deposited by Vacuum Cathodic Arc Plasma with Improved Electrochromic Performance, Sol Energy Mater Sol Cells, 182, 188–195 (DOI: 10.1016/j.solmat.2018.02.034)
49. Eren E., Karaca G.Y., Koc U., Oksuz L., Oksuz A.U., (2017), Electrochromic Characteristics of Radio Frequency Plasma Sputtered WO3 Thin Films onto Flexible Polyethylene Terephthalate Substrates, Thin Solid Films, 634, 40–50 (DOI: 10.1016/j.tsf.2017.05.009)
50. Zhi M., Huang W., Shi Q., Peng B., Ran K., (2016), Enhanced Electrochromic Performance of Vanadium Pentoxide/Reduced

Graphene Oxide Nanocomposite Film Prepared by the Sol–Gel Method, J Electrochem Soc, 163, H891 (DOI: 10.1149/2.0121610jes)

51. Bae J.-W., Koo B.-R., Ahn H.-J., (2019), Fe Doping Effect of Vanadium Oxide Films for Enhanced Switching Electrochromic Performances, Ceram Int, 45, 7137–7142 (DOI: 10.1016/j.ceramint.2018.12.219)
52. Vergaz R., Barrios D., Sánchez-Pena J.-M., Pozo-Gonzalo C., Salsamendi M., (2009), Relating Cyclic Voltammetry and Impedance Analysis in a Viologen Electrochromic Device, Sol Energy Mater Sol Cells, 93, 2125–2132 (DOI: 10.1016/j.solmat.2009.08.009)
53. Kandpal S., Gupta P.K., Kumar R., Misra R., (2024), Ferrocene-Functionalized Fulleropyrrolidine Derivative: A Performance Enhancer for Solid-State Electrochromic Devices, ACS Appl Opt Mater, 2, 158–165 (DOI: 10.1021/acsaom.3c00384)
54. Chaudhary A., Pathak D.K., Mishra S., Yogi P., Sagdeo P. R., Kumar R., (2018), Polythiophene -Viologen Bilayer for Electro-Trichromic Device, Sol Energy Mater Sol Cells, 188, 249–254 (DOI: 10.1016/j.solmat.2018.08.029)
55. Huang L.-M., Chen C.-H., Wen T.-C., (2006), Development and Characterization of Flexible Electrochromic Devices Based on Polyaniline and Poly(3,4-Ethylenedioxythiophene)-Poly(Styrene Sulfonic Acid), Electrochimica Acta, 51, 5858–5863 (DOI: 10.1016/j.electacta.2006.03.031)
56. Gaupp C.L., Welsh D.M., Reynolds J.R., (2002), Poly(ProDOT-Et2): A High-Contrast, High-Coloration Efficiency Electrochromic Polymer, Macromol Rapid Commun, 23, 885–889 (DOI: 10.1002/1521-3927.
57. Elool Dov N., Shankar S., Cohen D., Bendikov T., Rechav K., Shimon L.J.W., Lahav M., van der Boom M.E., (2017), Electrochromic Metallo-Organic Nanoscale Films: Fabrication, Color Range, and

Devices, J Am Chem Soc 139, 11471–11481 (DOI: 10.1021/jacs.7b04217)

58. Abe M., Futagawa H., Ono T., Yamada T., Kimizuka N., Hisaeda Y., (2015), An Electropolymerized Crystalline Film Incorporating Axially-Bound Metalloporphycenes: Remarkable Reversibility, Reproducibility, and Coloration Efficiency of Ruthenium(II/III)-Based Electrochromism, Inorg Chem, 54, 11061–11063 (DOI: 10.1021/acs.inorgchem.5b02129)
59. Sarmah S., Kashyap,S.S., Bera M.K., (2023), Dual Redox-Responsive Os/Ru-Based Alternated Heterobimetallic Supramolecular Polymer as a Multicolor Electrochromic Material for Camouflage Device, ACS Appl Electron Mater, 5, 1738–1749 (DOI: 10.1021/acsaelm.2c01765)
60. Fujii K., Santra D.C., Bera M.K., Wakahara T., Nagahata R., Higuchi M., (2023), Electrochromic Ru-Based Metallo-Supramolecular Polymer with a Layered Inorganic−Organic Hybrid Nanocomposite for Improved Electrochemical Properties, ACS Appl Polym Mater 5, 8808–8821 (DOI: 10.1021/acsapm.3c00837)
61. Hsiao L.-Y., Chang T.-H., Lu H.-C., Wang Y.-C., Lu Y.-A., Ho K.-C., Higuchi M., (2019), A Panchromatic Electrochromic Device Composed of Ru(II)/Fe(II)-Based Heterometallo-Supramolecular Polymer, J Mater Chem C, 7, 7554–7562 (DOI: 10.1039/C9TC01452G)
62. Liu J., Daphne Ma X.Y., Wang Z., Xu L., Xu T., He C., Wang F., Lu X., (2020), Highly Stable and Rapid Switching Electrochromic Thin Films Based on Metal–Organic Frameworks with Redox-Active Triphenylamine Ligands, ACS Appl Mater, Interfaces, 12, 7442–7450 (DOI: 10.1021/acsami.9b20388)

Chapter 4

Three-coordinated Cu(I) complexes for electrochromic devices with high coloration efficiency

4.1 Introduction

Cu(I) ions provide structural flexibility to form two-, three-, and four-coordinated structures, leading to unique photophysical properties that have enabled their applications in the development of highly efficient optoelectronic devices *[1–4]*. In previous chapters, we have used four-coordinated Cu(I)-based EC materials for the fabrication of rigid as well as flexible ECDS. These devices exhibit moderate performance in terms of working potential, switching time, coloration efficiency (up to 230 C/cm^2) and contrast ratio (about 40%). Additionally, there is a requirement of a complementary p-type material, poly(3-hexylthiophene-2,5-diyl) (P3HT) as an ion storage layer *[5,6]*. To improve the performance of ECDs, herein, we synthesized two three-coordinate Cu(I) complexes $[Cu(Sphos)(cmdf)]PF_6$ (**7**) and $[Cu(Xphos)(cmdf)]PF_6$ (**8**), with 9-cyanomethylene-4,5-diazafluorene (cmdf), having two CN substituents make it a strong acceptor unit which helps in better charge transfer transition in the molecule and bulky phosphine ligands, Dicyclohexyl(2′,6′-dimethoxy[1,1′-biphenyl]-2-yl)phosphane (Sphos) or Dicyclohexyl[2′,4′,6′-tris(propan-2-yl)[1,1′-biphenyl]-2-yl]phosphane (Xphos) which provide steric hindrance to stabilize three coordinated Cu(I) complexes. These complexes have been successfully integrated into both rigid and flexible ECDs which exhibit excellent electrochromic performance.

4.2 Experimental Section

4.2.1.1 Materials

Materials purchased from commercial vendors are used without further purification unless specifically indicated. All glassware is completely dried in a convection oven at 70 °C. The complex was synthesized under an inert N_2 atmosphere using standard Schlenk techniques. The Sphos and Xphos ligands were purchased from BLD Pharm, Commercial grade chemicals,

tetrathiafulvalene (TTF) (Sigma AldrichTM), lithium perchlorate(Sigma AldrichTM), acetonitrile (ACN, anhydrous, 99%, Sigma AldrichTM), and polyethylene oxide (PEO, Alfa Aesar, MW=100,000) were used as received for device fabrication. Indium doped tin oxide (ITO) coated glass substrate was purchased from Macwin India. ITO coated polyethylene terephthalate (PET) was purchased from Sigma AldrichTM.

4.2.1.2 Characterization methods

^{1}H, $^{13}C\{^{1}H\}$, and $^{31}P\{1H\}$ NMR were recorded on a Fourier transform nuclear magnetic resonance (NMR) spectrometer, model Bruker Avance 500 MHz spectrometers and AVANCE NEO Ascend 400 Bruker BioSpin International AG. ^{1}H and $^{13}C\{1H\}$ NMR spectra were referenced relative to the residual solvent peak. The abbreviations such as s (singlet), d (doublet), t (triplet), m (multiplet), etc. are used for the multiplicity assignment. High-resolution mass spectral analyses (HRMS) were recorded on a Bruker-Daltonics micrOTOF-Q II mass spectrometer. UV-Vis spectroscopy was performed on Agilent Cary 60 UV−vis G680A spectrophotometer in a quartz cuvette (1 cm ×1 cm). In-situ bias-dependent transmittance spectra were recorded using a λ = 365 spectrophotometer (PerkinElmer make) and a Keithley 2450 workstation. The electrochemical measurement was done using Metrohm-Multi Autolab M204 potentiostat.

4.3 Synthetic Details

4.3.1.1 General synthesis method of complexes 7 and 8

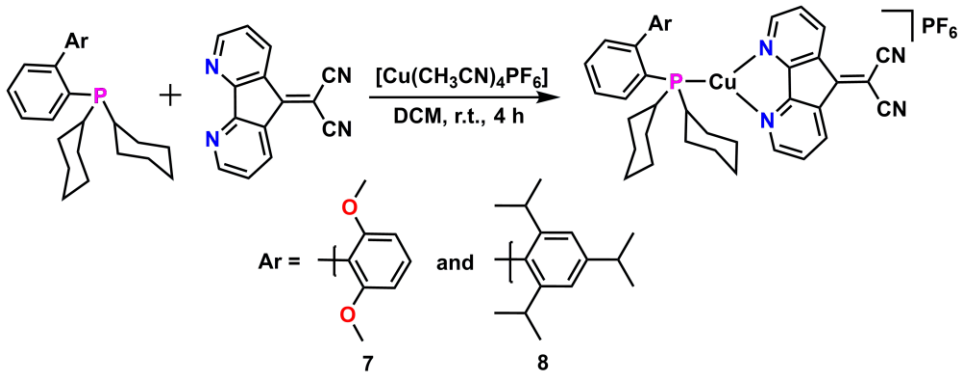

Scheme 4.1 General synthetic procedures of complexes **7** and **8**.

To a clean and dry Schenk tube, phosphine ligand (Sphos or Xphos) was dissolved in DCM and a [Cu $(CH_3CN)_4]PF_6$ solution in DCM was added. It kept on stirring for 2 hours at room temperature in the presence of an inert N_2 atmosphere. To this, cmdf ligand solution in DCM was added and it was stirred for a further 2 hours. The solvent was concentrated by rotary evaporation; the product was purified by recrystallization with a concentrated DCM solution with the addition of n-hexane to obtain a pure product. The purity of the complexes was confirmed by data obtained from multinuclear NMR and FT-IR spectroscopies as well as high-resolution mass spectrometry (HRMS).

4.3.1.1.1 Synthesis of [Sphos-Cu-cmdf]PF_6 (7):

Complex **7** was synthesized using **Scheme 4.1**, Sphos (0.268 mmol), [Cu $(CH_3CN)_4]PF_6$ (0.268 mmol) and cmdf (0.268 mmol) in DCM to give a yellow crystalline powder with 94% yield. **^{1}H NMR** (500 MHz, DMSO-d6) δ 8.83 (bs, 2H), 8.68 (d, *J* = 7.9 Hz, 2H), 7.80 – 7.72 (m, 3H), 7.45 (d, *J* = 8.7 Hz, 2H), 7.03 (s, 1H), 6.98 (q, *J* = 4.3 Hz, 1H), 6.46 (d, *J* = 8.9 Hz, 2H), 3.55 (s, 6H), 2.10 (t, *J* = 11.1 Hz, 2H), 1.90 – 1.83 (m, 2H), 1.76 – 1.61 (m, 6H), 1.58 – 1.52 (m, 2H), 1.35 – 1.26 (m, 4H), 1.14 (d, *J* = 4.0 Hz, 6H). **^{13}C{^{1}H} NMR** (126 MHz, DMSO-d6) δ 156.34, 153.66, 142.15, 141.99, 134.17, 132.31, 131.71, 131.65, 130.15, 129.72, 129.35, 127.08, 126.32, 117.91, 112.54, 103.90, 88.91, 55.10, 33.96, 33.78, 30.09, 30.02, 28.41, 26.27, 26.15, 25.72. **^{31}P{^{1}H} NMR** (202 MHz, DMSO-d6) δ 9.48, -144.19.

HRMS (ESI, m/z): Calcd for $C_{40}H_{41}CuN_4O_2P$ $[(M\text{-}PF_6)]^+$: 703.2258; Found: m/z 703.2242. **FTIR (cm^{-1})** 2921, 2845, 2235, 1577, 1469, 1430, 1409, 1245, 1167, 1105, 1049, 1000, 928, 875, 838, 778, 749, 671, 595, 556, 519, 460.

4.3.1.1.2 Synthesis of [Xphos-Cu-cmdf]PF_6 (8)

Complex **8** was synthesized using a similar general synthetic method, Xphos (0.268 mmol), [Cu $(CH_3CN)_4]PF_6$ (0.268 mmol) and cmdf (0.268 mmol) in DCM to obtain a yellow crystalline powder (95% yield). **^{1}H NMR** (400 MHz, DMSO-d6) δ 8.81 (s, 2H), 8.63 (d, *J* = 8.0 Hz, 2H), 7.85 – 7.80 (m, 1H), 7.68 (dd, *J* = 8.0, 4.5 Hz, 2H), 7.55 – 7.51 (m, 2H), 7.25 (q, *J* = 4.4 Hz, 1H), 7.09 (s, 2H), 2.85 (m, *J* = 7.3 Hz, 1H), 2.26 (m, *J* = 6.8 Hz, 2H), 2.12 – 2.02 (m, 2H), 1.91 (d, *J* = 10.5 Hz, 2H), 1.72 (d, *J* = 10.3 Hz, 2H), 1.65 (s, 4H), 1.55 (s, 2H), 1.23 (dd, *J* = 13.8, 6.8 Hz, 22H), 0.88 (d, *J* = 6.5 Hz, 6H). **^{13}C{^{1}H} NMR** (126 MHz, DMSO-d6) δ 158.37, 154.13, 148.18, 145.99, 145.09, 134.98, 133.55, 132.77, 132.01, 131.95, 129.86, 128.81, 128.52, 127.45, 127.41, 121.12, 112.59, 89.57, 34.84, 34.66, 33.34, 30.25, 29.77, 29.72, 29.24, 26.42, 26.32, 26.17, 25.81, 25.49, 23.68, 21.87. **^{31}P{^{1}H} NMR** (202 MHz, DMSO-d6) δ 5.02, -144.15. **HRMS** (ESI, m/z): Calcd for $C_{47}H_{55}CuN_4P$ $[(M\text{-}PF_6)]^+$: 769.3455; Found: m/z 769.3486. **FTIR (cm^{-1})** 2927, 2855, 2233, 1575, 1458,1411, 1267, 1173, 1117, 1054, 1000, 922, 834, 773, 554, 525, 478.

4.3.1.1.3 Synthesis of [Sphos-Cu-cmdf]ClO_4 (7-ClO_4)

A similar general synthetic method was used to synthesize complex **7-ClO_4**, Sphos (0.268 mmol), instead of $[Cu(CH_3CN)_4]PF_6$, $[Cu(CH_3CN)_4]ClO_4$ (0.268 mmol) was used as Cu(I) source and cmdf (0.268 mmol) in DCM to obtain a yellow powder (90% yield). **^{1}H NMR** (500 MHz, DMSO-d6) δ 8.77 (s, 2H), 8.67 (d, *J* = 8.1 Hz, 2H), 7.79 – 7.71 (m, 3H), 7.45 (dd, *J* = 6.3, 2.7 Hz, 2H), 7.04 (d, *J* = 9.5 Hz, 1H), 7.01 – 6.97 (m, 1H), 6.47 (d, *J* = 8.9 Hz, 2H), 3.56 (s, 6H), 2.12 (td, *J* = 12.1, 8.9 Hz, 2H), 1.87 (d, *J* = 11.1 Hz, 2H), 1.76 – 1.68 (m, 4H), 1.64 (d, *J* = 11.3 Hz, 2H), 1.55 (d, *J* = 12.4 Hz, 2H), 1.34 – 1.19 (m, 4H), 1.18 – 1.08 (m, 6H). **^{13}C{^{1}H} NMR** (126 MHz,

DMSO-d6) δ 157.83, 156.35, 154.83, 153.31, 134.51, 132.35, 131.72, 131.67, 130.19, 129.73, 129.36, 127.10, 127.07, 117.92, 117.85, 112.46, 103.89, 55.13, 33.95, 33.77, 30.12, 28.45, 26.28, 25.74. **$^{31}P\{^{1}H\}$ NMR** (202 MHz, DMSO-d6) δ 9.53.

4.4 Characterisations of complexes 7 and 8

The purity of both complexes was confirmed by data obtained from ^{1}H, $^{13}C\{^{1}H\}$ and $^{31}P\{^{1}H\}$ NMR spectroscopies (**Fig. 4.1-4.6**). The ^{1}H NMR spectra demonstrate characteristic signals of both phosphine and cmdf ligands. In the ^{1}H NMR spectra of complex **7**, the appearance of multiplets in the range of 7.78 to 6.46 ppm corresponds to the seven phenyl protons and singlets at 3.55 ppm for six methoxy protons, confirming the presence of Sphos ligand. Similarly, in the ^{1}H NMR spectra of complex **8,** the Xphos ligand is confirmed by the presence of six phenyl proton signals between 7.57 to 7.09 ppm and methylene proton of isopropyl group as a multiplet around 285 to 2.26 ppm while other aliphatic signals ranging from 2.08 to 0.88 ppm. The appearance of highly deshielded signals in ^{1}H NMR spectra of complex **7** and complex **8** at 8.83 (bs, 2H), 8.68 (d, 2H), 7.45 (d, 2H) and 8.81 (bs, 2H), 8.63 (d, 2H), 7.68 (dd, 2H) confirming the presence of cmdf ligand in both complexes. In $^{13}C\{^{1}H\}$ NMR spectra of complex **7**, a characteristic peak of methoxy carbons is observed at 55.10 ppm confirming the presence of Sphos ligand while in complex **8** the peaks around 23 ppm corresponding to methyl carbon and peaks at 29 and 33 ppm methylene carbons of isopropyl groups confirm the appearance of Xphos ligand. In addition, the peaks around 89 ppm corresponding to carbon between the two nitrile groups and peaks around 112 ppm concerning carbon atoms of nitrile group confirm the appearance of cmdf ligand in both complexes. The remaining characteristic peaks are observed in aromatic as well as aliphatic regions, confirming the formation of both complexes. Furthermore, two peaks are observed in $^{31}P\{^{1}H\}$ NMR spectra of both complexes, a singlet at 9.48 ppm and 5.02 ppm corresponding to the

phosphorous atom of coordinated phosphine ligands and a septet around -144 ppm with J_{PF} = ~710 Hz representing the presence of PF_6 counter ion. In addition, the HRMS spectrum of complexes **7** and **8** shows $[M\text{-}PF_6]^+$ peak at 703.2242 (calculated for $C_{40}H_{41}CuN_4O_2P$ = 703.2258) and 769.3486 (calculated for $C_{47}H_{55}CuN_4P$ = 769.3455), respectively, confirming the formation of both complexes.

4.4.1.1 Multinuclear NMR Spectra of complexes 7, 8 and 7-ClO_4

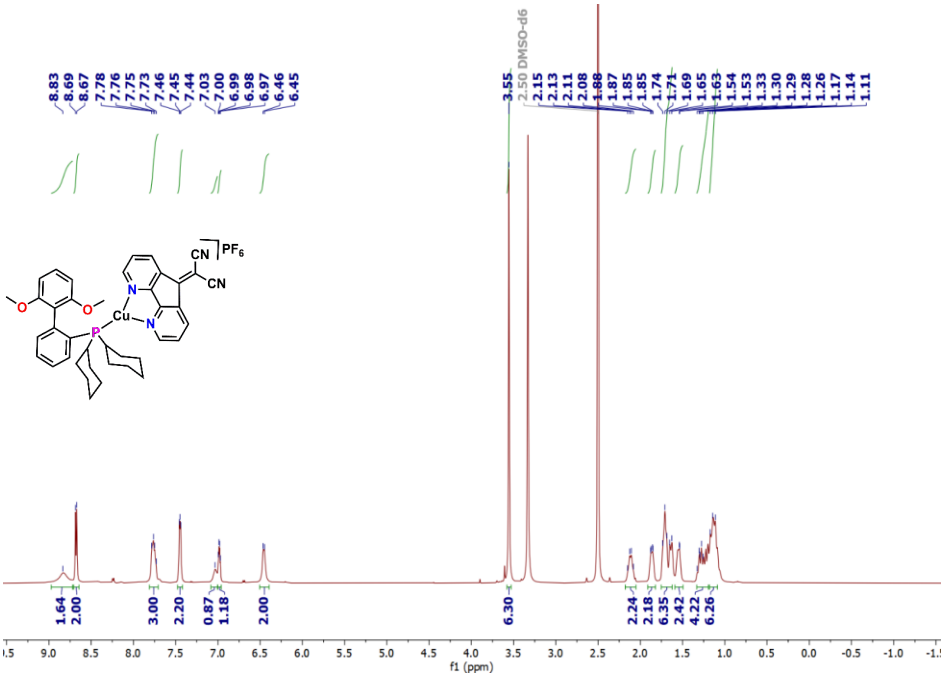

Fig. 4.1 ^{1}H NMR spectrum of complex **7** in DMSO-d6.

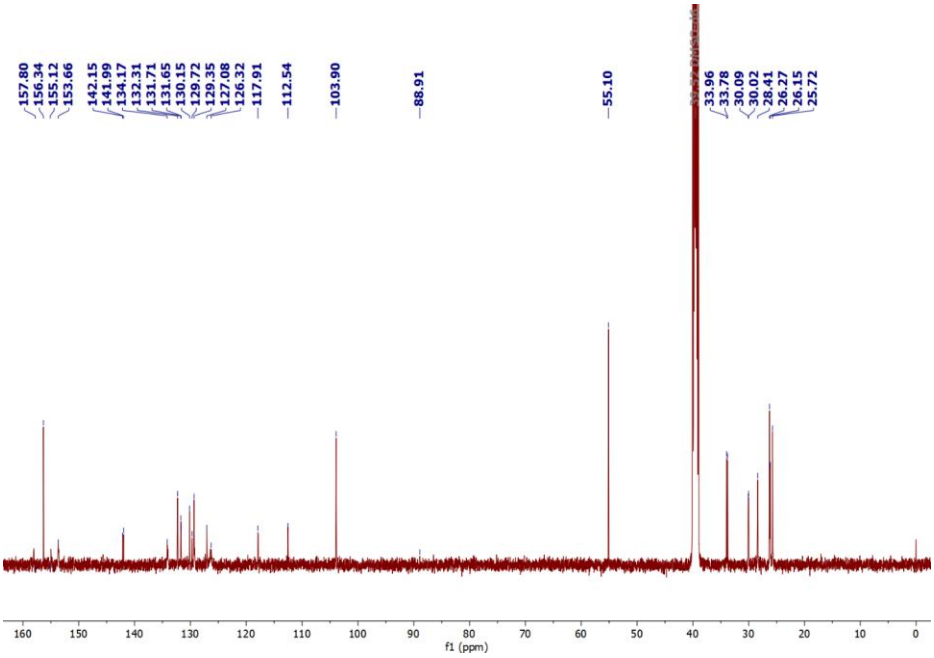

Fig. 4.2 $^{13}C\{^{1}H\}$ NMR spectrum of complex **7** in DMSO-d6.

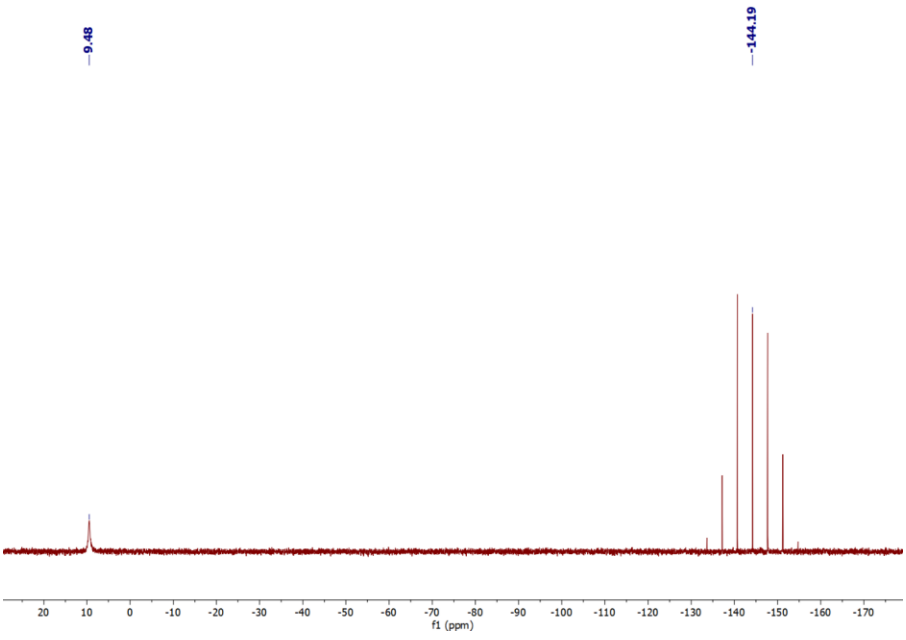

Fig. 4.3 $^{13}P\{^{1}H\}$ NMR spectrum of complex **7** in DMSO-d6.

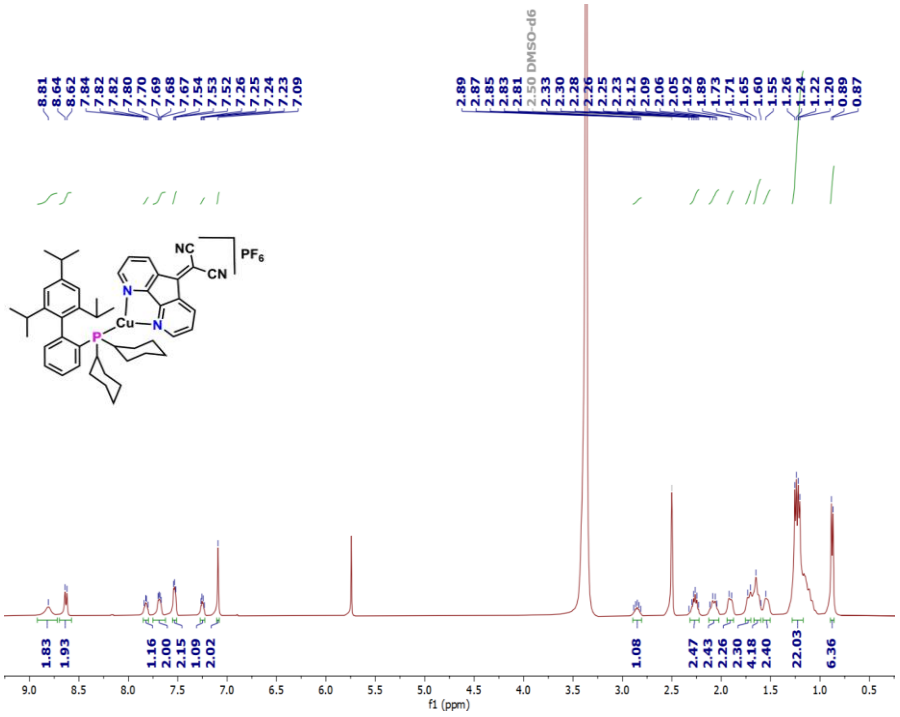

Fig. 4.4 ^{1}H NMR spectrum of complex **8** in DMSO-d6.

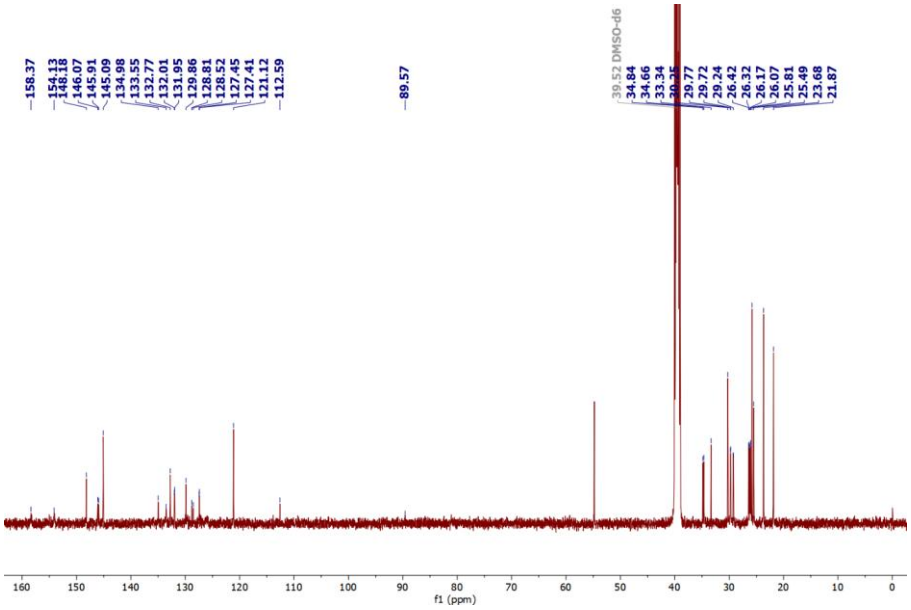

Fig. 4.5 ^{13}C{^{1}H} NMR spectrum of complex **8** in DMSO-d6.

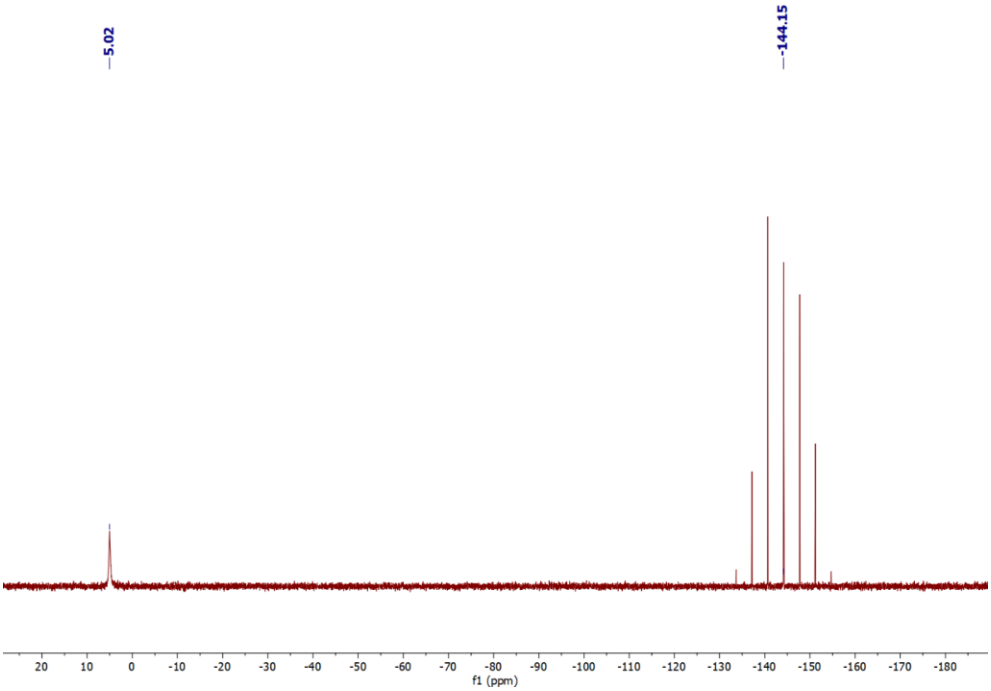

Fig. 4.6 $^{13}P\{^{1}H\}$ NMR spectrum of complex **8** in DMSO-d6.

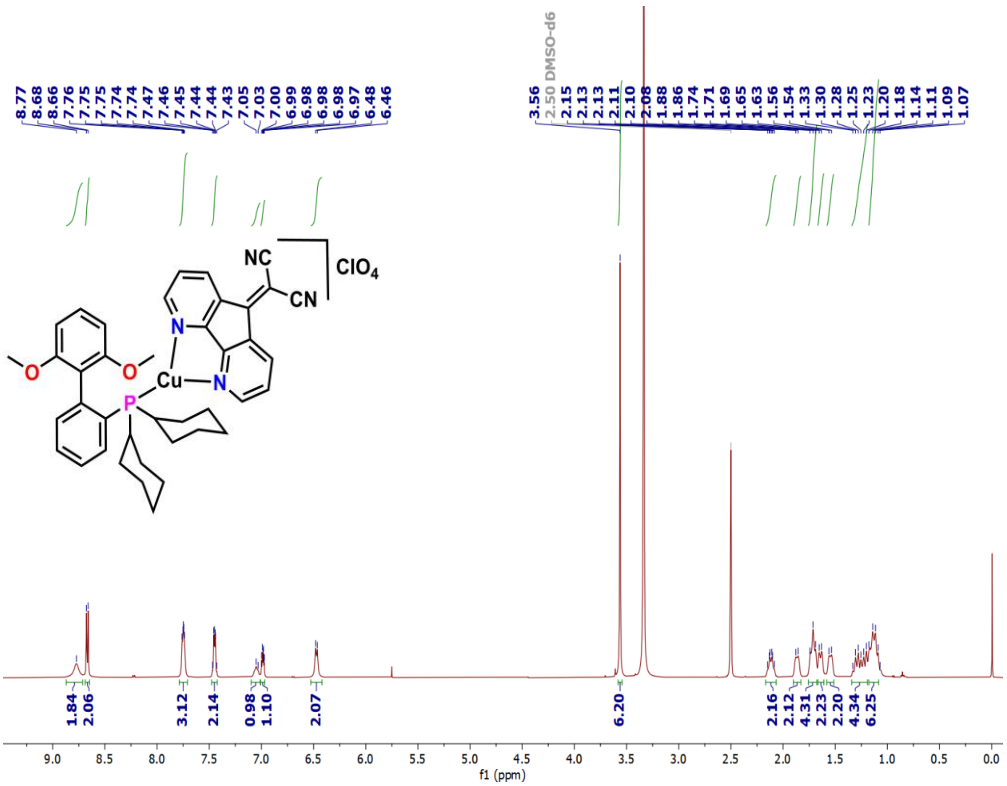

Fig. 4.7 ^{1}H NMR spectra of **7-ClO4** in DMSO-d6 (500 MHz)

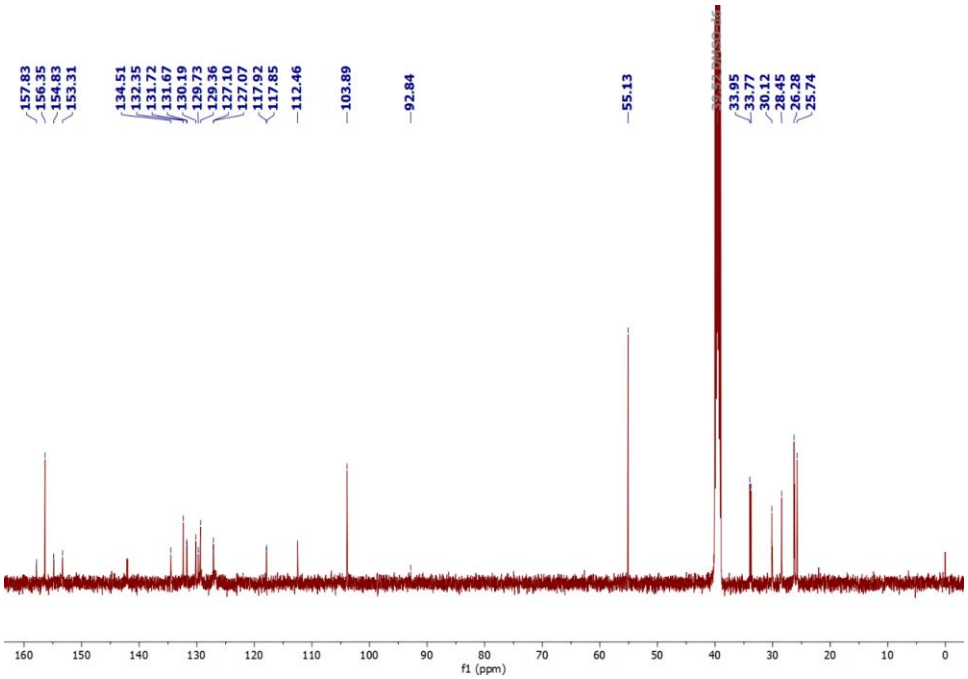

Fig. 4.8 $^{13}C\{^{1}H\}$ NMR spectra of **7-ClO$_4$** in DMSO-d6 (126 MHz).

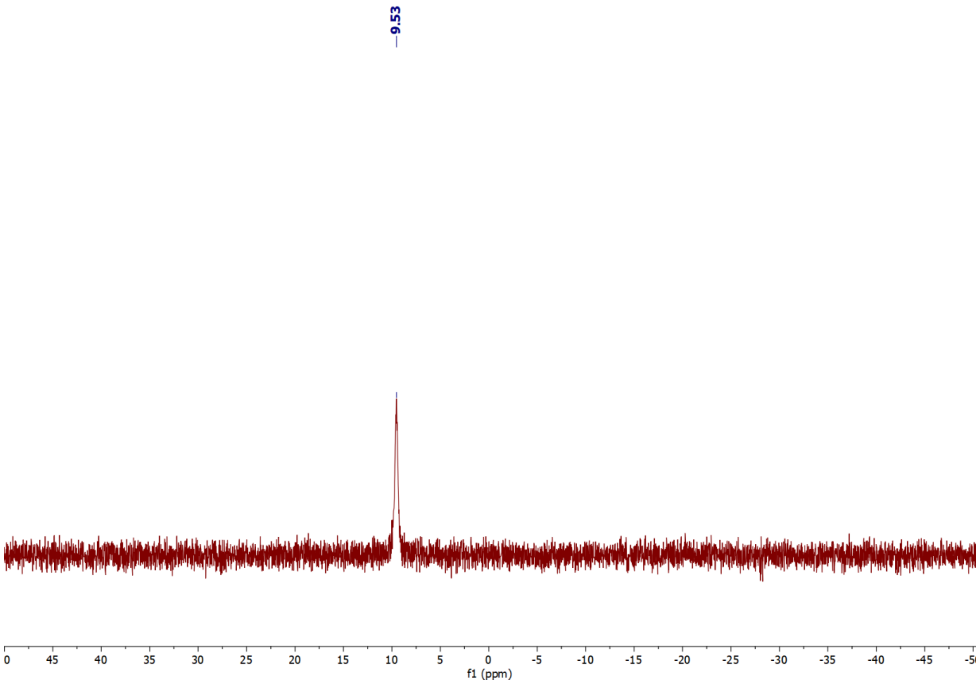

Fig. 4.9 $^{31}P\{^{1}H\}$ NMR spectra of **7-ClO$_4$** in DMSO-d6 (202 MHz).

4.4.1.2 Structural analysis

The molecular structures of both complexes were also authenticated by single-crystal X-ray diffraction (SC-XRD) analysis (**Fig. 4.10**). Crystals suitable for SC-XRD were obtained by the slow diffusion of n-hexane to a concentrated DCM solution of complexes at room temperature. The crystallographic data with structure refinement details are provided in **Table 4.1**. Complex **7** crystallizes in monoclinic crystal systems having a $P2_1$ space group whereas complex **8** crystallizes in triclinic crystal systems with a *P-1* space group. In the crystalline state, the Cu(I) center is found to be three-coordinated in which the central Cu(I) atom binds with two nitrogen atoms from the cmdf ligand and the phosphorous atom of the phosphine ligands. In both complexes, Cu1-P1 and Cu1-N1 bond distances are approximately 2.2 and 2.0 Å, respectively, which lie in the average range of reported Cu(I) complexes *[7–10]*. Interestingly, Cu1-N2 distance in complexes **7** and **8** is found to be 2.48 Å and 2.62 Å, respectively. Though the distance is less than the sum of the van der Waal's radii of both atoms but it is significantly higher than the reported Cu-N bond distances *[2,11]*. Probably the presence of a bulky phosphine ligand pushes one of the nitrogen atoms of the cmdf ligand away from the Cu atom in the solid state. This observation is more evident (Cu1-N2 = 2.62 Å) in complex **8** with a bulkier Xphos ligand. However, the presence of symmetrical protons of cmdf ligands in ^{1}H NMR (**Fig. 4.1** and **4.4**), suggests that both the N atoms are in a similar environment and equally coordinate with the Cu atom in the solution. The P1-Cu1-N1 bond angles in both complexes are about 152° while the P1-Cu1-N2 bond angles are 119.30° and 118.38°, respectively (**Table 4.2**).

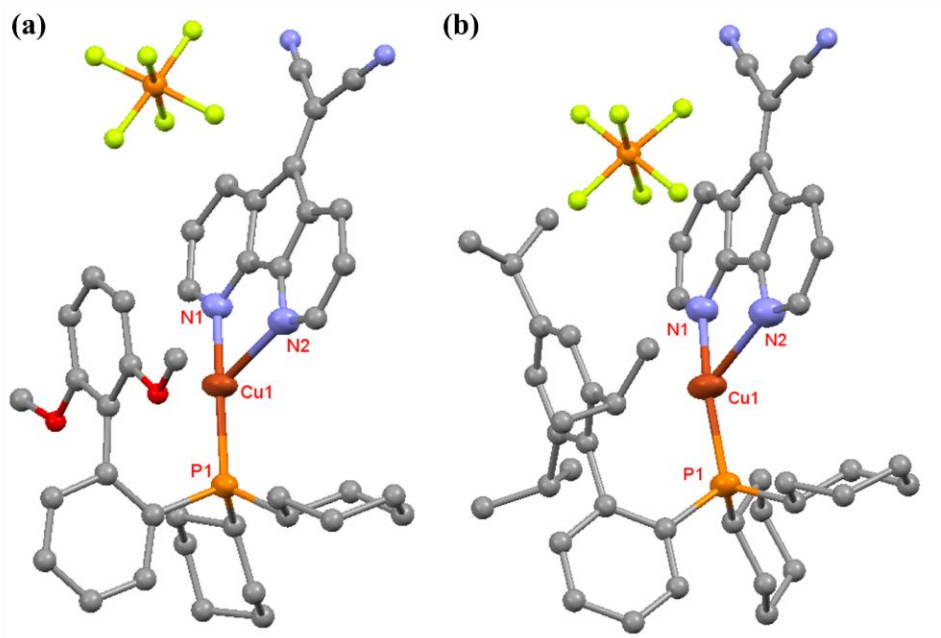

Fig. 4.10 Molecular structures of complexes **7** and **8**. Hydrogen atoms and solvent molecules are omitted for clarity.

Table 4.1 The crystallographic data with structure refinement details of complexes **7** and **8**.

Complex	**Complex 7**	**Complex 8**
Empirical formula	$C_{40}H_{41}CuF_6N_4O_2P_2$	$C_{48}H_{57}Cl_2CuF_6N_4P_2$
Formula weight	849.25	1000.35
Temperature/K	298	298
Crystal system	Monoclinic	Triclinic
Space group	$P2_1$	P-1
a/Å	9.7039(10)	10.2044(5)
b/Å	14.6586(14)	12.9024(7)
c/Å	14.3010(12)	19.1834(11)
α/°	90	87.228(4)
β/ °	100.635(9)	89.708(4)
γ/°	90	87.177(4)
V/ $Å^3$	1999.3(3)	2519.7(2)

Z	2	2
ρ_{calc}g/cm^{-3}	1.411	1.319
μ/mm^{-1}	0.694	0.661
R1 (R1 all data) [I > 2σ(I)]	0.0510	0.0590
wR2 (wR2 all data)	0.1258	0.1713
Data/restraints/parameters	6675/1/498	8698/18/613
GOF	1.051	1.052
CCDC number	**2431046**	**2431048**

Table 4.2 Selected Bond lengths (Å) and angles (°) of complexes **7** and **8**.

	Bond lengths (Å)			**Bond angles (°)**	
	7	**8**		**7**	**8**
P1-Cu1	2.18	2.20	**P1-Cu1-N1**	152.41	152.33
N1-Cu1	2.01	1.99	**P1-Cu1-N2**	119.30	118.38
N2-Cu1	2.485	2.62	**N1-Cu1-N2**	81.74	78.83

4.4.1.3 Weak interactions observed in complexes 7 and 8

Complex **7** exhibits weak intermolecular C-H···N interactions (2.730 Å) involving C-H bond of the methoxy group attached to the biphenyl ring of the Sphos ligand and the N atom of the nitrile group present on the cmdf ligand, also it shows C-H···N interaction (2.563 Å) between C-H of cmdf and N of nitrile present on cmdf of another molecule (**Fig. 4.11**). Further, complex **8** displays intramolecular C-H···F interactions (2.554 Å),

including C-H of the isopropyl group present on the Xphos ligand with fluorine of PF_6 counter ion (**Fig. 4.12**).

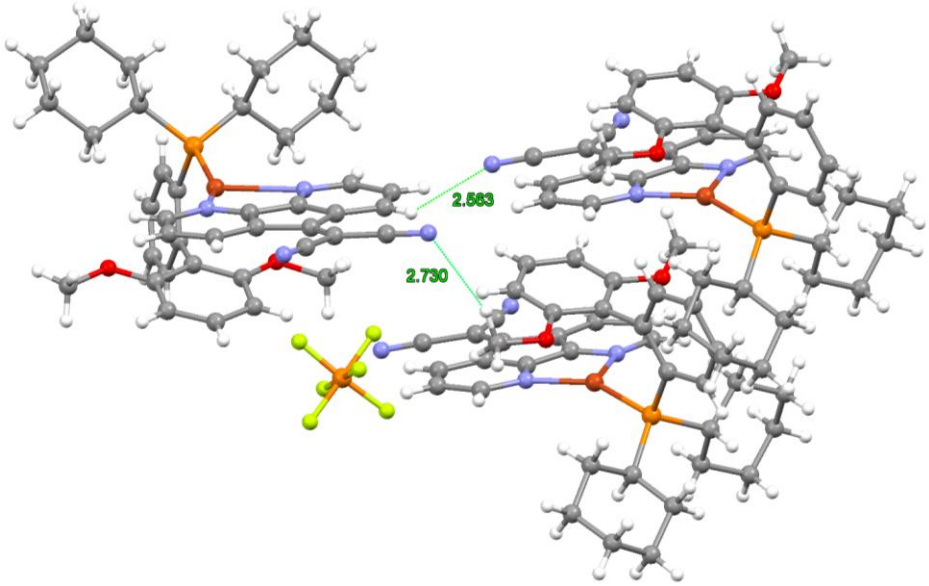

Fig. 4.11 Weak C-H···N interactions were observed in complex **7**.

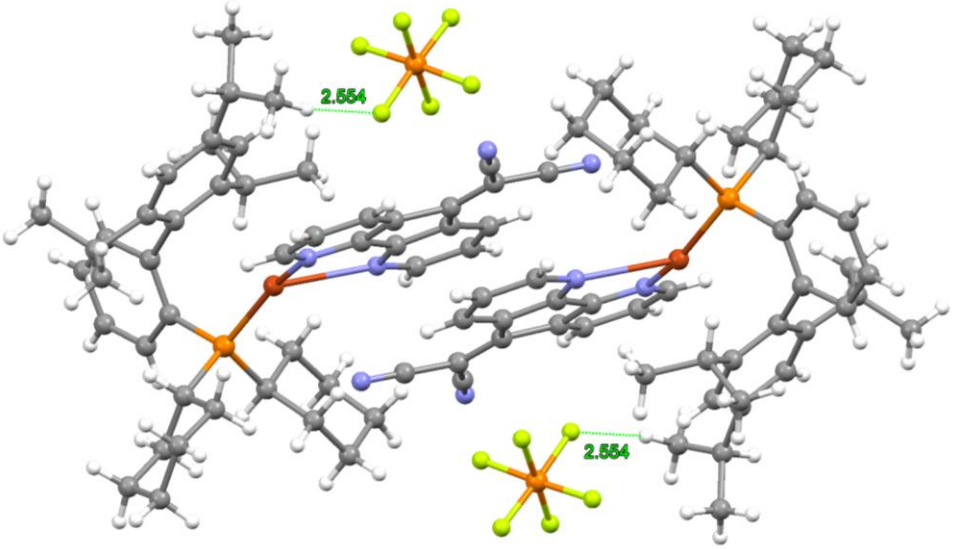

Fig. 4.12 Weak C-H···F interactions were observed in complex **8**.

4.4.1.4 Thermogravimetric analysis

Both compounds were found to be stable for several months at room temperature under ambient conditions. The thermogravimetric analysis performed on powder samples under an N_2 atmosphere with 10 °C/min heating rate suggests thermal stability till 260 and 180 °C for complexes **7** and **8**, respectively (**Fig. 4.13**). As discussed earlier, the presence of bulky Xphos ligand results in an elongated Cu1-N2 distance in **8**. So the lower thermal stability of **8** can be attributed to the steric effect that weakens the metal–ligand interactions, thereby reducing the overall stability of the complex and promoting early decomposition of **8**.

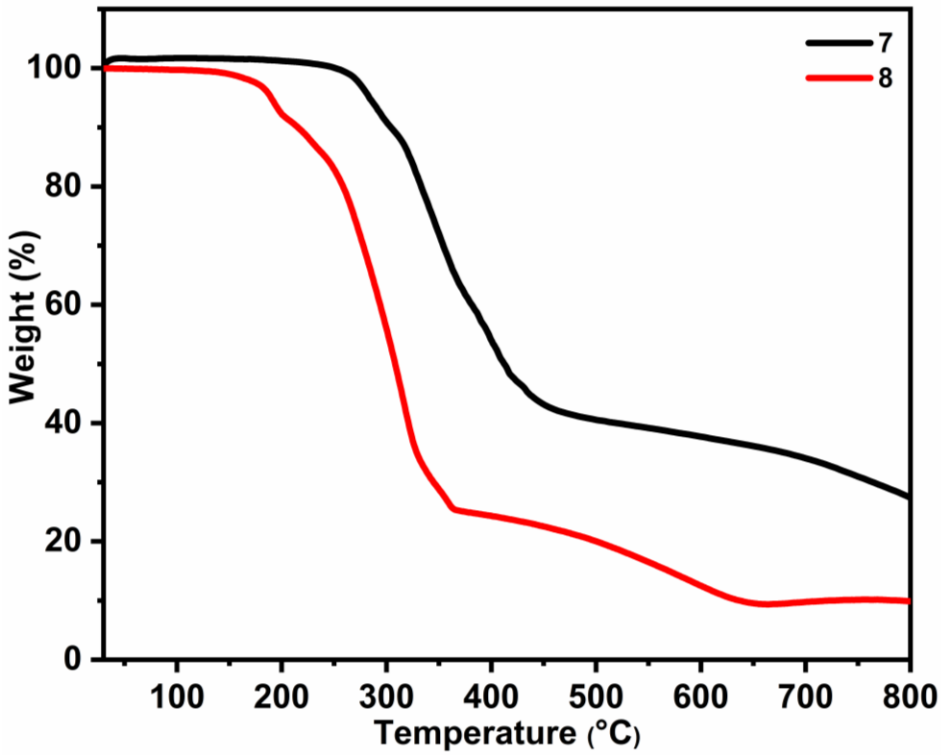

Fig. 4.13 TGA curve of complexes **7** and **8** under nitrogen atmosphere with the temperature heating rate of 10 °C min^{-1}.

4.5 Photophysical properties and theoretical calculations

UV-Vis spectroscopy was used to study the absorption properties of complexes **7** and **8** in DCM (0.1 mM) at room temperature and the spectra

are depicted in **Fig. 4.14a**. The absorption peaks are observed in the high-energy region from 258 to 350 nm, which is comparable to previously reported Cu(I) complexes, assigned as ligand-centered (LC) π-π* transitions within the ligands *[11–13]*. Additionally, the lowest energy band in the range of 370 to 480 nm which is attributed to the metal-to-ligand charge transfer transition *[14–16]*.

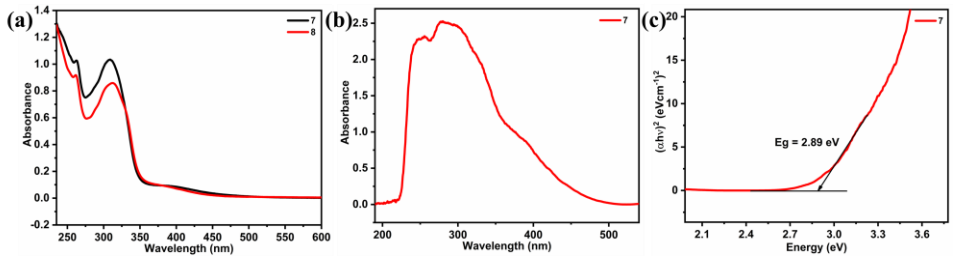

Fig. 4.14 a) Absorption spectrum of complexes **7** and **8**, recorded in DCM at room temperature, b) Solid state UV–Visible diffuse reflectance spectrum (DRS) of complex **7** at room temperature, c) Observed band gap of complex **7** based on Kubelka–Munk method calculated from DRS.

In DCM, both complexes show similar absorption properties; therefore, further studies were done only with complex **7**. The solid-state UV-visible diffuse reflectance spectrum (DRS) of complex **7** was performed on a powder sample and it is depicted in **Fig. 4.14b.** In the solid state, complex **7** shows absorption in the UV-Vis region (230-500 nm). In addition, by applying the Kubelka–Munk method to DRS spectra (**Fig. 4.14c**) *[17]*, the band gap energy was found to be 2.89 eV, suggesting complex **7** has a semiconducting nature similar to previously reported Cu(I) materials *[18–21]*.

As both complexes show similar absorption properties, the density-functional theory (DFT) and time-dependent density-functional theory (TDDFT) calculations were carried out on complex **7**. The theoretical calculation begins with the molecular structure obtained from the SCXRD analysis (**Fig. 4.15**). It is found that the highest occupied molecular orbital (HOMO) is mainly distributed on the Cu(I) atom with some contribution of

Sphos ligand. The lowest unoccupied molecular orbital (LUMO) is located on the cmdf ligand. The TD-DFT data suggests that the major electronic transition of the S_1 state is occurring from HOMO (Cu+Sphos) to LUMO (cmdf).

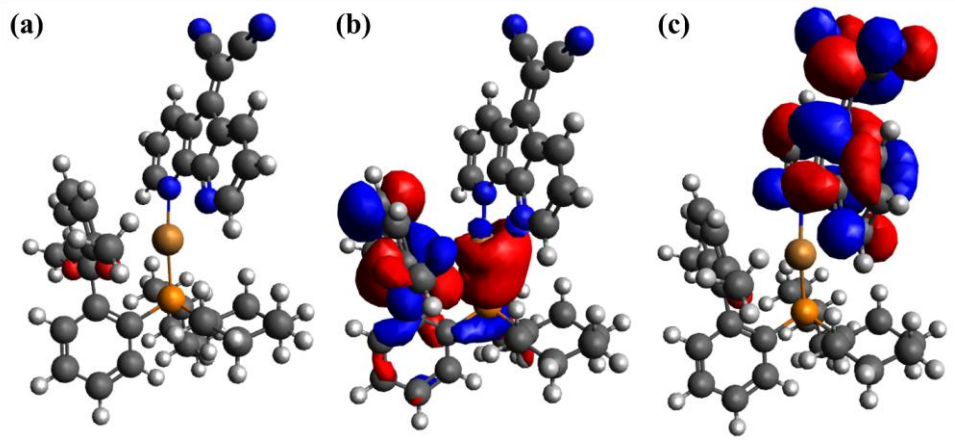

Fig. 4.15 a) Optimized molecular structure; b) HOMO and c) LUMO orbitals obtained from B3LYP/def2-TZVP level of theory (Cu = Brown, P = Orange, N = blue, O = red, C = black and H = grey). The counter ion is omitted for clarity.

Hence, it is concluded that the electronic transitions arise from copper(I) center to the π* orbital of the cmdf ligand, which is responsible for the low-energy transition.

4.6.1.1 Electrochemical studies

Both complexes show similar absorption properties, therefore, utilized to study the electrochemical properties. Electrochemical performance was studied in three electrode configurations with platinum wire as the counter and Ag/AgCl as the reference electrode. The blank ITO-coated glass substrate has been used as a working electrode. To prepare the electrochemical solution, roughly 5 mg of complex was added to 0.1 M $LiClO_4$ as a supporting electrolyte in ACN. The cyclic voltammetry (CV)

was recorded in the potential window of 3 V to -3 V at 100 mV/s scan rate (**Fig. 4.16**), Complex **7** shows redox couple at -1.8 V (reduction) and -0.3 V (oxidation), confirming its redox activity under negative potential, while **8** shows redox couple at -1.7 V (reduction) and -0.22 V (oxidation).

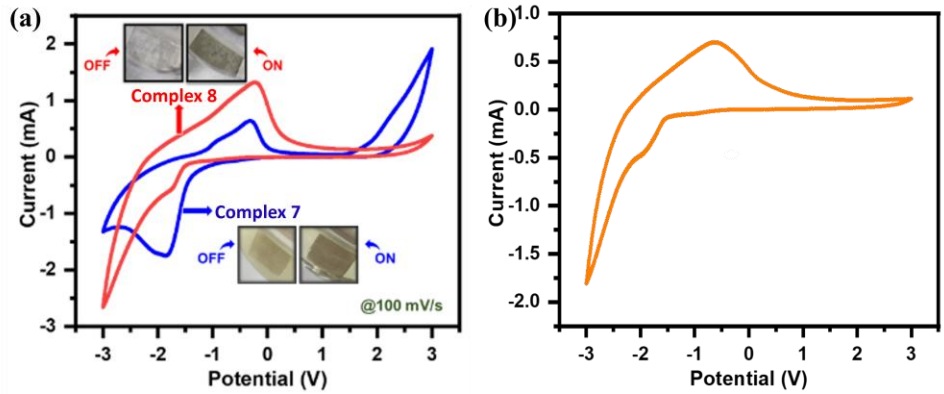

Fig. 4.16 (a) CV of complex **7** and **8** and observable color change (inset) and (b) CV of complex **7-ClO$_4$** at 100 mV/s scan rate.

During the reduction, a vivid color change was observed which is completely reversible when the opposite potential is applied for both **7** and **8** (**Fig. 4.16a, inset**). In the initial condition of complex **7**, a light-yellow which changes to a dark brown color when a negative bias is applied (approximately -1.5 V), again when a positive bias of the same potential is applied it comes back to its original light-yellow color. Additionally, complex **8** changes its color from colorless to brown by the application of negative potential. This phenomenon is reversible for both complexes makes them potential candidates for electrochromic applications. As both complexes are changing their color at negative bias, it should be used as an n-type EC active counter ion for designing a solid-state ECD. Since complex **7** exhibits a more prominent redox couple compared to complex **8**, therefore, complex **7** was used as EC active layer for the fabrication of ECD to investigate the EC properties.

Furthermore, to check the effect of counterion on EC properties, the PF_6 counter ion changed by ClO_4 and [Sphos-Cu-CMDF]ClO_4 (**7-ClO$_4$**) was

synthesised and characterized by NMR spectroscopy (**Fig.s 4.7-4.9**). The CV of the **7-ClO$_4$** was recorded using the similar method, which show reversible redox couple at -1.9 V (reduction) and -0.62 V (oxidation) (**Fig. 4.16b**). During the CV scan there is no any color change was observed in the **7-ClO$_4$** by the application of external bias. This experiment suggests the importance of PF_6 counterion in the EC properties.

4.6.1.2 Recipe for Rigid and Flexible ECDs Fabrication

Complex **7** proved to be an EC active counter ion when tested in a solution-based electrochemical cell, but practical implementation demands replication of color modulation performance in a solid-state device. Hence, a simple solid-state mono-layer ECD in the configuration "ITO/ TTF //complex **7**/ ITO" has been fabricated using TTF(Tetrathiafulvalene) as an ion storage layer by a flip-chip method *[22–26]*.

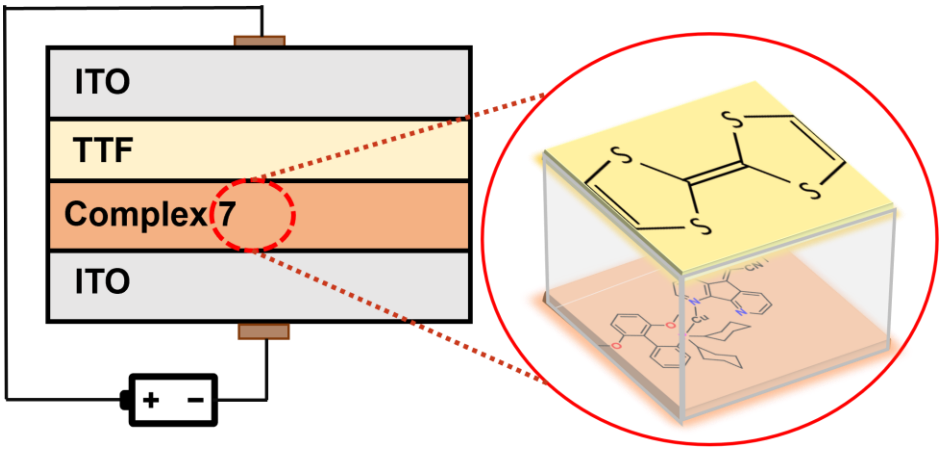

Fig. 4.17 Schematic of the monolayer ***complex 7-ECD*** with an actual photograph of the device in ON and OFF conditions.

4. Fabrication of solid-state **7**-electrochromic device (*7-ECD*).

e. Firstly, ITO-coated glass of dimension 2×1 cm^2 was used as an electrode, which was thoroughly cleaned by ultrasonication in a solution containing acetone, isopropanol and DI water in an equal ratio for 10 minutes.

f. Approximately 0.5 wt.% complex **7** solution in acetonitrile (ACN) was spin-coated over the cleaned ITO substrate at 200 rpm for 60 minutes and was dried at 80 °C for a few minutes.
g. The Tetrathiafulvalene (TTF) an ion storage layer was prepared by dissolving 0.5 wt.% TTF in ACN and was drop casted (~50 µL) over ITO and dried at 80 °C for 5 minutes.
h. The gel electrolyte was prepared by mixing 0.1 M $LiClO_4$ in ACN and 5 wt.% polyethylene oxide (PEO) in equal proportion. The prepared gel electrolyte was sandwiched in between the two above-prepared electrodes and was stuck together using the flip-chip method.

5. Fabrication of flexible P3HT and complex **7**-based electrochromic device (***f-P3HT-complex 7 ECD***).
    b. For the fabrication of a flexible device, the ITO was replaced by PET substrate and the same recipe was adopted for fabricating *f-P3HT-complex 7 ECD*.

4.6.1.3 Electrochromic Performances of ECDs

For practical use, complex **7** must be integrated into a solid-state device for various EC applications. Therefore, a basic solid-state monolayer device has been fabricated having the structure *"ITO/* complex **7***//TTF + gel electrolyte/ ITO"* as shown in the schematic (**Fig. 4.17**) by following a device fabrication **recipe 1**. Since complex **7** was identified as an n-type EC active counter ion, a suitable p-type material that doesn't change its color but donates an electron to the active material for reduction is needed. The TTF (Tetrathiafulvalene) is one such promising material, called ion storage layer *[27,28]*, which is used as a supporting layer to study the EC behaviour of complex **7**. The fabricated EC device (***complex 7-ECD***) shows a color change between light yellow and dark brown color, represented as OFF and ON states, respectively (**Fig. 4.18, insets**). During the unbiased condition,

the fabricated ***complex 7-ECD*** was observed to be transparent to light yellow in color, as soon as the bias of 1.4 V is applied to the TTF layer such that complex **7** layer is getting -1.4 V, the color of the device changes to brown color (**Fig. 4.17, inset**), following the redox mechanism between the complex **7** and TTF layer. Right after the removal of bias, the ***complex 7-ECD*** regains its original state due to the occurrence of reverse redox reaction between the TTF and complex **7**, demonstrating complete reversibility.

To further study the above phenomenon of color change between yellow and brown, a bias-dependent transmittance spectrum of ***complex 7-ECD*** was recorded in the range of 400 to 700 nm in the visible region (**Fig. 4.18a**). Originally during the OFF or unbiased condition, the device is light-yellow in color (bleached state) following the green curve, afterward when bias is applied (ON condition, 1.4 V, concerning TTF) the color of the device changes to brown color (colored state) following the orange curve (**Fig. 4.18a**). As seen from the transmittance spectra, the maximum change in transmittance was observed at 430 nm. In comparison to previously reported 4-coordinated Cu(I) complexes, less voltage is required for EC performance. The reduction is facilitated in complex **7** probably due to its 16-electron Cu center which would be difficult with an 18-electron center. An important EC performance parameter, called color contrast (CC), was calculated using Eq 1in the introduction *[23,29]*.

The calculated value of CC at 430 nm is 42%, which is exclusively due to the complex **7** material, showing its potential applications in ECDs. Another essential parameter, namely switching time, which is the time taken by ***complex 7-ECD*** to switch between the two colors (light yellow to brown to light yellow) was estimated by applying a square pulse of 1.4 V (10 seconds each). The switching time of ***complex 7-ECD*** is found to be 5.3 s for switching from light yellow to brown (colored state) and 4.5 s to switch back into light yellow color, which is determined at 90% of the device's

total coloration and bleaching phenomenon (**Fig. 4.18b**). Afterward, the ***complex 7-ECD*'s** cyclic stability was also tested by giving a continuous pulse train of 1.4 V (10 s). The device shows great cyclic stability for up to 1000 s or 50 cycles (**Fig. 4.18c**).

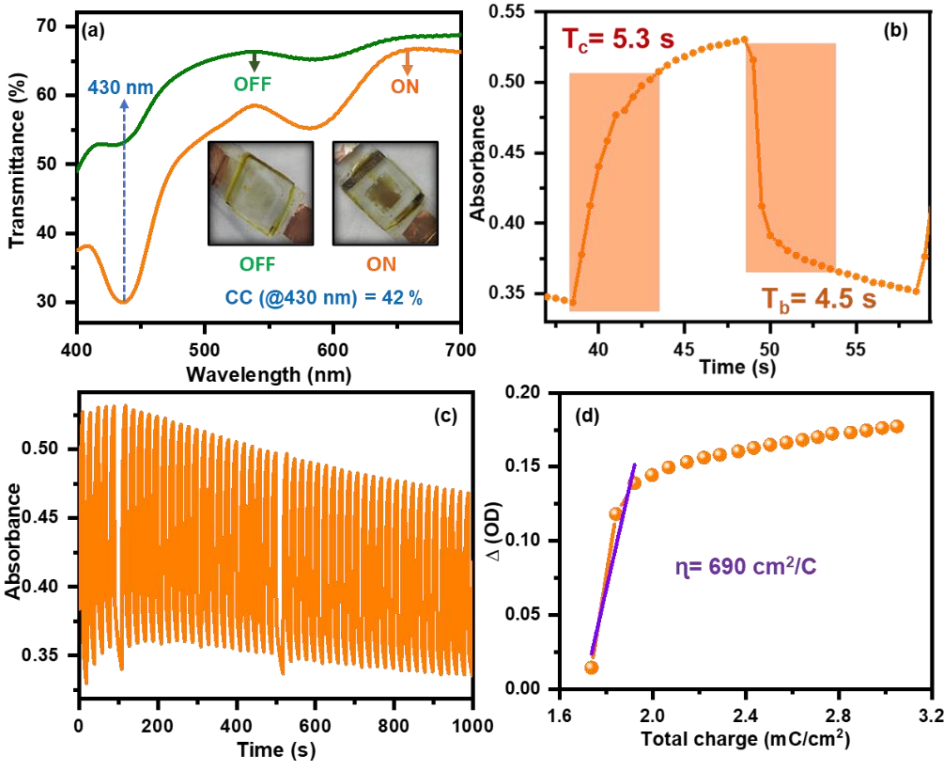

Fig. 4.18 (a) In-situ transmittance spectra of ***complex 7-ECD*** during ON and OFF conditions with actual photos of the device (inset) and (b) Single switching of the device (c) cyclic stability of the ***complex 7-ECD*** for 1000 seconds (d) variation in change in optical density as a function of total charge used for ***complex 7-ECD*** with marked slope.

A critical factor for judging the EC device performance is coloration efficiency (CE), which is found to be very high, about 690 cm^2/C (**Fig. 4.18d**) calculated from the charge density plot (**Fig. 4.19a**), which shows that the device is power efficient for EC display applications. The performance of ***complex 7-ECD*** with previously reported ECDs is presented in **Table 4.5.** The superior performance of ***complex 7-ECD*** in

terms of CC and CE demonstrates its potential for real-life application to make energy-efficient ECDs for various purposes.

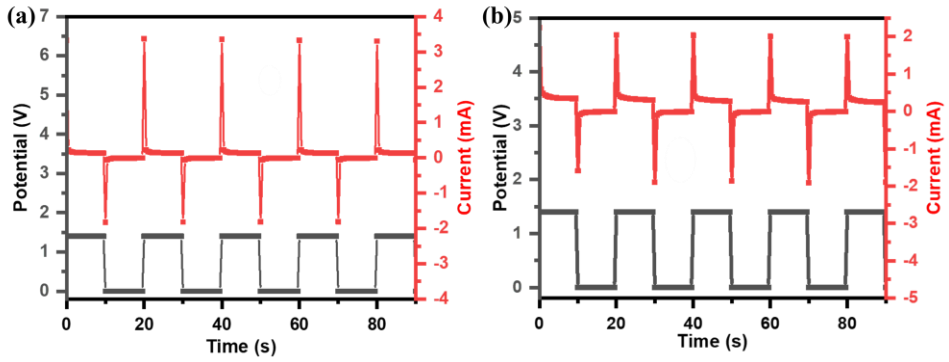

Fig. 4.19 Voltage & current vs time Graph for calculation charge density for a) ***7-ECD*** and b) ***f-7-ECD***.

Flexible ECDs could be used in the development of next-generation electronics; therefore, a flexible ECD using complex **7** (***f-complex 7-ECD***) was fabricated (**Recipe 2**). The ***f-complex 7-ECD*** has the structure of "PET/ complex **7**//TTF + gel electrolyte/PET". Firstly, the in-situ bias-dependent transmittance has been recorded by applying 1.4 V to the device in the wavelength range of 400 to 700 nm (**Fig. 4.20a**). At the OFF condition (unbiased), the device changed its color from transparent to light yellow and traced the pink curve. As the bias of 1.4 V is applied (ON condition), the device traces the purple curve and turns from light yellow to brown color due to the redox reaction taking place between the active material and TTF (**Fig. 4.20a, inset**). The observed CC (30% at 430 nm) is solely due to the complex **7** material as TTF is just helping in the redox reaction and not taking part in the color change. The decrease in CC in flexible form is due to the comparatively less ITO-coated PET substrate when compared with ITO-coated glass substrate.

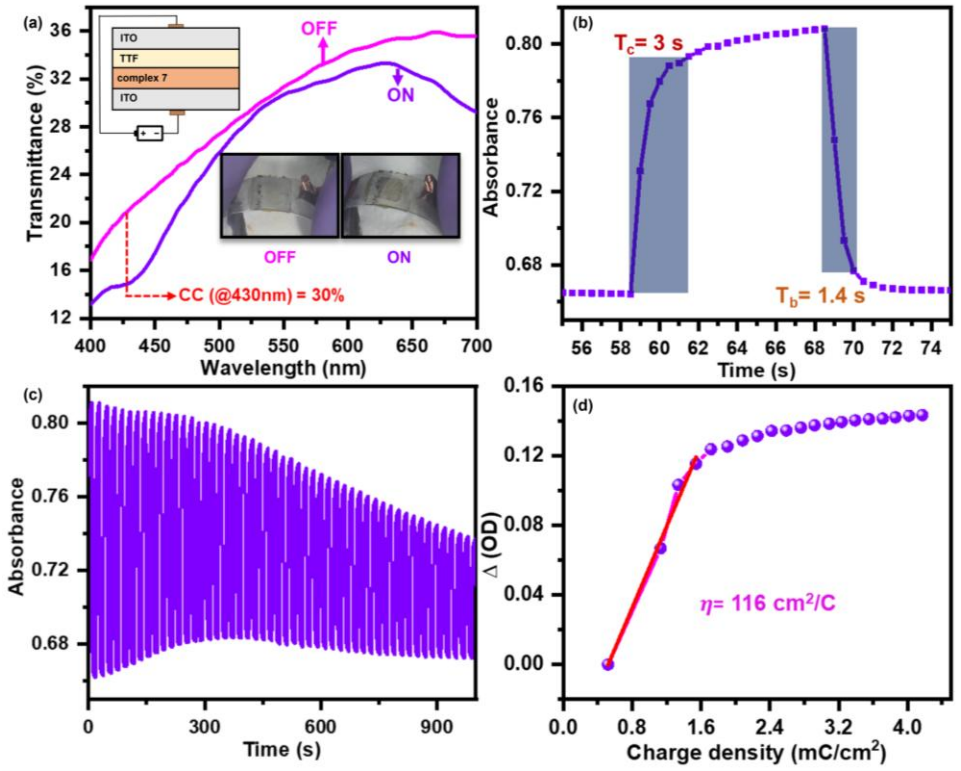

Fig. 4.20 (a) In-situ bias-dependent transmittance spectra of ***f-complex 7-ECD*** during ON and OFF conditions with actual photos of the device and (b) Single switching of the device (c) cyclic stability of the ***f-complex 7-ECD*** for 1000 seconds (d) Graph for evaluating coloration efficiency of the ***f-complex 7-ECD*** with marked slope.

The switching kinematics of the ***f-complex 7-ECD*** has been studied by applying a square pulse of 1.4 V for 10 seconds and the time was calculated at 90% of total coloration and bleaching. The estimated coloration and bleaching times are 3 s and 1.4 s, respectively. The ***f-complex 7-ECD*** gives good switching time when compared with solid-state ***complex 7-ECD***, which is mainly due to less change in transmittance value. Following that, to check the cyclic stability of the ***f-complex 7-ECD***, a pulse train of 1.4V is applied for 1000s (50 cycles). The device gives good cyclic stability up to 50 cycles with minimal comprise due to the less conducting ITO-coated PET substrate. The CE was also calculated for the ***f-complex 7-ECD***, giving a value of 116 cm^2/C. The decrease in CE in flexible form is due to the

lower value of ΔOD at 430 nm. A minimal compromise in the ***f-complex 7-ECD*** was observed when compared to the solid-state ***complex 7-ECD***, which is basically due to the less conducting ITO-coated PET substrate. By thoroughly investigating the performance of ECDs, it is concluded that the device shows excellent EC behaviour and could be a great choice for real-life applications for making flexible and wearable electronic devices.

Table 4.3 Comparison of ECD performances with reported EC materials.

Sr. No	EC systems or materials	CC or ΔT (%)	Response time (s) Coloration/ Bleaching	Coloration Efficiency (cm^2/C)	Ref.
1	**ITO/ complex 7/ TTF / ITO**	**42**	**5.3/4.5**	**690**	**This work**
2	ITO/P3HT/Cu(I) complex/ITO	45	0.4/1.4	191	*[6]*
3	ITO/P3HT/Cu(I) complex/ITO	38	0.8/0.5	230	*[30]*
4	ITO/$LiClO_4$ /PolyCu/ITO	-	1.35/1.04	-	*[31]*
5	ITO/ gel electrolyte /PolyCuFe/ITO	-	4.8/1.1	-	*[32]*
6	ITO/ WO_3–Nb_2O_5/ NiVOx/ ITO	-	7.0/0.7	35.2	*[33]*
7	WO_3 coated PET/ ITO film	21	3.56/ 11.32	626	*[34]*
8	WO_3/P3HT	60	0.3/0.5	378	*[35]*
9	V_2O_5:Fe (1%) EC film 1 M $LiClO_4$	46.29	2/3.7	47.3	*[36]*

10	ITO/ferrocene-Fc^+ /P3HT/viologen/ITO	-	0.5/0.9	355	*[37]*
11	ITO/P3HT/viologen/ITO	-	1.7/1.2	222	*[38]*
12	PANI–PSS/PC–$LiClO_4$	40.2	8.8/ 9.7	183	*[39]*
13	PANI-EV	75	0.5/0.8	110	*[40]*
14	PProDOT-Et_2	75	2/2	505	*[41]*
15	TAZ-3PTZBr	82.48	0.5/2.5	513.8	*[42]*
16	APV@TiO ECDs	78	0.53/0.16	374.93	*[43]*
17	Os-polypyridyl complex	39	0.5/0.5	230	*[44]*
18	Fe-polypyridyl complex	65	1/1	207	*[44]*
19	bithiophene−pyridine complex of ruthenium(III)−porphycene [Ru(TPrPc) (btp)$_2$]PF_6	-	3.7/2.3	178	*[45]*
20	ITO/PolyOsRu/ITO	58	0.34/0.78	404.39	*[46]*
21	ITO/PolyRu:LIIM (3:5)/ITO	58	0.29/1.71	645	*[47]*
22	PolyRuFe/PB ECD	52.7	0.2/0.3	525.1	*[48]*
23	CuTCA MOF	65	4.8/3.3		*[49]*
24	Ni-CHNDI, MOF-74type	73	2.1/1.9	260	*[50]*

25	Cu-HHTP-30C	40.2	3.2/5.9	632	*[51]*
26	Zn-NDI-74, MOF-74type	21	14/23	117	*[52]*
27	PET/P3HT+Co_3O_4/EV+WO_3/PET	50	1.2/2.5	420	*[53]*
28	nanoporous Sb-doped SnO2	58.35	0.5/0.6	440	*[54]*

4.7 Conclusion

We have synthesized three-coordinated heteroleptic Cu(I) complexes [Cu(Sphos)(cmdf)]PF_6 (**7**) and [Cu(Xphos)(cmdf)]PF_6 (**8**). Both complexes exhibit similar photophysical properties. Furthermore, complex **7** was found suitable for fabricating a solid-state as well as a flexible electrochromic device. The solid-state ***complex 7-ECD*** achieved a color contrast of 42% with a coloration efficiency of 690 cm^2/C, attributed solely due to the complex **7**, making it suitable for smart window applications. Additionally, the flexible ECD exhibited appreciable performance, underscoring its applicability to next-generation flexible smart wearable electronics. This study emphasizes the potential of Cu(I) complexes in the advancement of future electronic devices. The integration of such complexes into multifunctional hybrid materials may further expand their applicability in energy-efficient optoelectronic technologies.

4.8 References

1. Tao C., Li Y., Wang J., (2023), The Progress of Electrochromic Materials Based on Metal–Organic Frameworks, Coord Chem Rev, 475, 214891 (DOI: 10.1016/j.ccr.2022.214891)
2. Zhang Y., Schulz M., Wächtler M., Karnahl M., Dietzek B., (2018), Heteroleptic Diimine–Diphosphine Cu(I) Complexes as an Alternative towards Noble-Metal Based Photosensitizers: Design Strategies, Photophysical Properties and Perspective Applications, Coord Chem Rev, 356, 127–146 (DOI: 10.1016/j.ccr.2017.10.016)
3. Kumar A., Singh S., Mohammed M.K.A., Shalan A.E., (2021), Computational Modelling of Two Terminal CIGS/Perovskite Tandem Solar Cells with Power Conversion Efficiency of 23.1 %, Eur J Inorg Chem, 2021, 4959–4969 (DOI: 10.1002/ejic.202100214)
4. Kandpal S., Ghosh T., Rani C., Chaudhary A., Park J., Lee P.S., Kumar R., (2023), Multifunctional Electrochromic Devices for Energy Applications, ACS Energy Lett, 8, 1870–1886 (DOI: 10.1021/acsenergylett.3c00159)
5. Kharabe L.S., Ghosh T., Pandey D., Kumar R., Raghuvanshi A., (2024), Heteroleptic Cu(I) Complex with Vapochromism and Its Application as Electrochromic Material, Appl Organomet Chem, 38, e7451 (DOI: 10.1002/aoc.7451)
6. Kharabe L.S., Sahu B., Mishra S., Kumar R., Raghuvanshi A., (2025), Redox Dependent Color Modulating Copper(I) Complex for Flexible Electrochromic Device, ChemPhotoChem, e202400354 (DOI: 10.1002/cptc.202400354)
7. Shi L., Li B., (2009), A Series of CuI Complexes Containing 1,10-Phenanthroline Derivative Ligands: Synthesis, Characterization, Photophysical, and Oxygen-Sensing Properties, Eur J Inorg Chem, 2009, 2294–2302 (DOI:10.1002/ejic.200900123)
8. Farias G., M. Salla C.A., Heying R.S., J. Bortoluzzi A., F. Curcio S., Cazati T., Santos P.L. dos, P. Monkman A., de Souza B., H. Bechtold

I., (2020), Reducing Lifetime in Cu(i) Complexes with Thermally Activated Delayed Fluorescence and Phosphorescence Promoted by Chalcogenolate–Diimine Ligands, J Mater Chem C, 8, 14595–14604 (DOI: 10.1039/D0TC03660A)

9. Sun Z.-Z., Zhu N., Pan X., Wang G., Li Z.-F., Xin X.-L., Han H.-L., Feng Y.-B., Jin Q.-H., Yang Y.-P., (2021), A New Application of Terahertz Time-Domain Absorption Spectra in Luminescent Complexes: Characterization of the C–H···π Weak Interactions in Cu(i) Complexes Dalton Trans, 50, 10214–10224 (DOI: 10.1039/D1DT01023A)
10. Kakizoe D., Nishikawa M., Fujii Y., Tsubomura T., (2017), Photophysical Properties of Three Coordinated Copper(i) Complexes Bearing 1,10-Phenanthroline and a Monodentate Phosphine Ligand, Dalton Trans, 46, 14804–14811 (DOI: 10.1039/C7DT02938A)
11. Leoni E., Mohanraj J., Holler M., Mohankumar M., Nierengarten I., Monti F., Sournia-Saquet A., Delavaux-Nicot B., Nierengarten J.-F., Armaroli N., (2018), Heteroleptic Copper(I) Complexes Prepared from Phenanthroline and Bis-Phosphine Ligands: Rationalization of the Photophysical and Electrochemical Properties, Inorg Chem 57, 15537–15549 (DOI: 10.1021/acs.inorgchem.8b02879)
12. Li C., Mackenzie C.F.R., Said S.A., Pal A.K., Haghighatbin M.A., Babaei A., Sessolo M., Cordes D.B., Slawin A.M.Z., Kamer P.C.J., (2021), Wide-Bite-Angle Diphosphine Ligands in Thermally Activated Delayed Fluorescent Copper(I) Complexes: Impact on the Performance of Electroluminescence Applications, Inorg Chem, 60, 10323–10339 (DOI: 10.1021/acs.inorgchem.1c00804)
13. Jin X.-X., Li T., Shi D.-P., Luo L.-J., Su Q.-Q., Xiang J., Xu H.-B., Leung C.-F., Zeng M.-H., (2020), Luminescent Phosphine Copper(i) Complexes with Various Functionalized Bipyridine Ligands: Synthesis, Structures, Photophysics and Computational Study, New J Chem, 44, 13393–13400 (DOI: 10.1039/C9NJ05887G)

14. Keller S., Prescimone A., Bolink H., Sessolo M., Longo G., Martínez-Sarti L., M. Junquera-Hernández J., C. Constable E., Ortí E., E. Housecroft C., (2018), Luminescent Copper(i) Complexes with Bisphosphane and Halogen-Substituted 2,2′-Bipyridine Ligands, Dalton Trans, 47, 14263–14276 (DOI: 10.1039/C8DT01338A)
15. Fresta E., Weber M.D., Fernandez-Cestau J., Costa R.D., (2019), White Light-Emitting Electrochemical Cells Based on Deep-Red Cu(I) Complexes, Adv Opt Mater, 7, 1900830 (DOI: 10.1002/adom.201900830)
16. Zhang F., Guan Y., Chen X., Wang S., Liang D., Feng Y., Chen S., Li S., Li Z., Zhang F., (2017), Syntheses, Photoluminescence, and Electroluminescence of a Series of Sublimable Bipolar Cationic Cuprous Complexes with Thermally Activated Delayed Fluorescence, Inorg Chem, 56, 3742–3753 (DOI: 10.1021/acs.inorgchem.6b01847)
17. Makuła P., Pacia M., Macyk W., (2018), How To Correctly Determine the Band Gap Energy of Modified Semiconductor Photocatalysts Based on UV–Vis Spectra, J Phys Chem Lett, 9, 6814–6817 (DOI: 10.1021/acs.jpclett.8b02892)
18. Guo X., Yin D., Khaing K.K., Wang J., Luo Z., Zhang Y., (2021), Construction of MOF/COF Hybrids for Boosting Sunlight-Induced Fenton-like Photocatalytic Removal of Organic Pollutants, Inorg Chem, 60, 15557–15568 (DOI: 10.1021/acs.inorgchem.1c02198)
19. Wang J., Rao C., Lu L., Zhang S., Muddassir M., Liu J., (2021), Efficient Photocatalytic Degradation of Methyl Violet Using Two New 3D MOFs Directed by Different Carboxylate Spacers, CrystEngComm, 23, 741–747 (DOI: 10.1039/D0CE01632B)
20. Liu A., Zhu H., Kim M.-G., Kim J., Noh Y.-Y., (2021), Engineering Copper Iodide (CuI) for Multifunctional p-Type Transparent Semiconductors and Conductors, Adv Sci, 8, 2100546 (DOI: 10.1002/advs.202100546)

21. Pandey D., Mishra A., Kharabe L.S., Maurya S.K., Raghuvanshi A., (2024), Semiconducting Copper(I) Iodide 2D-Coordination Polymers for Efficient Sunlight-Driven Photocatalysis in Dye Degradation, Cryst Growth Des, 24, 6051–6059 (DOI: 10.1021/acs.cgd.4c00699)
22. Kandpal S., Ghosh T., Rani C., Rani S., Pathak D.K., Tanwar M., Bhatia R., Sameera I., Kumar R., (2022), MoS2 Nano-Flower Incorporation for Improving Organic-Organic Solid State Electrochromic Device Performance, Sol Energy Mater Sol Cells, 236, 111502 (DOI: 10.1016/j.solmat.2021.111502)
23. Kandpal S., Ghosh T., Rani C., Tanwar M., Sharma M., Rani S., Pathak D.K., Bhatia R., Sameera I., Jayabalan J., (2022), Bifunctional Application of Viologen-MoS2-CNT/Polythiophene Device as Electrochromic Diode and Half-Wave Rectifier, ACS Mater Au, 2, 293–300 (DOI: 10.1021/acsmaterialsau.1c00064)
24. Chaudhary A., Pathak D.K., Mishra S., Yogi P., Sagdeo P.R., Kumar R., (2019), Enhancing Viologen's Electrochromism by Incorporating Thiophene: A Step Toward All-Organic Flexible Device, Phys Status Solidi A, 216, 1800680 (DOI: 10.1002/pssa.201800680)
25. Mishra S., Yogi P., K. Saxena S., Roy S., R. Sagdeo P., Kumar R., (2017), Fast Electrochromic Display: Tetrathiafulvalene–Graphene Nanoflake as Facilitating Materials, J Mater Chem C, 5, 9504–9512 (DOI: 10.1039/C7TC02913F)
26. Min Kim Y., Li X., Kim K.-W., Hyun Kim S., Chul Moon H., (2019), Tetrathiafulvalene: Effective Organic Anodic Materials for WO3 - Based Electrochromic Devices, RSC Adv, 9, 19450–19456 (DOI: 10.1039/C9RA02840D)
27. Kharabe L.S., Sahu B., Mishra S., Kumar R., Raghuvanshi A., (2025), Redox Dependent Color Modulating Copper(I) Complex for Flexible Electrochromic Device, ChemPhotoChem, e202400354 (DOI: 10.1002/cptc.202400354)

28. Ghosh T., Bansal L., Kandpal S., Rani C., Tanwar M., Kumar R., (2023), Ambipolar All-Organic Solid-State Electrochromic Device Using Electrodeposited Polyaniline: Improving Performance by Design, ACS Appl Opt Mater, 1, 473–480 (DOI: 10.1021/acsaom.2c00115)
29. Sahu B., Bansal L., Ahlawat N., Ghanghass A., Rath D.K., Kaladi Chondath S., Kandpal S., Bhatia R., Sameera I., Kumar R., (2024), Mixed Chalcogenides Nanoflakes' Infrared Cutting Effect: Utilization in Thermal Soothing Electrochromic Goggles, ACS Appl Opt Mater, (DOI: 10.1021/acsaom.4c00325)
30. Kharabe L.S., Ghosh T., Pandey D., Kumar R., Raghuvanshi A., (2024), Heteroleptic Cu(I) Complex with Vapochromism and Its Application as Electrochromic Material, Appl Organomet Chem, 38, e7451 (DOI: 10.1002/aoc.7451)
31. Hossain Md.D., Chakraborty C., Rana U., Mondal S., Holdt H.-J., Higuchi M., (2020), Green-to-Black Electrochromic Copper(I)-Based Metallo-Supramolecular Polymer with a Perpendicularly Twisted Structure, ACS Appl Polym Mater, 2, 4449–4454 (DOI: 10.1021/acsapm.0c00559)
32. Hossain Md.D., Zhang J., Pandey R.K., Sato T., Higuchi M., (2014), A Heterometallo-Supramolecular Polymer with CuI and FeII Ions Introduced Alternately, Eur J Inorg Chem, 2014, 3763–3770 (DOI: 10.1002/ejic.201402468)
33. Tang C.-J., He J.-L., Jaing C.-C., Liang C.-J., Chou C.-H., Han C.-Y., Tien C.-L., (2019), An All-Solid-State Electrochromic Device Based on WO3–Nb2O5 Composite Films Prepared by Fast-Alternating Bipolar-Pulsed Reactive Magnetron Sputtering, Coatings, 9, 9, (DOI: 10.3390/coatings9010009)
34. Eren E., Karaca G.Y., Koc U., Oksuz L., Oksuz A.U., (2017), Electrochromic Characteristics of Radio Frequency Plasma Sputtered

WO3 Thin Films onto Flexible Polyethylene Terephthalate Substrates, Thin Solid Films, 634, 40–50 (DOI: 10.1016/j.tsf.2017.05.009)

35. Chaudhary A., K. Pathak D., Tanwar M., Koch J., Pfnür H., Kumar R., (2020), Polythiophene-nanoWO 3 Bilayer as an Electrochromic Infrared Filter: A Transparent Heat Shield, J Mater Chem C, 8, 1773–1780 (DOI: 10.1039/C9TC05523A)
36. Bae J.-W., Koo B.-R., Ahn H.-J., (2019), Fe Doping Effect of Vanadium Oxide Films for Enhanced Switching Electrochromic Performances, Ceram Int, 45, 7137–7142 (DOI: 10.1016/j.ceramint.2018.12.219)
37. Kandpal S., Gupta P.K., Kumar R., Misra R., (2024), Ferrocene-Functionalized Fulleropyrrolidine Derivative: A Performance Enhancer for Solid-State Electrochromic Devices, ACS Appl Opt Mater, 2, 158–165 (DOI: 10.1021/acsaom.3c00384)
38. Chaudhary A., Pathak D.K., Mishra S., Yogi P., Sagdeo P.R., Kumar, R., (2018), Polythiophene -Viologen Bilayer for Electro-Trichromic Device, Sol Energy Mater Sol Cells, 188, 249–254 (DOI: 10.1016/j.solmat.2018.08.029)
39. Huang L.-M., Chen C.-H., Wen T.-C., (2006), Development and Characterization of Flexible Electrochromic Devices Based on Polyaniline and Poly(3,4-Ethylenedioxythiophene)-Poly(Styrene Sulfonic Acid), Electrochimica Acta, 51, 5858–5863 (DOI: 10.1016/j.electacta.2006.03.031)
40. Ghosh T., Kandpal S., Rani C., Bansal L., Tanwar M., Kumar R., (2023), Multiwavelength Color Switching from Polyaniline-Viologen Bilayer: Inching toward Versatile All-Organic Flexible Electrochromic Device, Adv Electron Mater, 9, 2201042 (DOI: 10.1002/aelm.202201042)
41. Gaupp C.L., Welsh D.M., Reynolds J.R., (2002), Poly(ProDOT-Et2): A High-Contrast, High-Coloration Efficiency Electrochromic

Polymer, Macromol Rapid Commun, 23, 885–889 (DOI: 10.1002/1521-3927).

42. Gupta P.K., Bansal L., Kumar R., Misra R., (2025), Design, Synthesis, and Characterization of a Phenothiazine-Functionalized Triazine Derivative for Electrochromic Devices, ACS Appl Opt Mater, 3, 14–21 (DOI: 10.1021/acsaom.4c00345)
43. Deng B., Zhu Y., Wang X., Zhu J., Liu M., Liu M., He Y., Zhu C., Zhang C., Meng H., (2023), An Ultrafast, Energy-Efficient Electrochromic and Thermochromic Device for Smart Windows, Adv Mater, 35, 2302685 (DOI: 10.1002/adma.202302685)
44. Elool Dov N., Shankar S., Cohen D., Bendikov T., Rechav K., Shimon L.J.W., Lahav M. van der Boom M.E., (2017), Electrochromic Metallo-Organic Nanoscale Films: Fabrication, Color Range, and Devices, J Am Chem Soc, 139, 11471–11481 (DOI: 10.1021/jacs.7b04217)
45. Abe M., Futagawa H., Ono T., Yamada T., Kimizuka N., Hisaeda Y., (2015), An Electropolymerized Crystalline Film Incorporating Axially-Bound Metalloporphycenes: Remarkable Reversibility, Reproducibility, and Coloration Efficiency of Ruthenium(II/III)-Based Electrochromism, Inorg Chem, 54, 11061–11063 (DOI: 10.1021/acs.inorgchem.5b02129)
46. Sarmah S., Kashyap S.S., Bera M.K., (2023), Dual Redox-Responsive Os/Ru-Based Alternated Heterobimetallic Supramolecular Polymer as a Multicolor Electrochromic Material for Camouflage Devices, ACS Appl Electron Mater, 5, 1738–1749 (DOI: 10.1021/acsaelm.2c01765)
47. Fujii K., Santra D.C., Bera M.K., Wakahara T., Nagahata R., Higuchi, M., (2023), Electrochromic Ru-Based Metallo-Supramolecular Polymer with a Layered Inorganic−Organic Hybrid Nanocomposite for Improved Electrochemical Properties, ACS Appl Polym Mater, 5, 8808–8821 (DOI: 10.1021/acsapm.3c00837)

48. Hsiao L.-Y., Chang T.-H., Lu H.-C., Wang Y.-C., Lu Y.-A., Ho K.-C., Higuchi M., (2019), A Panchromatic Electrochromic Device Composed of Ru(II)/Fe(II)-Based Heterometallo-Supramolecular Polymer, J Mater Chem C, 7, 7554–7562 (DOI: 10.1039/C9TC01452G)
49. Liu J., Daphne Ma X.Y., Wang Z., X L., Xu T., He C., Wang F., Lu X., (2020), Highly Stable and Rapid Switching Electrochromic Thin Films Based on Metal–Organic Frameworks with Redox-Active Triphenylamine Ligands, ACS Appl Mater Interfaces, 12, 7442–7450 (DOI: 10.1021/acsami.9b20388)
50. Li R., Li K., Wang G., Li L., Zhang Q., Yan J., Chen Y., Zhang Q., Hou C., Li Y., (2018), Ion-Transport Design for High-Performance Na+-Based Electrochromics, ACS Nano 12, 3759–3768 (DOI: 10.1021/acsnano.8b00974)
51. Fan X., Pan M., Li X., Kong L., Kuchmizha A., Xu H., (2024), Research Progress of MOF Electrochromic Materials, Resour Chem Mater, 3, 230–245 (DOI: 10.1016/j.recm.2024.03.001)
52. Wu X., Wang K., Lin J., Yan D., Guo Z., Zhan H., (2021), A Thin Film of Naphthalenediimide-Based Metal-Organic Framework with Electrochromic Properties, J Colloid Interface Sci, 594, 73–79 (DOI: 10.1016/j.jcis.2021.02.083)
53. Kim W.-C., Kim J., Kim J.-H., Park D.-H., Park Y.-Y., Jang J.-S., Ahn S.-Y., Min K., Park K.-W., (2024), Ameliorating Electrochemical Performance of Li-Rich Mn-Based Cathodes for Li-Ion Batteries by Fe Substitution, J Mater Chem A, 12, 1135–1144 (DOI: 10.1039/D3TA06003A)
54. Kortz C., Hein A., Ciobanu M., Walder L., Oesterschulze E., (2019), Complementary Hybrid Electrodes for High Contrast Electrochromic Devices with Fast Response, Nat Commun, 10, 4874 (DOI: 10.1038/s41467-019-12617-4)

Chapter 5

Two Coordinated Mono and Bimetallic Cu(I) Complexes for Electrochromic Devices

5.1 Introduction

Synthesis of two coordinated Cu(I) complexes, one of the most important and rapidly growing areas due to their excellent performance in optoelectronics *[1–4]*. Though several monometallic two-coordinated Cu(I) complexes are reported, bimetallic two-coordinated Cu(I) complexes are unknown to date *[5–7]*. In this context, the exploration of bimetallic, two-coordinate Cu(I) complexes represents a compelling strategy to design novel photoluminescent systems with efficient emission properties. Though such types of Cu(I) complexes are used as emitters in light-emitting devices (OLEDs and LECs), the electrochromic performance is not explored.

In this study, we synthesize monometallic [SphosCuPhBz]PF_6 (**9**), [Cu(Sphos)(CNPhBz)]PF_6 (**10**), [Cu(Sphos)(NO_2PhBz)]PF_6 (**11**), [Cu(Xphos)(PhBz)]PF_6 (**12**), [Cu(Xphos)(CNPhBz)]PF_6 (**13**), [Cu(Xphos)(NO_2PhBz)]PF_6 (**14**) and bimetallic [(CuSphos)$_2$(PhBz)]PF_6 (**9a**), [(CuSphos)$_2$(CNPhBz)]PF_6 (**10a**), [(CuSphos)$_2$(NO_2PhBz)]PF_6 (**11a**), [(CuXphos)$_2$(PhBz)]PF_6 (**12a**), [(CuXphos)$_2$(CNPhBz)]PF_6 (**13a**), [(CuXphos)$_2$(NO_2PhBz)]PF_6 (**14a**) Cu(I) complexes. All the synthesized complexes were characterized by multinuclear NMR spectroscopic techniques. The structures of **9** and **12a** are authenticated by SC-XRD analysis. Substitution of PhBz ligands with CN and NO_2 was done to generalize the synthesis of two-coordinated Cu(I) complexes and investigate the impact of ligand substitution on their photophysical properties. The resulting complexes show absorption between 275 and 470 nm due to metal-to-ligand charge transfer (MLCT) transitions. These complexes display tunable emission across the UV-visible range, with nanosecond lifetimes (0.58–1.82 ns). To check the electrochromic properties, complexes **10** and **10a** were chosen. Both devices show good performance in terms of color contrast and switching time. To the best of our knowledge, this is the first report of electrochromic devices based on the mono and bimetallic Cu(I) complexes.

5.2 Experimental Section

5.2.1.1 Materials

Materials obtained from commercial suppliers were used without further purification unless otherwise stated. All glassware and magnetic stirring bars were dried in a convection oven at 70 °C. The complexation reactions were performed using standard schlenk techniques under an inert nitrogen gas atmosphere. The Sphos and Xphos ligands were purchased from BLD Pharm, Commercial grade chemicals, tetrathiafulvalene (TTF) (Sigma AldrichTM), lithium perchlorate(Sigma AldrichTM), acetonitrile (ACN, anhydrous, 99%, Sigma AldrichTM), and polyethylene oxide (PEO, Alfa Aesar, MW=100,000) were used as received for device fabrication. Indium doped tin oxide (ITO) coated glass substrate was purchased from Macwin India. ITO coated polyethylene terephthalate (PET) was purchased from Sigma AldrichTM.

5.2.1.2. Characterization methods

^{1}H, $^{13}C\{^{1}H\}$, and $^{31}P\{^{1}H\}$ NMR were recorded on a Fourier transform nuclear magnetic resonance (NMR) spectrometer, model Bruker Avance 500 MHz spectrometer. ^{1}H and $^{13}C\{^{1}H\}$NMR spectra were referenced relative to the residual solvent peak. High-resolution mass spectral analyses (HRMS) were recorded on a Bruker-Daltonics micrOTOF-Q II mass spectrometer. Single crystal X-ray analysis was performed on Saxi-CrysalisPro-abstract goniometer imported SAXI images and the data were collected at 293(2) K. Using Olex2 *[8]*, the structure was solved with the SHELXT structure solution program using Intrinsic Phasing and refined with the SHELXL refinement package using Least Squares minimization *[9]*. Thermogravimetric analysis was performed on the powder sample using METTLER TOLEDO TGA/DSC 1 STARe System having a heating rate of 10 °C min^{-1} under a nitrogen atmosphere. UV-Vis spectroscopy was performed on Agilent Cary 60 UV−vis spectrophotometer in a quartz

cuvette (1 cm ×1 cm). In-situ bias-dependent color modulation was studied using a Lambda 365 spectrophotometer (PerkinElmer make) and a Keithley 2450 workstation. The electrochemical measurement was done using a Metrohm-Multi Autolab M204 potentiostat. Cyclic Voltammetry was performed using an AUTOLAB, PGSTAT 12 (Ecochemie, B.V. Netherlands) with GPES software (version 4.9) in a conventional blank ITO-coated glass slide as the working electrode, the CV curve was recorded in a potential range of ±3 V and at a scan rate of 100 mV/s.

5.3 Synthetic Details

5.3.1.1 General synthetic procedure of CNPhBz and NO_2PhBz:

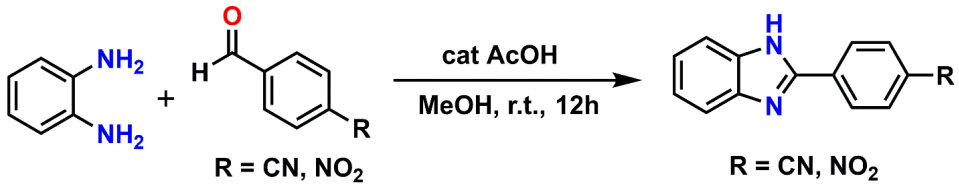

Scheme 5.1 Synthetic procedure of **CNPhBz** and **NO_2PhBz** ligands.

In an oven-dried round bottom flask, phenylenediamine and respective benzaldehyde (4 cyanobenzaldehyde or 4-nitrobenzaldehyde) were dissolved in methanol. To this catalytic amount of acetic acid (AcOH) was added. After stirring the reaction mixture at room temperature for 12 h, it was poured into cold water. A precipitate formed was subsequently filtered, washed with deionized water and the product was dried under a vacuum.

5.3.1.1.1 Synthesis of 2-(4-cyanophenyl)benzimidazole (CNPhBz):

A general procedure was used to synthesize CNPhBz, phenylenediamine (0.013 mol) and 4-cyanobenzaldehyde (0.013 mol) giving a yellow powder with 97% yield. **^{1}H NMR** (500 MHz, DMSO-d6) δ 13.19 (s, 1H), 8.34 (d, *J* = 8.1 Hz, 2H), 8.03 (d, *J* = 8.2 Hz, 2H), 7.72 (d, *J* = 7.6 Hz, 1H), 7.58 (d, *J* = 7.6 Hz, 1H), 7.26 (dd, *J* = 7.9, 7.8 Hz, 2H). **^{13}C{^{1}H} NMR**: (126 MHz, DMSO-d6) δ 149.42, 134.29, 132.99, 127.02, 122.86, 118.66, 111.92. **HRMS** (ESI): calculated for $C_{14}H_{10}N_3[M+H]^+$: 220.0869; found 220.0856.

5.3.1.1.2 Synthesis of 2-(4-nitrophenyl)benzimidazole (NO_2PhBz):

A similar general procedure was used to synthesize NO_2PhBz, phenylenediamine (0.013 mol) and 4-nitrobenzaldehyde (0.013 mol) to give a red powder with a 94% yield. **^{1}H NMR** (500 MHz, DMSO-d6) δ 13.29 (s, 1H), 8.46 – 8.36 (m, 4H), 7.74 (s, 1H), 7.59 (s, 1H), 7.26 (d, J = 8.2 Hz, 2H). **^{13}C{^{1}H} NMR** (126 MHz, DMSO-d6) δ 148.84, 147.61, 143.68, 135.87, 135.08, 127.21, 124.10, 123.42, 122.15, 119.30, 111.65. **HRMS** (ESI) calculated for $C_{13}H_{10}N_3O_2$ $[M+H]^+$: 240.0768; Found: 240.0750.

5.3.1.1.3 ^{1}H and ^{13}C{^{1}H} NMR spectrum of CNPhBz and NO_2PhBz:

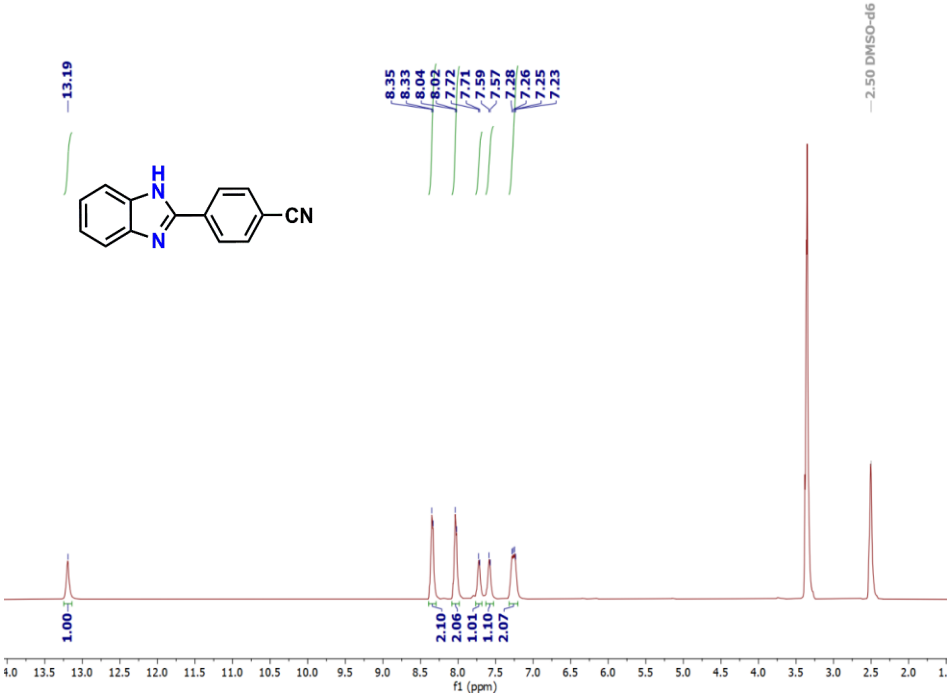

Fig. 5.1 ^{1}H NMR spectrum of **CNPhBz** in DMSO-d6 (500 MHz).

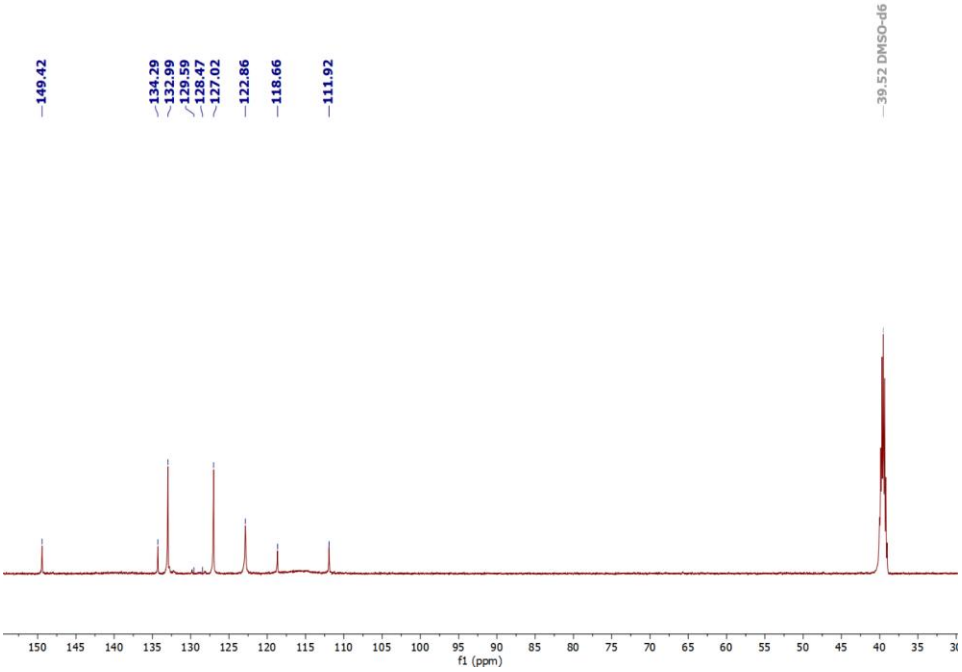

Fig. 5.2 $^{13}C\{^{1}H\}$ NMR spectrum of **CNPhBz** in DMSO-d6 (126 MHz).

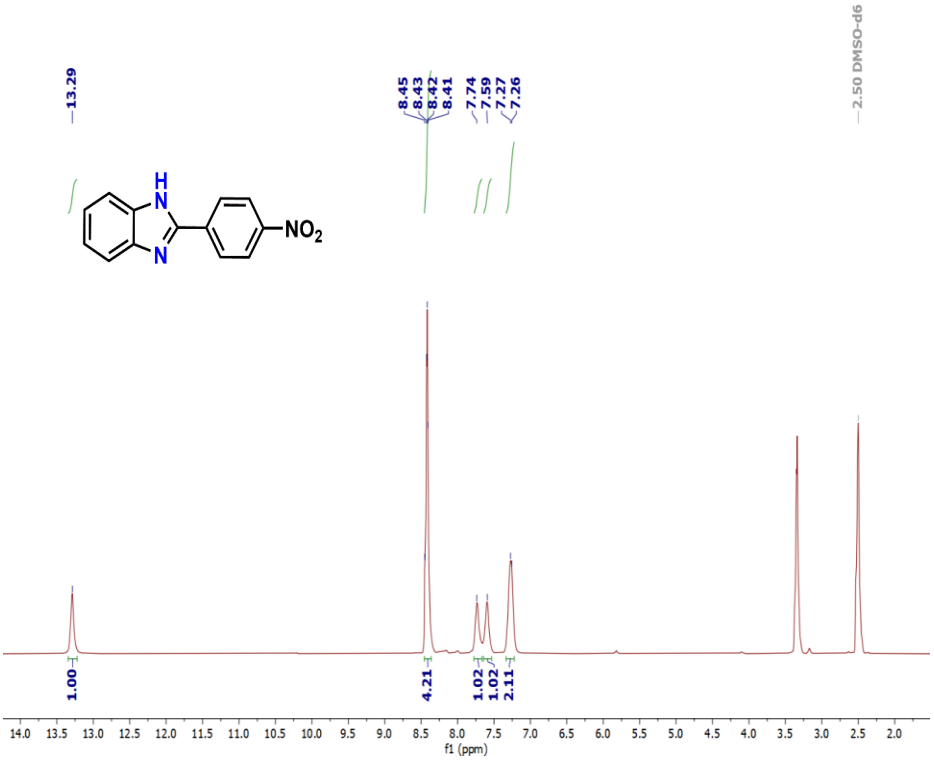

Fig. 5.3 ^{1}H NMR spectrum of **NO_2PhBz** in DMSO-d6 (500 MHz)

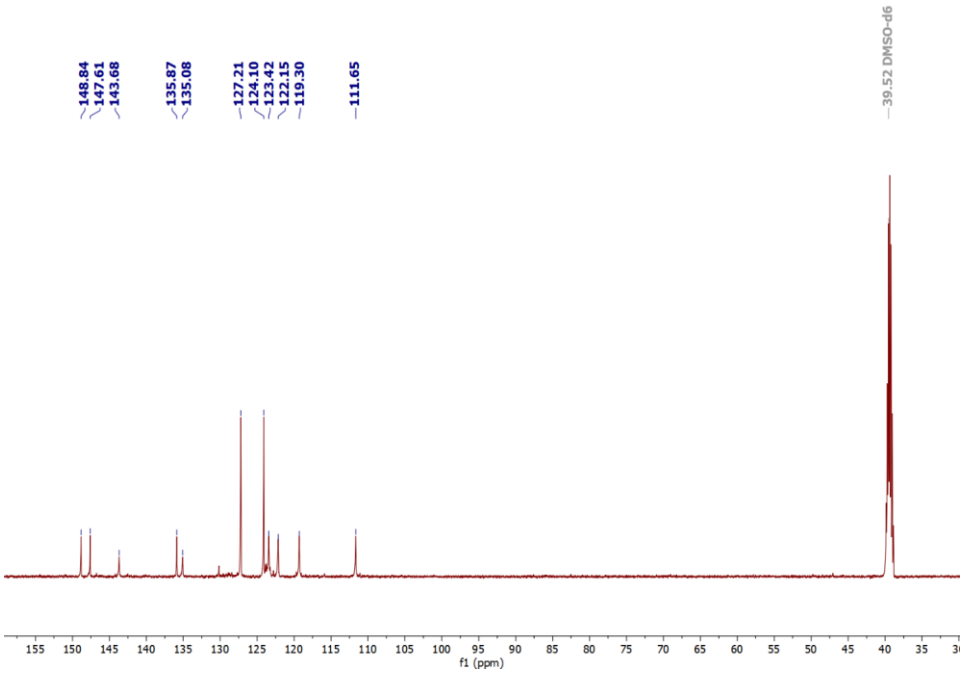

Fig. 5.4 $^{13}C\{^{1}H\}$ NMR spectrum of **NO_2PhBz** in DMSO-d6 (126 MHz).

5.3.1.2 General procedure for Synthesis of complexes

Using a standard schlenk technique, all complexes were synthesized in the presence of N_2 atmosphere. Monometallic complexes (**9-14)** were prepared by the addition of 1 equiv. of phosphine, PhBz/CNPhBz/NO_2PhBz ligands and $[Cu(CH_3CN)_4]PF_6$ at room temperature. Firstly, $[Cu(CH_3CN)_4]PF_6$ solution was added to the stirring Sphos or Xphos ligands in 5 mL of DCM and it was stirred for 2 hours. To this, the solution of PhBz/CNPhBz/NO_2PhBz ligands was added and kept on stirring for 2 hours. After completion of reaction, the solvent was concentrated by rotary evaporation and n-hexane was added to precipitate the product. The product was washed with n-hexane and dried under a high vacuum. It is reported that similar ionic compounds can be converted into neutral compounds in the presence of a base *[10]*. However, when the base was added to the solution of synthesized complexes **1-3**, formation of a white precipitate was observed which remains insoluble in all organic solvents. Similarly, bimetallic complexes (**9a-14a**) were prepared by the addition of 2 equiv. of phosphine and $[Cu(CH_3CN)_4]PF_6$ and other components are the same as

monometallic complexes. Probably, the PF_6 ion abstracts the acidic N-H proton of the ligand, leading to the formation of bimetallic complexes.

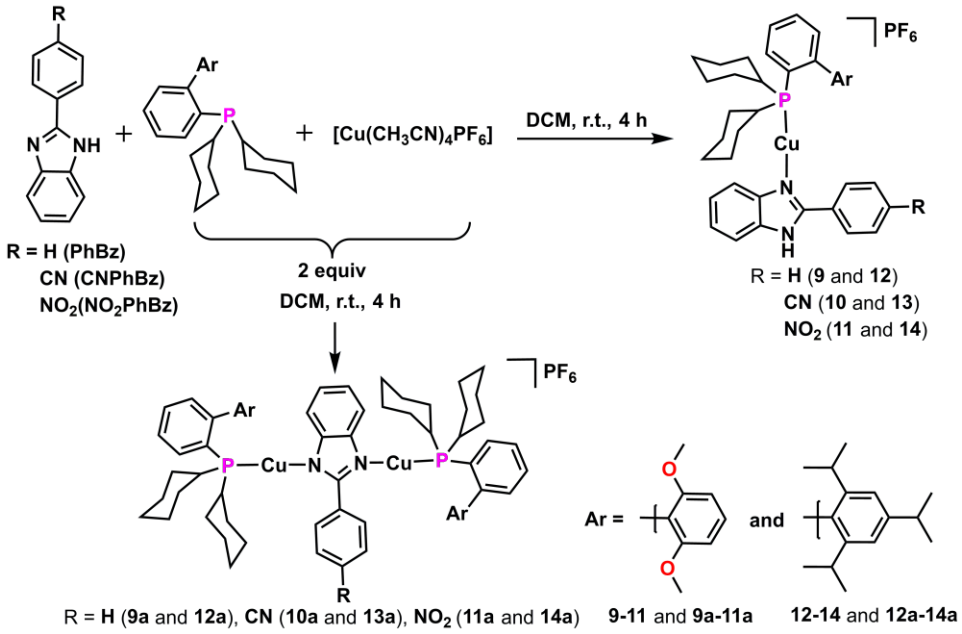

Scheme 5.2 Synthetic procedure of complexes **9-14** and **9a-14a**.

5.3.1.2.1 Synthesis of [SphosCuPhBz]PF_6(9)

A general procedure was used to synthesize complex **9**, Sphos (0.268 mmol), $Cu(CH_3CN)_4]PF_6$ (0.268 mmol) and PhBz (0.268 mmol) in DCM to give a white solid product in 91% yield. **^{1}H NMR** (500 MHz, DMSO-d6) δ 8.13 (d, *J* = 6.9 Hz, 2H), 7.78 (t, *J* = 8.2 Hz, 1H), 7.61 (s, 5H), 7.47 (d, *J* = 9.2 Hz, 2H), 7.37 (t, *J* = 6.6 Hz, 2H), 6.98 (p, *J* = 4.3 Hz, 1H), 6.79 (t, *J* = 9.2 Hz, 1H), 6.16 (d, *J* = 9.2 Hz, 2H), 3.38 (s, 6H), 2.28 (q, *J* = 12.2 Hz, 2H), 1.98 – 1.88 (m, 2H), 1.74 (t, *J* = 12.3 Hz, 4H), 1.68 (d, *J* = 12.7 Hz, 2H), 1.60 (d, *J* = 14.8 Hz, 2H), 1.35 (q, *J* = 12.8 Hz, 2H), 1.30 – 1.23 (m, 2H), 1.22 – 1.07 (m, 6H). **^{13}C{^{1}H} NMR** (126 MHz, DMSO-d6) δ 155.90, 150.08, 146.17, 141.90, 141.84, 132.29, 131.59, 131.53, 130.80, 130.71, 129.12, 129.06, 128.52, 127.14, 123.17, 118.12, 117.52, 117.49, 117.46, 116.83, 103.76, 54.75, 33.40, 33.21, 30.40, 28.58, 26.09, 26.00, 25.62. **^{31}P{^{1}H} NMR** (202 MHz, DMSO-d6) δ 11.96, -144.18. **HRMS** (ESI) calculated for $C_{39}H_{45}CuN_2O_2P$ $[M\text{-}PF_6]^+$: 667.2509; Found: 667.2518.

5.3.1.2.2 Synthesis of [SphosCuCNPhBz]PF_6(10)

Using a general procedure, complex **10** was synthesized, Sphos (0.268 mmol), $Cu(CH_3CN)_4]PF_6$ (0.268 mmol) and CNPhBz (0.268 mmol) in DCM to give yellow powder in 95% yield. **^{1}H NMR** (500 MHz, DMSO-d6) δ 13.40 (s, 1H), 8.32 (d, *J* = 6.9 Hz, 2H), 8.05 (d, *J* = 6.4 Hz, 2H), 7.71 (d, *J* = 5.3 Hz, 2H), 7.65 (s, 2H), 7.44 (d, *J* = 6.3 Hz, 2H), 7.30 (s, 2H), 7.00 (d, *J* = 4.7 Hz, 1H), 6.61 (s, 2H), 3.57 (s, 6H), 2.10 (s, 2H), 1.82 (d, *J* = 11.9 Hz, 2H), 1.76 – 1.62 (m, 6H), 1.56 – 1.44 (m, 2H), 1.29 (d, *J* = 13.1 Hz, 2H), 1.19 (d, *J* = 14.8 Hz, 2H), 1.10 (d, *J* = 14.8 Hz, 6H). **^{13}C{^{1}H} NMR** (126 MHz, DMSO-d6) δ 155.97, 149.81, 145.03, 141.88, 141.74, 135.37, 133.19, 132.75, 132.09, 131.48, 130.05, 129.21, 128.91, 128.68, 127.35, 126.83, 123.18, 118.09, 117.52, 117.45, 112.21, 103.78, 54.76, 33.46, 33.28, 29.90, 28.09, 25.97, 25.87, 25.49. **^{31}P{^{1}H} NMR** (202 MHz, DMSO-d6) δ 9.38, -144.19. HRMS (ESI) calculated for $C_{40}H_{45}CuN_3O_2P$ $[M\text{-}PF_6]^+$: 692.2462; Found: 692.2459.

5.3.1.2.3 Synthesis of complex [SphosCuNO$_2$PhBz]PF_6(11)

Complex **11** was synthesized by using a general procedure, Sphos (0.268 mmol), $Cu(CH_3CN)_4]PF_6$ (0.268 mmol) and NO_2PhBz (0.268 mmol) in DCM to obtain an orange crystalline powder in 80% yield. **^{1}H NMR** (500 MHz, DMSO-d6) δ 13.49 (s, 1H), 8.41 (d, *J* = 6.4 Hz, 4H), 7.71 (d, *J* = 7.5 Hz, 2H), 7.66 (s, 1H), 7.44 (d, *J* = 6.0 Hz, 2H), 7.32 (s, 2H), 7.27 (s, 1H), 7.00 (s, 1H), 6.61 (s, 2H), 3.59 (s, 6H), 2.09 (dd, *J* = 13.0, 6.0 Hz, 2H), 1.82 (d, *J* = 10.5 Hz, 2H), 1.75 – 1.60 (m, 6H), 1.51 (d, *J* = 11.7 Hz, 2H), 1.25 (d, *J* = 11.3 Hz, 4H), 1.10 (d, *J* = 13.3 Hz, 6H). **^{13}C{^{1}H} NMR** (126 MHz, DMSO-d6) δ 156.20, 149.18, 148.01, 142.11, 141.74, 135.35, 132.24, 131.66, 130.69, 130.19, 129.43, 128.98, 127.87, 127.44, 127.01, 126.45, 124.23, 123.97, 123.42, 117.72, 103.99, 54.96, 33.72, 33.54, 30.03, 28.19, 26.18, 26.08, 25.69. **^{31}P{^{1}H} NMR** (202 MHz, DMSO-d6) δ 9.36, -144.18. HRMS (ESI) calculated for $C_{39}H_{44}CuN_3O_4P$ $[M\text{-}PF_6]^+$: 712.2360; Found: 712.2357.

5.3.1.2.4 Synthesis of [XphosCuPhBz]PF_6(12)

General procedure was used to obtain complex **12**, Xphos (0.268 mmol), $Cu(CH_3CN)_4]PF_6$ (0.268 mmol) and PhBz (0.268 mmol) in DCM to give a white solid product in 93% yield. **^{1}H NMR** (500 MHz, DMSO-d6) δ 8.16 (s, 2H), 7.85 (t, *J* = 8.2 Hz, 1H), 7.65 (s, 2H), 7.57 (s, 4H), 7.54 (s, 2H), 7.29 (d, *J* = 4.4 Hz, 2H), 7.25 (d, *J* = 4.4 Hz, 1H), 6.94 (d, *J* = 8.2 Hz, 1H), 2.22 (sept, *J* = 6.4 Hz, 3H), 1.96 (d, *J* = 13.6 Hz, 1H), 1.74 (d, *J* = 12.2 Hz, 1H), 1.66 (d, *J* = 11.9 Hz, 4H), 1.61 – 1.55 (m, 2H), 1.23 (d, *J* = 8.4 Hz, 10H), 1.11 (d, *J* = 7.5 Hz, 6H), 0.98 (d, *J* = 7.3 Hz, 4H), 0.84 (d, *J* = 3.4 Hz, 6H), 0.82 (d, *J* = 3.7 Hz, 2H). **^{13}C{^{1}H} NMR** (101 MHz, DMSO-d6) δ 152.77, 147.92, 145.98, 144.93, 134.80, 132.73, 131.89, 131.82, 130.46, 129.96, 129.12, 128.91, 127.99, 127.30, 127.29, 126.81, 122.71, 121.59, 121.11, 114.88, 34.57, 34.33, 33.96, 32.71, 30.72, 30.07, 29.75, 29.42, 28.24, 25.68, 25.35, 24.55, 23.08, 21.58, 13.72, 11.01. **^{31}P{^{1}H} NMR** (202 MHz, DMSO-d6) δ 6.59, -144.19. **HRMS** (ESI) calculated for $C_{46}H_{59}CuN_2P$ $[M\text{-}PF_6]^+$: 733.3706; Found: 733.3733.

5.3.1.2.5 Synthesis of complex [XphosCuCNPhBz]PF_6(13)

A general procedure was used to synthesize complex **13**, Xphos (0.268 mmol), $Cu(CH_3CN)_4]PF_6$ (0.268 mmol) and CNPhBz (0.268 mmol) in DCM, a yellow powder was obtained in 89% yield. **^{1}H NMR** (500 MHz, DMSO-D6) δ 13.37 (s, 1H), 8.32 (d, *J* = 8.1 Hz, 2H), 8.02 (d, *J* = 7.2 Hz, 2H), 7.82 (t, *J* = 7.2 Hz, 1H), 7.64 (d, *J* = 8.2 Hz, 2H), 7.53 (d, *J* = 4.3 Hz, 2H), 7.27 (d, *J* = 5.2 Hz, 2H), 7.24 (d, *J* = 4.7 Hz, 1H), 7.04 (s, 2H), 2.22 (sept, *J* = 6.9 Hz, 3H), 2.10 (s, 2H), 1.96 – 1.89 (m, 2H), 1.73 (d, *J* = 13.6 Hz, 2H), 1.65 (d, *J* = 7.5 Hz, 4H), 1.54 (dd, *J* = 12.1, 5.6 Hz, 2H), 1.31 – 1.23 (m, 6H), 1.18 (d, *J* = 8.2 Hz, 11H), 1.09 (dd, *J* = 13.6, 7.2 Hz, 6H), 0.85 (d, *J* = 7.8 Hz, 6H). **^{13}C{^{1}H} NMR** (126 MHz, DMSO-d6) δ 153.52, 149.65, 147.89, 145.55, 144.86, 134.71, 134.65, 133.79, 132.70, 131.78, 131.72, 129.75, 128.22, 127.27, 127.02, 126.99, 123.50, 123.02, 120.97, 118.17, 111.86, 108.52, 34.62, 33.63, 30.66, 30.01, 29.76, 28.17, 25.61, 25.30, 24.48, 23.36, 22.17, 21.76, 21.55, 13.85, 13.65, 10.94. **^{31}P{^{1}H} NMR**

(202 MHz, DMSO-d6) δ 5.62, -144.19. **HRMS** (ESI) calculated for $C_{47}H_{58}CuN_3P$ $[M\text{-}PF_6]^+$: 758.3659; Found: 758.3639.

5.3.1.2.6 Synthesis of complex [XphosCuNO$_2$PhBz]PF$_6$(16)

Using a general procedure complex **14** was synthesized, Xphos (0.268 mmol), $Cu(CH_3CN)_4]PF_6$ (0.268 mmol) and NO_2PhBz (0.268 mmol) in DCM to give an orange powder in 78% yield. **^{1}H NMR** (500 MHz, DMSO-d6) δ 13.37 (s, 1H), 8.41 (d, *J* = 7.0 Hz, 2H), 7.81 (s, 2H), 7.66 (s, 2H), 7.52 (s, 2H), 7.28 (d, *J* = 8.2 Hz, 4H), 7.08 (s, 2H), 2.25 (sept, *J* = 7.4 Hz, 3H), 2.08 (s, 2H), 1.93 (s, 2H), 1.73 (s, 2H), 1.65 (s, 6H), 1.52 (s, 2H), 1.38 (d, *J* = 7.0 Hz, 4H), 1.22 (s, 10H), 1.10 (d, *J* = 22.6 Hz, 6H), 0.86 (d, *J* = 7.3 Hz, 6H). **^{13}C{^{1}H} NMR** (126 MHz, DMSO-d6) δ 153.53, 152.00, 151.60, 148.88, 147.67, 147.40, 145.67, 144.65, 142.20, 135.37, 134.49, 132.39, 131.56, 130.09, 129.57, 127.15, 123.79, 123.51, 120.75, 118.97, 34.44, 34.28, 33.66, 32.87, 30.43, 29.78, 29.54, 28.88, 25.38, 25.07, 23.15, 21.54, 21.33, 14.85, 13.42, 10.70. **^{31}P{^{1}H} NMR** (202 MHz, DMSO-d6) δ 5.44, -144.18. **HRMS** calculated for $C_{46}H_{58}CuN_3O_2P$ $[M\text{-}PF_6]^+$: 778.3557; Found: 778.3549.

5.3.1.2.7 Synthesis of [(SphosCu)$_2$PhBz]PF$_6$(9a)

A general procedure was used synthesis of complex **9a**, Sphos (0.268 mmol), $Cu(CH_3CN)_4]PF_6$ (0.268 mmol) and PhBz (0.134 mmol) in DCM to obtain a white solid in 93% yield. **^{1}H NMR** (500 MHz, DMSO-d6) δ 8.12 (s, 2H), 7.73 (t, *J* = 7.1 Hz, 2H), 7.61 (s, 4H), 7.45 (d, *J* = 5.2 Hz, 4H), 7.35 (d, *J* = 6.3 Hz, 2H), 7.11 (s, 1H), 6.99 (d, *J* = 6.1 Hz, 2H), 6.47 (d, *J* = 8.4 Hz, 4H), 3.51 (s, 12H), 2.15 (d, *J* = 11.0 Hz, 2H), 1.86 (q, *J* = 6.9 Hz, 4H), 1.74 (d, *J* = 10.1 Hz, 6H), 1.66 (d, *J* = 14.0 Hz, 6H), 1.55 (d, *J* = 3.7 Hz, 4H), 1.31 (d, *J* = 10.2 Hz, 4H), 1.25 – 1.16 (m, 6H), 1.12 (d, *J* = 8.1 Hz, 12H). **^{13}C{^{1}H} NMR** (101 MHz, DMSO-d6) δ 156.14, 146.15, 142.16, 141.97, 132.34, 131.71, 131.64, 131.19, 130.41, 129.36, 129.27, 128.96, 128.58, 127.57, 127.49, 127.19, 123.66, 118.00, 117.71, 117.63, 103.96, 54.86, 34.15, 33.73, 33.49, 30.91, 30.33, 28.44, 26.24, 26.13, 25.75, 22.43,

22.02, 13.91, 11.19. **$^{31}P\{^{1}H\}$ NMR** (202 MHz, DMSO-d6) δ 10.12, -140.68. **HRMS** calculated for $C_{65}H_{79}Cu_2N_2O_4P_2$ $[M\text{-}PF_6]^+$: 1139.4102; Found: 1139.4085.

5.3.1.2.8 Synthesis of $[(SphosCu)_2CNPhBz]PF_6$(10a)

Complex **10a** was synthesized by using a general procedure, Sphos (0.268 mmol), $Cu(CH_3CN)_4]PF_6$ (0.268 mmol) and CNPhBz (0.134 mmol) in DCM to obtain a yellow solid in 79% yield. **^{1}H NMR** (500 MHz, DMSO-d6) δ 8.32 (s, 2H), 8.04 (d, *J* = 7.6 Hz, 2H), 7.70 (s, 2H), 7.62 (s, 2H), 7.44 (t, *J* = 6.9 Hz, 4H), 7.30 (d, *J* = 8.7 Hz, 4H), 7.02 – 6.99 (m, 2H), 6.69 (d, *J* = 3.7 Hz, 4H), 3.59 (s, 12H), 1.81 (d, *J* = 12.8 Hz, 4H), 1.71 (d, *J* = 12.5 Hz, 6H), 1.63 (d, *J* = 11.7 Hz, 6H), 1.53 – 1.45 (m, 4H), 1.28 (d, *J* = 10.8 Hz, 4H), 1.18 (s, 2H), 1.10 (d, *J* = 5.8 Hz, 4H), 1.08 (d, *J* = 3.8 Hz, 4H), 1.05 (d, *J* = 6.1 Hz, 6H). **$^{13}C\{^{1}H\}$ NMR** (126 MHz, DMSO-d6) δ 156.12, 152.19, 151.21, 147.32, 142.04, 132.84, 132.12, 131.56, 131.51, 131.03, 129.78, 129.38, 126.91, 122.52, 117.89, 117.63, 117.57, 113.38, 112.32, 103.94, 54.89, 30.78, 29.89, 28.30, 28.06, 26.10, 26.00, 25.60, 24.61, 22.30, 21.89, 20.42, 13.98, 13.78, 11.06. **$^{31}P\{^{1}H\}$ NMR** (202 MHz, DMSO-d6) δ 9.20, -144.19. **HRMS** calculated for $C_{66}H_{78}Cu_2N_3O_4P_2$ $[M\text{-}PF_6]^+$: 1164.4054; Found: 1164.4023.

5.3.1.2.9 Synthesis of $[(SphosCu)_2NO_2PhBz]PF_6$(11a)

To obtain complex **11a**, a general procedure was used. Sphos (0.268 mmol), $Cu(CH_3CN)_4]PF_6$ (0.268 mmol) and NO_2PhBz (0.134 mmol) in DCM to give an orange solid in 82% yield. **^{1}H NMR** (500 MHz, DMSO-d6) δ 8.42 (s, 4H), 7.69 (d, *J* = 6.9 Hz, 4H), 7.43 (d, *J* = 6.6 Hz, 4H), 7.41 (dd, *J* = 7.5, 2.3 Hz, 2H), 7.33 (dd, *J* = 6.1, 2.9 Hz, 4H), 7.01 (dd, *J* = 4.2, 2.1 Hz, 2H), 6.65 (d, *J* = 8.7 Hz, 4H), 3.58 (s, 12H), 1.81 (d, *J* = 8.2 Hz, 4H), 1.71 (d, *J* = 11.0 Hz, 4H), 1.63 (d, *J* = 12.8 Hz, 12H), 1.50 (d, *J* = 6.7 Hz, 4H), 1.27 (d, *J* = 3.1 Hz, 4H), 1.23 (t, *J* = 3.4 Hz, 4H), 1.07 (d, *J* = 3.2 Hz, 12H). **$^{13}C\{^{1}H\}$ NMR** (126 MHz, DMSO-d6) δ 156.12, 149.38, 147.87, 146.80, 142.04, 141.89, 135.40, 132.07, 131.48, 129.96, 129.37, 127.71, 126.86, 124.13, 123.21, 117.86, 117.62, 114.83, 110.75, 103.93, 54.86, 34.00,

33.73, 33.55, 30.76, 27.97, 26.14, 26.09, 25.98, 25.59, 24.58, 22.28, 21.87, 13.75, 11.04. **$^{31}P\{^{1}H\}$ NMR** (202 MHz, DMSO-d6) δ 9.01, -144.19. **HRMS** calculated for $C_{65}H_{78}Cu_2N_2O_6P_2$ $[M\text{-}PF_6]^+$: 1184.3952; Found: 1184.3920.

5.3.1.2.10 Synthesis of $[(XphosCu)_2PhBz]PF_6$ (12a)

Using a general procedure, complex **12a** was synthesized, Xphos (0.268 mmol), $Cu(CH_3CN)_4]PF_6$ (0.268 mmol) and PhBz (0.134 mmol) in DCM to obtain a white solid with 87% yield. **^{1}H NMR** (500 MHz, DMSO-d6) δ 8.11 (d, *J* = 6.9 Hz, 2H), 7.82 (d, *J* = 6.6 Hz, 2H), 7.57 (s, 5H), 7.54 (d, *J* = 4.6 Hz, 4H), 7.29 (d, *J* = 5.2 Hz, 2H), 7.27 – 7.22 (m, 2H), 7.03 (s, 4H), 2.70 (p, *J* = 7.0 Hz, 2H), 2.23 (h, *J* = 7.0 Hz, 4H), 2.11 (t, *J* = 10.6 Hz, 4H), 1.95 (s, 4H), 1.74 (d, *J* = 13.9 Hz, 4H), 1.66 (q, *J* = 8.5, 7.8 Hz, 10H), 1.56 (dd, *J* = 11.9, 5.3 Hz, 4H), 1.24 (d, *J* = 3.2 Hz, 18H), 1.18 (d, *J* = 7.0 Hz, 16H), 1.14 (d, *J* = 7.0 Hz, 18H). **$^{13}C\{^{1}H\}$ NMR** (101 MHz, DMSO-d6) δ 154.39, 150.17, 147.89, 145.70, 144.92, 140.60, 134.78, 132.98, 132.68, 131.85, 130.75, 129.83, 128.96, 128.40, 128.02, 127.34, 127.06, 122.97, 121.01, 114.93, 114.50, 34.65, 34.42, 33.93, 32.87, 30.69, 30.04, 29.77, 29.26, 28.21, 26.24, 25.65, 25.33, 24.52, 23.23, 22.21, 21.80, 21.56, 13.69, 10.97. **$^{31}P\{^{1}H\}$ NMR** (202 MHz, DMSO-d6) δ 5.90, -144.19. **HRMS** calculated for $C_{79}H_{107}Cu_2N_2P_2$ $[M\text{-}PF_6]^+$: 1271.6496; Found: 1271.6447.

5.3.1.2.11 Synthesis of $[(XphosCu)_2CNPhBz]PF_6$ (13a)

A general procedure was used to obtain complex **13a**, Xphos (0.268 mmol), $Cu(CH_3CN)_4]PF_6$ (0.268 mmol) and CNPhBz (0.134 mmol) in DCM to give a yellow solid in 74% yield. **^{1}H NMR** (500 MHz, DMSO-d6) δ 8.32 (d, *J* = 8.4 Hz, 2H), 8.03 (d, *J* = 7.5 Hz, 2H), 7.81 (d, *J* = 4.7 Hz, 2H), 7.63 (d, *J* = 8.2 Hz, 2H), 7.51 (d, *J* = 4.6 Hz, 4H), 7.30 – 7.25 (m, 2H), 7.24 (q, *J* = 4.5 Hz, 2H), 7.07 (s, 4H), 2.92 – 2.78 (m, 2H), 2.26 – 2.20 (m, 4H), 1.92 (d, *J* = 11.3 Hz, 4H), 1.73 (d, *J* = 11.3 Hz, 4H), 1.65 (d, *J* = 4.9 Hz, 10H), 1.54 (dd, *J* = 10.8, 6.5 Hz, 4H), 1.28 (d, *J* = 6.0 Hz, 12H), 1.22 (d, *J* = 8.7 Hz, 32H), 1.14 – 1.04 (m, 12H). **$^{13}C\{^{1}H\}$ NMR** (126 MHz, DMSO-d6) δ 154.19, 149.80, 147.81, 145.84, 144.76, 141.55, 138.00, 134.59, 133.60, 132.63, 132.48, 131.62, 129.56, 128.80, 127.10, 126.85, 120.81, 117.83,

117.65, 115.24, 111.71, 35.02, 34.58, 34.34, 33.79, 33.53, 33.06, 30.56, 29.91, 29.60, 28.98, 28.92, 28.08, 26.69, 25.51, 25.20, 24.38, 23.38, 22.07, 21.67, 21.48, 13.75, 13.55, 10.84. **$^{31}P\{^{1}H\}$ NMR** (202 MHz, DMSO-d6) δ 5.46, -144.19. **HRMS** calculated for $C_{80}H_{106}Cu_2N_3P_2$ $[M\text{-}PF_6]^+$: 1296.6448; Found: 1298.6359.

5.3.1.2.12 Synthesis of $[(XphosCu)_2NO_2PhBz]PF_6$ (14a)

General procedure was used to synthesize complex **14a**, Xphos (0.268 mmol), $Cu(CH_3CN)_4]PF_6$ (0.268 mmol) and NO_2PhBz (0.134 mmol) in DCM to give an orange powder in 76% yield. **^{1}H NMR** (500 MHz, DMSO-d6) δ 8.41 (s, 4H), 7.81 (s, 2H), 7.65 (d, *J* = 8.9 Hz, 2H), 7.52 (d, *J* = 9.2 Hz, 4H), 7.29 – 7.25 (m, 2H), 7.24 – 7.22 (m, 2H), 7.06 (s, 4H), 2.86 (dd, *J* = 13.7, 7.0 Hz, 2H), 2.22 (q, *J* = 6.8 Hz, 4H), 1.96 – 1.90 (m, 4H), 1.74 (d, *J* = 13.0 Hz, 4H), 1.69 – 1.60 (m, 10H), 1.56 – 1.51 (m, 4H), 1.34 – 1.24 (m, 12H), 1.20 (d, *J* = 10.2 Hz, 32H), 1.11 (q, *J* = 7.2, 6.6 Hz, 12H). **$^{13}C\{^{1}H\}$ NMR** (126 MHz, DMSO-d6) δ 156.57, 152.30, 149.40, 147.90, 147.62, 145.80, 144.83, 135.50, 134.67, 134.61, 132.56, 131.75, 131.69, 130.15, 129.73, 127.30, 124.01, 123.69, 120.94, 119.24, 117.72, 34.64, 34.47, 33.88, 30.65, 30.35, 29.99, 29.09, 28.17, 26.78, 25.59, 25.27, 24.47, 23.42, 22.15, 21.56, 20.28, 19.57, 18.31, 13.84, 13.64, 10.93. **$^{31}P\{^{1}H\}$ NMR** (202 MHz, DMSO-d6) δ 5.51, -144.19. **HRMS** calculated for $C_{79}H_{106}Cu_2N_3O_2P_2$ $[M\text{-}PF_6]^+$: 1316.6347; Found: 1316.6285.

5.4 Characterisations

All the synthesized complexes are well characterized by multinuclear NMR spectroscopy and HRMS. The ^{1}H NMR of complexes **9-14** confirms the presence of both phosphine and PhBz ligands in a 1:1 ratio, whereas in bimetallic complexes **9a-14a,** the phosphine and PhBz ligands are present in 2:1 ratio. The presence of Sphos ligand in complexes **9-11** and **9a-11a** is confirmed by the appearance of multiplets in the 5.57 to 6.48 ppm range, which corresponds to the seven phenyl protons and singlets in the range of

3.38 to 3.59 ppm for six methoxy protons. Similarly, the presence of Xphos ligand in complexes **12-14** and **12a-14a** is confirmed by the six phenyl proton signals in the range of 6.85 to 7.99 ppm, peaks for methine protons of isopropyl group appear as a multiplet around 1.9 ppm and methyl protons as doublets from 1.68 to 0.36 ppm. In addition, the cyclohexyl protons of both phosphine ligands are observed in the range of 2.67 to 1.21 ppm. In all complexes, a highly deshielded proton in the range of 8.13 to 8.32 is attributed to the PhBz ligands. All other aromatic proton signals correspond to the phenyl rings of both PhBz as well as phosphine ligands.

$^{13}C\{^{1}H\}$ NMR spectra of all complexes exhibit a characteristic peak in the range of 152 to 156 ppm, representing the presence of a carbon atom between two N atoms of the PhBz ligands. In complexes **9-11** and **9a-11a**, the methoxy carbon of the Sphos ligand is observed around 54 ppm, while in complexes **12-14** and **12a-14a**, the methine carbon of the isopropyl group present on the Xphos ligand is observed around 22-24 ppm, while methyl carbons appear around 10-12 ppm. The other remaining carbons in an aromatic region correspond to the phenyl carbons of both ligands. Furthermore, the $^{31}P\{^{1}H\}$ NMR spectra of complexes **9-11** and **9a-11a** exhibit a singlet ranging from 9.01 to 11.96 ppm attributed to the Sphos ligand, while complexes **12-14** and **12a-14a** show a singlet in between 5.51 to 6.59 ppm, which confirms the presence of Xphos ligand. In all complexes, a characteristic septet around -144 ppm (J_{P-H} of ~112 Hz) is observed, which confirms the PF_6 counterion.

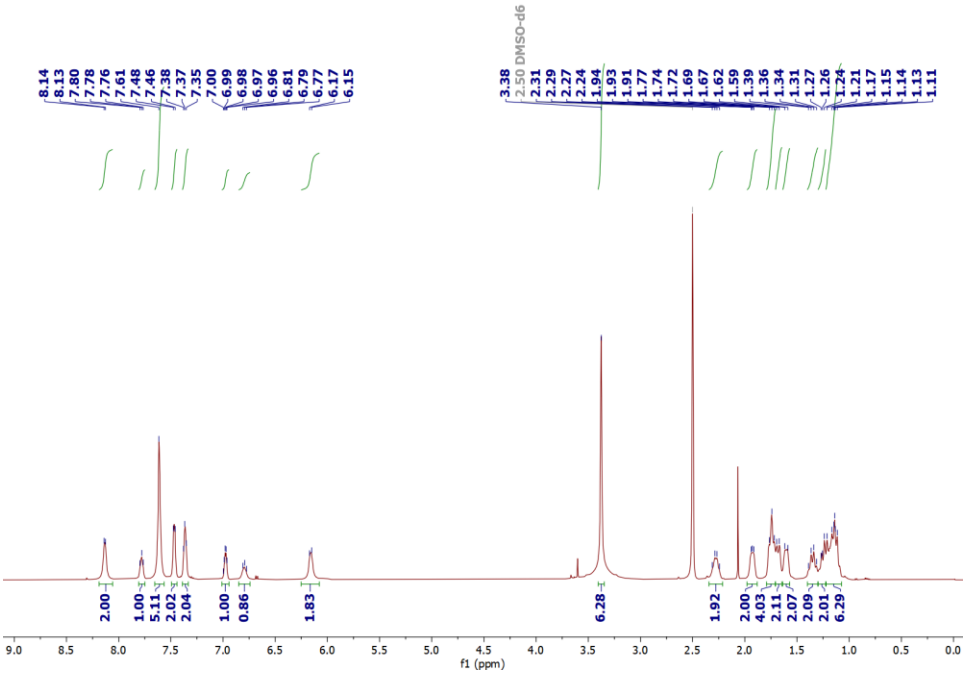

Fig. 5.5 ^{1}H NMR spectrum of **9** in DMSO-d6 (500 MHz).

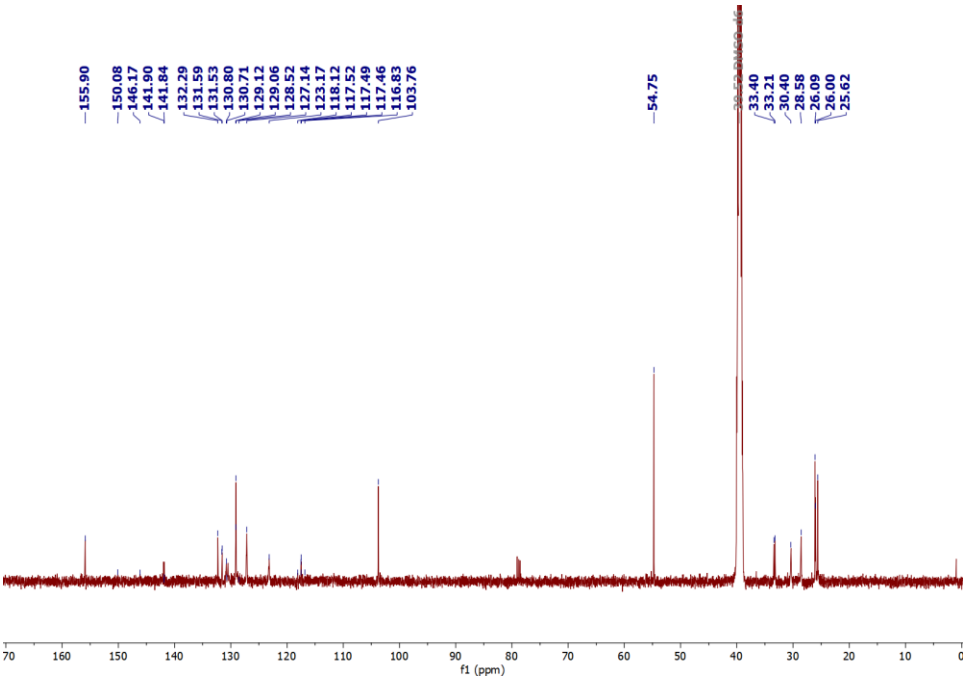

Fig. 5.6 ^{13}C{^{1}H} NMR spectrum of **9** in DMSO-d6 (126 MHz).

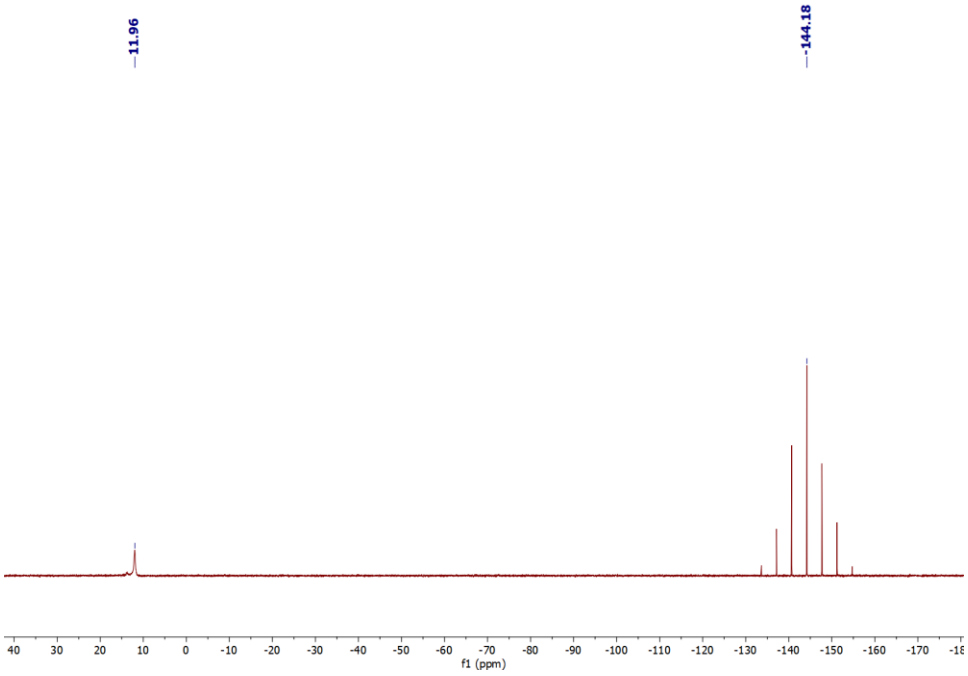

Fig. 5.7 $^{31}P\{^{1}H\}$ NMR spectrum of **9** in DMSO-d6 (202 MHz).

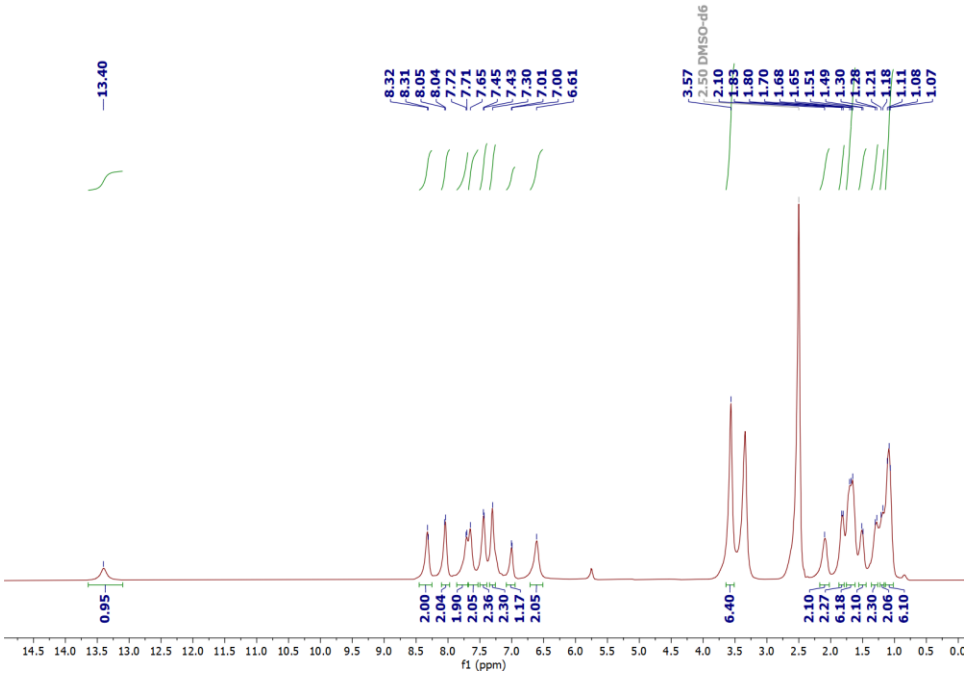

Fig. 5.8 ^{1}H NMR spectrum of **10** in DMSO-d6 (500 MHz).

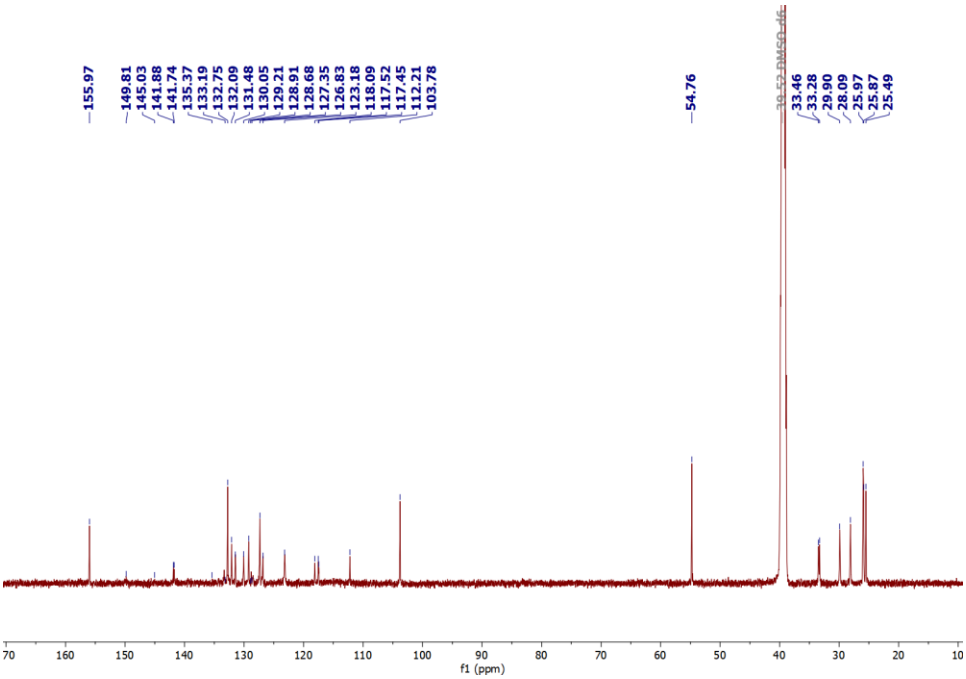

Fig. 5.9 $^{13}C\{^{1}H\}$ NMR spectrum of **10** in DMSO-d6 (126 MHz)

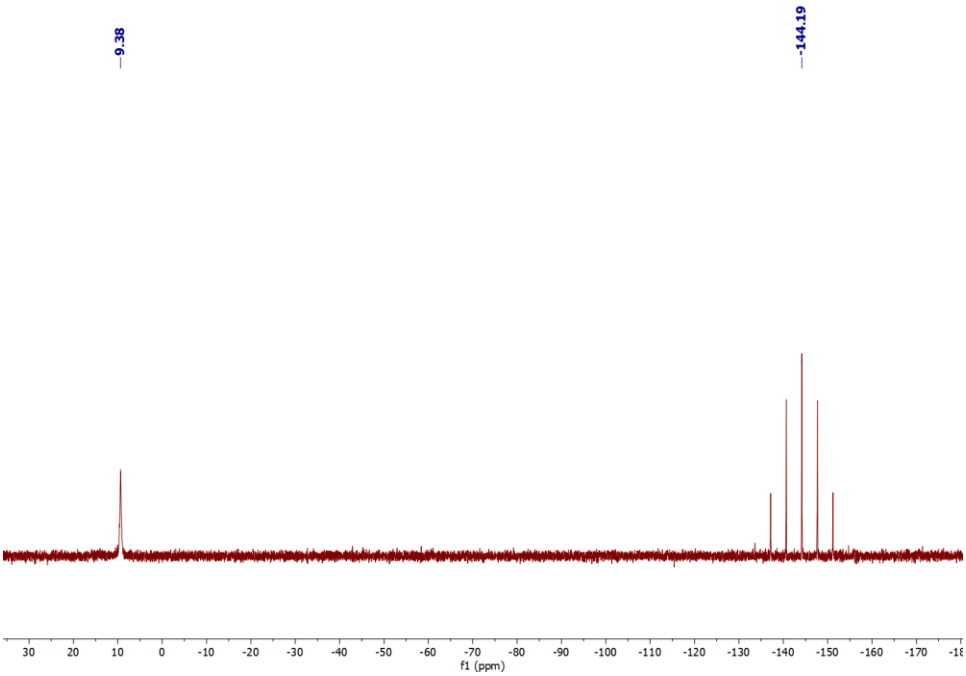

Fig. 5.10 $^{31}P\{^{1}H\}$ NMR spectrum of **10** in DMSO-d6 (202 MHz).

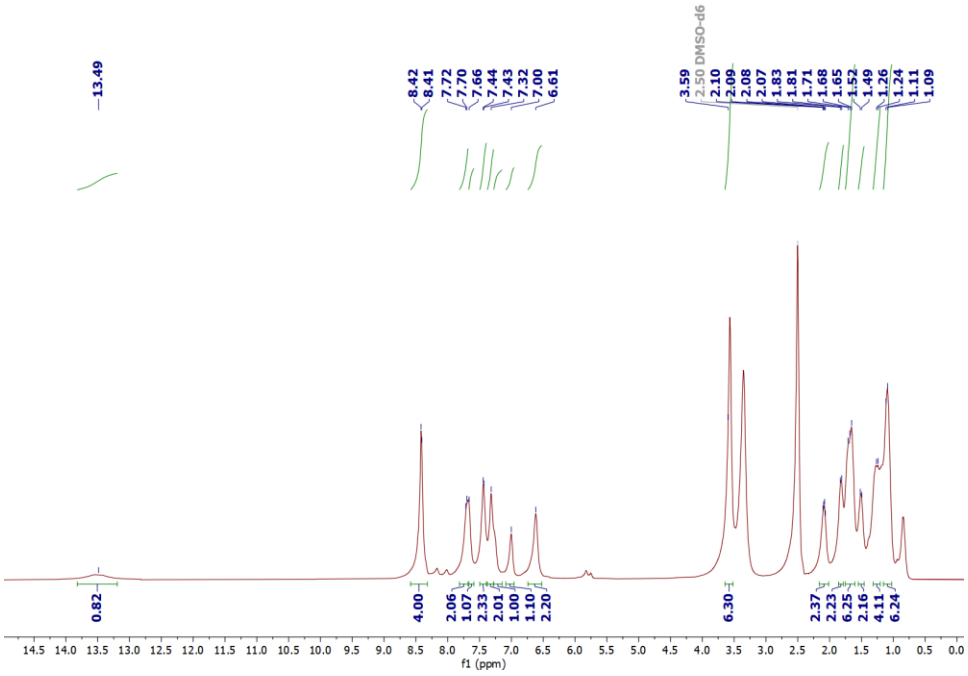

Fig. 5.11 ^{1}H NMR spectrum of **11** in DMSO-d6 (500 MHz).

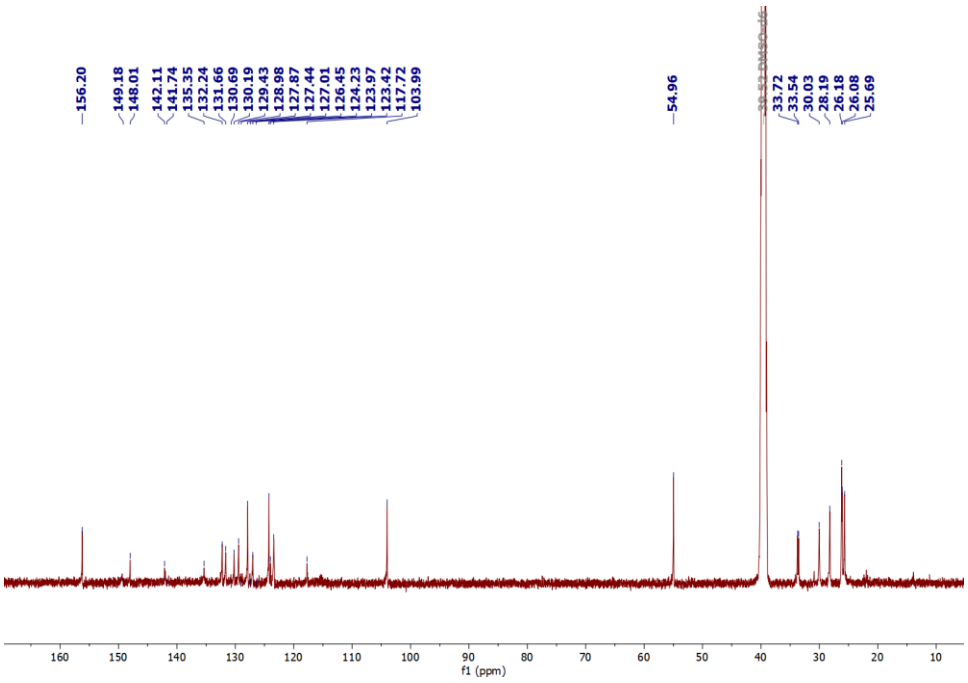

Fig. 5.12 ^{13}C{^{1}H} NMR spectrum of **11** in DMSO-d6 (126 MHz).

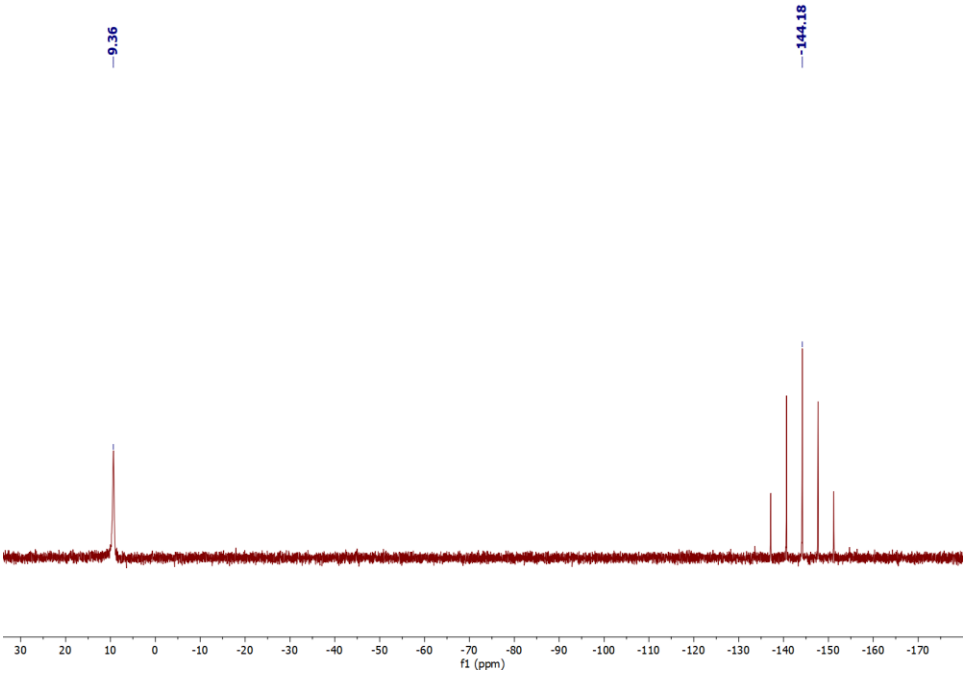

Fig. 5.13 $^{31}P\{^{1}H\}$ NMR spectrum of **11** in DMSO-d6 (202 MHz).

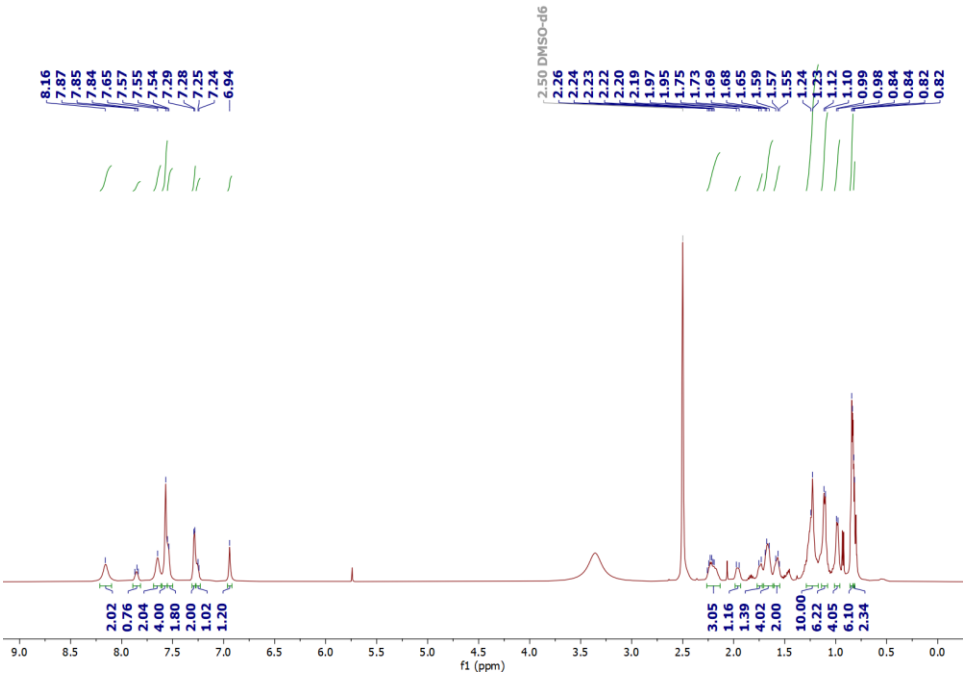

Fig. 5.14 ^{1}H NMR spectrum of **12** in DMSO-d6 (500 MHz).

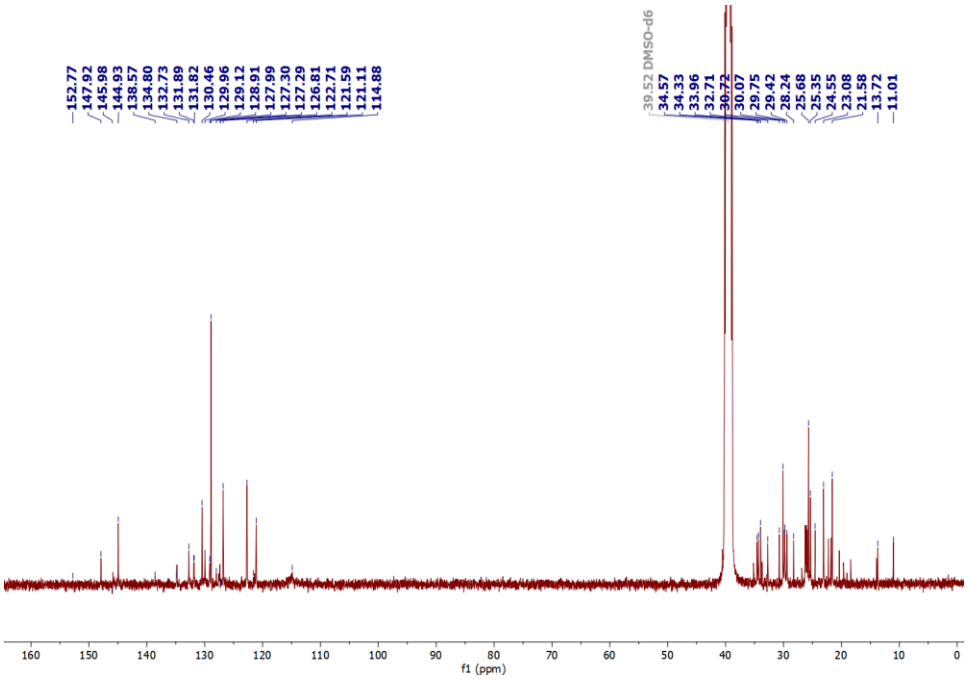

Fig. 5.15 $^{13}C\{^{1}H\}$ NMR spectrum of **12** in DMSO-d6 (126 MHz).

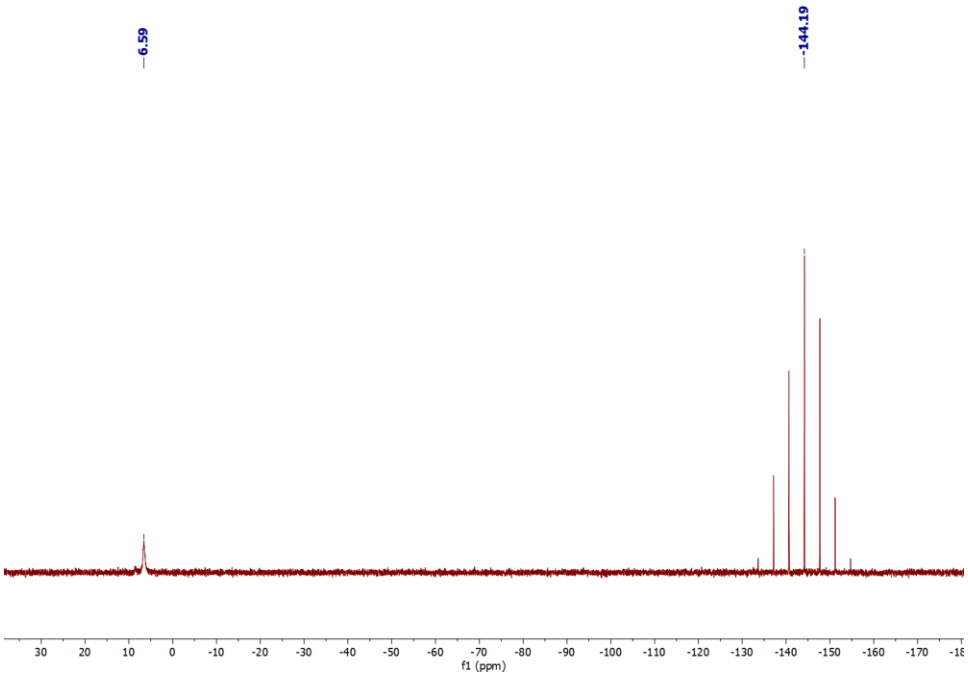

Fig. 5.16 $^{31}P\{^{1}H\}$ NMR spectrum of **12** in DMSO-d6 (202 MHz).

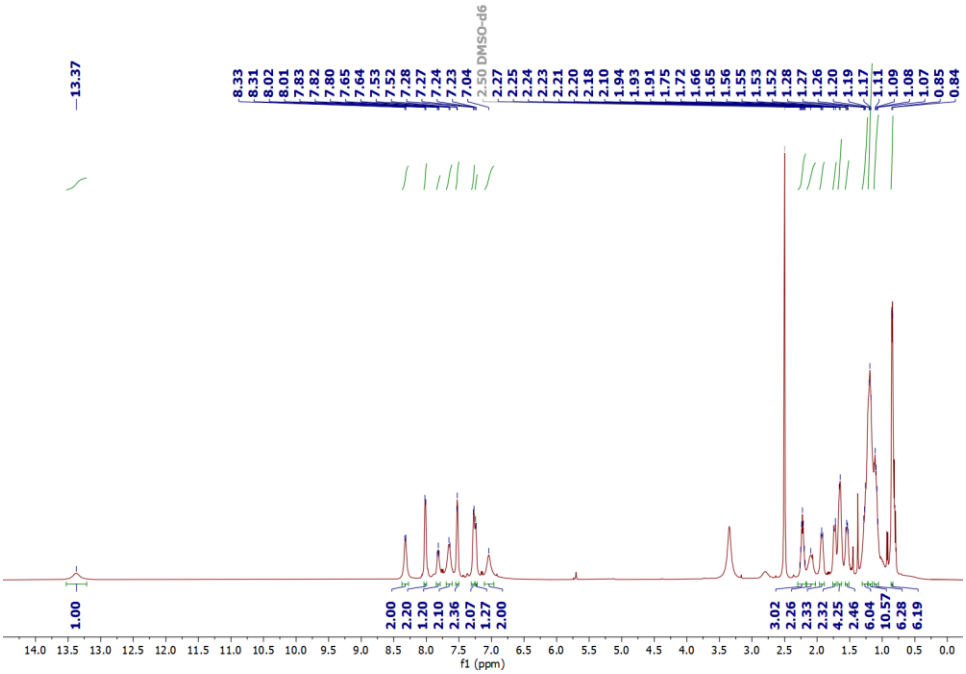

Fig. 5.17 ^{1}H NMR spectrum of **13** in DMSO-d6 (500 MHz).

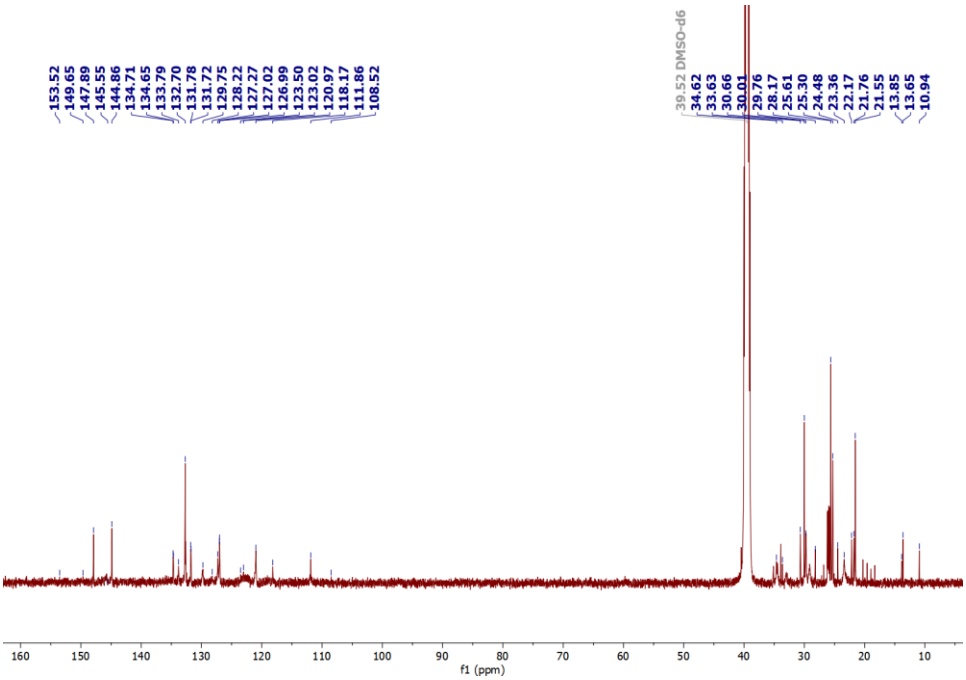

Fig. 5.18 ^{13}C{^{1}H} NMR spectrum of **13** in DMSO-d6 (126 MHz).

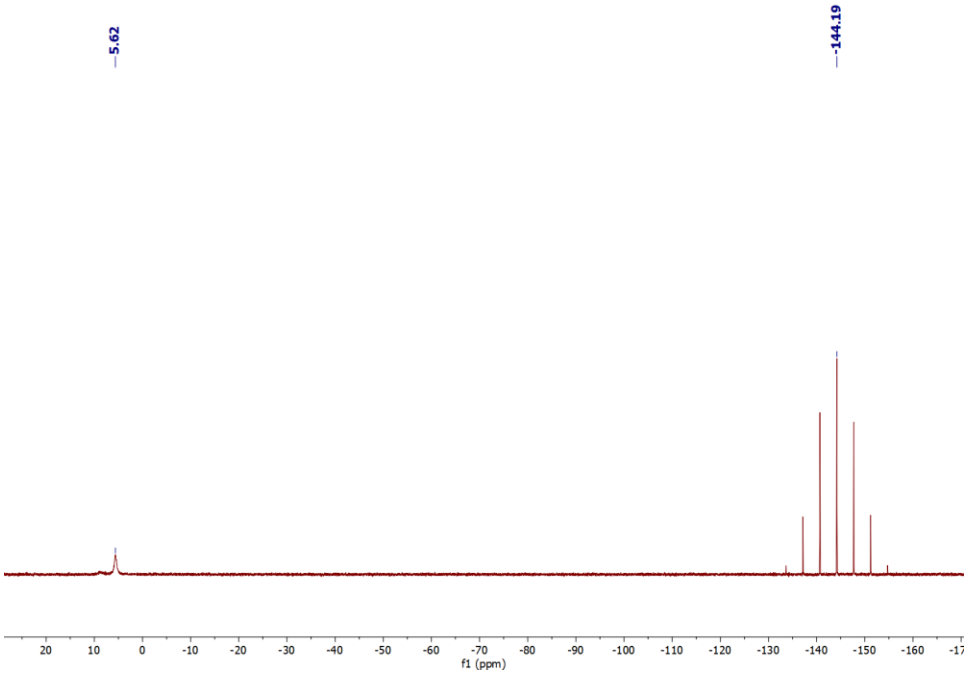

Fig. 5.19 $^{31}P\{^{1}H\}$ NMR spectrum of **13** in DMSO-d6 (202 MHz).

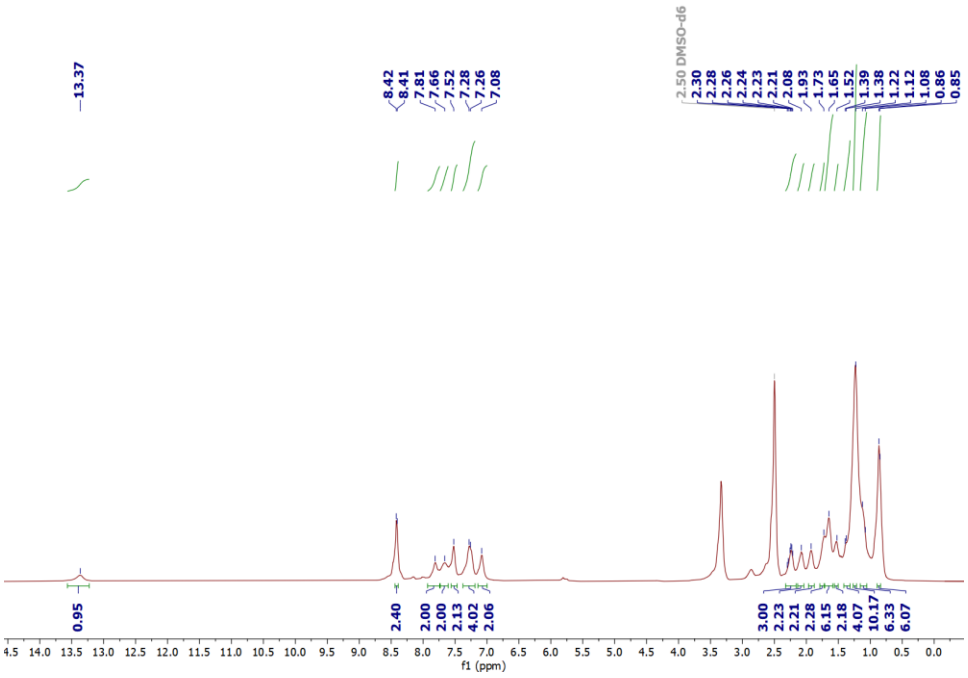

Fig. 5.20 ^{1}H NMR spectrum of **14** in DMSO-d6 (500 MHz).

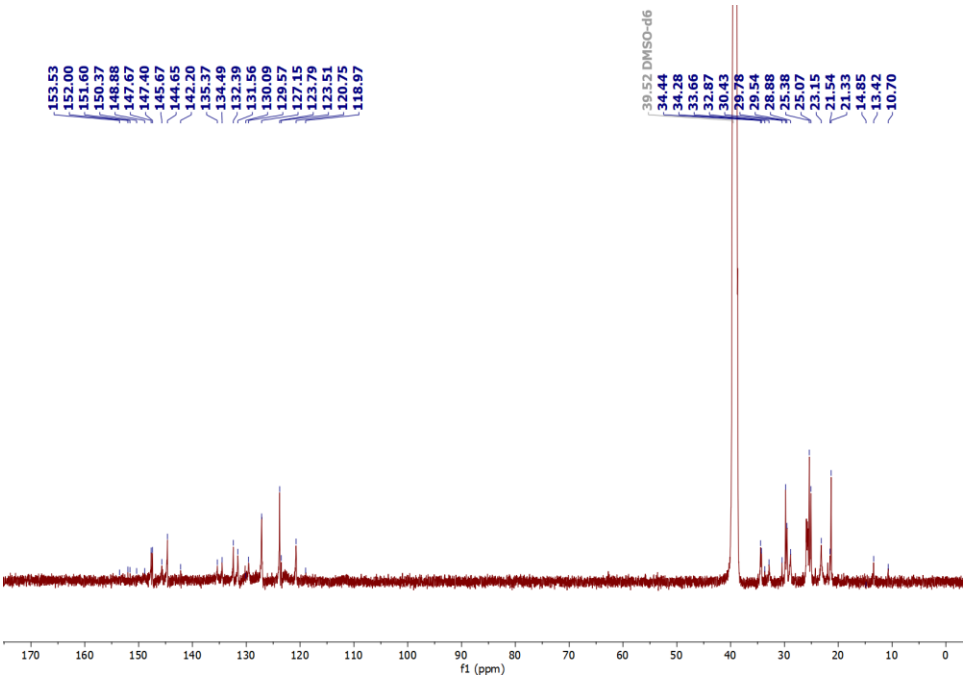

Fig. 5.21 $^{13}C\{^{1}H\}$ NMR spectrum of **14** in DMSO-d6 (126 MHz).

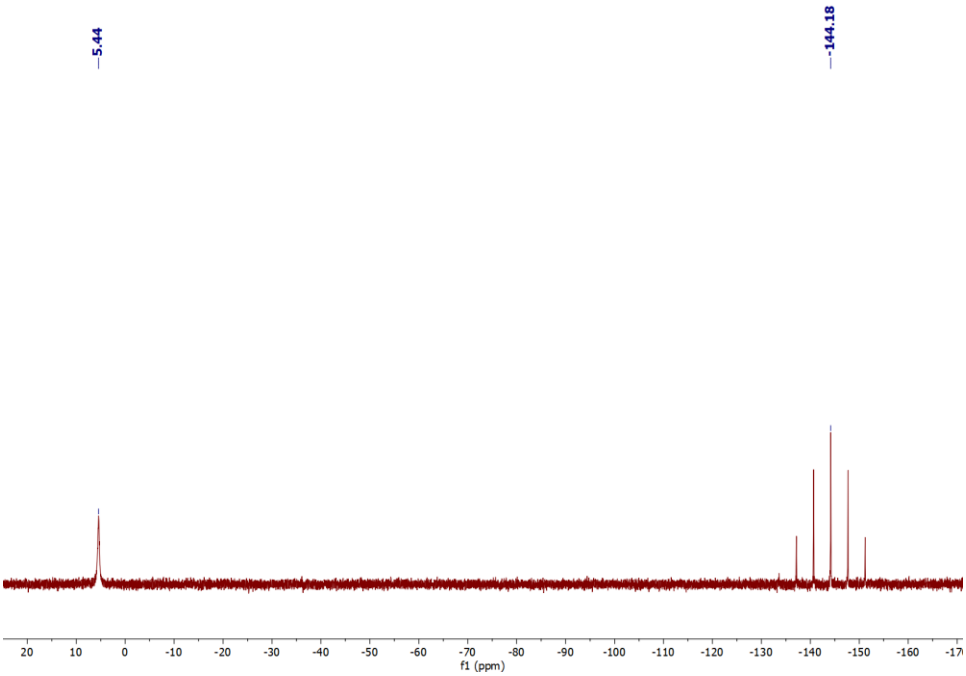

Fig. 5.22 $^{31}P\{^{1}H\}$ NMR spectrum of **14** in DMSO-d6 (202 MHz).

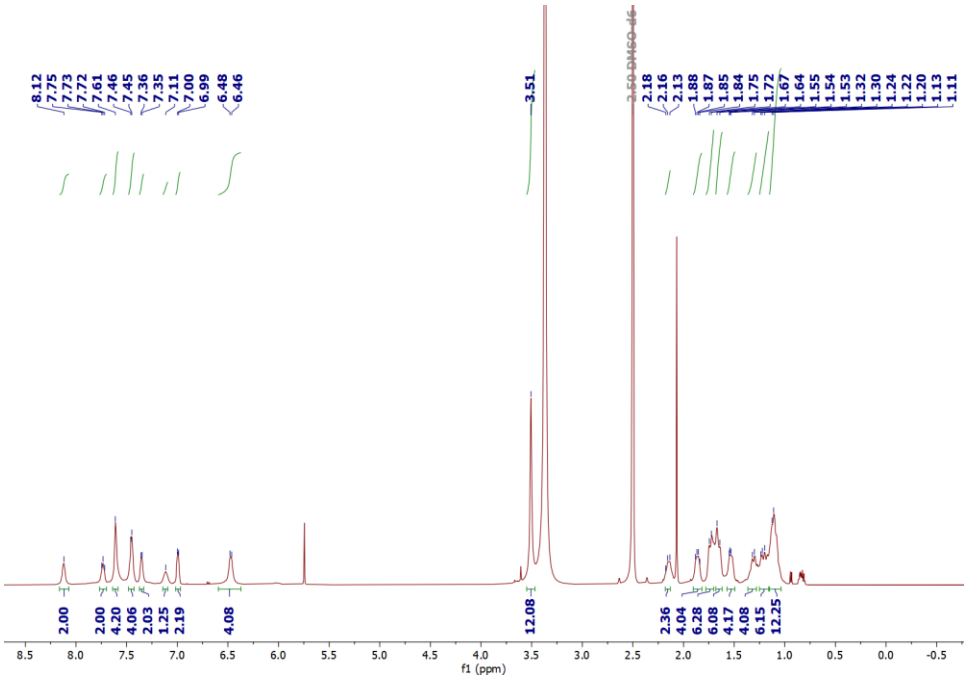

Fig. 5.23 ^{1}H NMR spectrum of **9a** in DMSO-d6 (500 MHz).

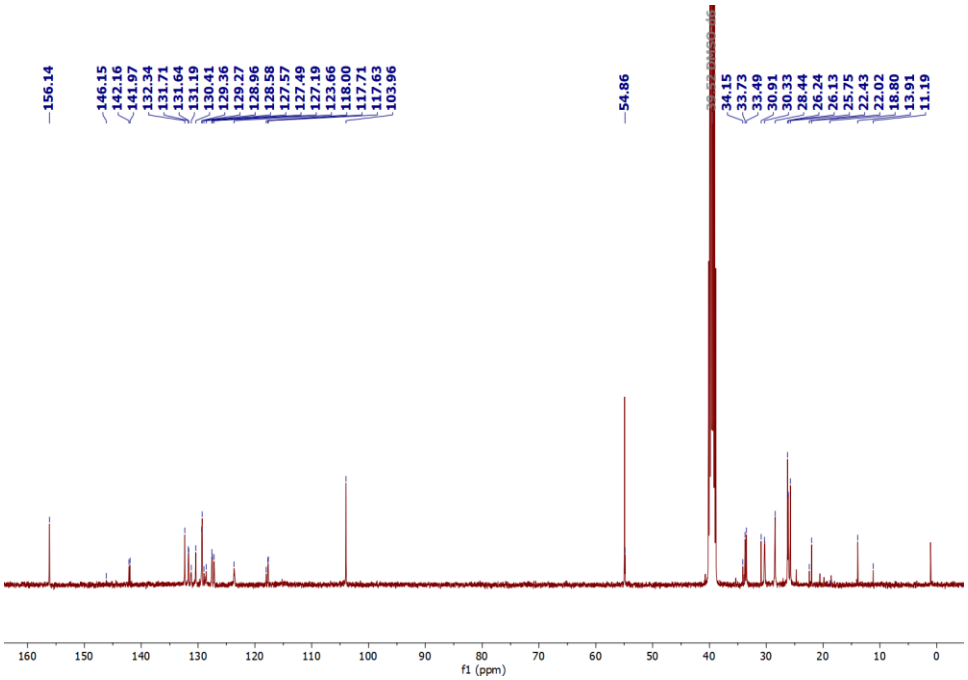

Fig. 5.24 ^{13}C{^{1}H} NMR spectrum of **9a** in DMSO-d6 (101 MHz).

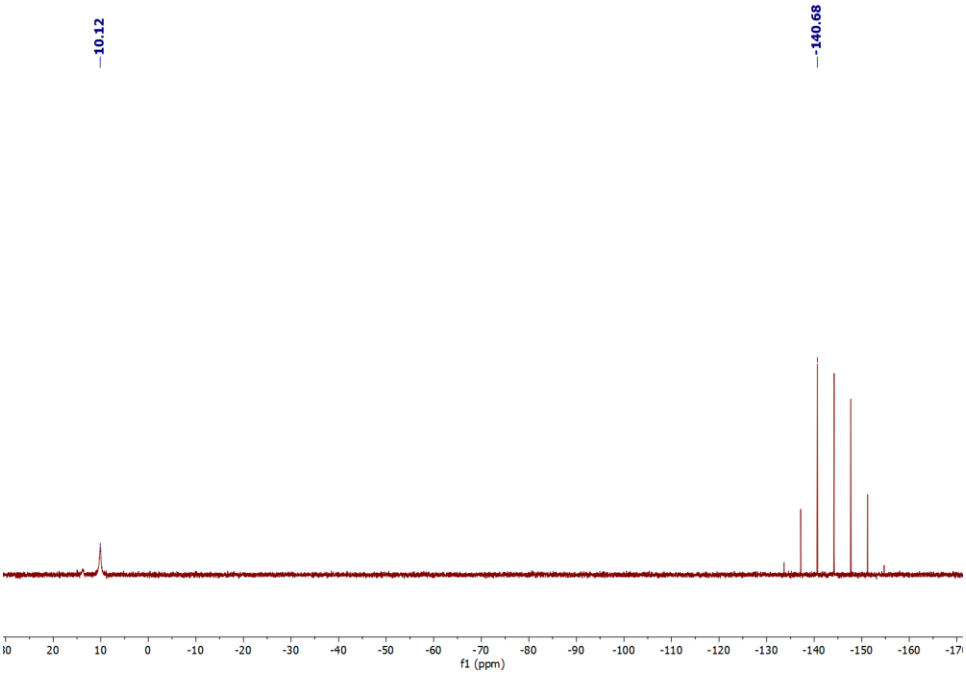

Fig. 5.25 $^{31}P\{^{1}H\}$ NMR spectrum of **9a** in DMSO-d6 (202 MHz).

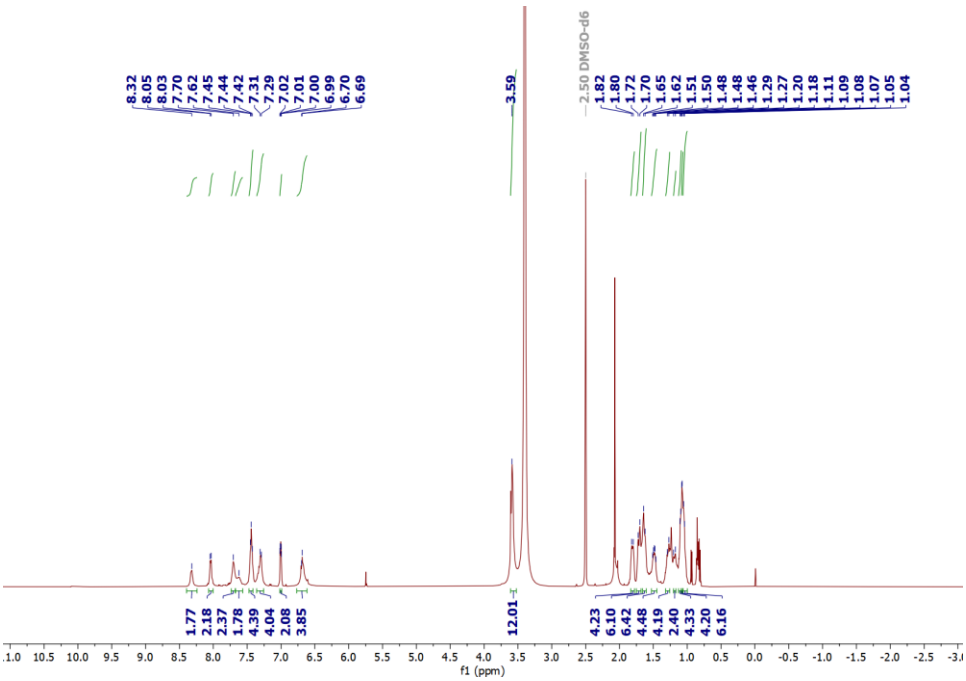

Fig. 5.26 ^{1}H NMR spectrum of **10a** in DMSO-d6 (500 MHz).

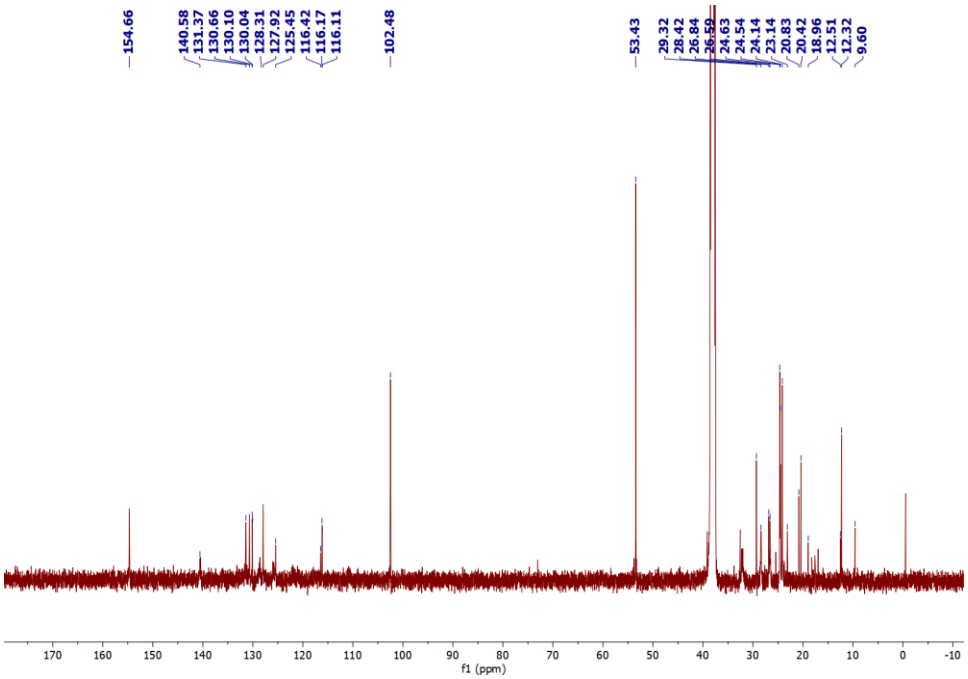

Fig. 5.27 $^{13}C\{^{1}H\}$ NMR spectrum of **10a** in DMSO-d6 (126 MHz).

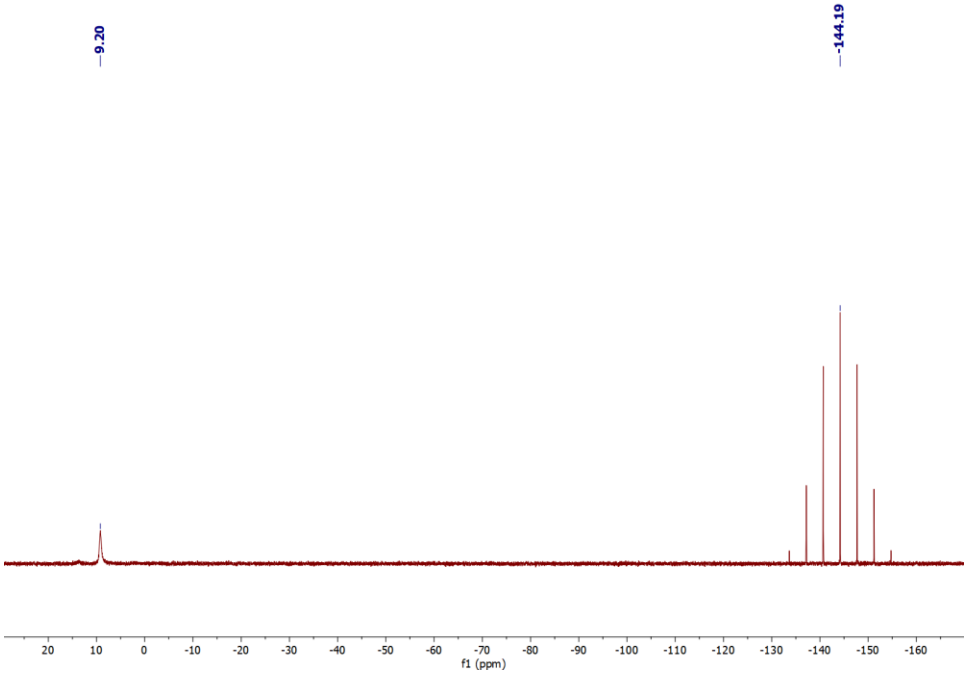

Fig. 5.28 $^{31}P\{^{1}H\}$ NMR spectrum of **10a** in DMSO-d6 (202 MHz).

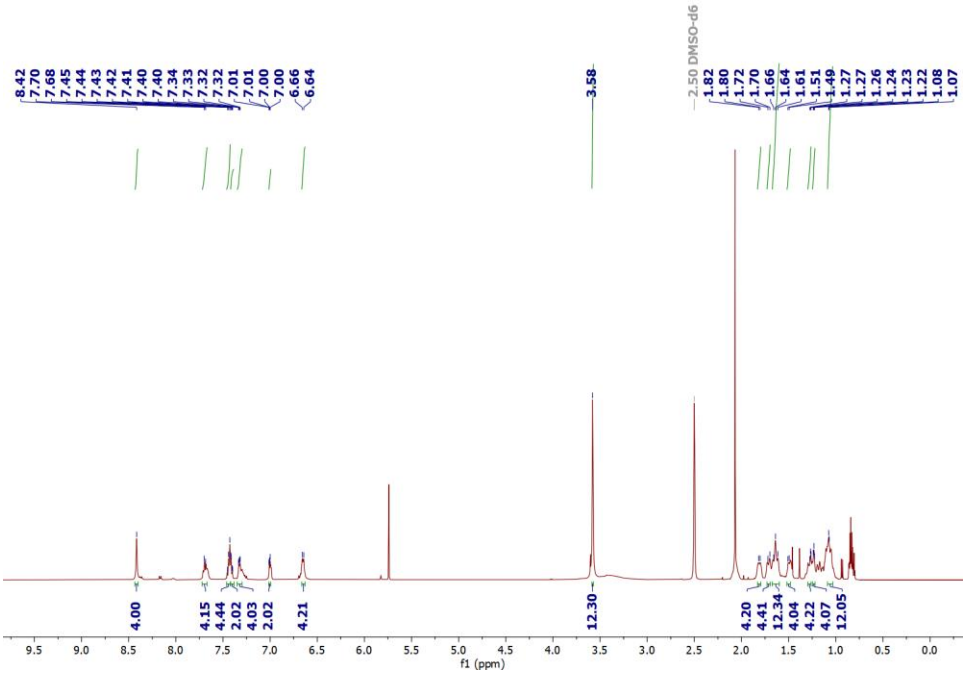

Fig. 5.29 ^{1}H NMR spectrum of **11a** in DMSO-d6 (500 MHz).

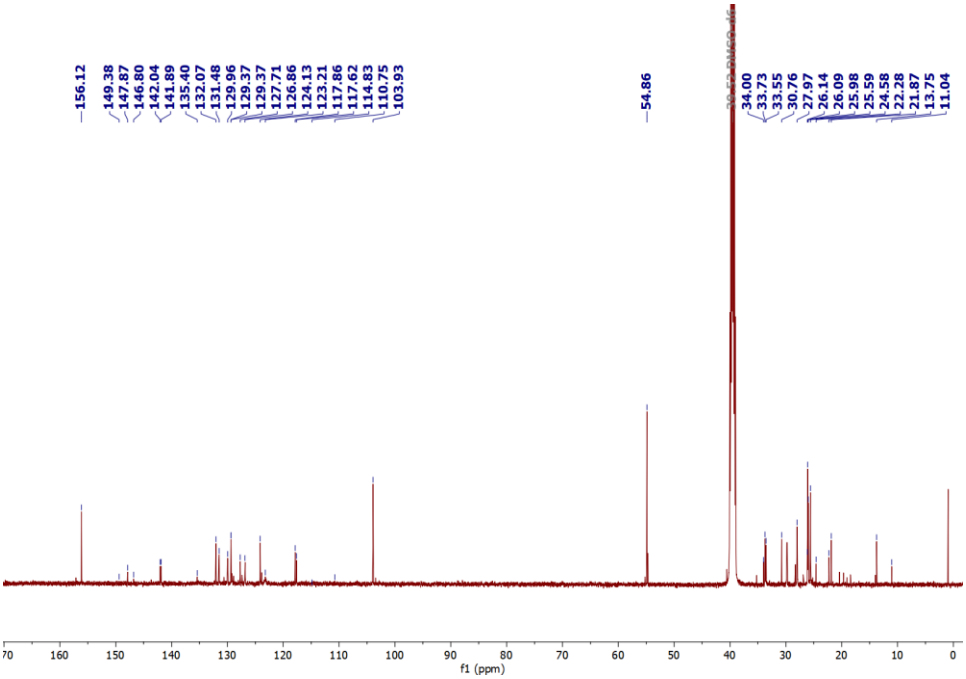

Fig. 5.30 ^{13}C{^{1}H} NMR spectrum of **11a** in DMSO-d6 (126 MHz).

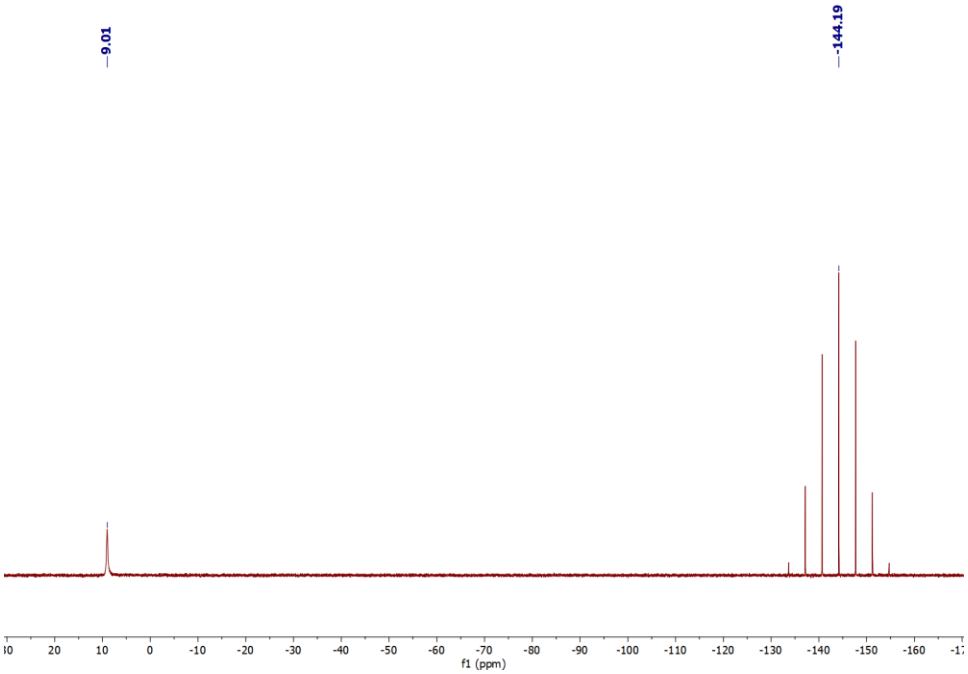

Fig. 5.31 $^{31}P\{^{1}H\}$ NMR spectrum of **11a** in DMSO-d6 (202 MHz).

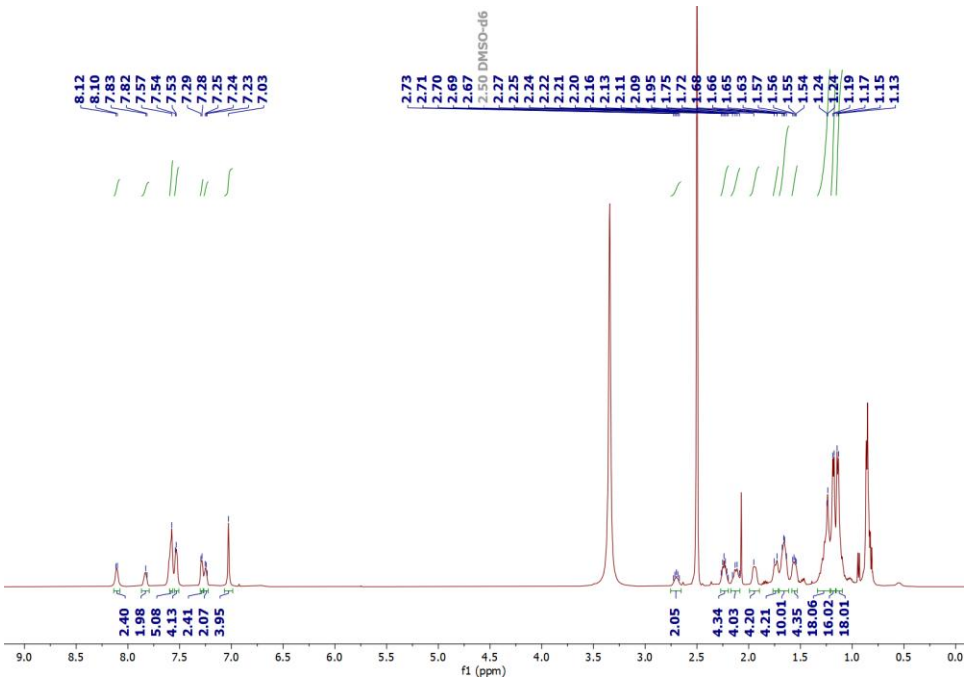

Fig. 5.32 ^{1}H NMR spectrum of **12a** in DMSO-d6 (500 MHz).

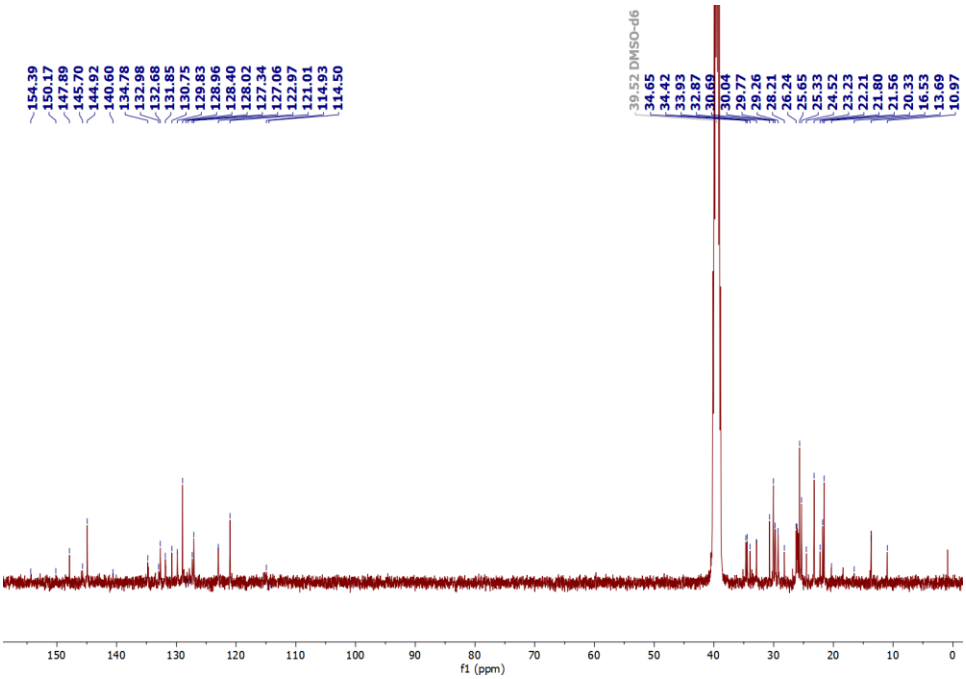

Fig. 5.33 $^{13}C\{^{1}H\}$ NMR spectrum of **12a** in DMSO-d6 (126 MHz).

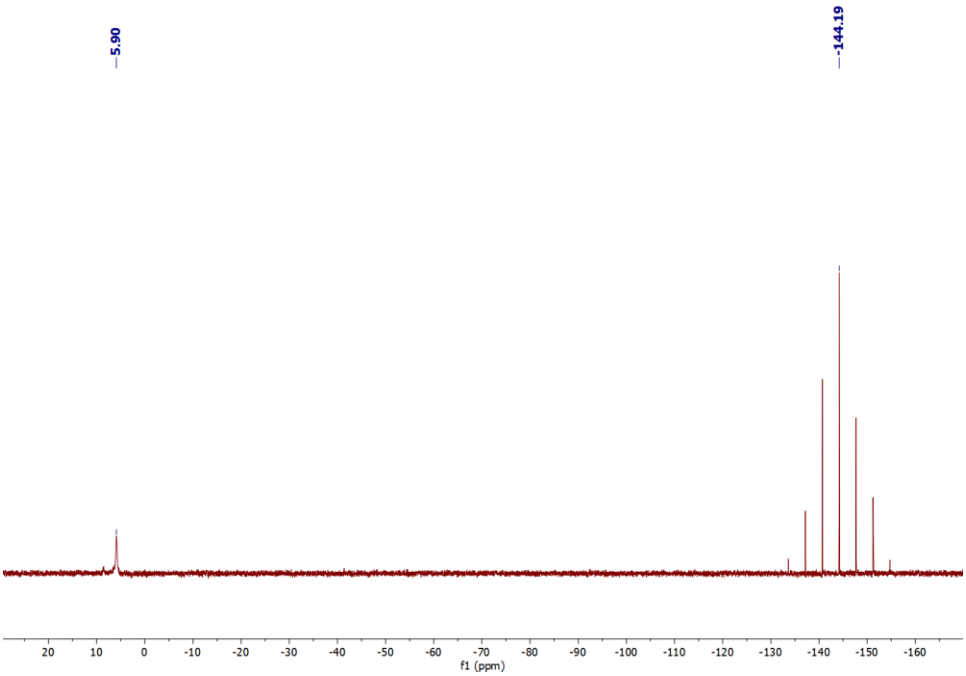

Fig. 5.34 $^{31}P\{^{1}H\}$ NMR spectrum of **12a** in DMSO-d6 (202 MHz).

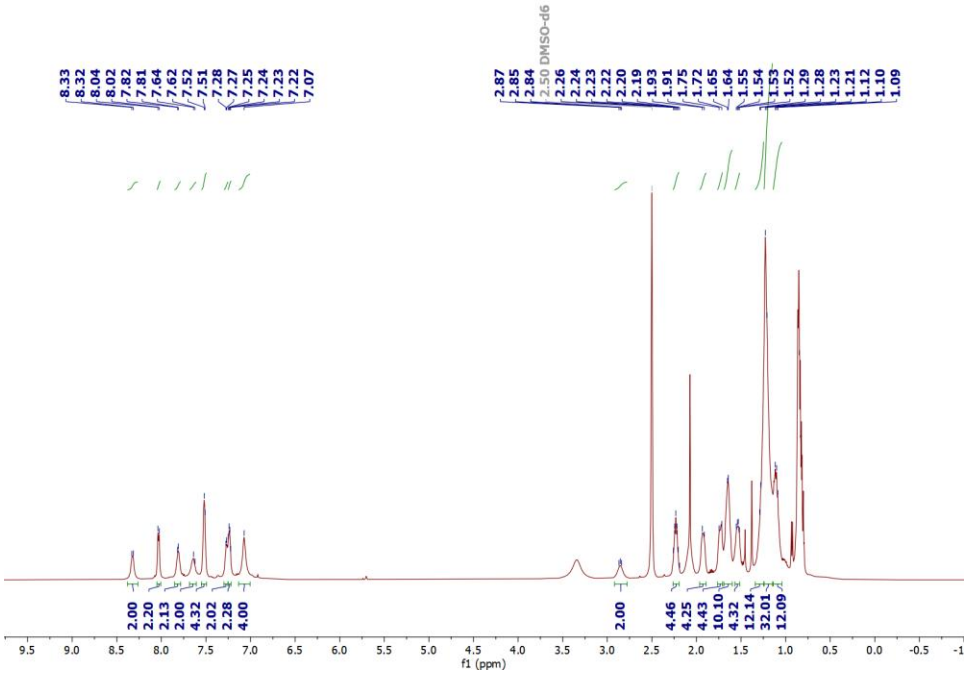

Fig. 5.35 ^{1}H NMR spectrum of **13a** in DMSO-d6 (500 MHz).

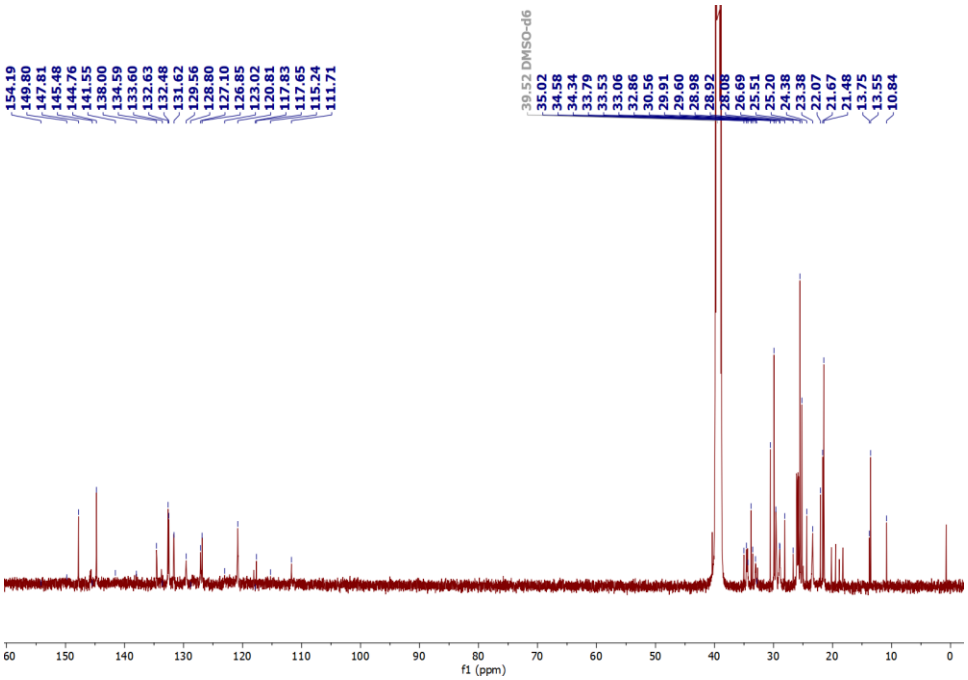

Fig. 5.36 ^{13}C{^{1}H} NMR spectrum of **13a** in DMSO-d6 (126 MHz).

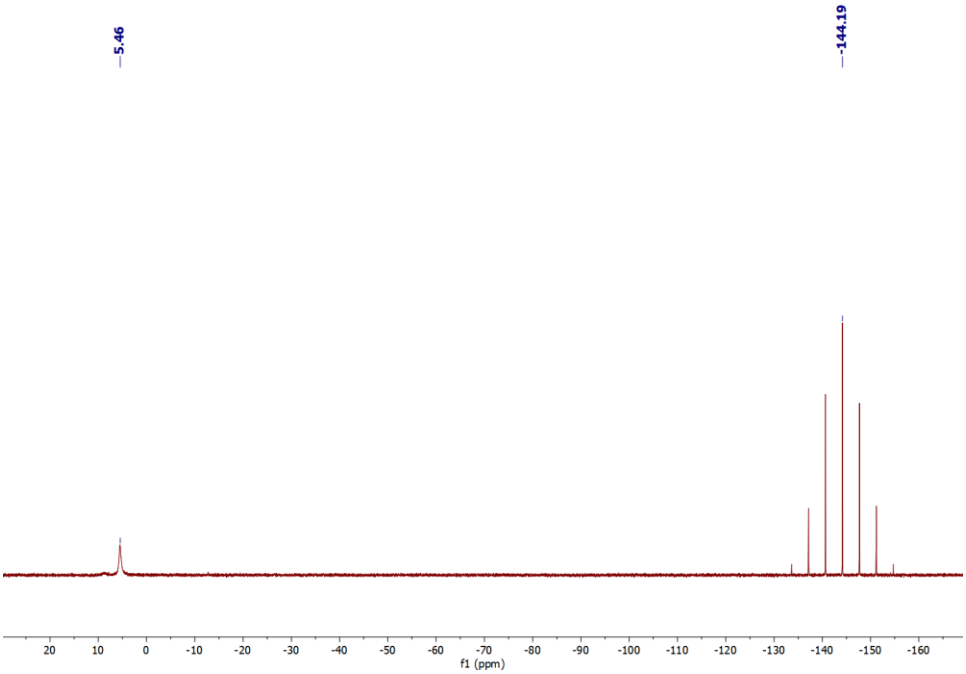

Fig. 5.37 $^{31}P\{^{1}H\}$ NMR spectrum of **13a** in DMSO-d6 (202 MHz).

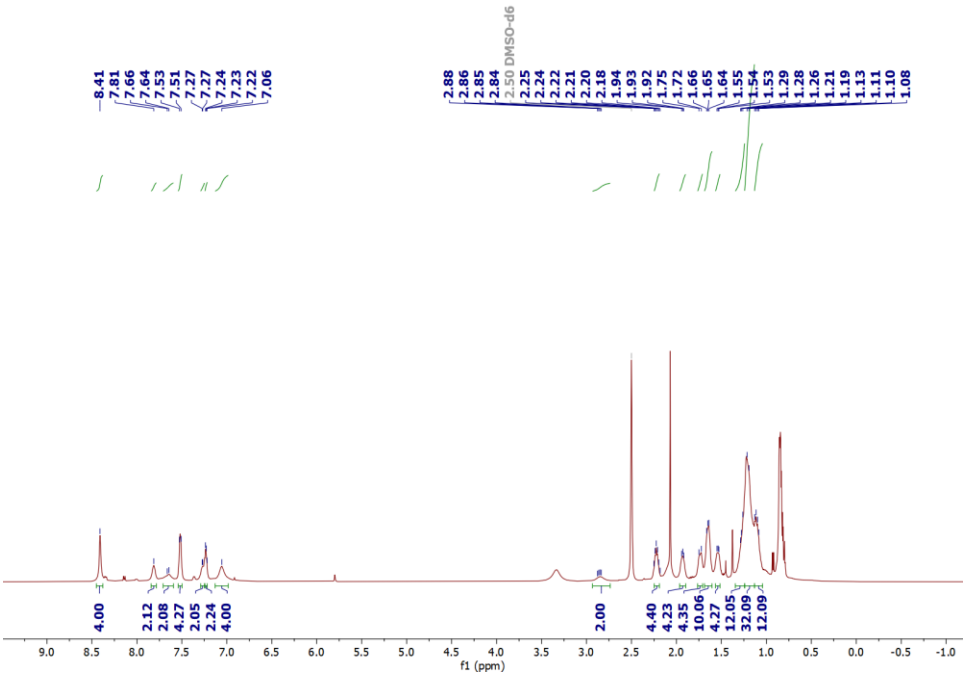

Fig. 5.38 ^{1}H NMR spectrum of **14a** in DMSO-d6 (500 MHz).

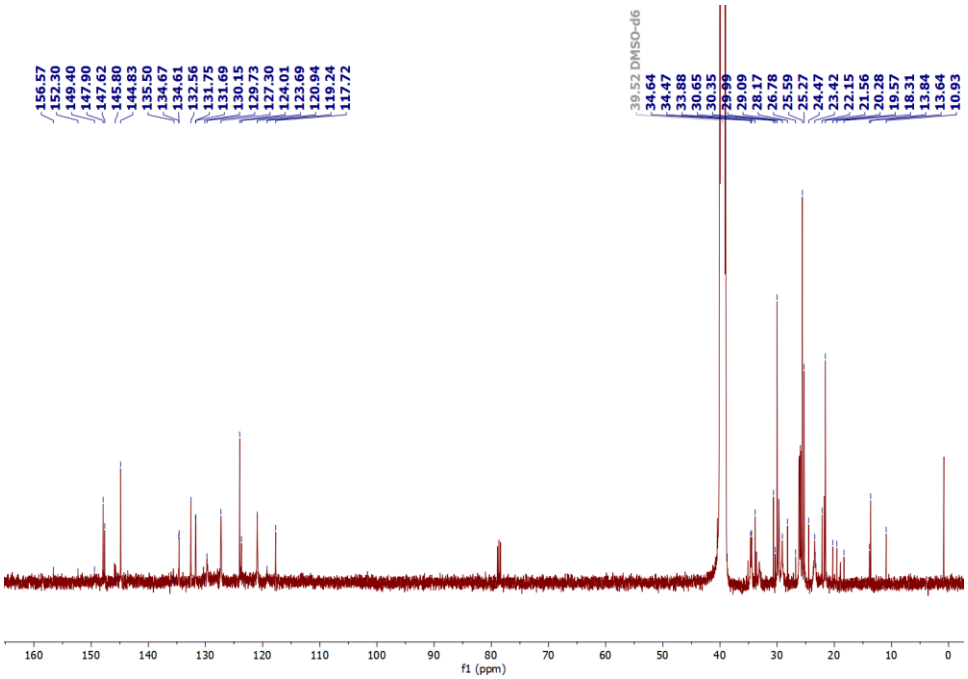

Fig. 5.39 $^{13}C\{^{1}H\}$ NMR spectrum of **14a** in DMSO-d6 (126 MHz).

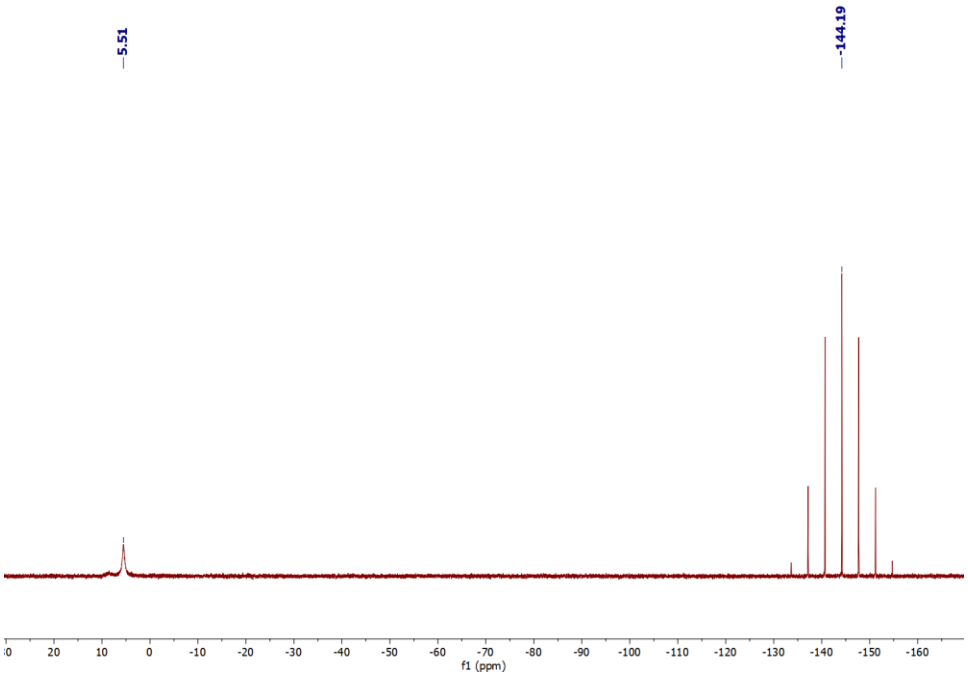

Fig. 5.40 $^{31}P\{^{1}H\}$ NMR spectrum of **14a** in DMSO-d6 (202 MHz).

5.4.1.1 Structural analysis

Single crystals of complexes **9** and **12a**, suitable for SC-XRD analysis, were grown by slow evaporation of a DCM solution with layering of n-hexane at room temperature. The obtained molecular structures are shown in **Fig. 5.41**. Both complexes crystallized in monoclinic crystal systems having P21/n and P21/c space groups, respectively. The complete crystallographic data and structure refinement details are summarized in **Table 5.1**.

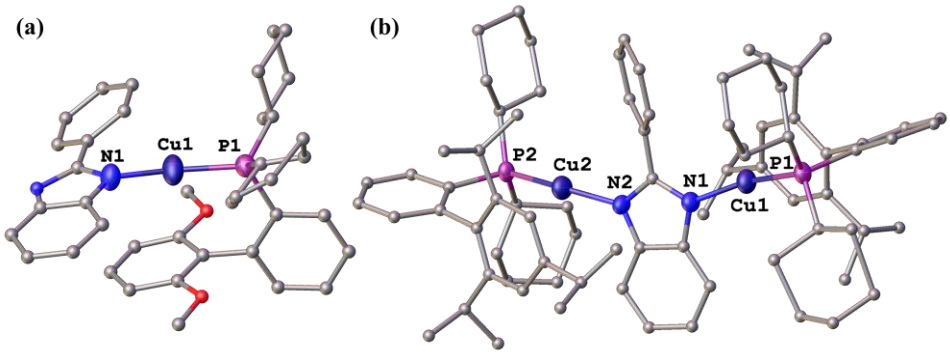

Fig. 5.41 Molecular structures of complexes 9 and 12a. Hydrogen atoms and counterions are omitted for clarity.

In both complexes, the coordination geometry around the Cu(I) center is found to be linear, in which the Cu(I) atom binds with one nitrogen atom of the PhBz ligand and one phosphorus atom from the phosphine ligand. In case of **12a** PhBz ligand acts as a bridging ligand between two copper atoms to form a bimetallic complex. A comparison of bond lengths and angles is tabulated in **Table 5.2**. It is found that the Cu-P bond distance in complex **9** is 2.14 Å, whereas in complex **12a** this distance is around 2.17 Å. The long bond distance in complex **12a** could be due to the bulky Xphos ligand compared to the Sphos ligand. Additionally, the Cu-N bond distances in both complexes are around 1.9 Å. Furthermore, the bond angle between P-Cu-N is found to be 160°, which confirms the near-linear geometry around the Cu(I) center, similar to previously reported linear carbene Cu(I) complexes *[1]*.

Table 5.1 Crystal and refinement data table of complexes **9** and **12a**.

Complex	**1**	**12a**
Empirical formula	$C_{28.5}H_{8.59}Cu_{0.5}F_3N_2OP$	$C_{79}H_{105.3}Cu_2F_6N_2P_3$
Formula weight	514.70	1417.64
Temperature/K	293(2)	293(2)
Crystal system	monoclinic	monoclinic
Space group	P21/n	P21/c
a/Å	15.1254(10)	16.4866(4)
b/Å	18.8491(9)	20.9077(6)
c/Å	15.8516(12)	23.1013(7)
α/°	90	90
β/ °	113.960(9)	100.555(3)
γ/°	90	90
Volume/ $Å^3$	4129.9(5)	7828.2(4)
Z	4	4
$\rho_{calc}g/cm^{-3}$	0.828	1.203
μ/mm^{-1}	0.345	0.660
R1 (R1 all data) [I > 2σ(I)]	0.2160	0.1340
wR2 (wR2 all data)	0.4921	0.3195
Data/restraints/parameters	7208/660/374	13766/273/864
GOF	1.639	1.035

Table 5.2 Selected bond lengths of complexes **9** and **12a**.

		Bond Length (Å)		Bond Angle (°)
9	P1-Cu1	2.144(3)	P1-Cu1-N1	161.9(5)
	N1-Cu1	1.873(13)		
12a	P1-Cu1	2.1667(15)	P1-Cu1-N1	162.04(16)
	P2-Cu2	2.1708(15)	P2-Cu2-N2	160.83(16)
	N1-Cu1	1.912(4)		
	N2-Cu2	1.917(4)		

5.4.1.2 Thermogravimetric analysis

The TGA curve suggests that all complexes were thermally stable up to 150-200 °C. The first step is about 10-15% weight loss due to decomposition of the counter ion, whereas the 65-70% weight loss is for the phosphine ligands. Additionally, decomposition of PhBz ligands begins starts from 300 °C.

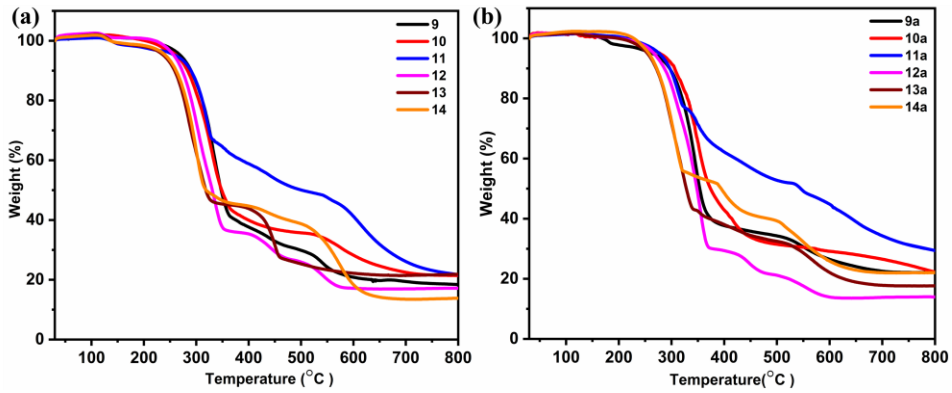

Fig. 5.42 TGA curve of a) **9-14** and b) **9a-14a** under nitrogen atmosphere with the temperature heating rate of 10 °C min^{-1}.

5.5 Photophysical properties and theoretical calculations

The UV-Vis absorption of all complexes was studied in acetonitrile (0.01 mM) solution, which is depicted in **Fig. 5.43**. The UV-Vis absorption spectra for monometallic and bimetallic complexes exhibit similar profiles, primarily influenced by the electronic nature of the PhBz ligands. Complexes containing PhBz ligands (**9**, **12**, **9a** and **12a**) show absorption at 300 nm, while complexes synthesized using CNPhBz (**10**, **13**, **10a** and **13a**) exhibit a bathochromic shift compared to PhBz-containing complexes, with maximum absorbance at 320 nm. Additionally, complexes containing more electron-withdrawing NO_2PhBz ligands (**11**, **14**, **11a** and **14a**) show further red-shifted absorption around 350 nm. These absorption band arises due to the spin-allowed metal-to-ligand charge transfer transition (MLCT) from the 3d orbital of the copper(I) to π* orbital of the PhBz ligands *[11–15]*.

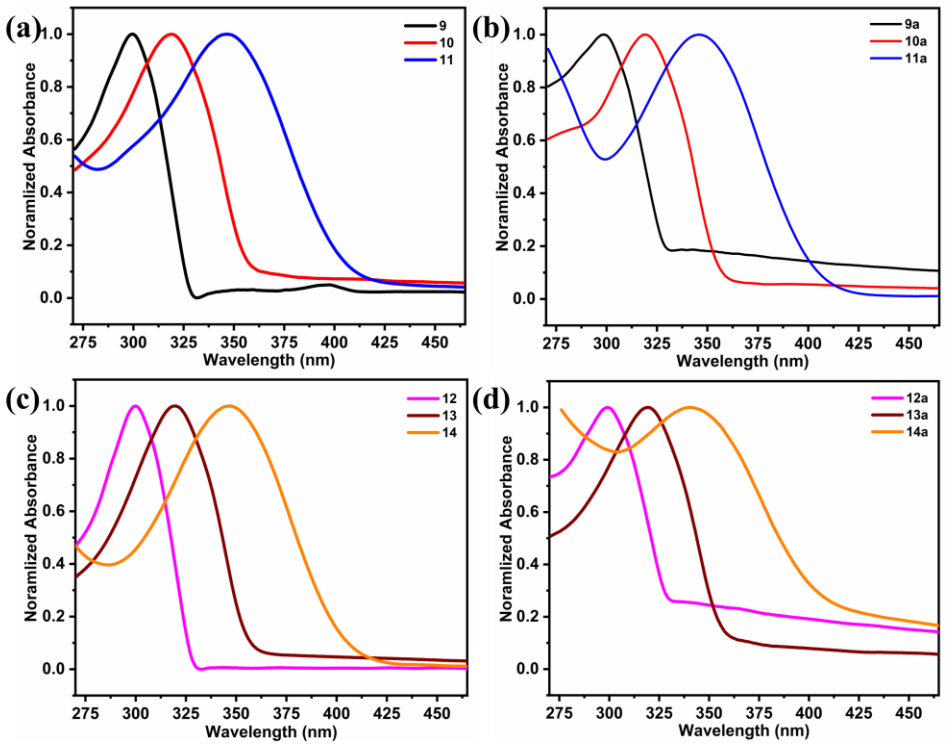

Fig. 5.43 Absorption spectra of a) **9-11**, b) **9a-11a**, c) **12-14** and **12a-14a** in ACN at room temperature.

To know the electronic transitions, theoretical calculations such as density functional theory (DFT) and time-dependent density functional theory (TD-DFT) were performed using the B3LYP with 6-31G (d, P) as functional and basis set. Based on the results of theoretical calculations, it was found that the HOMO is located on the Cu(I) center with some contributions of the phosphine ligands, whereas the LUMO is present on the PhBz ligands (**Fig. 5.44**). The calculated HOMO–LUMO energy gaps progressively decrease with increasing electron-withdrawing character of the ligand substituents, which is 3.68 eV for **9**, 3.20 eV for **10** while 2.94 eV for complex **11**, respectively. This trend highlights the stabilizing effect of electron-withdrawing groups (e.g., CN, NO_2) on the LUMO, thereby narrowing the energy gap and leading to red-shifted absorption features in complexes **10** and **11** compared to **9**. It is concluded that the electronic transitions occur from the copper(I) center 3d orbitals to the π* orbital of the PhBz ligands.

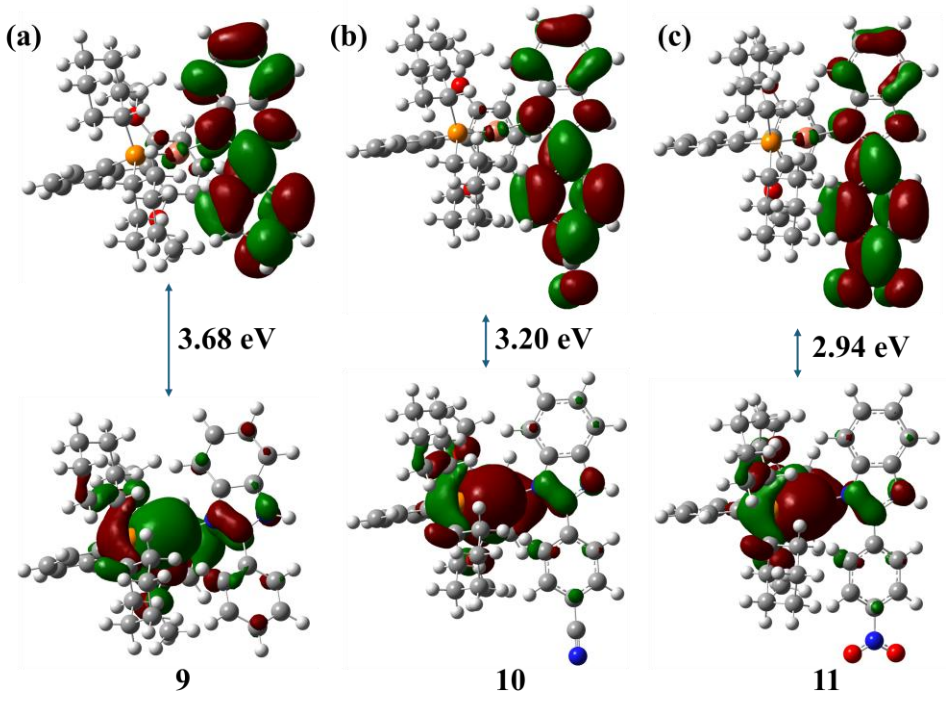

Fig. 5.44 Frontier molecular orbitals of complexes **9-11** obtained from B3LYP and 6-31G (d, P) level of theory. The counter ions are omitted for clarity.

Furthermore, we have compared the HOMO-LUMO between energy mono- and bimetallic complexes, which is presented in **Fig. 5.45**. It is found that in case of bimetallic complex the HOMO is located on phosphine, Cu(I) center as well as PhBz ligand whereas the LUMO is present on one of the phosphine ligand. This observation suggests that the charge transfer occurs via π-π* transitions. The HOMO-LUMO energy gap is increased in complex **12a** compared to **12**.

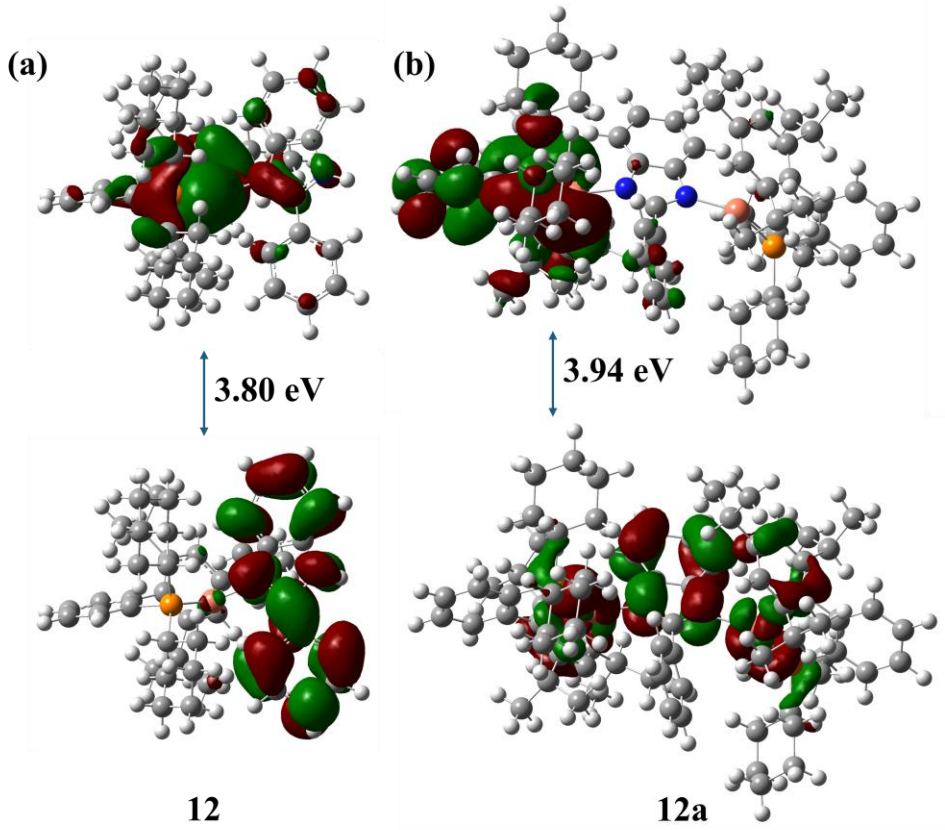

Fig. 5.45 Comparison between the HOMO-LUMO energy gap of mono (**12**) and bimetallic (**12a**) complexes.

All complexes exhibit emission in solution and the photoluminescence (PL) studies were performed in ACN solvent. The PL spectra and data are presented in **Fig. 5.46** and **Table 5.3**.

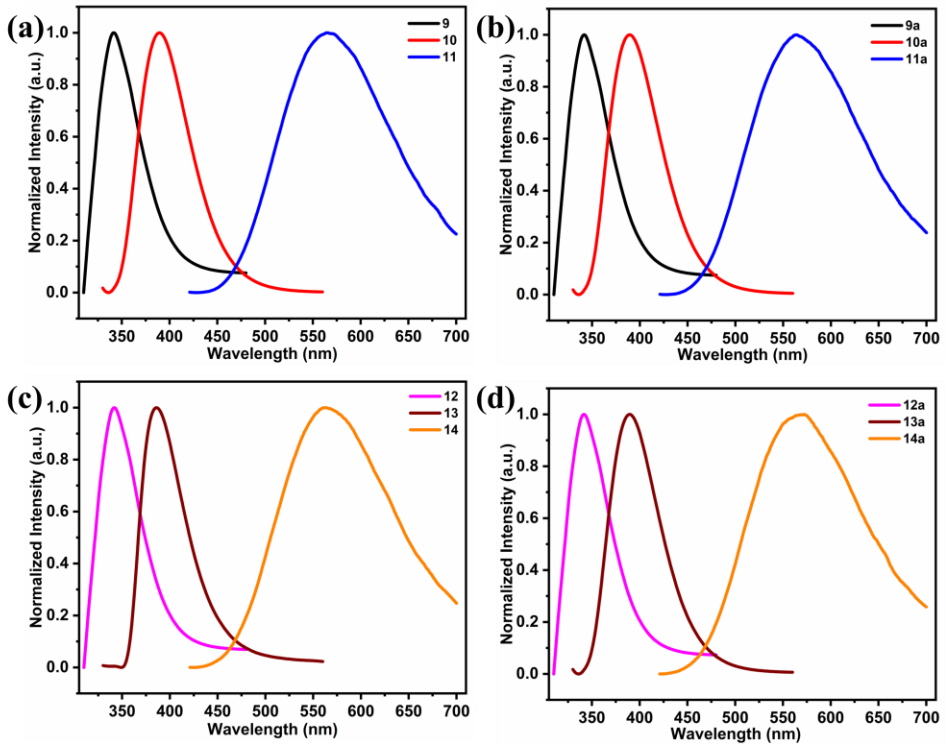

Fig. 5.46 Photoluminescence spectra of a) **9-11**, b) **9a-11a**, c) **12-14** and **12a-14a** in ACN at room temperature.

The emission spectrum demonstrates a structureless broad band spanning from UV to the orange region, specifically from 342 to 572 nm, depending on the electronic properties of PhBz ligands. Complexes **9**, **12**, **9a** and **12a** show emission at 342 nm with quantum yield up to 0.46 and lifetime of 1.69 to 1.74 ns, while complexes **10**, **13**, **10a** and **13a,** synthesized using CNPhBz, exhibit red-shifted emissions in the range of 386 to 389 nm having quantum yield of 0.11 to 0.17 and lifetime of 0.95 to 2.12 ns. Additionally, complexes **11**, **14**, **11a** and **14a**, which contain more electron-withdrawing NO_2PhBz ligands, show orange emission in between 562 to 572 nm with a low quantum yield and lifetimes ranging from 0.01 to 0.03 and 0.58 to 0.63 ns. As expected, complexes containing CNPhBz and NO_2PhBz ligands show red-shifted emissions compared to PhBz analogue. The trends observed in the emission spectrum correlate well with the absorption

spectra, supporting that the same electronic transitions are responsible for both processes.

Table 5.3 Photophysical data of ligands and complexes (in acetonitrile at room temperature).

Complex	Absorption (nm)	Emission (nm)	τ_{em} (ns)	Φ_{PL}[a]
9	300	342	1.74	0.21
10	320	389	2.12	0.11
11	350	566	0.58	0.03
12	300	342	1.81	0.37
13	320	386	2.82	0.17
14	350	562	0.59	0.02
9a	300	342	1.17	0.16
10a	320	389	2.02	0.12
11a	355	564	0.63	0.03
12a	300	342	1.69	0.46
13a	320	389	0.95	0.21
14a	350	572	0.60	0.01

[a]Relative quantum yield was calculated using the standard of quinine sulfate (0.1 M H_2SO_4) *[16]*.

Moreover, it is observed that in complexes **11**, **14**, **11a** and **14a,** the lifetime and quantum yield are significantly low compared to other complexes which could be due to the formation of twisted excited states, internal conversions, intermolecular interactions, intermolecular proton abstractions, thermal deactivation process, etc *[17–22]*. All complexes exhibit nanosecond lifetimes, suggesting a decay with a prompt fluorescence mechanism.

5.6 Electrochemical studies and Electrochromic behaviour.

The electrochemical activity of complexes **10**, **11**, **10a** and **11a** in solutions is evaluated from a three-electrode system consisting of blank ITO as the working, Pt wire as counter and Ag/AgCl as reference electrodes. The solution was prepared by adding 5 mg of the complex into the 0.1 M $LiClO_4$ in ACN. The cyclic voltammetry (CV) was carried out in the potential window of +3 V to -3 V at a scan rate of 100 mV/s (**Fig. 5.47**). As shown in **Fig. 5.47a** and **b**, complexes **10** and **10a** show similar redox couple peaks at -0.75 V (oxidation) and -2.5 V (reduction), confirming the redox nature of these complexes. During CV, it was observed that the complex was reversibly changing color from transparent to a dark black state (**Fig. 5.47a** and **b** insets), which is an important condition for the material to be called electrochromic active.

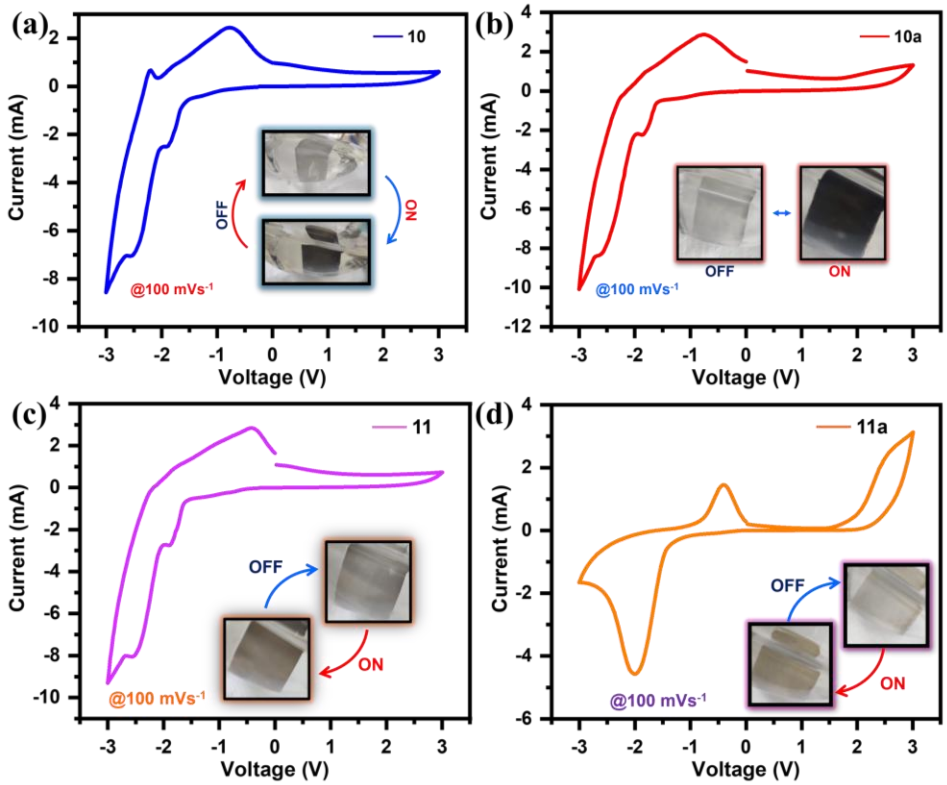

Fig. 5.47 Cyclic voltammetry curve of a) **10**, b) **10a**, c) **11** and d) **11a** studied using respective complex/ITO electrode in initial at ON (-2 V) and OFF (2 V) states with photographs of actual color change (Inset).

Additionally, complexes **11** and **11a** exhibit oxidation at the same potential of about -0.4 V, whereas different reductions occur at -2.5 and 2.0 V, respectively. During CV, it was observed that both complexes changed their colors from faint to a black state (**Figure 5.47c** and **d** insets). This study confirms the EC nature of complexes, suggesting that complexes **10**, **10a**, **11** and **11a** show the color change on the application of ±2 V.

5.6.1.1 Recipe for Rigid and Flexible ECDs Fabrication

For practical applications, the fabrication of electrochromic devices (ECDs) is essential. To this end, one monometallic complex (**11**) and one bimetallic complex (**11a**) were employed to construct a solid-state mono-layer device using TTF(Tetrathiafulvalene) as an ion storage layer having the configuration ITO//TTF//**11** or **11a**//ITO by a flip-chip method [23–27].

6. Fabrication of solid-state ***11****-ECD* or ***11a****-ECD*.

i. Firstly, ITO-coated glass of dimension 2×1 cm^2 was used as an electrode, which was thoroughly cleaned by ultrasonication in a solution containing acetone, isopropanol and DI water in an equal ratio for 10 minutes.

j. Approximately 0.5 wt.% complexes solution in acetonitrile (ACN) was spin-coated over the cleaned ITO substrate at 200 rpm for 60 minutes and was dried at 80 °C for a few minutes.

k. The Tetrathiafulvalene (TTF) an ion storage layer was prepared by dissolving 0.5 wt.% TTF in ACN and was drop casted (~50 µL) over ITO and dried at 80 °C for 5 minutes.

l. The gel electrolyte was prepared by mixing 0.1 M $LiClO_4$ in ACN and 5 wt.% polyethylene oxide (PEO) in equal proportion. The prepared gel electrolyte was sandwiched in between the two above-

prepared electrodes and was stuck together using the flip-chip method.

5.6.1.2 Electrochromic Performances of ECDs

As shown in **Fig. 5.48a**, it is observed that a color change between colorless and brown, a bias-dependent transmittance spectrum of ***complex 11-ECD*** was recorded in the range of 400 to 700 nm in the visible region. During the OFF or unbiased state, the device is colorless (bleached state) following the black curve, while bias is applied (ON condition, 2.2 V, concerning TTF) the color of the device changes to brown color (colored state) following the red curve (**Fig. 5.48a**). As seen from the transmittance spectra, the maximum change in transmittance was observed at 430 nm. The calculated value of CC at 430 nm is found to be 24%, which is exclusively due to the complex **11**, suggesting a reversible EC nature in ECDs.

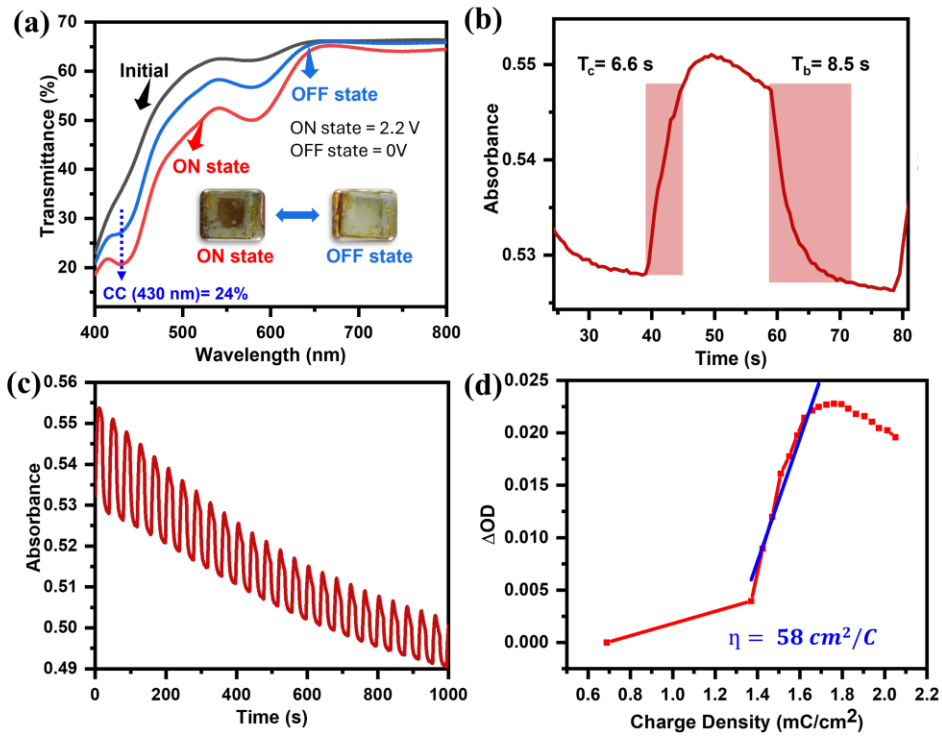

Fig. 5.48 (a) In-situ transmittance spectra of ***11-ECD*** during ON and OFF

conditions with actual photos of the device (inset) and (b) Single switching of the device (c) cyclic stability of the ***11-ECD*** for 1000 seconds (d) variation in change in optical density as a function of total charge used for ***11-ECD*** with marked slope.

The switching time of ***11-ECD*** is calculated and found to be 6.6 s for switching from colorless to brown color, whereas 8.5 s is required to switch back into the colorless state, which is determined at 90% of the device's total coloration and bleaching phenomenon (**Fig. 5.48b**). Furthermore, the ***complex 11-ECD*****'s** cyclic stability was also tested by giving a continuous pulse train of 2.2 V (10 s). The device shows less cyclic stability for up to 1000 s cycles, which could be due to less stability of the two coordinated Cu(I) complexes (**Fig. 5.48c**). Another main parameter of the ECD performance is coloration efficiency (CE), which is found to be 58 cm^2/C (**Fig. 5.48d**). The overall study suggests the EC nature of monometallic complex **11** and may be used for EC display applications.

As the monometallic complex shows moderate results in terms of CC, stability and EC. To improve the values of device performance, another rigid ECD using bimetallic complex **11a** (***11a-ECD***) was fabricated (**Recipe 5.6.1.1**). The ***11a-ECD*** has the structure of "ITO/**11a**//TTF + gel electrolyte/ITO". Initially, the in-situ bias-dependent transmittance has been recorded by applying 2.2 V to the device in the wavelength range of 400 to 700 nm. The device is colorless in the unbiased (OFF) state, the black curve (**Fig. 5.49a**). As the bias of 2.2 V is applied (ON condition), the device color changed from colorless to brown due to the redox reaction taking place between the **11a** and TTF (**Fig. 5.49a, red curve and inset**). The calculated CC was found to be 27.6% at 430 nm, which is due to the complex **11a,** because TTF is not taking part in the color change. The device kinematics has been studied by applying a square pulse of 2.2 V for 10 seconds and the time was calculated at 90% of the total coloration and

bleaching. The estimated switching times are 11.4 and 2.7 s, respectively, for coloration and bleaching (**Fig. 5.49b**).

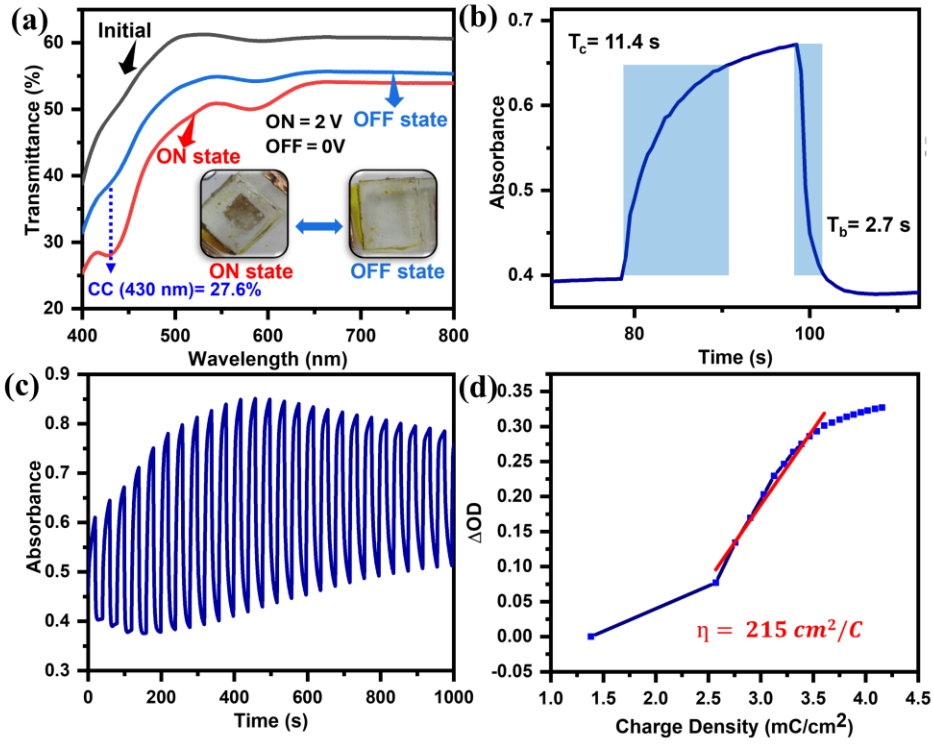

Fig. 5.49 (a) In-situ bias-dependent transmittance spectra of ***11a-ECD*** during ON and OFF conditions with actual photos of the device and (b) Single switching of the device (c) cyclic stability of the ***11a-ECD*** for 1000 seconds (d) Graph for evaluating coloration efficiency of the ***11a-ECD*** with marked slope.

Additionally, the cyclic stability of the ***11a-ECD*** was estimated by applying a pulse train of 2.2 V for 1000s (**Fig. 5.49c**) and the calculated EC value for this device is found to be 215 cm^2/C (**Fig. 5.49d**). The results suggest that ***11a-ECD*** exhibits good performance compared to ***11-ECD*** because the bimetallic **11a** complex is more stable compared to **11** during the operation of the device. Overall, a bimetallic complex containing ECD exhibits good results in terms of CC and CE; therefore, it could be used for the practical application of ECDs fabrication.

5.7 Conclusion

This work highlights the effectiveness of strategic ligand design in the development of low-coordinate Cu(I) complexes with tunable photophysical properties, offering potential for a variety of applications. In this study, we have synthesized and characterized a series of two-coordinate mono- and bimetallic Cu(I) complexes stabilized by bulky phosphine (Sphos and Xphos) and substituted 2-phenylbenzimidazole ligands. To the best of our knowledge, this is the first report describing two-coordinate bimetallic Cu(I) complexes with linear geometry. These complexes exhibit tunable photophysical properties, with fluorescence emission spanning the UV-visible region. Systematic ligand modification through electron-withdrawing substituents (CN and NO_2) on the PhBz ligand framework significantly influences the electronic structure by stabilizing the LUMO, resulting in a progressive narrowing of the HOMO–LUMO energy gap and corresponding red-shifted absorption and emission. Computational studies corroborate experimental trends and confirm the (M+L→L)CT nature of the emissive excited states. Additionally, complexes **11** and **11a** exhibit good reversible redox couple peaks with good color change from transparent to brown, which suggests the electrochromic behaviour of these complexes. The fabricated ***11-ECD*** exhibits CE of 58 cm^2/C with 6.6 and 8.5 switching times, whereas ***11-ECD*** shows a high CE of 215 cm^2/C compared to ***11-ECD*** having 11.4 and 2.7 switching times. By thoroughly investigating the performance of ECDs, it is concluded that the bimetallic complex containing devices show good EC properties and could be a great choice for real-life applications.

5.8 References

1. Hölzel T., Belyaev A., Terzi M., Stenzel L., Gernert M., Marian C.M., Steffen A., Ganter C., (2021), Linear Carbene Pyridine Copper Complexes with Sterically Demanding N,N′-Bis(Trityl)Imidazolylidene: Syntheses, Molecular Structures, and Photophysical Properties, Inorg Chem, 60, 18529–18543 (DOI: 10.1021/acs.inorgchem.1c03082)
2. Ying A., Huang Y.-H., Lu C.-H., Chen Z., Lee W.-K., Zeng X., Chen T., Cao X., Wu C.-C., Gong S., (2021), High-Efficiency Red Electroluminescence Based on a Carbene–Cu(I)–Acridine Complex, ACS Appl Mater Interfaces, 13, 13478–13486 (DOI: 10.1021/acsami.0c22109)
3. Lüdtke N., Föller J., Marian C.M., (2020), Understanding the Luminescence Properties of Cu(I) Complexes: A Quantum Chemical Perusal, Phys Chem Chem Phys, 22, 23530–23544 (DOI: 10.1039/D0CP04654J)
4. Shi S., R. Collins L., F. Mahon M., I. Djurovich P., E. Thompson M., K. Whittlesey, M., (2017), Synthesis and Characterization of Phosphorescent Two-Coordinate Copper(i) Complexes Bearing Diamidocarbene Ligands, Dalton Trans, 46, 745–752 (DOI: 10.1039/C6DT04016K)
5. Hamze R., Peltier J.L., Sylvinson D., Jung M., Cardenas J., Haiges R., Soleilhavoup M., Jazzar R., Djurovich P.I., Bertrand G., (2019), Eliminating Nonradiative Decay in Cu(I) Emitters: >99% Quantum Efficiency and Microsecond Lifetime, Science, 363, 601–606 (DOI: 10.1126/science.aav2865)
6. Li T.-Y., Zheng S.-J., Djurovich P.I., Thompson M.E., (2024), Two-Coordinate Thermally Activated Delayed Fluorescence Coinage Metal Complexes: Molecular Design, Photophysical Characters, and Device Application, Chem Rev, 124, 4332–4392 (DOI: 10.1021/acs.chemrev.3c00761)

7. Song X.-F., Li Z.-W., Chen W.-K., Gao Y.-J., Cui G., (2022), Thermally Activated Delayed Fluorescence Mechanism of a Bicyclic “Carbene–Metal–Amide” Copper Compound: DFT/MRCI Studies and Roles of Excited-State Structure Relaxation, Inorg Chem, 61, 7673–7681 (DOI: 10.1021/acs.inorgchem.1c03603)
8. Dolomanov O.V., Bourhis L.J., Gildea R.J., Howard J. a. K., Puschmann H., (2009), OLEX2: A Complete Structure Solution, Refinement and Analysis Program, J Appl Crystallogr, 42, 339–341 (DOI: 10.1107/S0021889808042726.
9. Sheldrick G.M., Schneider T.R., (1997), SHELXL: High-Resolution Refinement. In Methods in Enzymology; Macromolecular Crystallography Part B; Academic Press, 277, 319–343
10. Wu T.-C., Zhao F.-Z., Hu Q.-L., Cui Y.-S., Huang T.-H., Zheng D., Liu Q., Lei Y. Jia, L., Luo C., (2020), Structural Characterization, DFT Studied, Luminescent Properties of Cationic/Neutral Three-Coordinated Copper (I) Complexes and Application in Warm-White Light-Emitting Diode, Appl Organomet Chem, 34, e5691 (DOI: 10.1002/aoc.5691)
11. Zhang Y., Schulz M., Wächtler M., Karnahl M., Dietzek B., (2018) Heteroleptic Diimine–Diphosphine Cu(I) Complexes as an Alternative towards Noble-Metal Based Photosensitizers: Design Strategies, Photophysical Properties and Perspective Applications, Coord Chem Rev, 356, 127–146 (DOI: 10.1016/j.ccr.2017.10.016)
12. Kharabe L.S., Ghosh T., Pandey D., Kumar R., Raghuvanshi A., (2024), Heteroleptic Cu(I) Complex with Vapochromism and Its Application as Electrochromic Material, Appl Organomet Chem, 38, e7451 (DOI: 10.1002/aoc.7451)
13. Wada A., Zhang Q., Yasuda T., Takasu I., Enomoto S., Adachi C., (2012), Efficient Luminescence from a Copper(i) Complex Doped in Organic Light-Emitting Diodes by Suppressing C–H Vibrational

Quenching, Chem Commun, 48, 5340–5342 (DOI: 10.1039/C2CC31509B)

14. Vogler A., Kunkely H., (2002), Excited State Properties of Transition Metal Phosphine Complexes, Coord Chem Rev, 230, 243–251 (DOI: 10.1016/S0010-8545(01)00438-6)
15. Li Z.-X., Kuang X.-N., Wang G., Zhu N., Sun Z.-Z., Han H.-L., Yang Y.-P., Li Z.-F., Xin X.-L., Jin Q.-H., (2021), A Series of Luminescent Cu(i) Complexes Based on the Diphosphine Ligand and Diimine Ligand: Weak Intermolecular Interactions, Terahertz Spectroscopy and Photoproperties, CrystEngComm, 23, 8323–8333 (DOI: 10.1039/D1CE01132D)
16. Wong K.-L., Bünzli J.-C.G., Tanner P.A., (2020), Quantum Yield and Brightness, J Lumin, 224, 117256 (DOI: 10.1016/j.jlumin.2020.117256)
17. Mahesha P., Shetty N.S., Sinha R.K., Kulkarni S.D., Shetty P., Shreeja S.R., Lewis P.M., (2022), Synthesis, DFT, and Photophysical Studies of Substituted Pyridine Carbonitrile Derivatives, J Mol Struct, 1270, 133958 (DOI: 10.1016/j.molstruc.2022.133958)
18. Demchenko A.P., (2020), Photobleaching of Organic Fluorophores: Quantitative Characterization, Mechanisms, Protection*, Methods Appl Fluoresc, 8, 022001 (DOI: 10.1088/2050-6120/ab7365)
19. Gandioso A., Contreras S., Melnyk I., Oliva J., Nonell S., Velasco D., García-Amorós J., Marchán V., (2017), Development of Green/Red-Absorbing Chromophores Based on a Coumarin Scaffold That Are Useful as Caging Groups, J Org Chem, 82, 5398–5408 (DOI: 10.1021/acs.joc.7b00788)
20. Xu C., (2010), Photophysical Properties of a New Ternary Europium Complex with 2-Thenoyltrifluoroacetone and 5-Nitro-1,10-Phenanthroline, J Rare Earths, 28, 854–857 (DOI: 10.1016/S1002-0721(09)60229-5)

21. Shi S., Liu J., Li J., C., (2005), Zheng, K.; P. Tan, C.; M. Chen, L.; N. Ji, L. Electronic Effect of Different Positions of the –NO 2 Group on the DNA-Intercalator of Chiral Complexes [Ru(Bpy) 2 L] 2+ (L = o -Npip, m -Npip and p -Npip), Dalton Trans, 0, 2038–2046 (DOI: 10.1039/B501112D)
22. Sonoda Y., Tsuzuki S., Goto M., Tohnai N., Yoshida M., (2010), Fluorescence Spectroscopic Properties of Nitro-Substituted Diphenylpolyenes: Effects of Intramolecular Planarization and Intermolecular Interactions in Crystals, J Phys Chem A, 114, 172–182 (DOI: 10.1021/jp907441p)
23. Kandpal S., Ghosh T., Rani C., Rani S., Pathak D.K., Tanwar M., Bhatia R., Sameera I., Kumar R., (2022), MoS2 Nano-Flower Incorporation for Improving Organic-Organic Solid State Electrochromic Device Performance, Sol Energy Mater Sol Cells, 236, 111502 (DOI: 10.1016/j.solmat.2021.111502)
24. Kandpal S., Ghosh T., Rani C., Tanwar M., Sharma M., Rani S., Pathak D.K., Bhatia R., Sameera I., Jayabalan J., (2022), Bifunctional Application of Viologen-MoS2-CNT/Polythiophene Device as Electrochromic Diode and Half-Wave Rectifier, ACS Mater Au, 2, 293–300 (DOI: 10.1021/acsmaterialsau.1c00064)
25. Chaudhary A., Pathak D.K., Mishra S., Yogi P., Sagdeo P.R., Kumar R., (2019), Enhancing Viologen's Electrochromism by Incorporating Thiophene: A Step Toward All-Organic Flexible Device, Phys Status Solidi A, 216, 1800680 (DOI: 10.1002/pssa.201800680)
26. Mishra S., Yogi P., K. Saxena S., Roy S., R. Sagdeo P., Kumar R., (2017), Fast Electrochromic Display: Tetrathiafulvalene–Graphene Nanoflake as Facilitating Materials, J Mater Chem C, 5, 9504–9512 (DOI: 10.1039/C7TC02913F)
27. Min Kim Y., Li X., Kim K.-W., Hyun Kim S., Chul Moon H., (2019), Tetrathiafulvalene: Effective Organic Anodic Materials for WO 3 -

Based Electrochromic Devices, RSC Adv, 9, 19450–19456 (DOI: 10.1039/C9RA02840D)

Chapter 6

General conclusion and future scope

6.1 Conclusions

This thesis reports the systematic design, synthesis, and comprehensive characterization of a diverse family of two-, three-, and four-coordinate ionic Cu(I) complexes. The investigated systems include four-coordinate complexes, $[Cu(PPh_3)_2(dicnq)]PF_6$ (**1**), $[Cu(DPEphos)(dicnq)]PF_6$ (**2**) and $[Cu(Xantphos)(dicnq)]PF_6$ (**3**), $[Cu(PPh_3)_2(cmdf)]PF_6$ (**4**), $[Cu(DPEphos)(cmdf)]PF_6$ (**5**) and $[Cu(Xantphos)(cmdf)]PF_6$ (**6**); three-coordinated complexes, $[Cu(Sphos)cmdf]PF_6$ (**7**) and $[Cu(Xphos)(cmdf)]PF_6$ (**8**); two-coordinate monometallic complexes $[Cu(Sphos)(CNPhBz)]PF_6$ (**10**), $[Cu(Sphos)(NO_2PhBz)]PF_6$ (**11**), $[Cu(Xphos)(PhBz)]PF_6$ (**12**), $[Cu(Xphos)(CNPhBz)]PF_6$ (**13**), $[Cu(Xphos)(NO_2PhBz)]PF_6$ (**14**) as well as their corresponding bimetallic complexes $[(CuSphos)_2(PhBz)]PF_6$ (**9a**), $[(CuSphos)_2(CNPhBz)]PF_6$ (**10a**), $[(CuSphos)_2(NO_2PhBz)]PF_6$ (**11a**), $[(CuXphos)_2(PhBz)]PF_6$ (**12a**), $[(Cu(Xphos)_2(CNPhBz)]PF_6$ (**13a**), $[(CuXphos)_2(NO_2PhBz)]PF_6$ (**14a**).

All complexes were rigorously characterized using complementary spectroscopic, electrochemical, and structural techniques, enabling clear correlations between coordination environment, ligand architecture and physicochemical properties.

A major outcome of this work is the successful translation of molecular Cu(I) complexes into ECDs architectures. Most of the synthesized complexes were effectively integrated into solid-state as well as flexible ECD. Their electrochromic performance metrics, including color contrast, coloration efficiency and switching time were systematically evaluated and summarized in **Table 6.1**. These results demonstrate that ionic Cu(I) complexes can serve as viable electrochromic active materials, offering a molecular-level alternative to conventional inorganic oxides and polymer-based systems.

Table 6.1 Comparison of ECD performance between all the Cu(I) complexes used for the ECD fabrications.

Complexes	EC System	Wavelength (nm)	CC (%)	Response time (s)	CE (cm^2/C)
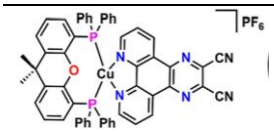	ITO//P3HT//3//ITO	520 800	40 38	0.8/0.5 2/1	230 120
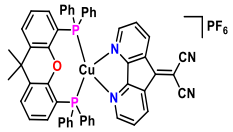	ITO//TTF//6//ITO	515	15	6.9/6.7	-
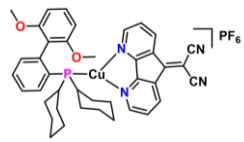	ITO//P3HT//6//ITO **ITO//TTF//7//ITO**	515 **430**	45 **42**	0.4/1.4 **5.3/4.5**	191 **690**
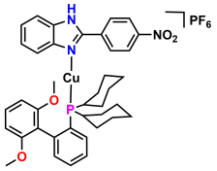	ITO//TTF//11//ITO	430	24	6.6 and 8.5	58
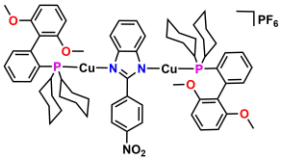	ITO//TTF//11a//ITO	430	27	11.4 and 2.7	215

Notably, the three-coordinate Cu(I) complex exhibit superior electrochromic performance, particularly in terms of coloration efficiency. This enhancement can be attributed to their electronically unsaturated coordination environment, which facilitates reversible redox processes and efficient charge injection at relatively low operating voltages. The observed performance is comparable to, and in some cases exceeds, that of previously reported electrochromic materials.

Overall, this thesis establishes clear structure-property-function relationships linking coordination geometry, ligand architecture and device-level electrochromic behavior. The findings not only expand the fundamental understanding of Cu(I) coordination chemistry but also provide practical design principles for the development of next-generation, low-cost, and energy-efficient electrochromic materials. The modular nature of the ligand frameworks employed herein offers ample scope for future optimization, including tuning of redox potentials, enhancement of long-term device stability, and extension toward multifunctional applications.

6.2 Future scopes

The outcomes of this thesis establish ionic Cu(I) complexes as promising molecular platforms for electrochromic and optoelectronic applications, while simultaneously highlighting several opportunities for further advancement. One of the most immediate future directions lies in ligand framework optimization. Systematic incorporation of π-extended, redox-active, or electronically asymmetric ligands could enable finer control over redox potentials, optical bandgaps, and color tunability.

The modular nature of the Cu(I) coordination chemistry developed in this thesis also offers opportunities to expand beyond electrochromism toward multifunctional materials. Integration of luminescent and electrochromic properties within a single molecular system could lead to dual-mode devices for smart displays or adaptive optics. Furthermore, the redox activity and coordination flexibility of these complexes suggest potential applicability in chemical sensing, particularly for redox-active gases or vapors, where simultaneous optical and electrical signal transduction may be exploited.

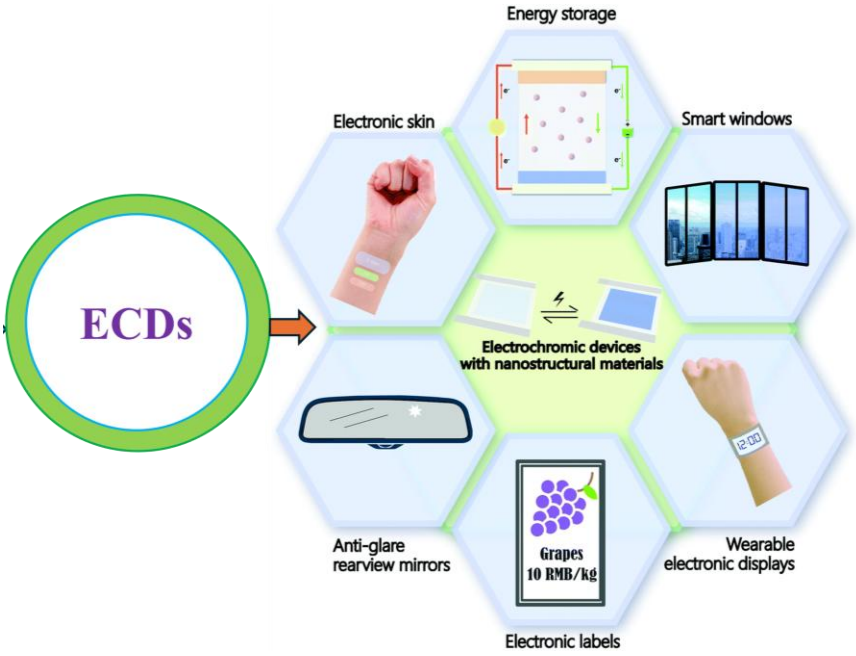

Fig. 6.1 Applications of ECDs.

In summary, the findings presented in this thesis provide a robust foundation for continued exploration of Cu(I)-based functional materials. Through combined advances in molecular design, device engineering, and mechanistic understanding, this research can be extended toward technologically relevant, low-cost, and energy-efficient electrochromic and optoelectronic systems.